

# THÈSE

Pour obtenir le grade de

## DOCTEUR DE L'UNIVERSITÉ SAVOIE MONT BLANC

Spécialité : **Physique Subatomique et Astroparticules**

Arrêté ministériel : 25 Mai 2016

Présentée par

**Gitanjali PODDAR**

Thèse dirigée par **Emmanuel SAUVAN** et  
codirigée par **Narei LORENZO MARTINEZ**

préparée au sein du **Laboratoire d'Annecy de Physique des  
Particules**  
dans l'**École Doctorale de Physique de Grenoble**

# Étude de la diffusion Z-photon et mise à niveau de la carte de calibration électronique à argon liquide avec le détecteur ATLAS

Thèse soutenue publiquement le **06 octobre 2023**,  
devant le jury composé de :

**M. David CHARLTON**

Professeur, University of Birmingham, Rapporteur

**M. Claude CHARLOT**

Directeur de recherche, Laboratoire Leprince-Ringuet, Rapporteur

**M. Stephane JEZEQUEL**

Directeur de recherche, Laboratoire d'Annecy de Physique des  
Particules, Examinateur

**M. Sven MENKE**

Chercheur, Max-Planck-Institut für Physik, Examinateur

**Mme Caroline COLLARD**

Directrice de recherche, Institut Pluridisciplinaire Hubert Curie,  
Examinatrice

**Mme Lucia DI CIACCIO**

Professeur de Classe Exceptionnelle, Laboratoire d'Annecy de Physique  
des Particules, Examinatrice

# Acknowledgements

I express my deep gratitude to Dave Charlton, Claude Charlot, Caroline Collard, Lucia Di Ciaccio, Stephane Jezequel and Sven Menke for graciously agreeing to serve on my jury. Their invaluable feedback, insightful comments, and constructive discussions have been instrumental in significantly enhancing the quality and depth of my academic work.

A special and heartfelt acknowledgement is dedicated to my supervisor, Narei Lorenzo Martinez, whose unwavering guidance has been a cornerstone throughout this journey. Her unique approach, treating me as a valued collaborator rather than adhering to the conventional student-mentor dynamic, has truly reshaped my academic experience. Furthermore, her exceptional work ethic, characterised by diligence, humility, and kindness, remains a profound source of inspiration. I am wholeheartedly committed to embodying these admirable qualities in all my future endeavours as a researcher.

I extend my gratitude to my thesis director, Emmanuel Sauvan, for his expert insights that played a pivotal role in improving various aspects of my research. I am also thankful for the spirit of excellence instilled by him in my development as a researcher.

A special mention is due to Cyril Drancourt and Richard Hermel for their invaluable support on the calibration project. Their dedicated efforts, particularly amidst the complexities posed by the pandemic, are truly commendable. Additionally, my gratitude extends to the OMEGA team in Palaiseau for their technical expertise and collaborative efforts, contributing significantly to the refinement of my thesis.

Heartfelt appreciation is directed to the entire ATLAS team at LAPP for the enriching discussions and support over the years, with particular gratitude to Lucia Di Ciaccio and Iro Koletsou for their insightful contributions to the diboson analysis, thereby elevating the quality of my work.

At this point, I would like to thank my collaborator in the diboson analysis, Qibin Liu. I am genuinely grateful for having such a committed and caring teammate, making our collaboration a true pleasure.

A huge shoutout goes to my friends in Annecy, particularly Alexandre, Antho, Camille, Dan, Dani, Dimitris, Ele, Feli, Giulia, Iuri, Léo, Luka, Manon, Matteo, Monica, Quim, and Silvia, for transforming this place into a home. From quarantine lunches to extended coffee breaks and chalet weekends, these moments will be dearly missed. I feel extremely blessed to have had such a supportive community.

Lastly, I convey my deepest gratitude to my parents and family, whose unwavering support has been a constant in my life. I am forever thankful for everything they have done for me.

# Contents

<b>1</b>	<b>Introduction</b>	<b>5</b>
<b>2</b>	<b>Theoretical Foundation</b>	<b>8</b>
2.1	Standard Model . . . . .	8
2.1.1	Electromagnetic Interactions . . . . .	10
2.1.2	Electroweak Interactions . . . . .	12
2.1.3	The Higgs Mechanism . . . . .	14
2.2	Vector Boson Scattering . . . . .	16
2.2.1	Motivation . . . . .	17
2.2.2	Effective Field Theory . . . . .	19
<b>3</b>	<b>Experimental Apparatus</b>	<b>20</b>
3.1	The Large Hadron Collider . . . . .	20
3.1.1	Operation Parameters . . . . .	22
3.1.2	Operation Timeline . . . . .	23
3.2	The ATLAS Detector . . . . .	23
3.2.1	Coordinate System . . . . .	25
3.2.2	Inner Detector . . . . .	26
3.2.3	Calorimeters . . . . .	28
3.2.4	Muon Spectrometer . . . . .	30
3.2.5	Trigger and Data Acquisition . . . . .	31
<b>4</b>	<b>Electronic Calibration for Liquid Argon Calorimeter</b>	<b>33</b>
4.1	Readout Electronics . . . . .	33
4.1.1	Principle of Signal Readout . . . . .	34
4.2	Electronic Calibration System . . . . .	36
4.2.1	Principle of Calibration . . . . .	36
4.2.2	Calibration Board . . . . .	37
4.3	Energy Reconstruction . . . . .	39
4.4	Electronic Calibration Upgrade for HL-LHC . . . . .	39
4.4.1	Motivations for Calibration Upgrade . . . . .	40
<b>5</b>	<b>Liquid Argon Calibration ASIC Prototype for HL-LHC</b>	<b>41</b>
5.1	Specifications of Calibration ASIC . . . . .	41
5.2	Developments of Calibration ASIC Prototypes . . . . .	47
5.3	Test of CASA Prototype . . . . .	49
5.3.1	Proton Irradiation . . . . .	50
5.3.2	X-ray Irradiation . . . . .	55
5.4	Current Status of Calibration ASIC Prototype . . . . .	57
<b>6</b>	<b>Liquid Argon Calibration Board Prototype for HL-LHC</b>	<b>58</b>

6.1	Specifications of Calibration Board . . . . .	58
6.2	Design and Components of Calibration Board . . . . .	60
6.2.1	Layout . . . . .	60
6.2.2	Specifications . . . . .	61
6.2.3	Calibration Run Patterns . . . . .	62
6.3	Test of CABANON Prototype . . . . .	63
6.3.1	Description . . . . .	63
6.3.2	Test Objectives . . . . .	65
6.3.3	Test Bench Setup . . . . .	65
6.4	Results of CABANON Prototype . . . . .	67
6.4.1	Operation of Components . . . . .	68
6.4.2	Simultaneous Pulsing of Multiple Channels . . . . .	69
6.4.3	DAC Linearity . . . . .	70
6.4.4	Pulser Linearity . . . . .	73
6.4.5	Crosstalk . . . . .	76
6.4.6	Uniformity . . . . .	79
6.5	Current Status of Calibration Board Prototype . . . . .	84
<b>7</b>	<b>Vector Boson Scattering at LHC</b>	<b>86</b>
7.1	Motivation . . . . .	88
7.2	Experimental Signature . . . . .	89
7.3	Measurement Objectives . . . . .	90
<b>8</b>	<b>Simulation</b>	<b>92</b>
8.1	Simulation of Proton Collisions . . . . .	92
8.1.1	Event Generation . . . . .	92
8.1.2	Detector Simulation . . . . .	94
8.2	Simulated Samples . . . . .	94
8.2.1	Signal Sample . . . . .	94
8.2.2	Background Samples . . . . .	95
<b>9</b>	<b>Object Reconstruction</b>	<b>96</b>
9.1	Low-Level Objects . . . . .	97
9.1.1	Tracks . . . . .	97
9.1.2	Vertices . . . . .	98
9.1.3	Topological Clusters . . . . .	98
9.1.4	Particle-Flow Objects . . . . .	98
9.2	High-Level Objects . . . . .	99
9.2.1	Electrons and Photons . . . . .	99
9.2.2	Muons . . . . .	101
9.2.3	Jets . . . . .	103
9.3	Object Selection . . . . .	106
<b>10</b>	<b>Uncertainties</b>	<b>111</b>
10.1	Experimental Uncertainties . . . . .	111
10.2	Theoretical Uncertainties . . . . .	112
<b>11</b>	<b>Analysis Strategy</b>	<b>118</b>
11.1	Event Selection . . . . .	118
11.2	Background Estimation . . . . .	120

---

11.2.1	QCD- $Z\gamma jj$	122
11.2.2	$Z$ +jets	122
11.2.3	$t\bar{t}\gamma$	125
11.2.4	Other	126
11.3	Measurement Regions	126
<b>12</b>	<b>Inclusive Measurements</b>	<b>129</b>
12.1	Profile Likelihood Fit	129
12.2	Fit Procedure	131
12.2.1	Treatment of Systematic Uncertainties	131
12.3	Measurement of Cross Section	135
12.4	Results	137
12.4.1	EW- $Z\gamma jj$	137
12.4.2	$Z\gamma jj$	144
<b>13</b>	<b>Differential Measurements</b>	<b>149</b>
13.1	Unfolding	149
13.1.1	Unfolding Inputs	150
13.1.2	Profile Likelihood Unfolding	151
13.2	Variables and Binning	152
13.3	Unfolding Procedure	153
13.4	Results	158
13.4.1	EW- $Z\gamma jj$	158
13.4.2	$Z\gamma jj$	162
<b>14</b>	<b>Conclusion</b>	<b>164</b>
<b>A</b>	<b>Comparison of Tools: HistFactory and TRExFitter</b>	<b>166</b>
<b>B</b>	<b>Comparison of Unfolding Algorithms and Tools</b>	<b>170</b>
B.1	Regularisation	171
B.2	Unfolding Setup	171
B.3	Unfolding Results	172
	<b>Bibliography</b>	<b>174</b>

# Chapter 1.

## Introduction

The 20th century witnessed an unprecedented surge in the exploration of the fundamental building blocks of the universe, driven significantly by the rise of quantum physics. This exploration culminated in the development of the Standard Model (SM), a comprehensive theoretical framework explaining fundamental particles and their interactions. Over the years, the predictions of the SM have undergone rigorous scrutiny, reaching a historic milestone with the discovery of the Higgs boson in 2012, serving as a robust confirmation of its validity. However, both theoretical arguments and experimental evidence strongly suggest its limitations as the ultimate theory governing particle physics.

Consequently, experiments at particle accelerators, such as the ATLAS detector at the Large Hadron Collider (LHC), gain paramount importance. They play a crucial role in testing the SM predictions and potentially uncovering indications of new particles or interactions beyond its established framework.

One particularly effective approach for assessing the SM involves examining the electroweak production of a vector boson pair associated with two jets. This method, notable for probing vector boson scattering (VBS) processes, provides direct insights into the electroweak (EW) sector of the SM. Accordingly, this thesis focuses on examining the electroweak production of a  $Z$  boson and photon accompanied by two jets (EW- $Z\gamma jj$ ). This study is important since it can access quartic gauge couplings  $WWZ\gamma$ ,  $ZZZ\gamma$ ,  $ZZ\gamma\gamma$  and  $Z\gamma\gamma\gamma$ . The last three couplings are explicitly prohibited at the lowest order in the SM. Any deviation from the SM predictions for these couplings could signify hints of new physics beyond the SM.

However, observing the EW- $Z\gamma jj$  process at the LHC poses significant challenges due to its low production rate and presence of substantial background events. Evidence of the process was found by both ATLAS and CMS detectors using proton-proton collision data collected in 2015 and 2016. Subsequently, ATLAS and CMS observed it using data collected from 2015 to 2018. This thesis details the analytical approach that led to the discovery of the EW- $Z\gamma jj$  process, utilising data recorded by the ATLAS detector from 2015 to 2018. Additionally, the thesis includes differential cross-section measurements for the EW- $Z\gamma jj$  process, which is pivotal for future Effective Field Theory (EFT) studies and refining the existing Monte Carlo description.

Furthermore, in anticipation of increased radiation doses at the upcoming High Luminosity Large Hadron Collider (HL-LHC), various components of the ATLAS detector require upgrades. Consequently, this thesis also focuses on upgrades of the electronic calibration boards for the ATLAS liquid argon electromagnetic calorimeter. This critical undertaking aims to ensure a good detector resolution, vital for achieving precise measurements of the energies of electrons, photons, and hadrons with the ATLAS detector. The findings from these investigations

will play a pivotal role in both the design and testing of the final calibration board for the HL-LHC.

The thesis unfolds with Chapters 2 and 3 laying the theoretical foundation for the VBS process and introducing the reader to the ATLAS detector. Following this introduction, the thesis is divided into two main segments: the initial part (Chapters 4-6) focusing on upgrades of the electronic calibration board, and the subsequent part (Chapters 7-13) delving into the analysis of the  $Z\gamma jj$  process with the ATLAS detector. Finally, Chapter 14 contains concluding remarks.

# Personal Contributions

- Chapter 5.3: I actively participated in irradiation tests and conducted data analysis.
- Chapter 6.3: I played a key role in the development of LabVIEW tests for controlling the board from the test bench located at LAPP.
- Chapter 6.4: I carried out all tests involving the calibration board prototype and conducted data analysis.
- Chapter 8.2 and Chapters 11.1-11.2: I applied selection criteria and computed relevant variables for both signal and background samples at the detector level. Additionally, I generated all signal samples at the particle level and computed corresponding particle-level variables too.
- Chapter 11.3: I carried out extensive studies to determine the most suitable region for measuring the EW- $Z\gamma jj$  process.
- Chapter 12.2: I formulated the comprehensive procedure for executing the fitting process.
- Chapter 12.4: The entirety of the results presented in this chapter is my own work.
- Chapter 13.2: I was responsible for devising the optimisation strategy for binning.
- Chapter 13.3: I developed the procedure for unfolding the EW- $Z\gamma jj$  processes and computed the essential inputs required for configuring the unfolding process.
- Chapter 13.4: I am the sole contributor to all the differential measurements related to the EW- $Z\gamma jj$  process.
- All studies in the appendices were conducted by me.

# Chapter 2.

## Theoretical Foundation

The goal of particle physics is to understand the elementary constituents of matter and the interactions between them. At the core of this field lies the *Standard Model* (SM), a well-tested theory that explains a wide range of phenomena and encapsulates our current understanding of particle physics. It serves as the theoretical foundation for all modern particle physics.

In this chapter, Section 2.1 provides an overview of the essential components of the Standard Model. It describes the mathematical framework underlying the SM, with an emphasis on electroweak theory, to facilitate the understanding of  $Z\gamma$  vector boson scattering as a probe for new physics, which is discussed in Section 2.2. For an in-depth exploration of the underlying principles, readers may refer to [1] and [2].

### 2.1. Standard Model

The Standard Model classifies particles into two distinct groups: *fermions* and *bosons*. Fermions, characterised by half-integer spin<sup>1</sup>, obeys the Pauli exclusion principle [3] which forbids two identical fermions from occupying the same quantum state simultaneously. On the other hand, bosons, with integer spin, do not face such restrictions and can occupy the same quantum state without limitation.

The fermions can be further classified into two groups: *leptons* and *quarks*, as seen in Figure 2.1. Leptons are organised into three doublets, known as generations. Each doublet consists of a negatively charged lepton (electron  $e$ , muon  $\mu$ , tau  $\tau$ ) and its corresponding neutral lepton ( $\nu_e, \nu_\mu, \nu_\tau$ ):

$$\begin{pmatrix} \nu_e \\ e \end{pmatrix}, \begin{pmatrix} \nu_\mu \\ \mu \end{pmatrix}, \begin{pmatrix} \nu_\tau \\ \tau \end{pmatrix}$$

The distinguishing factor between generations is the mass of the particles. Higher-generation particles have greater mass than their counterparts in lower generations. Moreover, heavier particles are unstable and tend to decay into lower-generation particles until they reach the most stable first generation.

---

<sup>1</sup> The spin of a particle corresponds to its intrinsic angular momentum

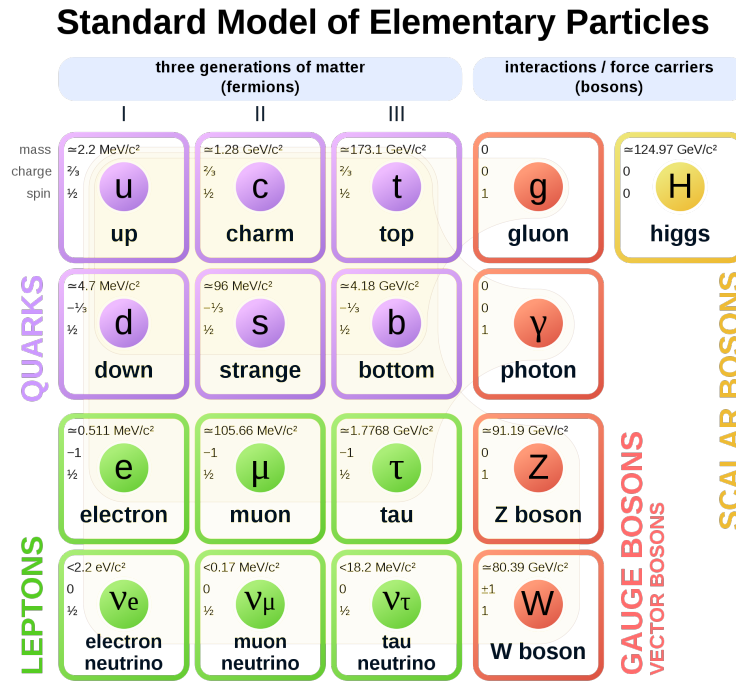


**Figure 2.1.:** Standard Model of elementary particles

Quarks, like leptons, are also divided into three generations. Each generation includes two quarks, one with an electric charge of  $+2/3e$  and the other with a charge of  $-1/3e$ :

$$\begin{pmatrix} u \\ d \end{pmatrix}, \begin{pmatrix} c \\ s \end{pmatrix}, \begin{pmatrix} t \\ b \end{pmatrix}$$

Unlike leptons, quarks cannot exist in isolation due to their *color charge*. Thus, quarks combine to form composite particles called *hadrons*, which do not possess any net color charge.

These fermions interact with each other via four fundamental forces: the *strong* force, the *electromagnetic* (EM) force, the *weak* force and the *gravitational* force. The SM is a quantum field theory (QFT), a theoretical framework that combines principles from both special relativity and quantum physics. The gravitational force, on the other hand, is based on Einstein's theory of general relativity (GR). Since a theory unifying GR and QFT has not been formulated successfully till date, gravity is the only force that is excluded from the SM. In addition, it should be kept in mind that gravity is by far the weakest force at the subatomic level. Thus, gravitational interactions for elementary particles can generally be ignored anyway.

The key idea behind QFT is that every particle in the universe is an excitation of a quantum field that is defined over all space and time. For example, the electron particle is simply a quantum excitation of the electron field that pervades throughout the universe. Similarly, force-carrying vector (spin-1) particles, also known as *gauge bosons* or *vector bosons*, are excitations of the SM force fields. A description of the SM forces, along with their corresponding gauge bosons, is shown in Table 2.1. The properties of these gauge bosons (such as mass, charge and spin) is depicted in Figure 2.1.

Interaction	Gauge boson	Matter particles involved
Strong	gluon	quarks
Electromagnetic	photon	quarks, charged leptons
Weak	$W^\pm, Z$ bosons	all

**Table 2.1.:** A comparison of forces in SM.

The final piece of the SM is the scalar (spin-0) *Higgs boson* [4]. It is simply a quantum excitation of the all-pervading *Higgs field*, which is a field responsible for generating the mass of all elementary particles.

Furthermore, in accordance with QFT, each fermion has an associated *antiparticle* with the same mass but opposite quantum charges (such as the electric charge  $Q$ ). For example, the antiparticle of an electron with  $Q = -1e$  is the anti-electron/positron with  $Q = +1e$  [5]. These anti-particles are also included in the SM, but have not been depicted in Figure 2.1.

The following sections provide a mathematical formulation of electroweak vector bosons, i.e.  $W^\pm, Z$ , and  $\gamma$ , based on the principles of QFT.

### 2.1.1. Electromagnetic Interactions

The dynamics of a field in QFT is governed by the *Lagrangian density*  $\mathcal{L}$ . It is often called just the Lagrangian. For example, the Lagrangian of a matter (or fermion) field  $\psi$  at spacetime  $x$  can be decomposed into a term representing the kinetic energy of the matter field  $\mathcal{L}_{matter}$  and a term representing its mass  $\mathcal{L}_{mass}$ . It is then written as

$$\begin{aligned}\mathcal{L} &= \mathcal{L}_{matter} + \mathcal{L}_{mass} \\ &= \bar{\psi}(x)(i\gamma^\mu\partial_\mu)\psi(x) - m\bar{\psi}(x)\psi(x)\end{aligned}\tag{2.1}$$

where  $\gamma^\mu$  are Dirac matrices [2],  $m$  is the particle mass and  $\bar{\psi}$  is the anti-matter field.

This Lagrangian remains invariant under phase rotations in the complex plane. In other words, if the field  $\psi$  is rotated by an angle  $\alpha$  in spacetime as follows,

$$\psi(x) \rightarrow e^{i\alpha}\psi(x)\tag{2.2}$$

then the Lagrangian in Equation 2.1 does not change. Such spacetime transformations that leave a Lagrangian invariant are known as *gauge transformations*. In addition, gauge transformations are often classified into a gauge group or symmetry group. For example, the transformations in Equation 2.2 represent the  $U(1)$  symmetry group.

In Equation 2.2, the parameter  $\alpha$  does not vary with spacetime  $x$ . For this reason, the symmetry is called a *global* symmetry, i.e., the field changes by the same amount at every point in spacetime.

Conversely, if  $\alpha(x)$  is spacetime dependent, i.e. the field changes by different amounts at different points in spacetime, the Lagrangian is no longer invariant with respect to *local*  $U(1)$  gauge transformations. In order to restore local symmetry, the derivative  $\partial_\mu$  is replaced by

the *covariant derivative*  $D_\mu$  given by

$$\partial_\mu \rightarrow D_\mu = \partial_\mu + igA_\mu(x) \quad (2.3)$$

where  $A_\mu(x)$  is a new field known as the *gauge field*. It will also transform under local gauge transformation as follows

$$A_\mu(x) \rightarrow A_\mu(x) - \frac{1}{g}\partial_\mu(\alpha(x)) \quad (2.4)$$

The parameter  $g$  in Equations 2.3 and 2.4 is the *gauge coupling parameter*. It denotes how strongly the gauge field  $A_\mu(x)$  interacts with the matter field  $\psi(x)$ .

From Equations 2.2, 2.3 and 2.4, it can then be shown that  $D_\mu\psi(x)$  transforms as

$$\begin{aligned} D_\mu\psi(x) &\rightarrow \partial_\mu(e^{i\alpha(x)}\psi(x)) + ig\left(A_\mu(x) - \frac{1}{g}\partial_\mu(\alpha(x))\right)e^{i\alpha(x)}\psi(x) \\ &= e^{i\alpha(x)}D_\mu\psi(x) \end{aligned}$$

such that the term  $\bar{\psi}(x)i\gamma^\mu D_\mu\psi(x)$  is invariant under local gauge transformations. Consequently, the Lagrangian is also invariant under local transformations.

Hence, in general, gauge fields corresponding to a symmetry group are introduced in theory to produce a Lagrangian that is invariant under local transformations. This is known as *gauge theory*.

Lastly, a kinetic term for the gauge field  $A_\mu$  has to be included in the Lagrangian<sup>2</sup>. This additional term should not break the local gauge invariance of the Lagrangian. It can be written as

$$\mathcal{L}_{gauge} = -\frac{1}{4}F^{\mu\nu}(x)F_{\mu\nu}(x)$$

where  $F_{\mu\nu}(x)$  is a gauge invariant object itself known as the *field strength tensor*. This is given by

$$F_{\mu\nu}(x) = \partial_\mu A_\nu(x) - \partial_\nu A_\mu(x)$$

Here, the gauge field  $A_\mu$  can be identified as the photon gauge field. The final Lagrangian, invariant under local  $U(1)$  transformations, is then written as

$$\begin{aligned} \mathcal{L} &= \mathcal{L}_{matter} + \mathcal{L}_{mass} + \mathcal{L}_{gauge} \\ &= \bar{\psi}(x)(i\gamma^\mu D_\mu - m)\psi(x) - \frac{1}{4}F^{\mu\nu}(x)F_{\mu\nu}(x) \end{aligned} \quad (2.5)$$

Equation 2.5 describes the Lagrangian of Quantum Electrodynamics (QED) [1] [2] for a single flavour of charged fermions.

---

<sup>2</sup> The Lagrangian combines the kinetic energy and potential energy of a field to describe its dynamics. The kinetic energy represents the energy associated with the field motion, while the potential energy represents the energy associated with the field itself.

It should be noted that an additional mass term for the gauge bosons of the form  $-\frac{m^2}{2}A^\mu A_\mu$  would break the local gauge invariance of the Lagrangian. Thus, photons are massless.

### 2.1.2. Electroweak Interactions

In the previous section, it was shown how the photon arises as a gauge field associated with local  $U(1)$  symmetry. In this section, a similar gauge theory approach for  $W^\pm$  and  $Z$  bosons is followed. This will eventually lead to the electroweak unification [6].

As a starting point, the symmetry group considered for weak interactions is  $SU(2)$ . It is represented by,

$$\psi(x) \rightarrow e^{i\vec{T}\vec{\alpha}}\psi(x)$$

Here,  $\psi$  is a doublet and  $\vec{T}$  are the three generators of the  $SU(2)$  group that define the  $SU(2)$  algebra. They can be written in terms of Pauli spin matrices  $\vec{\sigma}$

$$\vec{T} = \frac{1}{2}\vec{\sigma} \quad (2.6)$$

and  $\vec{\sigma}$  is given by

$$\sigma_a = \begin{pmatrix} 0 & 1 \\ 1 & 0 \end{pmatrix}, \sigma_b = \begin{pmatrix} 0 & -i \\ i & 0 \end{pmatrix}, \sigma_c = \begin{pmatrix} 1 & 0 \\ 0 & -1 \end{pmatrix} \quad (2.7)$$

Consequently, local gauge invariance leads to the appearance of three new gauge fields  $W_\mu^1, W_\mu^2, W_\mu^3$  along with a gauge coupling parameter  $g$ . The experimentally observed  $W_\mu^\pm$  boson fields [7] [8] can then be written as a combination of gauge fields  $W_\mu^1$  and  $W_\mu^2$  as follows

$$W_\mu^\pm = \frac{W_\mu^1 \mp iW_\mu^2}{\sqrt{2}}$$

Experimentally, it was found that the  $W_\mu^\pm$  bosons couple to left-handed fermions<sup>3</sup> only. Consequently, the gauge fields  $W_\mu^1$  and  $W_\mu^2$  should interact in the same way. The symmetry group is thus modified to  $SU(2)_L$ , where the index  $L$  indicates that the gauge fields associated with the  $SU(2)$  group couple to a doublet of left-handed fermions.

The third gauge field  $W_\mu^3$  has no electric charge. However, it cannot play the role of the neutral  $Z$  boson. This is because  $W_\mu^3$  couples to left-handed fermions only (from  $SU(2)_L$  symmetry), whereas the  $Z$  boson interacts with right-handed fermions as well.

In order to solve this problem, an additional  $U(1)_Y$  symmetry is considered. Here, the index  $Y$  denotes the conserved charge associated with  $U(1)$  symmetry. It is known as the *hypercharge*. This is in accordance with Noether's theorem [9] which states that for every continuous symmetry, a conserved quantity exists. Similarly, the conserved charge associated with the  $SU(2)$  symmetry is the *third component of weak isospin*  $I_3$ . These charges are related to the

---

<sup>3</sup> In the limit of massless fermions, fermions possess intrinsic *handedness* or helicity. Left-handed fermions have their spin opposite to their momentum, while right-handed fermions have their spin aligned with their momentum.

more familiar electric charge  $Q$  via the Gell-Mann-Nishijima formula [10] given by

$$Q = I_3 + \frac{Y}{2}$$

Now, local  $U(1)_Y$  gauge invariance leads to the appearance of another new gauge field  $B_\mu$  along with a gauge coupling parameter  $g'$ . The experimentally observed  $Z_\mu$  boson [11] [12] field and photon field  $A_\mu$  can then be obtained by mixing the  $W_\mu^3$  and  $B_\mu$  gauge fields as follows

$$\begin{pmatrix} A_\mu \\ Z_\mu \end{pmatrix} = \begin{pmatrix} \cos \theta_W & \sin \theta_W \\ -\sin \theta_W & \cos \theta_W \end{pmatrix} \begin{pmatrix} B_\mu \\ W_\mu^3 \end{pmatrix} \quad (2.8)$$

where  $\theta_W$  is the *weak mixing angle* for  $B_\mu$  and  $W_\mu^3$  fields.

Hence, in short, the photon,  $Z$  and  $W^\pm$  bosons arise from a gauge theory based on  $SU(2)_L \times U(1)_Y$  symmetry. This unified description of EM and electroweak gauge bosons is the electroweak (EW) theory.

The corresponding gauge invariant Lagrangian of the EW theory [1] [2] can then be broken down as  $\mathcal{L} = \mathcal{L}_{matter} + \mathcal{L}_{gauge}$ . Here,

$$\mathcal{L}_{matter} = \bar{\psi}_L i \gamma^\mu D_\mu \psi_L + \bar{\psi}_R i \gamma^\mu D_\mu \psi_R$$

where  $D_\mu$  is now the covariant derivative corresponding to the  $SU(2)_L \times U(1)_Y$  group. Here,  $\psi_L$  is a doublet and  $\psi_R$  is a singlet<sup>4</sup>. Following the syntax of Equation 2.3, it can be written as

$$D_\mu = \partial_\mu + ig T_a W_\mu^a + i \frac{g'}{2} Y B_\mu$$

where  $a = 1, 2, 3$ . Lastly,

$$\mathcal{L}_{gauge} = -\frac{1}{4} W_a^{\mu\nu} W_{\mu\nu}^a - \frac{1}{4} B^{\mu\nu} B_{\mu\nu} \quad (2.9)$$

where  $W_{\mu\nu}^a$  and  $B_{\mu\nu}$  are the field strength tensors associated with  $W_\mu^a$  and  $B_\mu$  respectively. They are defined as

$$B_{\mu\nu} = \partial_\mu B_\nu - \partial_\nu B_\mu$$

$$W_{\mu\nu}^a = \partial_\mu W_\nu^a - \partial_\nu W_\mu^a - g \epsilon^{abc} W_\mu^b W_\nu^c \quad (2.10)$$

The last term in Equation 2.10 is necessary to conserve the local gauge invariance. Specifically, the  $SU(2)_L$  generators  $T^a$  do not commute<sup>5</sup>. From equations 2.6 and 2.7, this commutator is given by

$$[T^a, T^b] = \left[ \frac{1}{2} \sigma^a, \frac{1}{2} \sigma^b \right] = \frac{1}{4} [\sigma^a, \sigma^b] = \frac{1}{2} i \epsilon^{abc} \sigma_c = i \epsilon^{abc} T_c \quad (2.11)$$

<sup>4</sup> In the Standard Model, neutrinos are only right-handed. Thus, right-handed fermion singlets are  $e_R, \mu_R, \tau_R, u_R, d_R, c_R, s_R, t_R$  and  $b_R$ .

<sup>5</sup> Mathematically, commutator between two matrices A and B is given by  $[A, B] = AB - BA$

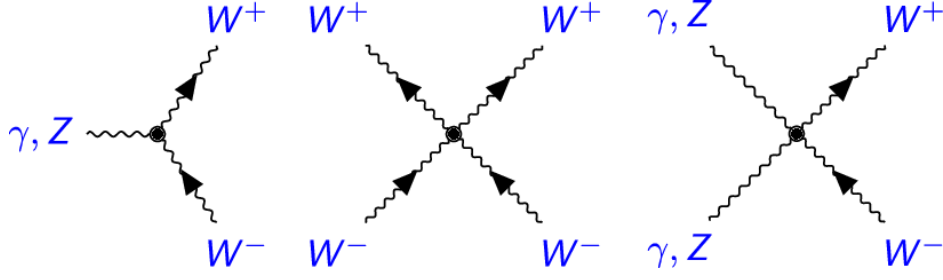


**Figure 2.2.:** Self-interactions of electroweak gauge bosons

Then, Equation 2.9 gives rise to self triple ( $WWZ, WW\gamma$ ) and quartic ( $WWWW, WWZZ, WWZ\gamma, WW\gamma\gamma$ ) terms, as seen in Figure 2.2. It should be noted that a pair of charge  $W$  bosons are always present and no neutral quartic gauge couplings<sup>6</sup> exist in the SM.

### 2.1.3. The Higgs Mechanism

It should be noted that, in order to maintain the local  $SU(2)_L \times U(1)_Y$  gauge symmetry, the EW Lagrangian constructed so far does not include any mass terms. However, this implies that all fermions and gauge bosons are massless, which contradicts our observations in nature, as evidenced by the non-zero mass values depicted in Figure 2.1. The solution to this conundrum is provided by the *Higgs mechanism* [4] [13].

This mechanism introduces a  $SU(2)_L$  doublet  $\phi$  to the EW theory. It is called the *Higgs doublet* and is given by

$$\phi = \begin{pmatrix} \phi^+ \\ \phi^0 \end{pmatrix}$$

where  $\phi^+$  is a complex scalar field with electric charge  $+1e$ , and  $\phi^0$  is a complex scalar field with no electric charge.

The corresponding Lagrangian is then written as

$$\mathcal{L}_{Higgs} = (D_\mu \phi)^\dagger (D_\mu \phi) - V(\phi) \quad (2.12)$$

where, the first term represents the kinetic energy of the Higgs doublet, and the second term represents its potential. This potential  $V(\phi)$  is further defined as

$$V(\phi) = \mu^2 \phi^\dagger \phi + \lambda (\phi^\dagger \phi)^2 = \mu^2 |\phi|^2 + \lambda |\phi|^4$$

where  $\lambda$  and  $\mu^2$  are parameters that define the shape of the Higgs potential.

It should be kept in mind that  $\mathcal{L}_{Higgs}$  is invariant under  $SU(2)_L \times U(1)_Y$  transformations. Hence, it can be included in the EW Lagrangian. Consequently, introducing  $\phi$  to the EW theory is also justified.

Now, in order to keep the theory stable, the potential must have a finite and stable minimum. Hence,  $\lambda$  is kept positive to ensure that the potential is bounded from below. The minimum

<sup>6</sup> Neutral quartic gauge couplings involve  $Z$  or  $\gamma$  only

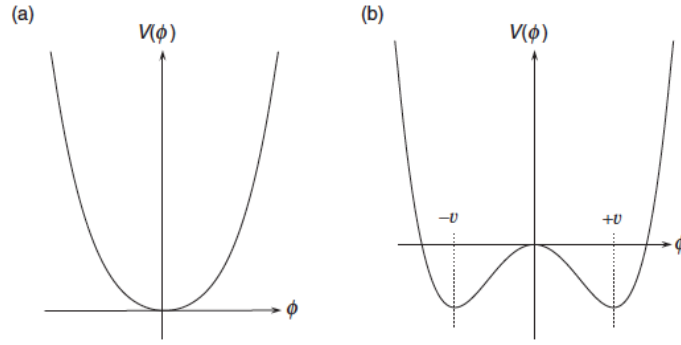


**Figure 2.3.:** A representation of the 1-dimensional potential  $V(\phi)$  for a)  $\mu^2 > 0$  and b)  $\mu^2 < 0$  when  $\lambda > 0$

of the Higgs potential, or in other words, the state with minimal energy is known as *vacuum state*  $\phi_0$ . It depends on the sign of  $\mu^2$ , as follows

- If  $\mu^2$  is positive, there is only one vacuum state given by

$$\phi_0 = \begin{pmatrix} 0 \\ 0 \end{pmatrix}$$

A representation of the corresponding 1-dimensional potential is shown in Figure 2.3(a). It should be noted that the potential is invariant under the transformation  $\phi \rightarrow -\phi$ . Consequently,  $\mathcal{L}_{Higgs}$  is also invariant or symmetric under  $\phi \rightarrow -\phi$ .

- If  $\mu^2$  is negative, there are an infinite number of stable vacuum states. Two of them are given by

$$\phi_0 = \begin{pmatrix} 0 \\ \pm v \end{pmatrix}$$

Here, the parameter  $v$  is known as the *vacuum expectation value*. It is given by

$$v^2 = -\frac{\mu^2}{\lambda}$$

A representation of the corresponding 1-dimensional potential is shown in Figure 2.3(b).

Among these two stable vacuum states, a choice has to be made between  $+v$  and  $-v$ . Consequently, the Higgs potential is no longer invariant under the transformation  $\phi \rightarrow -\phi$ . This leads to the symmetry of  $\mathcal{L}_{Higgs}$  being broken, and the corresponding phenomenon is known as *electroweak symmetry breaking* (ESMB).

In the Higgs mechanism,  $\mu^2 < 0$  and the arbitrarily chosen vacuum state is

$$\phi_0 = \frac{1}{\sqrt{2}} \begin{pmatrix} 0 \\ v \end{pmatrix}$$

It is always possible to find a  $SU(2)_L \times U(1)_Y$  gauge transformation such that the vacuum state transforms as

$$\phi_0 = \frac{1}{\sqrt{2}} \begin{pmatrix} 0 \\ v + h \end{pmatrix}$$

This field  $h$  is the spin-0 Higgs field.

In summary, the basic idea of the Higgs mechanism is to introduce a scalar Higgs doublet  $\phi$  whose potential  $V(\phi)$  has several stable vacuum states. When one of these vacuum states with a non-zero vacuum expectation value is chosen to be the minimum of  $V(\phi)$ , the symmetry of  $\mathcal{L}_{Higgs}$  breaks and the Higgs field arises.

All particles acquire their masses through interactions with this Higgs field. When considering the electroweak gauge bosons, these interactions can be determined by evaluating the kinetic term of  $\mathcal{L}_{Higgs}$  for  $\phi = \phi_0$ . This kinetic term is written as

$$\begin{aligned} (D_\mu \phi_0)^\dagger (D_\mu \phi_0) &= \frac{1}{2} \left| \left( \partial_\mu + igT_a W_\mu^a + i\frac{g'}{2} Y B_\mu \right) \begin{pmatrix} 0 \\ v + h \end{pmatrix} \right|^2 \\ &= \frac{1}{2} (\partial_\mu h)^2 + \frac{1}{8} g^2 (v + h)^2 |W_\mu^1 + iW_\mu^2|^2 + \frac{1}{8} (v + h)^2 |gW_\mu^3 - g'B_\mu|^2 \end{aligned}$$

Recalling that the mass term for bosons is of the form  $-\frac{m^2}{2} X^\mu X_\mu$ , only the terms that are quadratic in the gauge fields needs to be examined. These terms are

$$\frac{1}{8} v^2 g^2 (W_\mu^1 W^{1,\mu} + W_\mu^2 W^{2,\mu}) + \frac{1}{8} v^2 (gW_\mu^3 - g'B_\mu)(gW^{3,\mu} - g'B^\mu)$$

Using Equation 2.8, these terms can be re-written in terms of physical gauge fields. Then, the terms that are quadratic in  $W^\pm$ ,  $Z$  and  $A$  are

$$\left(\frac{1}{2}vg\right)^2 W_\mu^+ W^{-,\mu} + \frac{1}{8}v^2(g^2 + g'^2)Z_\mu Z^\mu + 0 \cdot A_\mu A^\mu$$

Accordingly, the masses of the EW gauge bosons are given by

$$M_W = \frac{1}{2}vg; \quad M_Z = \frac{1}{2}v\sqrt{g^2 + g'^2}; \quad M_A = 0 \quad (2.13)$$

## 2.2. Vector Boson Scattering

Despite its remarkable success, the Standard Model has several shortcomings, such as:

- It does not incorporate the force of gravity into its framework. This is one of the fundamental forces in nature, but its description requires a separate theory such as general relativity.
- It only accounts for about 5% of the total energy content of the universe, and does not provide an explanation for dark matter, which is inferred from its gravitational effects, nor dark energy, which is believed to be responsible for the accelerating expansion of the universe.

- It does not explain why the universe contains significantly more matter than antimatter. This matter-antimatter asymmetry is one of the fundamental puzzles in cosmology.
- It has a number of parameters that are not predicted or explained by the theory itself. The values of these parameters must be determined experimentally, and some of them appear to be finely-tuned to match observed data. This fine-tuning is considered unsatisfactory and suggests that there may be a more fundamental theory that provides natural explanations for these parameters.

These limitations indicate that the SM is an incomplete theory and that there may be new physics beyond the SM that can address these issues. One of the ways to probe the existence of new physics is by investigating *vector boson scattering* (VBS) processes, which refers to any process of the form  $VV \rightarrow VV$ , where the electroweak vector boson  $V$  can be  $W$ ,  $Z$ , or  $\gamma$ .

### 2.2.1. Motivation

In QFT, particles are considered *polarised* when their spin vector  $\vec{S}$  exhibits a preferred direction relative to their momentum  $\vec{p}$ . This polarisation is quantified by the helicity, given by  $h = \vec{S} \cdot \frac{\vec{p}}{|\vec{p}|}$ . For spin-1 particles with a non-zero mass, like the  $W$  and  $Z$  bosons, the helicity can assume three values:  $\pm 1$  and  $0$ . In the case of massless spin-1 particles, like the photon, the helicity is limited to  $\pm 1$ . A helicity value of  $0$  corresponds to longitudinal polarisation, while transverse polarisation is associated with  $h = \pm 1$ .

The two transverse polarisation states<sup>7</sup> of a massless vector boson travelling along the  $z$  axis can be written as [1]

$$\epsilon_{\pm}^{\mu} = \mp \frac{1}{\sqrt{2}}(0, 1, \pm i, 0) \quad (2.14)$$

while massive vector bosons can also exist in a longitudinal polarisation state given by

$$\epsilon_L^{\mu} = \frac{1}{m}(p_z, 0, 0, E) \quad (2.15)$$

where  $E$  and  $m$  are energy and mass of the vector boson, respectively.

From equations 2.14 and 2.15, it follows that the VBS cross-section<sup>8</sup> for longitudinally polarised bosons scales as  $E/m$ , while the cross-section for transversely polarised bosons remains constant. Figure 2.4 (a)+(b) displays the cross-section of longitudinally polarised VBS, considering its triple and quartic couplings. The corresponding Feynman diagrams are depicted in the upper row of Figure 2.5. Initially, the cross-section scales with the center-of-mass energy  $\sqrt{s}$ . However, at around 1.2 TeV, unitarity is violated<sup>9</sup>. Figure 2.4 (a)+(b)+(c) demonstrates that including the coupling between vector bosons and a light SM Higgs boson with a mass around 100 GeV restores unitarity. The corresponding Feynman diagrams are shown in the lower row of Figure 2.5.

<sup>7</sup> Boson wave functions are written in terms of the polarisation four vector  $\epsilon^{\mu}$ :  $B^{\mu} = \epsilon^{\mu} e^{-ip \cdot x} = \epsilon^{\mu} e^{-i(\vec{p} \cdot \vec{x} - E \cdot t)}$ , where  $\vec{p}$  and  $E$  are momentum and energy of the boson respectively

<sup>8</sup> In particle physics, a cross section of a given process expresses the probability that the process occurs.

<sup>9</sup> Unitarity is a fundamental principle in quantum field theory that ensures the conservation of total probability in scattering processes. This means that the cross section, which represents the probability of a scattering event,  $\sigma$  cannot grow to arbitrarily high values.

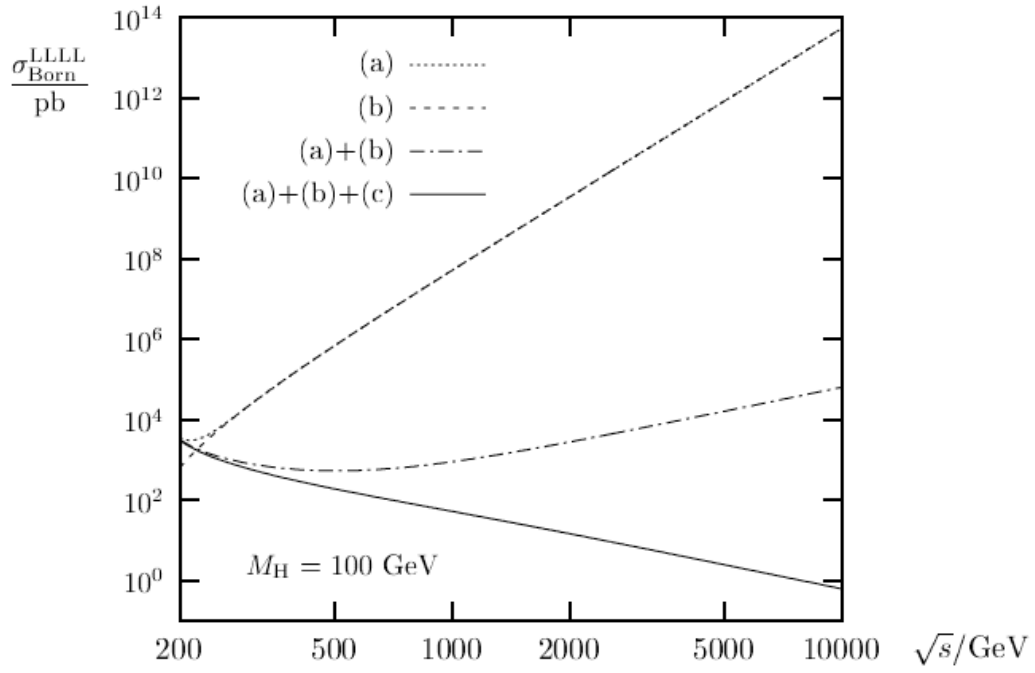


**Figure 2.4.:** The cross-sections for the scattering of longitudinally polarised vector bosons including (a) three-boson interaction, (b) four-boson interaction, and (c) Higgs to vector boson coupling[14]

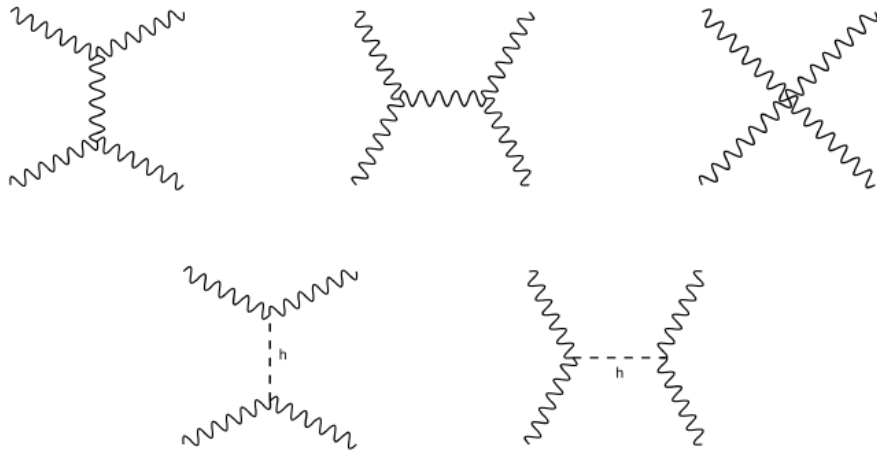


**Figure 2.5.:** The interactions of the vector bosons in VBS processes, mediated by the triple (upper left two) and quartic (upper right) gauge boson self-couplings, and by a Higgs boson (lower row).

In 2012, the ATLAS and CMS collaborations discovered the Higgs boson at a mass of  $\sim 125$  GeV [15] [16]. However, if its properties deviate from SM predictions, the VBS cross-section will increase at a specific high energy scale, indicating the necessity of introducing new physics to restore unitarity. Similar arguments apply to the self-interactions between gauge bosons, where deviations in the triple and quartic gauge couplings from the SM predictions will lead to a larger cross-section. Furthermore, the inclusion of neutral quartic gauge couplings, which are prohibited in the SM (as seen in Figure 2.2), will also enhance the cross-section. Consequently, precise measurements of VBS cross-sections can potentially unveil new physics beyond the Standard Model.

### 2.2.2. Effective Field Theory

In the absence of a specific theory for new physics, the framework of *effective field theory* (EFT) [2] provides a model-independent approach to interpret potential anomalous gauge couplings. It assumes that new physics exists at a higher energy scale than currently accessible, with the SM serving as a low-energy approximation.

The effective Lagrangian, as shown in Equation 2.16, extends the SM Lagrangian by including additional terms representing new interactions between SM particles through higher-dimensional  $d$  operators  $\mathcal{O}_i^d$ . The Wilson coefficients  $c_i$  parameterise the strength of these new interactions, and the energy scale of new physics is denoted by  $\Lambda$ .

$$\mathcal{L}_{\text{EFT}} = \mathcal{L}_{\text{SM}} + \sum_i \frac{c_i}{\Lambda^2} \mathcal{O}_i^{(d=6)} + \sum_i \frac{c_i}{\Lambda^4} \mathcal{O}_i^{(d=8)} + \dots \quad (2.16)$$

The higher-order terms in the EFT expansion are suppressed by a factor of  $1/\Lambda^{d-4}$ . Consequently, the lower-dimension operators (dimension-6 and dimension-8) have the most significant impact on deviations from SM predictions. Among them, dimension-6 operators can impact both triple and quartic gauge couplings, while dimension-8 operators exclusively modify quartic gauge couplings.

To summarise, VBS processes play a crucial role in probing anomalous gauge couplings. By examining VBS interactions, we can investigate the influence of dimension-6 and dimension-8 EFT operators and determine limits on the associated Wilson coefficients. Such investigations enhance our understanding of potential new physics phenomena that extend beyond the Standard Model.

## Chapter 3.

# Experimental Apparatus

In particle physics, high energies are essential for creating new particles and investigating the fundamental structure of matter. Up to the early 1950s, cosmic rays were the only source of such high-energy particles, and their study yielded important discoveries such as positrons and pions. However, cosmic ray experiments are now limited to specific scenarios, and the predominant method for conducting experiments involves the use of *particle accelerators*, which are machines designed specifically to generate high-energy particle beams. This method offers a notable advantage: the ability to control the particle type and energy precisely, as desired by the experimenter.

Once the particle beam is established, it is directed towards a target to induce interactions. There are two types of such accelerator-based experiments: *fixed-target experiments*, where the target remains stationary in the laboratory, and *collider experiments*, where two particle beams travelling in nearly opposite directions are brought together to collide at a small or zero crossing angle. In both cases, after the collision occurs, information about the resulting particles (eg energy, trajectory) is deduced by observing their interactions with material of *detectors* placed near the interaction region. The data collected is subsequently analysed by physicists to explore various aspects of particle physics.

The world's largest and most powerful particle accelerator is the Large Hadron Collider (LHC) [17]. It is a circular colliding experiment located at the European Organisation for Nuclear Research (CERN) on the Switzerland-France border near Geneva. Since its initiation in 2009, the LHC has been at the forefront of major scientific achievements. One such milestone was the discovery of the Higgs boson in 2012 by the ATLAS [18] and CMS [19] experiments, which are two of the main detectors at the LHC. With its continued operations, the LHC continues to play a key role in expanding the frontiers of particle physics.

This thesis carries out work conducted with ATLAS detector of the LHC. In Section 3.1, a comprehensive overview of the LHC is presented, encompassing its design and operational aspects; and section 3.2 offers a description of the ATLAS detector and its subsystems.

### 3.1. The Large Hadron Collider

Situated 100 meters below ground level, the Large Hadron Collider (LHC) occupies a tunnel with a circumference of 27 kilometres and a width of 3.8 meters. Its primary function is to accelerate two beams of proton or lead ions in opposing directions, achieving speeds close to the speed of light. This thesis will specifically focus on the proton beams.

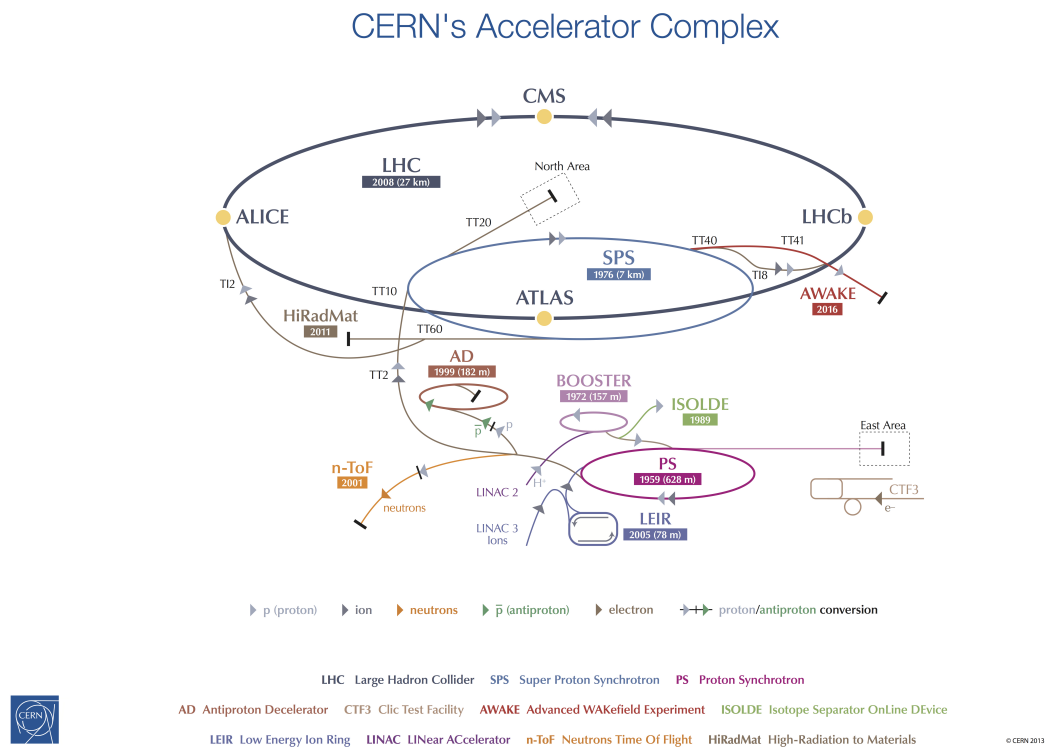


**Figure 3.1.:** The accelerator complex at CERN [20]

The journey of the high-energy proton beams within the LHC commences in a series of smaller accelerators found within the CERN complex, as depicted in Figure 3.1. Initially, protons are extracted from ionised hydrogen gas and accelerated to 50 MeV using the Linear Accelerator-2 (LINAC-2)<sup>1</sup>. Subsequently, an additional boost of energy is provided by the Proton Synchrotron Booster (BOOSTER), elevating the energy level to 1.4 GeV. The protons then undergo further acceleration in the Proton Synchrotron (PS) until they reach an energy of 25 GeV. Upon exiting the PS, the protons are directed to the Super Proton Synchrotron (SPS), where their energy level reaches 450 GeV. Finally, the SPS injects the protons into the LHC ring at two injection sites, resulting in the generation of counter-circulating beams.

These proton beams continue their circulation within the LHC, progressively accelerating to a current maximum energy of 6.8 TeV. To maintain this circulation, the LHC relies on various components. In particular, radio-frequency<sup>2</sup> cavities are utilised to accelerate the protons, while dipole magnets are responsible for bending the protons along their circular path. Additionally, quadrupole magnets are used to focus the beams near the points of collision.

Collisions between the proton beams occur at four specific interaction points (IP) situated around the LHC tunnel, where the main experiments are housed (as depicted in Figure 3.1): A Large Ion Collider Experiment (ALICE) [21], A Toroidal LHC ApparatuS (ATLAS), Compact Muon Solenoid (CMS), and Large Hadron Collider Beauty (LHCb [22]). The

<sup>1</sup> Replaced by LINAC-4 after 2018

<sup>2</sup> An RF cavity, or radio frequency cavity, is a device used in particle accelerators to provide the necessary energy to accelerate charged particles. It operates by generating electromagnetic fields that oscillate at a specific radio frequency, imparting energy to the particles as they pass through the cavity.

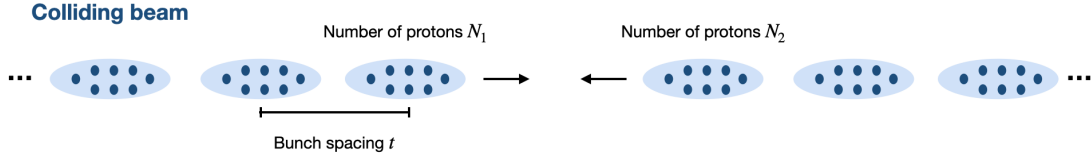


**Figure 3.2.:** Colliding beam structure at the LHC. Nominal values of  $N_1$  and  $N_2$  are  $1.5 \times 10^{11}$  protons and  $t$  is 25 ns.

ATLAS and CMS experiments are versatile detectors designed to cover a wide range of physics programs, including precise measurements of Standard Model processes and the exploration of new physics phenomena. The LHCb experiment specialises in conducting high-precision measurements of b-quark physics and investigating CP violation. On the other hand, the ALICE experiment is specifically dedicated to the study of quark-gluon plasma formed during heavy-ion collisions.

An important aspect of the LHC design is that the proton beams are not a continuous stream of protons but rather a bunched structure, as seen in Figure 3.2. Each bunched beam is designed to contain 2808 proton bunches, with approximately  $1.5 \times 10^{11}$  protons in each bunch and a spacing of 25 ns between them. As a result, when proton beams collide, multiple interactions occur per bunch crossing. These additional interactions, that are not the primary proton-proton collision of interest, are collectively known as *pileup*.

### 3.1.1. Operation Parameters

In accelerator physics, two of the important parameters that characterise the performance and capabilities of a particle collider are centre-of-mass energy and luminosity.

Centre-of-mass energy  $\sqrt{s}$  represents the total energy available for particle collisions. It determines the maximum energy at which new particles can be produced and allows for the exploration of new physics phenomena. For proton collisions at the LHC, the design objective was to achieve  $\sqrt{s} = 14$  TeV, with each proton beam having an energy of 7 TeV<sup>3</sup>.

The other significant parameter in accelerator physics is the instantaneous luminosity  $L'$ , which quantifies the number of collisions of unit time and of unit cross-sectional area. It is calculated using the following formula [23]:

$$L' = \frac{fN_1N_2}{4\pi\sigma_x\sigma_y} \quad (3.1)$$

where  $N_1$  and  $N_2$  represent the number of protons per bunch,  $f$  corresponds to the bunch crossing frequency, and  $\sigma_x$  and  $\sigma_y$  denote the horizontal and vertical dimensions of the colliding bunch, respectively.

To quantify the amount of data collected by the detector over its operational period, it is convenient to define the integrated luminosity  $L$  as  $L = \int L' dt$ . The unit of measurement for  $L$  is commonly expressed as inverse of a barn ( $\text{b}^{-1}$ ), where 1 barn (b) is equal to  $10^{-28} \text{ m}^2$ .

<sup>3</sup> In collider physics, centre-of mass energy  $\sqrt{s} = E_1 + E_2$  where  $E_1$  and  $E_2$  are the energy of the two colliding beams

In conclusion, the number of events  $N_{events}$  produced in a specific physics process can be mathematically expressed as:

$$N_{events} = L \times \sigma(\sqrt{s}) \quad (3.2)$$

where, the cross section  $\sigma$  serves as a metric in particle physics to quantify the likelihood of an interaction occurring. It is conventionally measured in barns and depends on the centre-of-mass energy. Equation 3.2 thus highlights the importance of achieving both a high luminosity and centre-of-mass energy to allow for a greater production of rare events and facilitates the generation of a large quantity of particles for detailed analysis.

### 3.1.2. Operation Timeline

The operational timeline of the LHC, depicted in Figure 3.3, can be divided into three distinct periods, each marked by extended shutdowns dedicated to maintenance and upgrades. The initial period, known as Run-1, lasted from 2009 to 2013, during which the LHC operated at  $\sqrt{s}=7$  TeV and 8 TeV. The subsequent period, referred to as Run-2, spanned from 2015 to 2018 and witnessed the production of proton-proton collision data at  $\sqrt{s}=13$  TeV. Notably, it achieved an instantaneous luminosity of  $2.1 \times 10^{34} \text{cm}^{-2}\text{s}^{-1}$ , which was twice the design instantaneous luminosity. Run-3, a new phase of data-taking, commenced in 2022 and is projected to continue until 2026. During this run, the LHC is delivering proton-proton collisions at a remarkable world record of  $\sqrt{s}=13.6$  TeV.

Looking ahead, the next milestone is the High-Luminosity Large Hadron Collider (HL-LHC) project [24], which involves upgrading the LHC to achieve an instantaneous luminosity 5 to 7.5 times higher than the design value. It is expected to commence operations in 2029. This ambitious upgrade will significantly enhance the physics reach of the LHC, enabling the collection of large amounts of data.

One approach to increase luminosity at the LHC is by maximising the number of protons in each bunch. However, this strategy has the drawback of leading to increased pileup, which introduces low-energy deposits and negatively impacts event reconstruction. Moreover, the high luminosity levels result in the degradation of detector components due to elevated radiation levels. To address these effects, it is crucial to implement detector upgrades that can handle the growing luminosity.

In this thesis, the analysis section focuses on the data collected by the ATLAS detector during Run-2, which corresponds to a total integrated luminosity of  $140 \text{fb}^{-1}$ . Additionally, a portion of this thesis also focuses on the upgrade work carried out for the HL-LHC.

## 3.2. The ATLAS Detector

The ATLAS detector has a massive cylindrical structure, measuring 44 meters in length and 25 meters in diameter, weighing 7000 tonnes. At its core is the LHC beam pipe, where proton-proton collisions occur near the geometric centre. The detector is composed of concentric layers of sub-detector systems arranged around the beam line, each designed to record specific particle types. It is divided into a barrel and two endcap regions, providing comprehensive coverage of the entire  $4\pi$  solid angle. Figure 3.4 illustrates the detector and its subsystems,

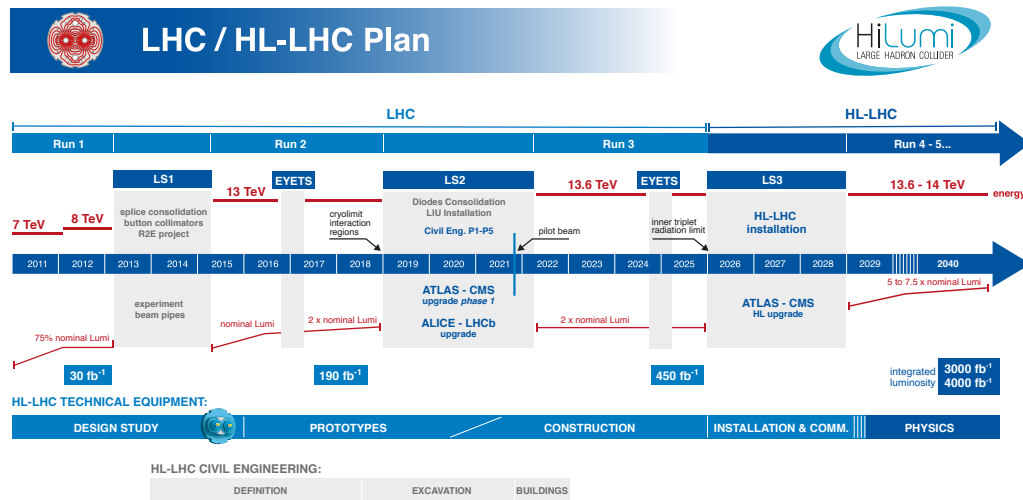


**Figure 3.3.:** The LHC and HL-LHC baseline plan, showing the centre-of-mass energy (upper red lines) and instantaneous luminosity (lower red lines). The cumulative integrated luminosity at the end of each period is also indicated. [25]

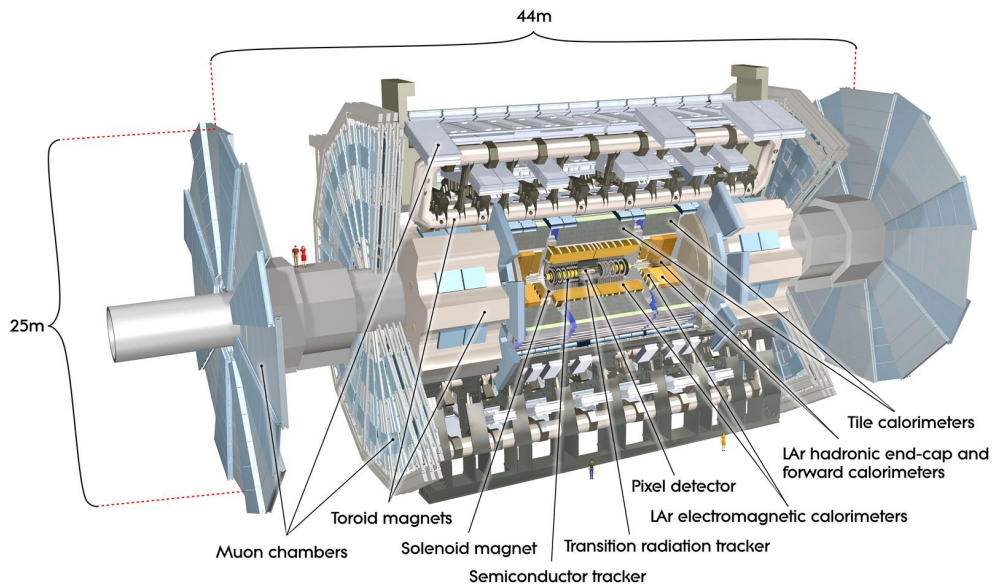


**Figure 3.4.:** The ATLAS detector and its sub-systems[26]

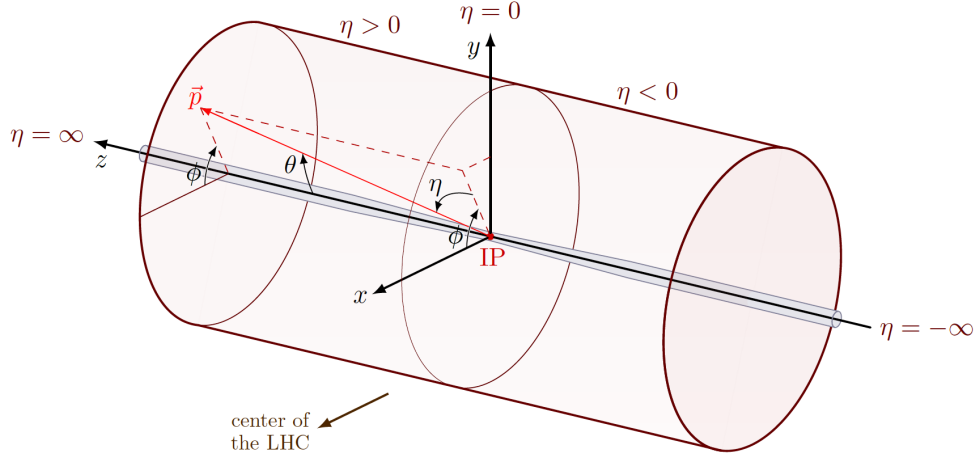


**Figure 3.5.:** The ATLAS coordinate system

which will be further explained in the following sections. Lastly, it should be noted that the described detector setup corresponds to Run-2 configuration.

### 3.2.1. Coordinate System

The ATLAS detector exhibits a cylindrical symmetry around the beam axis and a forward-backward symmetry with respect to the collision point. Thus, it uses a right-handed coordinate system, depicted in Figure 3.5, where the origin is positioned at the nominal interaction point (IP) and the  $z$ -axis is aligned along the beam pipe. The  $x - y$  plane is defined perpendicular to the beam, with the positive  $x$ -direction pointing towards the centre of the LHC and the  $y$ -axis oriented upwards. Furthermore, to account for the cylindrical symmetry, the ATLAS detector also employs a spherical coordinate system  $(r, \phi, \theta)$ , illustrated again in Figure 3.5. The radial coordinate,  $r$ , quantifies the distance from the  $z$ -axis. The azimuthal angle,  $\phi$ , encompasses the rotation around the  $z$ -axis, while the polar angle,  $\theta$ , represents the angle from the positive  $z$ -axis.

At the LHC, it is advantageous to work with variables that maintain Lorentz invariance for boosts along the beam axis.<sup>4</sup> One such variable is the *transverse momentum*  $p_T$  given by

$$p_T = \sqrt{p_x^2 + p_y^2} \quad (3.3)$$

where  $p_x$  and  $p_y$  represent the projection of the momentum of the particle along the  $x$  and  $y$  axes, respectively. In contrast, the *longitudinal momentum*  $p_z$  is not Lorentz invariant, and thus, it is replaced by rapidity  $y$  defined as

$$y = \frac{1}{2} \ln \frac{E + p_z}{E - p_z} \quad (3.4)$$

<sup>4</sup> Lorentz invariance is a fundamental principle stating that the laws of physics remain unchanged under Lorentz transformations, which are mathematical equations that relate measurements in different reference frames. A Lorentz boost is a specific transformation that links changes in velocity or momentum across different reference frames. Specifically, at the LHC, boosts occur when particles in the beam undergo acceleration, deceleration, or collision. Consequently, Lorentz invariance along the beam axis facilitates the analysis of experimental data irrespective of the motion between the observer and the studied particle.

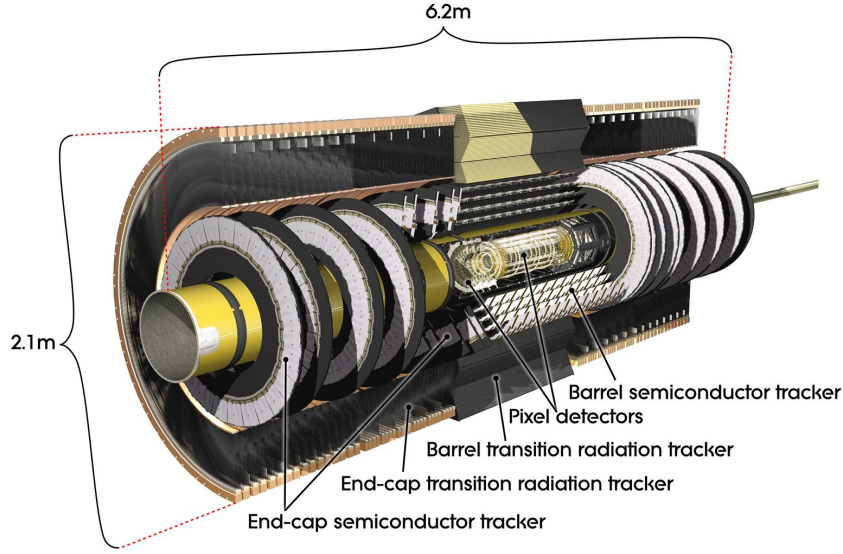


Figure 3.6.: The ATLAS Inner Detector[27]

where  $E$  is the energy of the particle. Although rapidity itself is not a Lorentz invariant variable, differences in rapidity remain invariant under boosts in the beam direction.

For highly energetic particles with  $E \gg m$ , rapidity simplifies to *pseudorapidity*  $\eta$  given by

$$\eta = -\ln\left(\tan\frac{\theta}{2}\right) \quad (3.5)$$

Based on the definition,  $\eta$  covers the range  $[-\infty, \infty]$ , where  $|\eta| \rightarrow 0$  corresponds to particles in the central region of the detector, while  $|\eta| \rightarrow \infty$  corresponds to particles in the forward or backward regions, as depicted in Figure 3.5. In the case of the ATLAS detector, the  $|\eta|$  coverage extends from 0 to 4.9. Furthermore, since the polar angle is not Lorentz invariant, pseudorapidity is the preferred variable. Consequently, positions within the detector can be described in the  $(\eta, \phi)$  plane. This allows distances between particles to be expressed as:

$$\Delta R = \sqrt{(\Delta\phi)^2 + (\Delta\eta)^2} \quad (3.6)$$

### 3.2.2. Inner Detector

The Inner Detector (ID) [18] is the sub-detector situated closest to the interaction point. It operates within a 2T magnetic field that aligns parallel to the beam axis, generated by a superconducting solenoid surrounding it. This magnetic field causes charged particles to follow curved paths, where the radius of curvature is inversely proportional to their transverse momentum  $p_T$ . The main objectives of the ID are to reconstruct charged particle trajectories (known as *tracks*), identify vertices<sup>5</sup>, and determine the curvature radius for precise measurements of  $p_T$ .

<sup>5</sup> In particle physics, a vertex is where particles interact or are produced

ID Sub-system	Element size [ $\mu\text{m}$ ]	Intrinsic resolution [ $\mu\text{m}$ ]
IBL	$50 \times 250$	$8 \times 40$
Pixel	$50 \times 400$	$10 \times 115$
SCT	80	$17 \times 580$
TRT	4000	130

**Table 3.1.:** The size and resolution of components in each ID sub-system. The intrinsic resolution of the IBL, the Pixel and the SCT is reported along  $r - \phi$  and  $z$ , while for TRT is only along  $r - \phi$  plane.

The ID is designed as a cylindrical structure approximately 6m long and with a radius of about 1m. It consists of three sub-detectors arranged in layers from the beam pipe outward, as seen in Figure 3.6: the Pixel detector with the Insertable B-Layer (IBL), the Semi-Conductor Tracker (SCT), and the Transition Radiation Tracker (TRT). The sub-detectors positioned nearer to the beam exhibit higher resolution and have smaller components (see in Table 3.1).

- The Pixel and SCT detectors, composed of silicon, utilise semiconductor technology. As a charged particle traverses these silicon detectors, it creates electron-hole pairs. These mobile carriers subsequently drift to the electrodes, in presence of an electric field, to produce an electrical signal. By analysing the signals or *hits* collected from multiple layers of silicon detectors, the trajectory of the particle can be determined.
  - The Pixel detector utilises high-resolution silicon pixel sensors. It consists of three concentric cylinders in the central barrel and three disks on each side as end-caps, providing coverage within  $|\eta| < 2.5$ . During Long Shutdown 1, an additional layer, known as the IBL, was incorporated closer to the beam line in order to enhance the identification of  $b$ -quarks. The IBL covers  $|\eta| < 3$  and does not have separate barrel and end-cap regions due to its proximity to the interaction point. The Pixel detector, along with the IBL, achieves precise vertex reconstruction owing to its high resolution and close proximity to the interaction point.
  - The SCT detector features four cylindrical layers in the barrel and nine disks in the end-caps. It covers a range of  $|\eta| < 2.5$  around the interaction point. The SCT employs silicon strips that simplifies manufacturing but reduces resolution. Nevertheless, the SCT provides additional tracking and plays a significant role in measuring particle momentum.
- The TRT utilises gas-filled drift tubes, called *straws*. In a principle similar to the silicon trackers, when a charged particle traverses these straws, the gas within them becomes ionised, and the resulting charges are collected by electrodes in the tube, thus generating a hit. Although the resolution of the TRT is lower than silicon trackers, it compensates by processing a larger number of hits. Additionally, longer track lengths within the TRT contribute to improved momentum measurements. Furthermore, the TRT aids in particle identification by detecting *transition radiation*, which occurs when charged particles traverse different media. To induce this radiation, polypropylene-polyethylene foils are placed between each straw in the TRT. The intensity of this radiation is particularly significant for high-energy particles with low mass, thus enhancing the

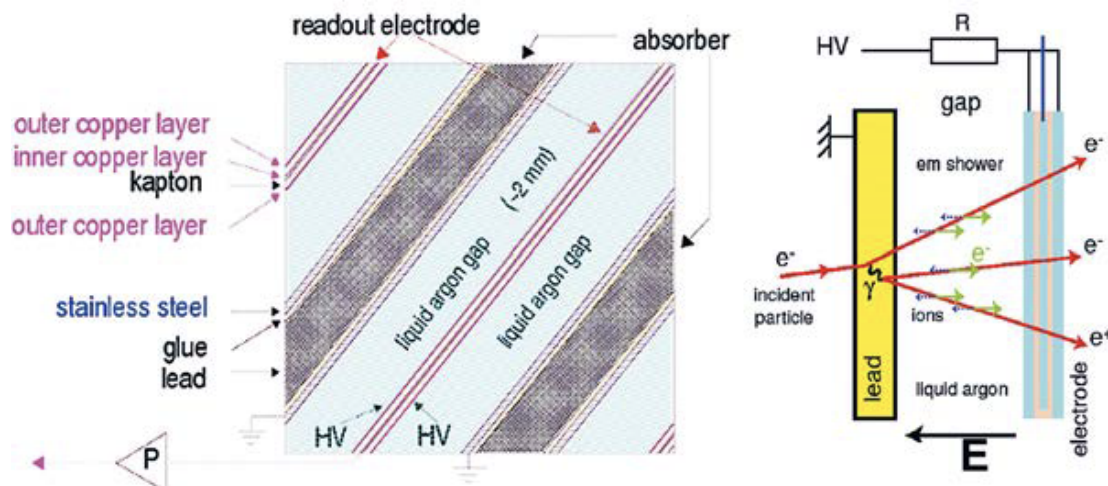


**Figure 3.7.:** Left: Stack of absorbers, readout electrodes and LAr gaps as realised in a ATLAS LAr calorimeter [28], Right: Ionisation signal produced in a LAr gap.

ability to distinguish between electrons and light charged hadrons such as pions. Lastly, the TRT provides coverage within  $|\eta| < 2$ .

### 3.2.3. Calorimeters

The calorimeters of the ATLAS detector are positioned outside the solenoid magnet that encloses the inner detector. Their primary function is to absorb photons, electrons and hadrons<sup>6</sup> and transfer their energies into measurable signals.

These calorimeters are constructed using alternating layers of *absorber* material and *active* regions. The absorber, made of a dense material, stops incoming particles and helps them deposit their energy. More precisely, when incoming particles interact with the absorber, they create a cascade of lower energy secondary particles called a *shower*. Meanwhile, the active region consists of scintillators or ionisation chambers that generate measurable signals when shower particles interact with them. These signals are then measured to determine the energy of the original particle.

The calorimeters of the ATLAS detector can be categorised into two types based on the technology employed:

- **LAr Calorimeters [25]:** These calorimeters utilise liquid argon as active medium. Liquid argon is chosen for its resistance to radiation and its efficient ionisation capabilities. In the active region, a high voltage is applied between the absorber and readout electrode. As a charged particle passes through the active medium, it generates an ionisation signal, which is detected by the electrodes. Figure 3.7 illustrates this principle.
- **Tile Calorimeters [29]:** These calorimeters employ plastic scintillating tiles as active medium. When a charged particle traverses the active region, it produces scintillation, which is the emission of light by the scintillator material due to energy deposition. This

<sup>6</sup> Muons and neutrinos are able to traverse through the calorimeters without being absorbed

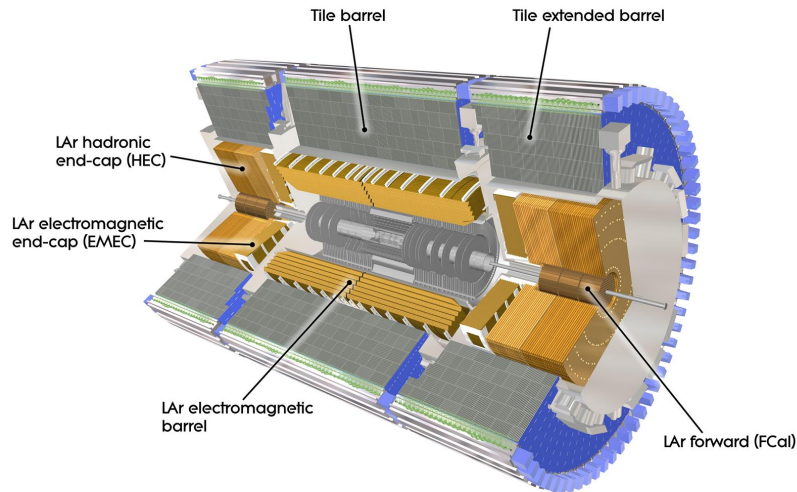


**Figure 3.8.:** The ATLAS calorimeter[30]

light is then transmitted through fibers and photomultiplier tubes, resulting in the generation of an electronic signal.

Furthermore, the calorimeters can be classified according to the type of particle showers they detect: electromagnetic showers induced by photons and electrons, or hadronic showers induced by hadrons such as neutrons and pions. Consequently, the ATLAS calorimeters are broadly divided into distinct sub-systems, taking into account both the type of particle shower as well as their placement within the detector:

- **Electromagnetic (EM) Calorimeters:** These are LAr calorimeters with lead as the absorber material. They are designed with an accordion geometry to ensure uniform acceptance without any gaps. Figure 3.8 provides a visual representation of the EM calorimeter and its sub-detectors:
  - **EM Barrel (EMB) calorimeter:** It covers the region  $|\eta| < 1.475$  and comprises three layers with varying granularity and depths. The first layer is finely segmented in the  $\eta$  direction, which helps in distinguishing between photons and neutral pions that decay into two nearby photons.
  - **EM EndCap (EMEC) calorimeter:** It covers the range  $1.375 < |\eta| < 3.2$  and consists of two coaxial wheels on each side of the EMB. Its structure is similar to that of the EMB, but aligned radially.

In addition, a pre-sampler detector is integrated between the inner detector and the EM calorimeter, specifically in the region of  $|\eta| < 1.8$ . This pre-sampler measures the energy loss experienced by electrons and photons before they enter the calorimeters.

- **Hadronic Calorimeters:** These calorimeters employ both LAr ionisation technology and tile scintillation technology. Figure 3.8 provides a visual representation of the sub-detectors of the hadronic calorimeters:

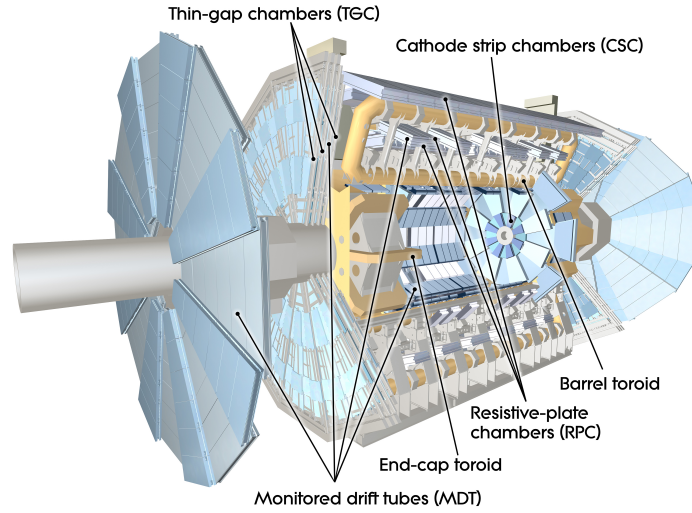


**Figure 3.9.:** The ATLAS Muon Spectrometer[31]

- Tile Barrel and Tile Extended Barrel calorimeter - These segments utilise plastic scintillating tiles as the active medium, with the former covering  $|\eta| < 0.9$  and the latter covering  $0.8 < |\eta| < 1.7$ .
- Hadronic endcap (HEC) calorimeter - Similar to the EMEC, it utilises LAr as active component, but copper serves as passive absorption material. This component consists of two wheels with a coverage of  $1.5 < |\eta| < 3.2$ .
- Forward Calorimeters (FCal): These calorimeters are positioned 4.7 meters away from the interaction point and is in close proximity to the endcap calorimeters, as depicted in Figure 3.8. It consists of three sub-components, namely one electromagnetic calorimeter and two hadronic calorimeters. It covers a range of  $3.1 < |\eta| < 4.9$ . In terms of construction, all three layers of the FCal utilise liquid argon as the active medium. However, the electromagnetic calorimeter incorporates copper as the passive medium, while the two hadronic calorimeters utilise tungsten. The primary objective of the FCal is to measure and record the energy of highly energetic particles that traverse close to the beam.

### 3.2.4. Muon Spectrometer

In order to traverse the entire calorimeter system without energy loss, a particle must be non-interacting or minimally ionising. Neutrinos belong to the former category, making their detection challenging for any detector component. However, muons exhibit minimal ionisation, leading to the need of a specialised set of detectors known as the muon spectrometer (MS) [32] for their measurement. Consequently, muons often exhibit clean signatures as their reconstruction primarily relies on interactions within the MS.

The ATLAS muon spectrometer (MS), shown in Figure 3.9, operates within a strong magnetic field generated by superconducting toroids. This magnetic field plays a crucial role in measuring the momenta of muons based on their track curvature. The MS consists of four different sub-detectors, each equipped with gaseous chambers that undergo ionisation when charged particles pass through them, resulting in the generation of a signal. Two of the sub-detectors

are located in the barrel region with a peak 3.9 T magnetic field, while the other two sub-detectors are situated in the endcap region with a peak 4.1 T magnetic field. Within each of these regions, one sub-detector is responsible for providing an approximate measurement of the muon momentum, enabling quick identification of muons for event triggering, while the other sub-detector is specifically designed to precisely determine the muon momentum. In particular,

- The precision tracking chambers primarily utilise monitored drift tubes (MDTs) in the barrel and endcap regions, covering a wide range of  $|\eta| < 2.7$ . MDTs are gas-filled tubes equipped with a central wire to collect ionisation signals when a particle passes through. In the innermost layer of the endcaps, where muon rates are higher at low angles, cathode strip chambers (CSCs) are used instead owing to their ability to withstand higher particle flux. These detectors feature thin metal cathode strips with gas-filled gaps. Additionally, they are surrounded by anode wires to collect the ionisation signals.
- The fast muon triggering system, covering  $|\eta| < 2.4$ , incorporates Resistive Plate Chambers (RPCs) in the barrel region and Thin Gap Chambers (TGCs) in the endcap region. RPCs consist of gas-filled parallel electrode plates subjected to a strong electric field. This configuration leads to the generation of ionisation avalanches when a particle passes through the chamber, resulting in fast signals. TGCs operate similar to CSCs, but utilise smaller wire distances and a stronger electric field, enabling faster signal generation. Both RPCs and TGCs offer timing resolutions below 5 ns, which is shorter than the LHC bunch crossing time of 25 ns, thereby ensuring efficient triggering.

### 3.2.5. Trigger and Data Acquisition

The LHC collides proton bunches at a high rate of 40 MHz, resulting in a significant amount of data. Storing and processing all of these data is not feasible. Hence, the trigger system selectively records a subset of events that have potential importance for physics analyses.

The ATLAS trigger system consists of two levels: the Level 1 (L1) trigger and the High-Level Trigger (HLT) [18]. The L1 trigger operates at the hardware level and reduces the event rate from 40 MHz to 100 kHz. It quickly analyses inputs from low granularity calorimeters and muon chambers to make prompt decisions. Within a  $2.5\mu\text{s}$  time window after each bunch crossing, the L1 trigger identifies interesting events. The HLT operates at the software level and applies advanced tracking and reconstruction algorithms to the events selected by L1. It further reduces the event rate to 1 kHz. The data from the HLT is then transmitted to the LHC Computing Grid, a distributed computing infrastructure with servers located globally. The primary role of the LHC Computing Grid is to process the collision data and provide computational resources for analyses to ATLAS collaboration members.

## Part I.

## Chapter 4.

# Electronic Calibration for Liquid Argon Calorimeter

The nominal resolution for a particle with energy  $E$  is given by [33]

$$\frac{\sigma}{E} = \frac{a}{\sqrt{E}} \oplus \frac{b}{E} \oplus c \quad (4.1)$$

where  $a$  accounts for statistical fluctuations in the energy measurement,  $b$  accounts for electronic noise and pileup and  $c$  accounts for fluctuations in the detector response and imperfections in the detector construction. The first two terms are inversely proportional to the energy of the particle or the square root of it, whereas the *constant term*  $c$  depends solely on the characteristics of the detector and not on the energy of the particle. As a result, the constant term becomes the dominant factor in determining the resolution at high energies.

Electronic calibration aims to minimise fluctuations that could contribute to the constant term by equalising the response of the detector across all readout channels. It is performed using calibration pulses of known amplitude that are injected into the detector cell to probe its electronic response. Additionally, any non-uniformity in the calibration system itself can contribute to the constant resolution term too. Consequently, a highly-precise calibration system is crucial to achieve excellent measurements of particle energies over the entire range.

By design, the constant term in the energy resolution of the LAr electromagnetic calorimeter is  $\sim 0.7\%$ . In order to achieve this, the readout electronics response should be equalised to better than  $0.25\%$  over the entire energy range. The same calibration system is also used for the liquid argon hadronic and forward calorimeters. [34]

In the following sections, the calibration system for the liquid argon calorimeter and its proposed upgrade is described. In particular, Section 4.1 outlines the LAr readout electronics, Section 4.2 describes the LAr calibration system, Section 4.3 focuses on the energy computation process in LAr calorimeters, and lastly Sec 4.4 highlights the need to upgrade the calibration system for the High-Luminosity LHC.

### 4.1. Readout Electronics

The LAr readout electronics system [25] is designed to record energies spanning from 50 MeV to approximately 3 TeV for 182,468 detector cells. The architecture, shown in Figure 4.1, consists of two primary components: the radiation-hard Front-End (FE) electronics which

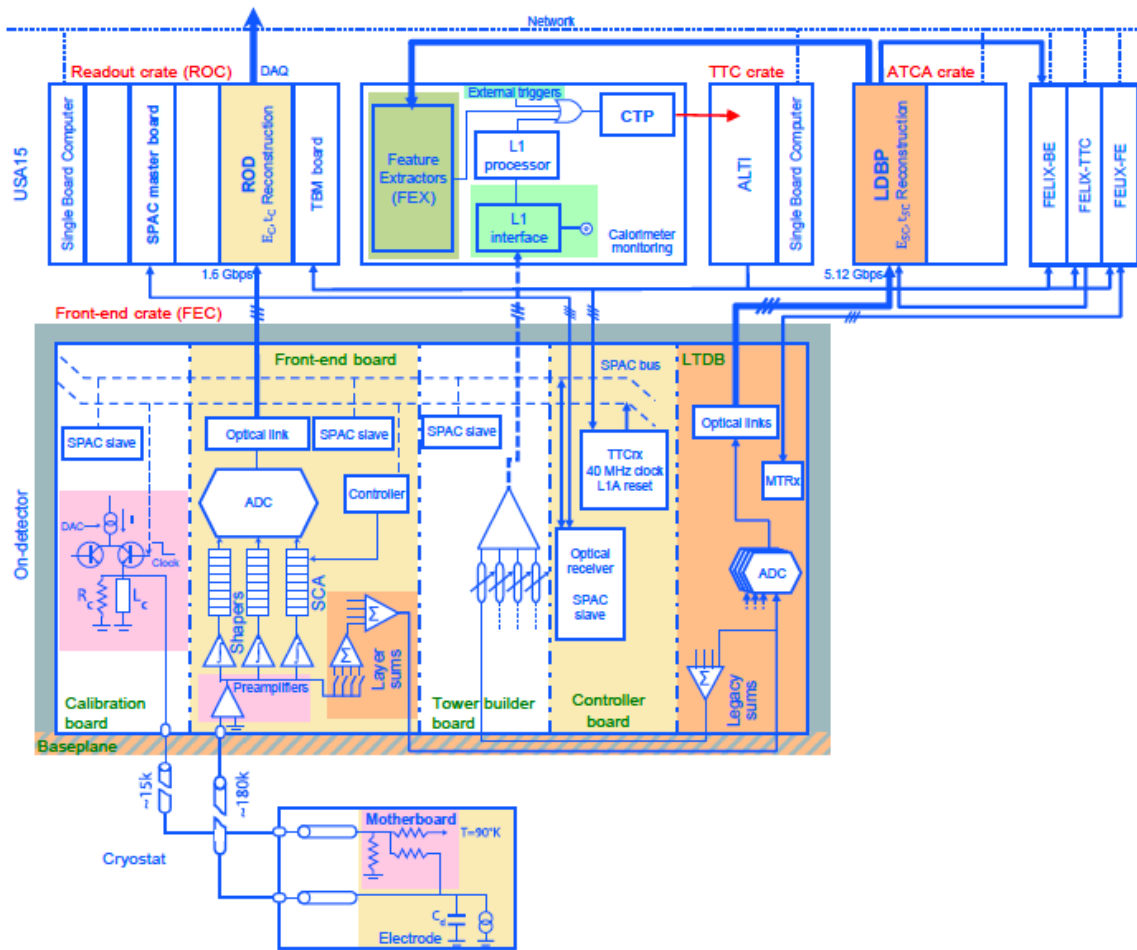


**Figure 4.1.:** The schematic block diagram of the current LAr readout electronics architecture. In this representation, the LAr ionisation signal proceeds upwards, through the front-end crates mounted on the detector to the off-detector electronics. This diagram is valid for the electromagnetic calorimeters; the HEC and FCal have additional electronics inside the endcap cryostats. [25]

are positioned on the detector, and the Back-End (BE) electronics situated in the USA15 counting room away from the detector.

The FE system consists of Front End Boards (FEB) that are responsible for the readout and digitisation of the calorimeter signals, calibration boards that inject precise pulses in order to calibrate the readout-electronics, boards dedicated to generating analog sums for the Level 1 trigger, as well as additional control and monitoring boards. The BE system mainly consists of Readout Driver (ROD) boards that reconstructs the energy and timing of the calorimeter signal.

#### 4.1.1. Principle of Signal Readout

Charged particles that are incident on a detector cell form particle showers and ionise the liquid argon within the active gaps. The resulting ionisation electrons move through the gap

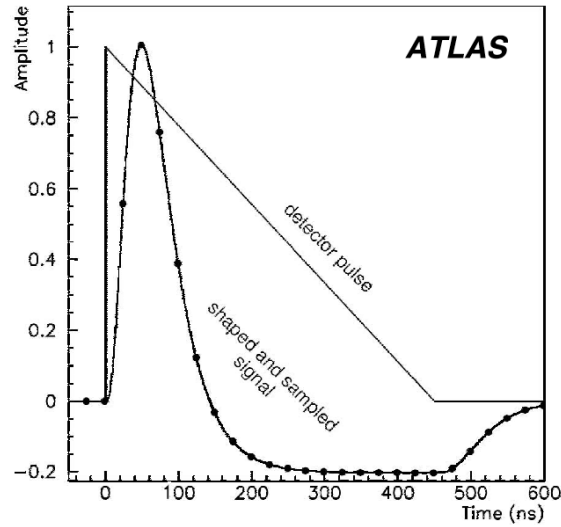


**Figure 4.2.:** Shapes of the LAr calorimeter current pulse in the detector and of the signal output after bipolar shaping. The dots indicate an ideal position of samples separated at LHC bunch crossing frequency.[28]

under the influence of a high voltage, creating a triangular signal pulse (shown in Figure 4.2) whose magnitude is directly proportional to the energy released by the incident particle.

The signal is then processed by front-end boards (see Figure 4.1), where it is transmitted through two paths<sup>1</sup>: the analog path for the Level 1 calorimeter trigger system, and the digital path for physics reconstruction. In both paths, the signal is amplified using a pre-amplifier and shaped using a bipolar CR-RC<sup>2</sup> filter to optimise the signal-to-noise ratio. Within the digital path, the signal is divided into three overlapping linear gain scales to accommodate the wide dynamic range required for the expected physics signals (see next paragraph). At this stage, the signal is sampled at the LHC bunch-crossing frequency (40 MHz) and temporarily stored in an analog pipeline called Switched Capacitor Array (SCA). This shaped and sampled signal is shown in Figure 4.2. Upon acceptance by the Level 1 trigger, the analog value retrieved from the SCA is digitised using a 12-bit analog-to-digital converter (ADC) and transmitted with the proper gain to the Back-End electronics.

### Electronic Gain

The three FEB gain scales, namely high, medium, and low, pertain to distinct configurations of the front-end electronics amplification employed for reading signals from the detector elements.

- **High gain:** This setting provides a higher amplification factor for the signals. It is typically used for detecting and measuring low-energy particles or signals with low amplitudes. The high gain setting allows for increased sensitivity and precise measurements in situations where the signal amplitudes are small.
- **Medium gain:** This setting offers a moderate amplification factor. It is often used for detecting and measuring signals of intermediate amplitudes. The medium gain setting

<sup>1</sup> Note: this refers to the Run-2 configuration

provides a balanced amplification level suitable for a wide range of particle energies or signal strengths.

- Low gain: This setting provides a lower amplification factor. It is used for detecting and measuring high-energy particles or signals with large amplitudes. The low gain setting is employed to prevent signal saturation in situations where the incoming signals have higher amplitudes, ensuring that the readout electronics can accurately measure and process the signals.

By having multiple gain settings, the ATLAS detector can adapt to different particle energies and signal strengths, optimising the readout process for various physics scenarios.

## 4.2. Electronic Calibration System

The electronic calibration of the LAr calorimeter [25] [28] is performed using calibration boards installed in front end crates (as shown in Figure 4.1). Its goal is to inject current pulses, that mimic the liquid argon ionisation ("physics") pulse, of precisely known amplitude on a detector cell in order to probe its electronic response.

### 4.2.1. Principle of Calibration

As mentioned before, an ionisation pulse takes the form of a triangular pulse, characterised by the typical drift time in the LAr gap. However, reproducing a similar pulse using electronic circuits poses difficulties. As a solution, an exponential calibration pulse is chosen, with the decay time adjusted to closely approximate the desired triangular shape, particularly in the initial phase of the pulse. Despite this optimisation, there remains a residual disparity in shape between the physics pulse and the calibration pulse. To address this, the properties of the calibration pulse are directly measured and incorporated into the electronic calibration process.

The use of fast shaping for the LAr calorimeter makes the detector response sensitive to the time dependence of the ionisation signal. Thus, the calibration signal needs to be distributed directly at the input of the detector cell<sup>2</sup>. Meanwhile, to avoid exposure to high radiation flux, all active components of the calibration system need to be kept outside the cryostat. Consequently, a voltage-driven calibration system was chosen for the present calibration board with only the injection resistors in the liquid argon cryostat. These injection resistors are precise at the 0.1% level, show little sensitivity to stray capacitances and are radiation-hard.

The schematic of the current calibration system is shown in Figure 4.3. In this system, an exponential signal is generated from a precise current  $I_{DAC}$  using an inductor  $L$ . By default, the transistor  $Q_1$  is allowing current to flow through the inductor. When the *command* transistor  $Q_2$  is closed, the current is redirected to the ground cutting  $Q_1$  off. At this point, the magnetic energy stored in the inductor is transferred to the resistance  $R_0$  and an exponentially decaying voltage pulse is produced: [25]

$$-R_0 I_{DAC} e^{-\frac{t}{\tau_{cal}}} \quad (4.2)$$

<sup>2</sup> In the FCal, the calibration signal is injected into the FEB and not the detector cell to avoid the high radiation levels

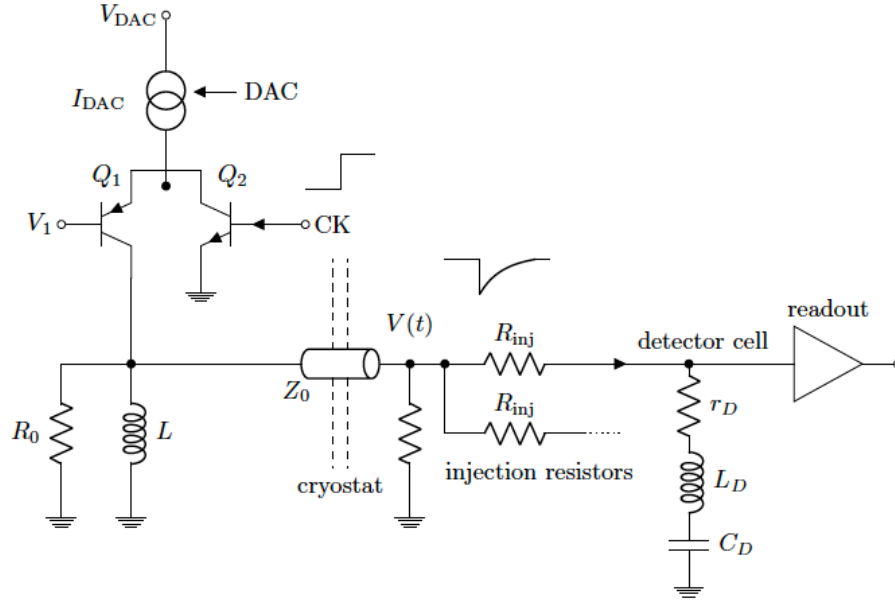


**Figure 4.3.:** Voltage driven calibration schema for the ATLAS LAr calorimeter. Left part of the diagram is located on the electronics calibration board, while the right part corresponds to the distribution of the signal to the calorimeter cells done with precision injection resistors in the liquid argon.[28]

where  $\tau_{\text{cal}} = 2L/R_0$ . Typically, the component responsible for providing the inductance  $L$  also has a minor resistive component  $r$  that impacts the exponential waveform. Considering this effect, the calibration pulse adopts the form:

$$-R_0 I_{DAC} [(1 - f_{\text{step}}) e^{-\frac{t}{\tau_{\text{cal}}}}] \quad (4.3)$$

where  $f_{\text{step}} = \frac{r}{r + \frac{R_0}{2}}$ ,  $f_{\text{step}} \in [0, 1]$  and now  $\tau_{\text{cal}} = \frac{L}{r + \frac{R_0}{2}}$ .

This signal is then propagated inside the cryostat with a cable of impedance  $Z_0 = R_0$ , that is terminated on both ends with a precision resistance network equivalent to  $R_0$  in order to minimise any reflection of the signal.

#### 4.2.2. Calibration Board

An image of the current calibration board [34], comprising 128 calibration channels, is shown in Figure 4.4. Each channel injects exponential pulses, characterised by a fast rise time (below 1 ns) and a long decay time ( $\sim 450$  ns), simultaneously onto a fixed number of detector cells. This number ranges from 1 to 32 depending on the layer and detector.

The board is equipped with a 16-bit digital-to-analog converter (DAC) that sets the amplitude of the calibration pulses. This DAC voltage is distributed across the board via low offset operational amplifiers (op-amps), and converted to a precise current ( $I_{DAC}$ ) using an external 0.1% resistor. The calibration pulse is then generated, according to the principle described in section 4.2.1, using a high-frequency switch (i.e. pair of PMOS/NPN transistors  $Q_1$  and  $Q_2$ ), an inductor  $L$  and a resistance  $R_0$  for each calibration channel of the board.

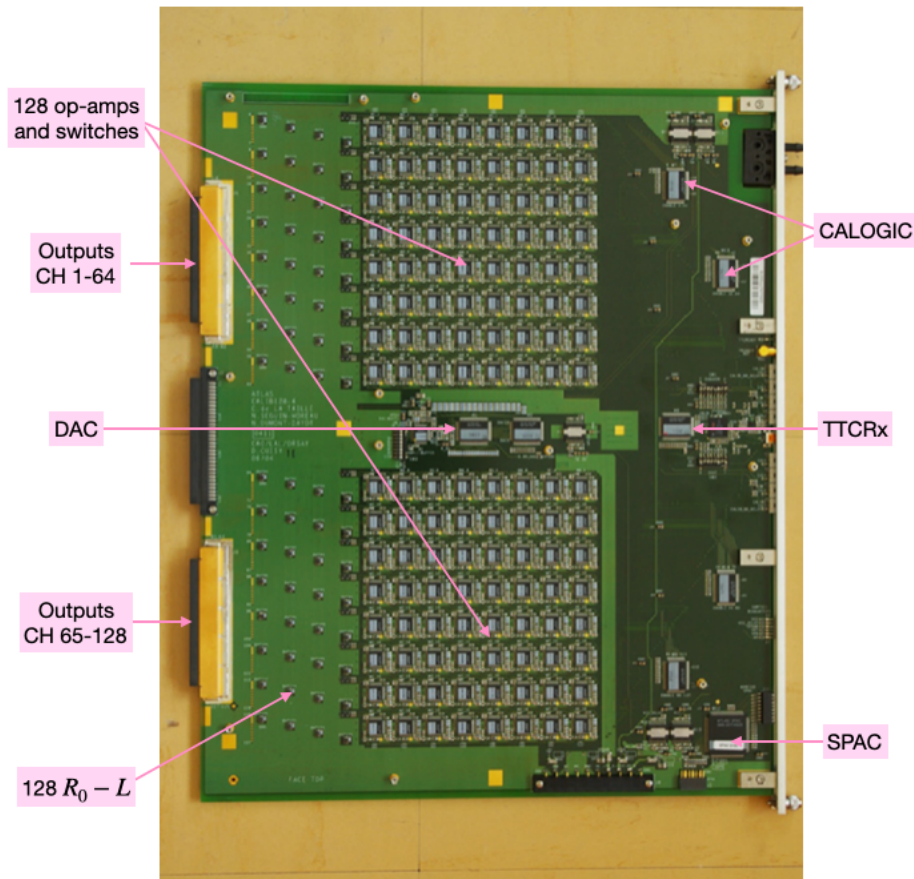


**Figure 4.4.:** Existing ATLAS LAr calibration board. Left side of the board corresponds to the analog architecture, and right side to the digital part. The size of the board, determined by the front end crate where it is placed, is  $410 \times 490 \text{ mm}^2$ .

The digital part of the board manages the communication with the external world, the loading of parameters, and the control of the board. Its main components (seen in Figure 4.4) are:

- *CALOGIC* These six chips have been specifically designed to manage the board control logic: four of them control the 128 channels of the board, one of them configures the DAC and the last one generates calibration/reset commands.
- *TTCRx* As the calibration board must generate commands synchronous to the LHC machine, this chip receives commands from the ATLAS TTC (Timing Trigger Control) system and distributes the 40 MHz clock to the different digital chips.
- *SPAC slave*<sup>3</sup> It handles the connection to the external world and drives the other chips of the board using I2C protocol.

Since the board is placed in the front end crate, all its components are radiation hard. Moreover, the calibration system is highly accurate (integral non-linearity better than 0.1%), extremely stable (stability better than 0.1% with respect to time and temperature) and has excellent precision (uniformity among channels below 0.25%).

<sup>3</sup> The SPAC (Serial Protocol for ATLAS Calorimeter) has been specially designed for the ATLAS calorimeters

### 4.3. Energy Reconstruction

In order to determine the raw energy deposited in a specific cell  $E_{\text{cell}}$ , the amplitude of the pulse  $A$  is converted from ADC units to energy in MeV using the following formula: [35]

$$E_{\text{cell}} = F_{\mu\text{A} \rightarrow \text{MeV}} \times F_{\text{DAC} \rightarrow \mu\text{A}} \times \left( \frac{M_{\text{phys}}}{M_{\text{cali}}} \right)^{-1} \times G \times A \quad (4.4)$$

- $G$  is the cell electronic gain determined from calibration runs and is used to convert the pulse amplitude from ADC units to current in DAC units as set on the calibration board
- $\frac{M_{\text{phys}}}{M_{\text{cali}}}$  corrects for the difference in maxima between the calibration pulse and the physics pulse
- $F_{\text{DAC} \rightarrow \mu\text{A}}$  converts current measured in calibration board DAC units to  $\mu\text{A}$  and accounts for the values of the injection resistors
- $F_{\mu\text{A} \rightarrow \text{MeV}}$  converts reconstructed pulse current from  $\mu\text{A}$  to energy in MeV

All calibration constants used in the cell energy reconstruction, except for  $F_{\text{DAC} \rightarrow \mu\text{A}}$  and  $F_{\mu\text{A} \rightarrow \text{MeV}}$ , are determined through calibration runs (see below). These constants undergo continuous monitoring and validation to ensure the best electronic calibration of the LAr detectors at any given time. The  $F_{\text{DAC} \rightarrow \mu\text{A}}$  and  $F_{\mu\text{A} \rightarrow \text{MeV}}$  conversion factors are obtained from first-principle calculations, and then refined by comparing the detector response to real data from beam tests and corresponding Monte Carlo simulations.

**Calibration runs:** During periods without beam, such as the time between LHC fills, a series of dedicated calibration runs are conducted: Pedestals, Delays, and Ramps. Pedestal runs measure the baseline level and noise properties of a cell's readout electronics, ramp runs measure the readout gains, and delay runs measure the pulse shape for each readout cell. Additionally, an independent set of calibration runs is performed for each of the three LAr electronic readout gains. [25]

### 4.4. Electronic Calibration Upgrade for HL-LHC

The High-Luminosity Large Hadron Collider (HL-LHC) project is an upgrade of the LHC that aims to reach an instantaneous luminosity of 5 to 7.5 times higher than the nominal LHC value. In order to achieve this accelerator performance, major upgrades will be carried out during Long Shutdown 3 (2026-2028), as shown in the timeline in Figure 3.3.

In particular, the existing ATLAS LAr readout electronics need to be completely replaced mainly due to i) increased radiation exposure on the LAr front-end components, and ii) incompatibility with the proposed ATLAS trigger updates in order to combat greater pileup at the HL-LHC. Consequently, new calibration boards will be installed on the detector as well.

#### 4.4.1. Motivations for Calibration Upgrade

Since no changes are foreseen in the LAr cryostat, the existing voltage driven calibration scheme (described in Section 4.2.1) will be used in the HL-LHC as well. However, the current calibration boards must be replaced for the following main reasons: [25]

- The existing calibration boards were developed using DMILL [36] technology. However, the limited availability of spare components and boards, coupled with the unavailability of DMILL technology for manufacturing additional components in case of malfunction, necessitates the development of new radiation-hard calibration boards for the HL-LHC.
- In some regions of the calorimeter, the pre-amplifiers will be replaced to avoid saturation. This renders the standard CMOS technology<sup>4</sup>, used in high-frequency switches of the current calibration boards, unsuitable for calibration over the necessary dynamic range. Thus, new calibration boards need to be developed with alternative high voltage technologies.
- The current boards are controlled via the SPAC protocol that will not be supported in the HL-LHC. Thus, new calibration boards need to be developed that will be compatible with the alternate lpGBT (Low Power GigaBit Transceiver) [37] data transmission scheme instead.
- The existing boards rely on dedicated voltage lines that will not be compatible with the upcoming HL-LHC FEB voltage power distribution scheme. This further emphasises the need to design new calibration boards.

---

<sup>4</sup> CMOS (Complementary Metal-Oxide-Semiconductor) technology is a widely used semiconductor fabrication process known for its low power consumption, high noise immunity, and high integration density. It utilises complementary pairs of p-type and n-type transistors to create integrated circuits.

## Chapter 5.

# Liquid Argon Calibration ASIC Prototype for HL-LHC

The main element of the calibration board is the calibration ASIC<sup>1</sup> that consists of:

- Analog Section: HF switch, or "pulser", that generates the pulse
- Digital Section:
  - DAC that sets the amplitude of the calibration pulse
  - The link between the analog section of the calibration ASIC and the lpGBT chip. Its main functions include selecting the desired calibration channel(s), setting the DAC value, and delivering command pulse<sup>2</sup>.

The subsequent sections provide a comprehensive overview of the calibration ASIC prototype for the High-Luminosity LHC. Specifically, section 5.1 describes the requirements and specifications of the ASIC, while section 5.2 delves into the various prototypes developed for the LHC. Lastly, section 5.3 presents the findings from the prototype that I investigated, with a particular focus on my involvement in the irradiation tests, and section 5.4 summarises the current status of the project.

### 5.1. Specifications of Calibration ASIC

The main specifications of the calibration ASIC are as follows [25] [38]:

- **Uniformity and Linearity**
  - (i) Integral non-linearity (INL) of the DAC output, i.e. a measure of the deviation in linearity between injected DAC value and measured DAC value, should be better than 0.1% in the high gain range, better than 0.2% in the intermediate range and better than 1% in the low range of the FEB. Mathematically, INL is given by

$$\text{INL (\%)} = \frac{\text{measured value-best fit value}}{\text{maximum measured value}} \times 100 \quad (5.1)$$

A highly linear DAC is needed to interpolate calibration DAC values.

---

<sup>1</sup> Application Specific Integrated Circuit

<sup>2</sup> The command pulse is applied to the command transistor  $Q_2$  within the HF switch, allowing it to be toggled on or off.

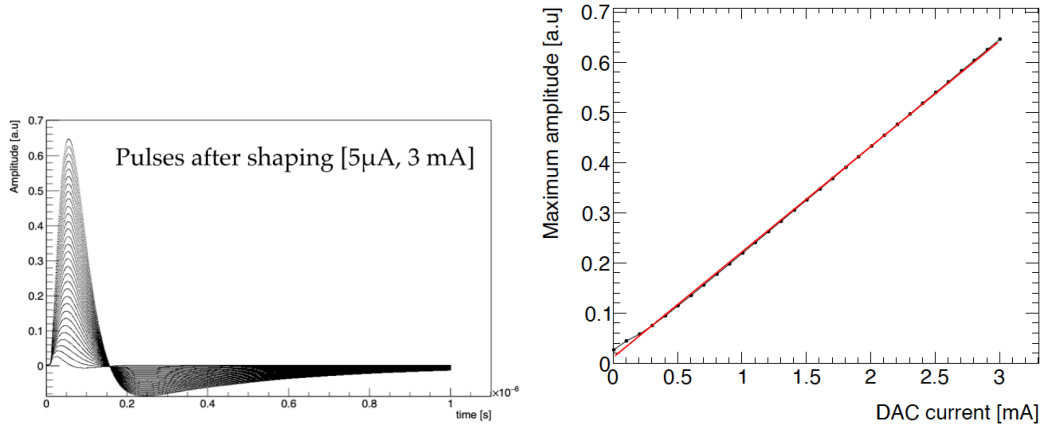


**Figure 5.1.:** Left: Pulse amplitude as a function of time for injected DAC ranging from  $5\ \mu\text{A}$  to  $3\ \text{mA}$ ; Right: Extracted maximum amplitude as a function of the injected DAC. The data, represented in black, shows an output signal when  $\text{DAC}=0$ . This is the injected current. The red line corresponds to the best fit to compute the INL. [39]

- (ii) Integral non-linearity of the pulser output after shaping, i.e. a measure of the deviation in linearity between maximum pulse amplitude and DAC value, should be better than  $0.1\%$  in the high gain range, better than  $0.2\%$  in the intermediate range and better than  $1\%$  in the low range. This is needed to correct the FEB response accurately.
- (iii) Calibration pulse rise time, which refers to the duration it takes for the pulse to increase from  $20\%$  to  $80\%$  of its maximum amplitude, should be within  $0.5$  and  $1.5\ \text{ns}$

The primary factor influencing the rise time is the characteristics of the HF switch transistors. Thus, the HF switch be carefully designed to fulfil this requirement.

- (iv) Pulse distortion introduced by parasitic inductive paths must be kept at a minimum, i.e. *injected current* should be at most  $50\ \mu\text{A}$

The experience with the current calibration board has shown that an output signal is detected even when the input DAC is set to zero (see Figure 5.1). This signal, referred to as *injected current*, arises due to unavoidable parasitic couplings on the transistors employed in the HF switch. Fortunately, it does not pose a significant problem for the calibration procedure as it primarily represents an offset that can be corrected.

To account for it, two methods can be employed. The first method involves subtracting the parasitic pulse from all pulses at larger currents. The second method entails measuring all pulse amplitudes at a fixed time, specifically the peak time for pulses with larger amplitudes. This approach works because the injected charge acts as the derivative of the signal, such that when a fixed time is taken, the parasitic signal should be cancelled out. Both approaches facilitate the recovery of pulse linearity at low currents.

Nonetheless, it is crucial to keep the injected current minimal to ensure accurate measurement of the readout response within the relevant dynamic range. An

estimated tolerable level of approximately  $50 \mu\text{A}$  for the injected current has been determined. This value corresponds to around 500 MeV in an EMB front cell (from Equation 4.4, which is equivalent to approximately 2% or less of the FEB high gain range. It is imperative to design the HF switch accordingly to address this consideration.

- **Dynamic Range**

- (i) Dynamic range of 16-bits

The LAr calorimeter is designed to record energies spanning from  $\sim 50$  MeV up to 3 TeV. In order to generate calibration pulses over this energy range, given a LSB (Least Significant Bit) of 50 MeV, the dynamic range should be 16-bits<sup>3</sup>.

- (ii) DAC amplitude should range from  $5 \mu\text{A}$  to 300 mA

In some regions of the calorimeter, the 5 mA pre-amplifiers will be replaced by 10 mA ones in order to avoid saturation. Through simulation studies, it has been determined that the maximum input current expected for these new pre-amplifiers is  $\sim 7.5$  mA. This implies that  $I_{DAC}$  should also cover at least 75% of the dynamic range provided by the new pre-amplifiers<sup>4</sup>. Consequently, the maximum value of  $I_{DAC}$  should be at least 300 mA.

$I_{DAC}=5 \mu\text{A}$  corresponds to energy deposits of MIPs (Minimum Ionising Particles) in the calorimeter, i.e. approximately 50 MeV and 250 MeV in the EMB front and middle cells respectively. Since the detector's response to MIPs is crucial for interlayer calibration, the minimum DAC amplitude should be  $5 \mu\text{A}$ .

- (iii) Pulse voltage should range up to 7.5 V, i.e. the pulser should be implemented in HV-CMOS technology

In order to reach  $I_{DAC}$  of 300 mA, the pulser should deliver voltage pulses up to 7.5 V. The standard CMOS technology (used in the existing pulsers) cannot be used since they are limited to 3.3 V. Thus, the new pulser has to be implemented in the HV-CMOS technology.

<sup>3</sup> Number of bits =  $\log_2(\text{Max. energy}/\text{LSB}) \approx 16$

<sup>4</sup> In FEB, the injection resistor is  $1 \text{ k}\Omega$ , while in the calibration board, it is  $25 \Omega$ . Using the formula for current ( $I = V/R$ ), we can determine that 1 mA for the pre-amplifier corresponds to 1V in the FEB ( $1\text{mA} \times 1\text{k}\Omega = 1\text{V}$ ), which is equivalent to 40 mA for the calibration DAC ( $1\text{V} / 25 \Omega = 40 \text{ mA}$ ).

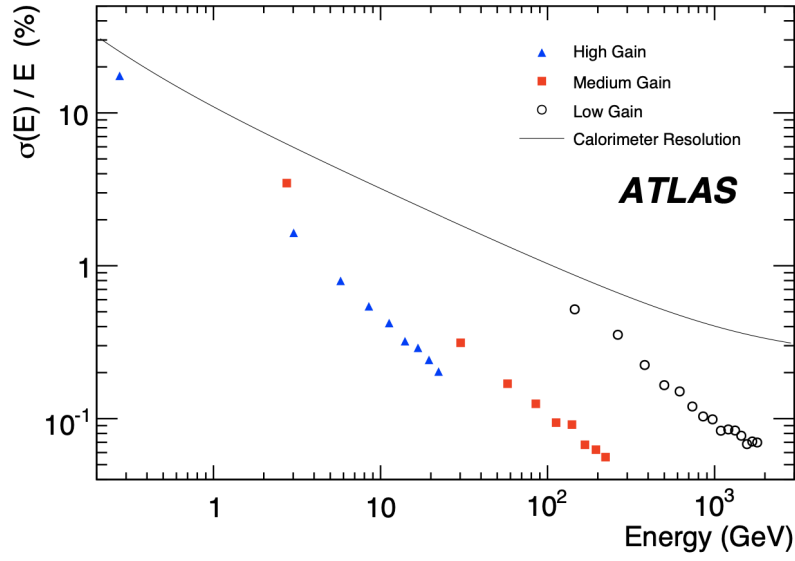


**Figure 5.2.:** Energy resolution versus energy of a representative EMB second layer channel, as measured during Ramp runs. The points represent the data, while the solid curve shows a parametrization of the total calorimeter energy resolution, given by equation 4.1. [40]

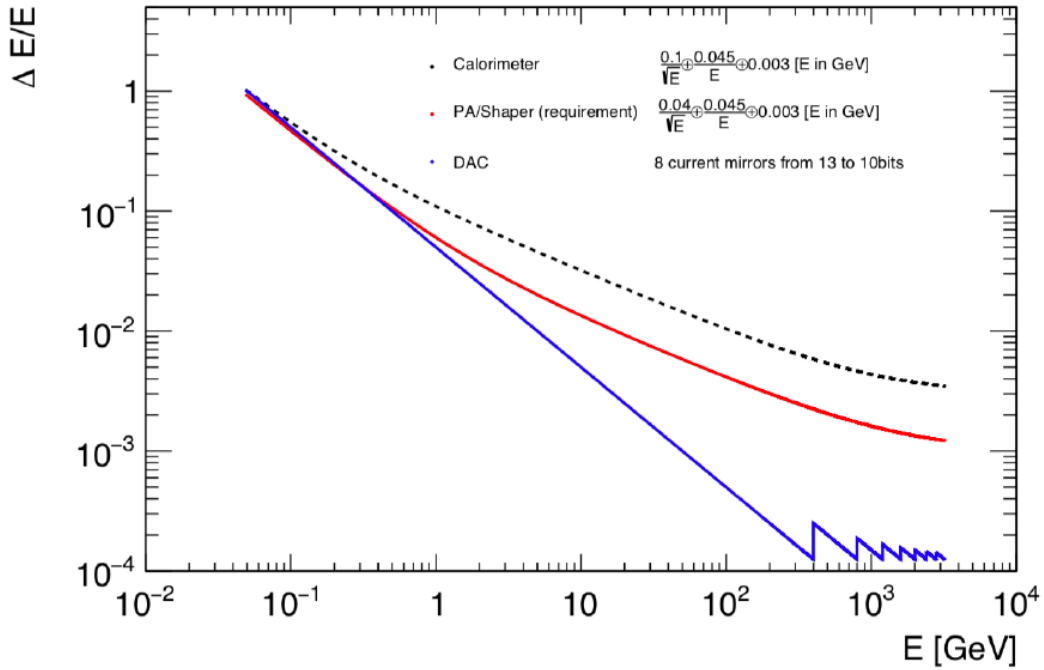


**Figure 5.3.:** Relative energy resolution of a calibration DAC with a true 13-bits resolution in the range up to 40 mA, and implementing the additional 3-bits to cover the 16-bits range with additional gain factors, compared to the expected FEB pre-amplifier and shaper noise performance and the intrinsic calorimeter resolution. [38]

Position	TID [Gy]	NIEL [ $n_{eq}/\text{cm}^2$ ]	SEE [ $h/\text{cm}^2$ ]
FEC (barrel)	1400 (1.5)	$4.1 \times 10^{13}$ (2)	$1.0 \times 10^{13}$ (3)
FEC (endcap)	210 (1.5)	$6.0 \times 10^{12}$ (2)	$1.2 \times 10^{12}$ (3)

**Table 5.1.:** Radiation tolerance requirements for the operation at the HL-LHC for a total luminosity of  $4000\text{fb}^{-1}$ , including safety factors given in brackets. This table supersedes Table 3.1 from the LAr Phase-II Electronics Upgrade TDR [25] and is based on the most recent simulations.

### • Resolution

- (i) The system should have a LSB of at least  $5 \mu\text{A}$

This specification arises from the previously mentioned requirements of a 16-bit dynamic range with  $I_{DAC}$  ranging from  $5 \mu\text{A}$  to  $\sim 300 \text{ mA}$ <sup>5</sup>.

- (ii) DAC should have a resolution of 13-bits

As stated before, the calibration system needs a dynamic range of 16-bits. However, achieving this range does not necessitate a 16-bit DAC. This is due to the fact that the energy resolution at intermediate and high energy ranges is dominated by the intrinsic calorimeter resolution itself.

The matter can be further understood via Figure 5.2 that shows the relative energy resolution for a second layer channel in the EMB. In this channel, the local constant term  $c$  of the resolution function (Equation 4.1) is  $0.25\%$ <sup>6</sup>. And from the plot, it can be seen that the energy resolution for medium and low gain (i.e. particles with intermediate and high energies) remains roughly below  $c$  most of the time.

Consequently, the calibration DAC could have a resolution of around 10-11 bits, with additional gain factors implemented to achieve the required 16-bit dynamic range. As an example, figure 5.3 shows the relative energy resolution achieved using a 13-bit calibration DAC (that is equivalent to  $40 \text{ mA}$ , given LSB of  $5 \mu\text{A}$ ) combined with 8 current mirrors to implement the additional 3 bits. It can be seen that the resolution for  $I_{DAC} > 40 \text{ mA}$  is always better than the expected readout noise and calorimeter resolution.

### • Stability

- (i) Tolerance to radiation levels expected at the HL-LHC

The radiation tolerance specifications for the Front End Crates (FEC) are shown in Table 5.1. In this table, TID (Total Ionising Dose) quantifies the cumulative long-term degradation caused by ionising radiation. NIEL (Non-Ionising Energy Loss) describes the atomic displacements resulting from radiation, where the energy is dissipated as lattice vibrations. Lastly, SEE (Single Event Effects) refer to any detectable alteration in the condition or operation of a system caused by the

<sup>5</sup>  $\text{LSB} = I_{DAC} \text{ range} / 2^{16}$

<sup>6</sup> The global constant term across the entire electromagnetic calorimeter remains  $0.7\%$ , but the local constant term depends on the calorimeter region

impact of a solitary energetic particle. These effects can be categorised into two types: "soft" or temporary errors that can be reversed, and "hard" or permanent consequences that lead to lasting deterioration. Since the calibration boards are located in the FECs, the calibration ASIC needs to sustain these radiation levels.

- (ii) The ASIC should be stable to variations in time and temperature. In particular, it should maintain a stability level of better than 0.1% over the course of a full year of data-taking. Furthermore, it should demonstrate stability with respect to temperature in the FECs that is better than 0.1% per degree.

## • Design of Calibration ASIC

### (i) Calibration DAC

The calibration board needs to fulfil two specific requirements:

- (a) it should simultaneously operate 16 out of 128 calibration lines at maximum DAC current (i.e.  $I_{DAC}=300$  mA) while adhering to the linearity and uniformity specifications discussed above. This functionality is crucial for efficiently conducting calibration runs.
- (b) it should simultaneously operate all 128 calibration lines, but at a reduced DAC current, while allowing for a relaxed uniformity requirement of  $\sim 1\%$  between the channels of the EM calorimeter. For instance, an input  $I_{DAC}$  of 10 mA corresponds to approximately 100 GeV in the middle EMB cells. This setup enables the detection of a signal in all gains of the FEB2, which is beneficial for debugging purposes.

These requirements have implications for the design of the calibration ASICs. In contrast to the current calibration board, where a single DAC serves all 128 calibration lines, the new calibration board will have multiple DACs, with each DAC serving a smaller subset of calibration lines.

The optimal ratio between the number of DACs and calibration lines depends on various factors. On one hand, having a small number of calibration lines per DAC would provide greater flexibility in using the calibration board, as it would allow a large number of calibration lines to be simultaneously enabled at different current values. However, this approach may introduce challenges when it comes to the design of the board layout.

For efficient routing on the calibration board, an optimal configuration would involve incorporating 32 DACs. This implies that each calibration ASIC should comprise 1 DAC, 4 HF switches and the digital link.

### (ii) Calibration HF Switch

As previously stated, the HF switch for the new calibration ASIC requires HV-CMOS technology to deliver voltage pulses up to 7.5V. The ATLAS collaboration has chosen XT018 (180 nm) technology from the XFAB foundry for this purpose. However, the radiation hardness of this technology has not been tested in the context of HL-LHC doses. Therefore, during the development phases of the calibration ASIC, it is essential to verify the performance of the chosen design under XFAB technology with respect to irradiation.

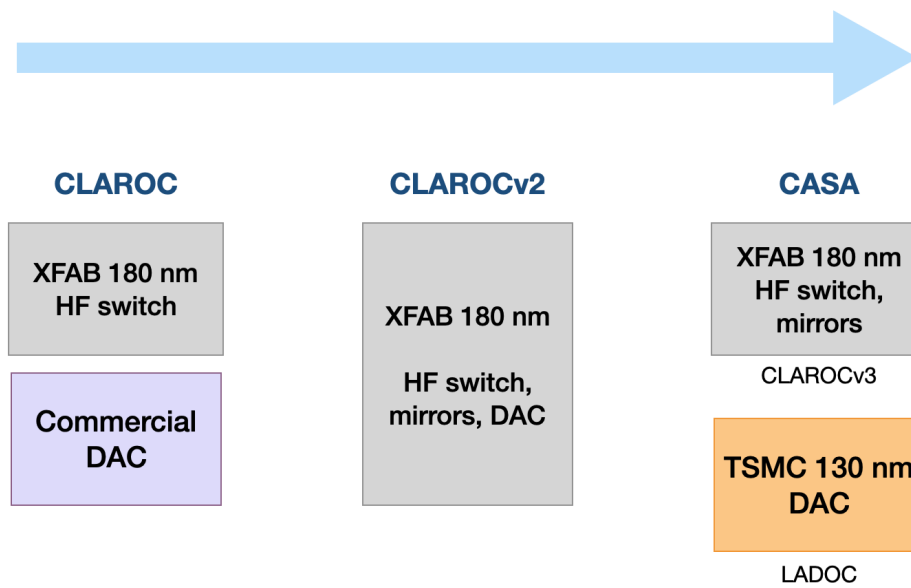


**Figure 5.4.:** Schematic denoting the developments of calibration ASIC prototype for HL-LHC

## 5.2. Developments of Calibration ASIC Prototypes

Several rounds of calibration ASIC prototypes for the HL-LHC have been developed so far. A schematic of the progress has been illustrated in Figure 5.4. These prototypes are:

- **Prototype I (2018)**

The first calibration ASIC prototype, named CLAROC [41] (Calibration of Liquid Argon Output Chip), had a primary focus on evaluating the performance of the HF switch using the new XFAB technology [42]. Consequently, the prototype incorporated only the XFAB HF switch, while the DAC was obtained externally from a commercial component. Furthermore, the prototype featured six distinct configurations of the HF switch, varying in transistor size and placement. These configurations were implemented to assess and identify the optimal configuration for integration into the final calibration ASIC.

This prototype exhibited excellent performance: in particular, irradiation up to 50 kGy did not result in any degradation of the HF switch performance. This surpasses the required TID threshold of 1.4 kGy (Table 5.1). Additionally, the parasitic injected current was well under control too.

- **Prototype II (2020)**

Due to the highly promising results obtained from the first prototype, the objective of the second prototype was to integrate the DAC using the same XFAB technology. This complete prototype, known as CLAROCv2 [39], consisted of the following components:

- 4 HF switches

Once again, the prototype included four distinct HF switches to identify the most suitable design for the final calibration ASIC.

- 16-bit DAC
  - (i) A custom-made, common 13-bit DAC comprising a 10-bit DAC (of LSB  $5 \mu\text{A}$ ) along with 7 current mirror<sup>7</sup> thermometers to make the 3-bit tunable gain. Each thermometer replicates the 10-bit DAC structure itself.
  - (ii) 8 current mirrors to implement the additional 3 bits in the DAC.

Therefore, the equation for calculating DAC current is given by

$$I_{DAC} = m \cdot (n \cdot \text{LSB}_{10\text{bits}} + t \cdot I_t) \quad (5.2)$$

where  $m$  is the number of mirrors,  $n$  denotes the 10-bit DAC code and  $t$  signifies the number of thermometers. The LSB is  $5 \mu\text{A}$ , and the thermometer current  $I_t$  is approximately  $5 \text{ mA}$ <sup>8</sup>. As an example, to achieve an  $I_{DAC}$  of  $40 \text{ mA}$ , the configuration would be  $m = 4, n = 1000$  and  $t = 2$ .

- Digital "slow-control" setup to configure the ASIC

It should be noted that the design of the prototype fulfils many calibration ASIC specifications outlined previously. However, it encountered two significant issues:

- (i) The non-linearity of the DAC was greater than anticipated, primarily due to the distinct steps between thermometers and mirrors.
- (ii) When exposed to irradiation, there was substantial drift in the threshold voltage  $V_{th}$ <sup>9</sup>, rendering the slow-control function inoperative.

### • Prototype III (2021)

Based on the insights gained from the second prototype, the approach for the third prototype was to fabricate the DAC using TSMC (130 nm) technology [43]. This technology is well-established for radiation hardness and has been successfully utilised in other ASICs within the HL-LHC project. The DAC was then interfaced to the HF switch developed in XFAB technology. This prototype has been named CASA (Calibration ASIC for ATLAS), consists of two main components:

- CLAROCv3: this chip incorporates the HF switch and 3-bit DAC (mirror gain) in the XFAB technology. In this prototype, all HF switches were identical, representing the switch design with the most favourable INL performance in CLAROCv2.
- LADOC (Link and DAC of CLAROC): this chip implements the 13-bit DAC as well as digital commands for both CLAROCv3 and LADOC itself.

It is worth mentioning that two versions of LADOC were developed: LADOC1, which features long transistors, and LADOC1A, designed with a more traditional and resilient architecture. Simulation results indicate superior linearity for LADOC1, but limited practical experience exists with this variant. Consequently, tests must be conducted on both versions to determine the optimal choice.

<sup>7</sup> A current mirror is a circuit arrangement used in electronics to copy or mirror the current flowing in one circuit to another.

<sup>8</sup> The current value of the thermometer, that is a replica of the 10-bit DAC, corresponds to the maximum current value of the 10-bit DAC.

<sup>9</sup> Threshold voltage  $V_{th}$  is the voltage across the transistor (i.e.  $Q_1$  or  $Q_2$ ) when no current flows through it



**Figure 5.5.:** Image of CASA test board, denoting its two main components: CLAROCv3 and LADOC

Moreover, the prototype implemented improved inter-digitization of thermometers and mirrors to enhance the DAC linearity. The results of this prototype have been discussed in the next section.

### 5.3. Test of CASA Prototype

The CASA test board, shown in Figure 5.5, was subject to various tests resulting in the following novel conclusions:

- LADOC demonstrated excellent linearity performance on its own. LADOC1 exhibited a linearity within 0.02%, while LADOC1A had a linearity of 0.06%, indicating that LADOC1 was more effective. However, when LADOC was combined with CLAROCv3, the linearity experienced a significant degradation. The degradation reached 0.7% for CLAROCv3+LADOC1 and 0.3% for CLAROCv3+LADOC1A, surpassing the specified limit of 0.1%.
- Over a duration of approximately 1 hour and 500 acquisitions, both LADOC and CLAROCv3 exhibited stable outputs with respect to time.
- When subjected to varying temperatures in a climatic chamber, the output current of LADOC was observed to decrease as the temperature increased. Furthermore, this decrease was more pronounced in LADOC1 due to its higher sensitivity to fluctuations in transistor voltage.

The CASA prototype also underwent two types of irradiation tests: i) proton irradiation at Paul Scherrer Institut (PSI), Switzerland to test SEE and NIEL effect and ii) X-ray irradiation at CERN to test TID effect. These tests were essential to understand how the chip prototype behaves under different radiation conditions expected at the LHC. The experimental setups

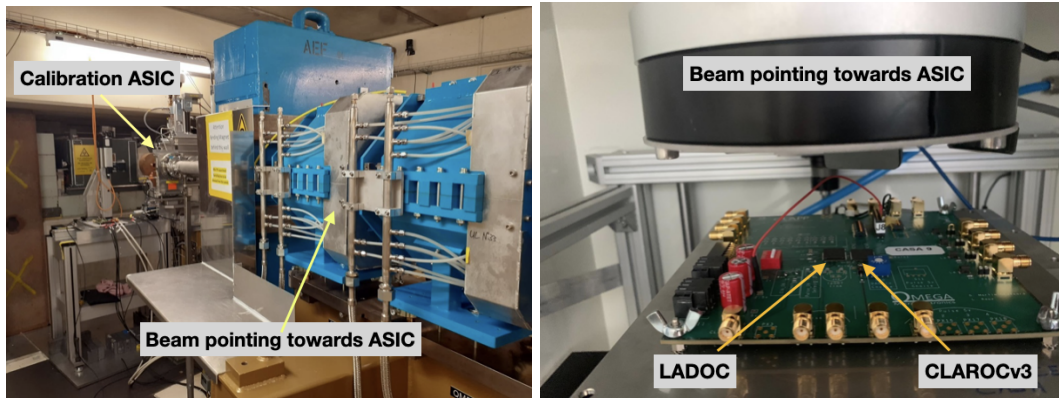


**Figure 5.6.:** Left: Proton irradiation setup at PSI; Right: X-ray irradiation setup at CERN

for these tests are depicted in Figure 5.6. The results of these tests are described in the subsequent sections.

### 5.3.1. Proton Irradiation

The PIF (Proton Irradiation Facility) machine at PSI was utilised to conduct proton irradiation tests on the nights of September 18th and 19th, 2021<sup>10</sup>. The nominal proton beam used in these tests had a flux of  $1.8 \times 10^9$  protons/cm<sup>2</sup>/s and an energy of approximately 200 MeV.

During the irradiation tests, the CASA prototype, with a LADOC1 ASIC, was exposed to a maximum dose of 50 kGy, surpassing the required TID of 1400 Gy. Additionally, it achieved a net NIEL dose of  $9.3 \times 10^{13}$  protons/cm<sup>2</sup>, exceeding the specified requirement of  $4.1 \times 10^{13}$  protons/cm<sup>2</sup> as mentioned in Table 5.1.<sup>11</sup>

The following tests were conducted:

- **Linearity of LADOC1 DAC**

Figure 5.7 shows the correlation between the measured and injected DAC values in LADOC1 ASIC at different hours of irradiation on September 19th. The DAC used in LADOC is a 13-bit device with a LSB of 5  $\mu$ A, allowing for a range of up to 40 mA. It is worth noting that each hour of irradiation corresponds to an approximate dose of 3.5 kGy. As a result, the plot provides valuable insights into the linearity of the 13-bit DAC up to a TID of approximately 30 kGy, surpassing the required threshold of 1.4 kGy.

Figure 5.8 illustrates the corresponding integral non-linearity (INL) defined in Equation 5.1. Remarkably, the INL of the DAC remains below the specified level of 0.1%, even after full irradiation.

Similar results were also obtained for the irradiation conducted on September 18th. Thus, it can be concluded that the 13-bit DAC is highly linear under irradiation.

- **Performance of CLAROCv3**

<sup>10</sup> Due to the use of the proton beam for medical treatment during the day, the tests had to be conducted on two different nights.

<sup>11</sup> Exceeding the specified doses was necessary to fulfill all requirements for TID, NIEL and SEE.

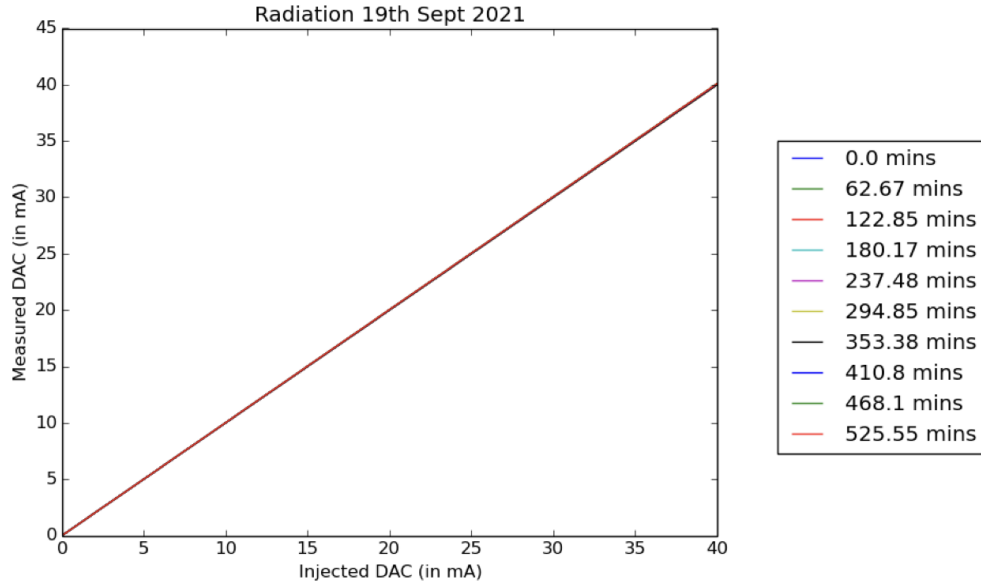


**Figure 5.7.:** Measured vs. injected DAC in LADOC1 ASIC for different hours of proton irradiation on September 19th. The legend depicts the duration since start of irradiation.

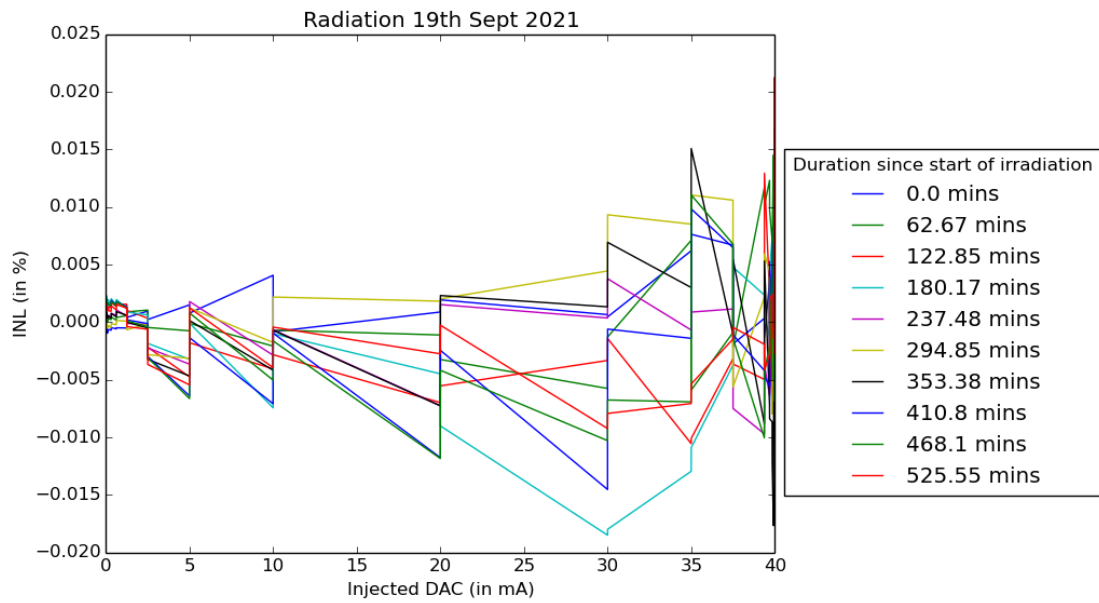


**Figure 5.8.:** DAC integral non-linearity vs. injected DAC in LADOC1 ASIC for different hours of proton irradiation on September 19th. The legend depicts the duration since start of irradiation.

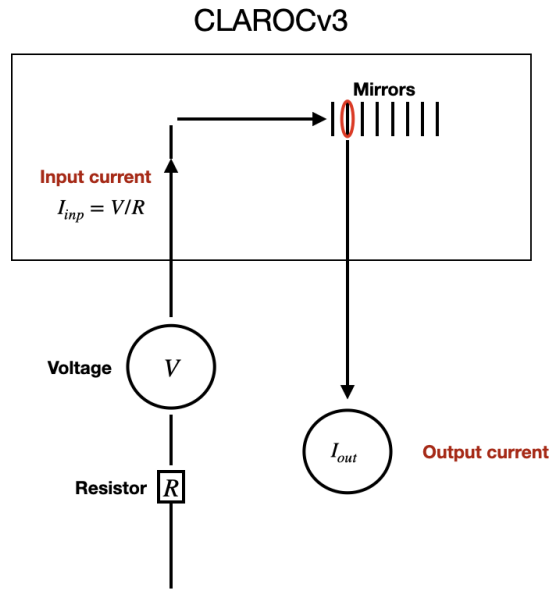


**Figure 5.9.:** Schematic setup to assess the performance of CLAROCv3 under irradiation.

To evaluate the performance of CLAROCv3 under irradiation, a predetermined input current  $I_{inp}$  was applied to one of the mirrors, and the corresponding output current  $I_{meas}$  from that mirror was measured. Ideally, these two values should be identical. A schematic of the setup is shown in Figure 5.9.

Figure 5.10 illustrates the variation of input current through the second mirror in CLAROCv3 with respect to the duration of irradiation. The plot shows that the board underwent irradiation for approximately 900 minutes across the two nights, with  $\sim 350$  minutes on the first night (18th Sept). It also highlights the specific time periods when the proton flux deviated from the nominal value of  $1.8 \times 10^9$  protons/cm<sup>2</sup>/s.

It can be seen that the input current does not remain stable under irradiation. More particularly,

- (i) Previous studies on CLAROCv2 have established that exposure to irradiation induces a shift in the threshold voltage  $V_{th}$  of the transistors in the HF switch. As a result, at the onset of irradiation, there is a decrease in the input current.
- (ii) As time progresses, an annealing effect<sup>12</sup> takes place, leading to an increase in the input current. This effect is particularly prominent at the beginning of a new night run when the material can recover from radiation effects or when there are changes in the flux.

Figure 5.11 presents the correlation between the ratio of the output and input current through the second mirror in CLAROCv3 and the duration of irradiation. In other words, the plot depicts the change in mirror gain as a function of irradiation.

<sup>12</sup> Annealing is a heat treatment process that modifies material properties by heating it to a specific temperature and then slowly cooling it. It relieves stress, enhances crystalline structure, and improves mechanical properties. It is widely used in metallurgy and manufacturing to increase ductility

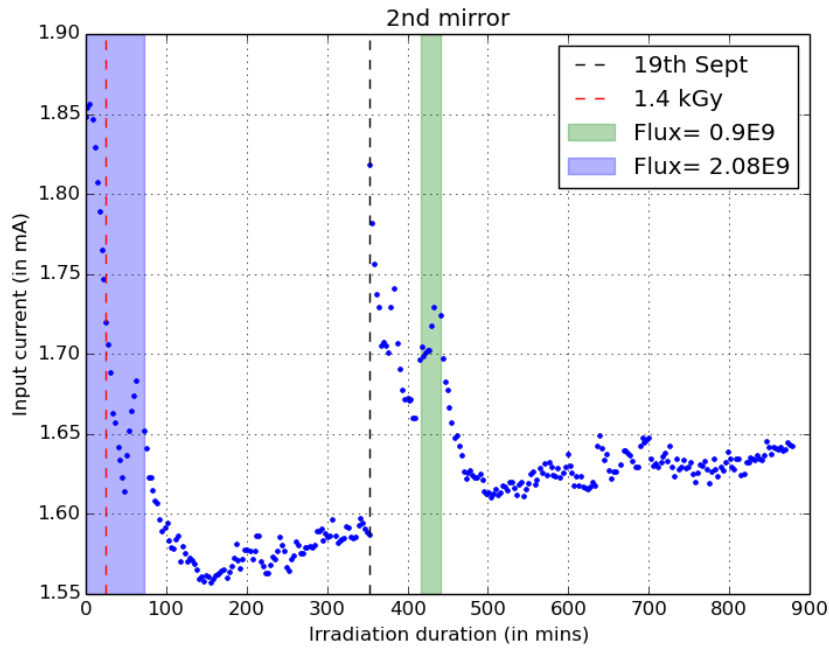


**Figure 5.10.:** Variation of input current through the second mirror of CLAROCv3 during proton irradiation. The plot highlights time periods of proton flux deviation from the nominal value of  $1.8 \times 10^9$  protons/cm<sup>2</sup>/s and shows the duration needed to reach the specified TID of 1.4 kGy. It also marks the start of the second night of irradiation on September 19th.

It can be seen that the mirror gain initially decreases with time. This decline can be attributed to the decrease in input current at the beginning of irradiation, as depicted in Figure 5.10. And after approximately 100 minutes of irradiation, equivalent to  $\sim 5.5$  kGy of radiation, the mirror gain starts to increase. This phenomenon could be attributed to the degradation of mirrors under irradiation.

Nevertheless, it is important to note that within the specified TID dose limit of 1.4 kGy, there is only a slight gain change observed in the mirror. This suggests that the mirror operates reasonably well within the specified dose range, but higher doses can potentially compromise its stability.

Finally, the output current was sequentially measured for all 8 mirrors, enabling the calculation of the spread in the output current. This spread is determined by normalising the difference between the maximum and minimum current values with respect to the average current. Similarly, the input current was recorded for each of the 8 consecutive measurements, allowing for the calculation of the spread in input current. Ideally, the spread in currents should remain constant under irradiation. Furthermore, analysing the spread helps to uncorrelate specific mirror effects, contributing to a better understanding of the system.

Figure 5.12 illustrates the spread in input current and spread in output current as a function of irradiation duration. Initially, the spread in input current increases due to the shift in threshold voltage  $V_{th}$ , and then stabilises over time. However, the output

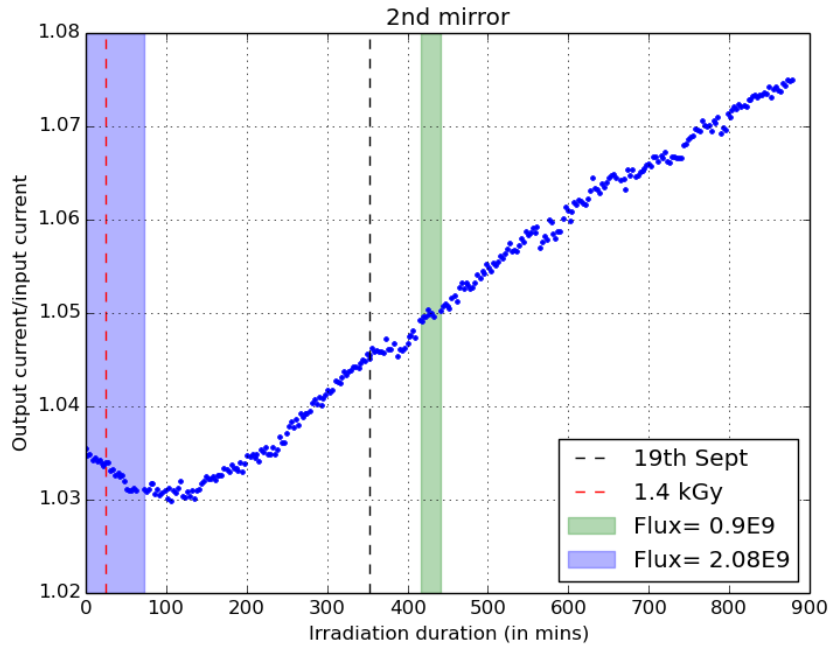


**Figure 5.11.:** Mirror gain, i.e. ratio of output and input current, for second mirror of CLAROCv3 during proton irradiation. The plot highlights time periods of proton flux deviation from the nominal value of  $1.8 \times 10^9$  protons/cm<sup>2</sup>/s and shows the duration needed to reach the specified TID of 1.4 kGy. It also marks the start of the second night of irradiation on September 19th.

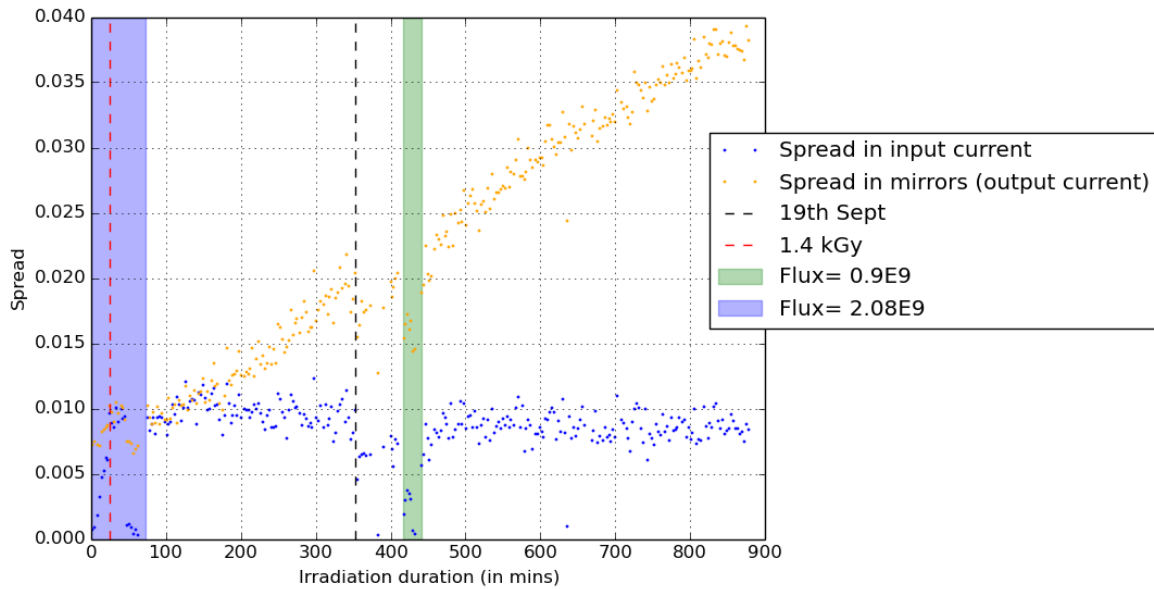


**Figure 5.12.:** Spread in input current and output current during proton irradiation. The plot highlights time periods of proton flux deviation from the nominal value of  $1.8 \times 10^9$  protons/cm<sup>2</sup>/s and shows the duration needed to reach the specified TID of 1.4 kGy. It also marks the start of the second night of irradiation on September 19th.

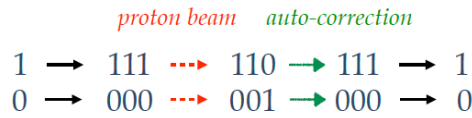


**Figure 5.13.:** Auto-correct mode for SEU studies

current continues to increase after approximately 100 minutes of irradiation. Again, this can be attributed to the degradation of mirrors under irradiation.

It is worth noting that upto the required dose of 1.4 kGy, there is no significant dispersion in mirrors, indicating that the mirrors maintain their performance within the required dose range.

#### • Single Event Effects on LADOC1

In this test, two kinds of single event errors were examined:

- (i) Single Event Upset (SEU): categorised as a soft error, SEU entails a temporary modification that can be undone by executing a reset or rewriting procedure, effectively returning the system to its normal functioning state.

To investigate the impact of SEU on LADOC1, I2C errors were observed over the course of two radiation-exposed nights, with a cumulative dose reaching twice the required NIEL dose. By utilizing an auto-correcting mode (as seen in Figure 5.13) and comparing the transmitted and received values, no errors were detected. However, upon deactivating the auto-correction mode, errors were observed, albeit with difficulty in estimating their occurrence rate.

Since the auto-correct mode will be the default mode for HL-LHC, SEU effects will be handled effectively.

- (ii) Single Event Latchup (SEL): Categorised as a hard error, SEL encompasses a potentially damaging situation caused by parasitic circuit elements. In a typical SEL event, the device's current may surpass the maximum current specification, posing a risk of device destruction if not adequately limited.

To assess the influence of SEL on LADOC1, the current consumption was monitored during two nights of irradiation. It was determined that there was no excessive current consumption, even when exposed to radiation twice the required dose.

### 5.3.2. X-ray Irradiation

Between September 20th and September 24th, 2021, the CASA prototype, with LADOC1A ASIC, underwent X-ray irradiation at CERN. The tests employed a X-ray beam with an energy of around 160 keV and a dose rate of 19 kGy/hour. During the irradiation tests, the CASA prototype was exposed to a maximum dose of 5.25 kGy, exceeding the required TID of 1400 Gy.

In this irradiation campaign, the linearity of LADOC1A DAC was examined.

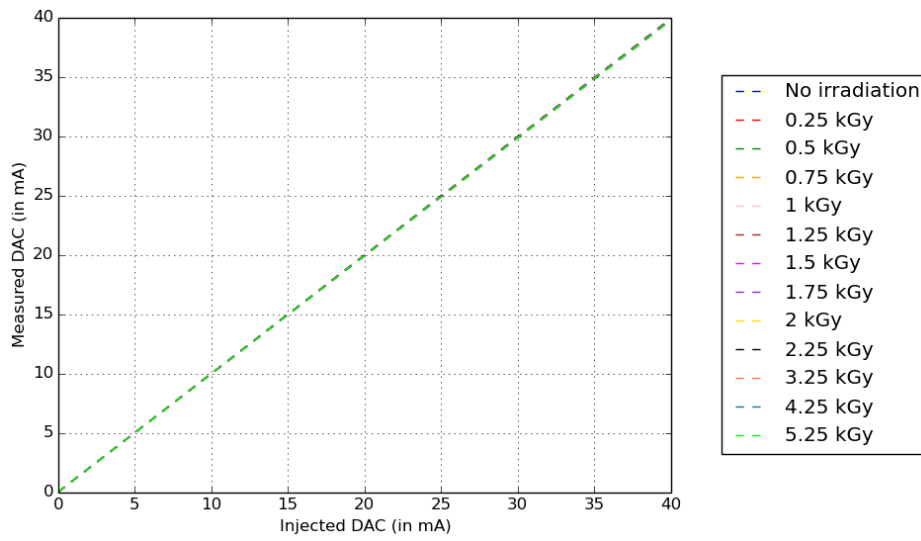


**Figure 5.14.:** Measured vs. injected DAC in LADOC1A ASIC during X-ray irradiation. The legend depicts the TID doses.

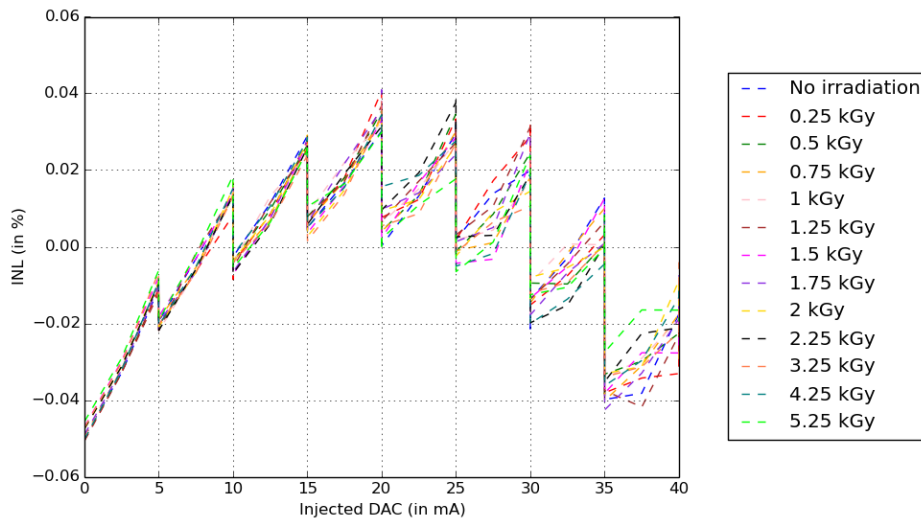


**Figure 5.15.:** DAC integral non-linearity vs. injected DAC in LADOC1A ASIC during X-ray irradiation. The legend depicts the TID doses.

Figure 5.14 depicts the relationship between the measured and injected DAC values in the LADOC1A ASIC during X-ray irradiation. This graph provides valuable insights into the linearity of the 13-bit DAC, demonstrating its stable performance up to a TID of 5.25 kGy.

Figure 5.15 displays the corresponding integral non-linearity (INL) of the DAC. The observed steps occurring at every 5mA signify the addition of a thermometer in the 13-bit DAC. Remarkably, even after complete irradiation, the INL of the DAC remains below the specified level of 0.1%. This reaffirms that the 13-bit DAC exhibits highly linear behaviour when exposed to radiation.

## 5.4. Current Status of Calibration ASIC Prototype

The CASA prototype successfully fulfilled most of the calibration ASIC specification requirements. However, it faced some notable issues:

- (i) Although the linearity of LADOC itself demonstrated excellent performance, a significant degradation in linearity was observed when it was combined with CLAROCv3.
- (ii) The LADOC DAC was not stable with respect to variations in temperature.
- (iii) When exposed to irradiation, a substantial drift in the threshold voltage ( $V_{th}$ ) was observed. This rendered the CLAROC ineffective and impacted the mirror gain.

Consequently, a new calibration ASIC prototype, named CASAv2, was developed with two primary components:

- CLAROCv4 in XFAB 180 nm technology: This chip incorporates the HF switch and includes only one mirror with a constant gain of 8 in order to overcome the mirror spread issue. Additionally, an amplifier has been added to compensate for the  $V_{th}$  shift and improve the mirror gain.
- LADOCv2 in TSMC 130 nm technology: This chip extends the precision of the LADOC1 DAC (selected for its superior performance in CASA studies) from 13 bits to 16 bits. As a result, LADOCv2 generates a range of  $I_{DAC}$  up to 40 mA with a LSB of  $0.625 \mu\text{A}$ . It also provides 2.5V digital commands to CLAROCv4 (compared to the 1.2V commands in LADOC1) for better functionality in a radiative environment.

Tests conducted on LADOCv2 demonstrated that it met all the specifications, except for stability in temperature. Consequently, new LADOC prototype is under development to address the small temperature dependence of 0.12% for  $\pm 1$  degree variation.

In the case of CASAv2, which comprises LADOCv2 and CLAROCv4, the linearity tests demonstrated compliance with the specifications up to approximately 200 mA. However, saturation occurred when the current exceeded 200 mA. Fortunately, this issue can be readily resolved by increasing the power supply voltage from 5 to 5.5V.

Irradiation tests are currently scheduled to evaluate the performance of CASAv2 in a radiation environment.

## Chapter 6.

# Liquid Argon Calibration Board Prototype for HL-LHC

The objective of the calibration board is to inject exponential current pulses of known amplitude on the detector cell in order to probe its electronic response. In line with the voltage-driven scheme explained in Section 4.2.1, the calibration board comprises the following main components:

- Analog Section:
  - Calibration ASIC: This component is responsible for configuring the pulse amplitude and generating the pulses.
  - Resistor  $R_0$  and Inductance  $L$ : These elements play a crucial role in defining the shape of the pulse.
- Digital Section: This section is responsible for facilitating the transfer of clock signals, control signals and data.

A overview of the prototype for the HL-LHC calibration board is provided in the following sections. Section 6.1 outlines the specifications and requirements for the board, while Section 6.2 delves into the design considerations and component prerequisites. In Sections 6.3 and 6.4, the focus is directed towards my study of the first calibration board prototype, including the design and execution of tests, as well as the subsequent analysis. Lastly, Section 6.5 provides an update on the current status of the calibration board.

## 6.1. Specifications of Calibration Board

The main requirements of the calibration board for the HL-LHC are as follows: [25] [44]

- **Uniformity**

Uniformity among channels should be better than 0.2% in EMB and EMEC, better than 1% in HEC and better than 2% in FCal

As discussed in Chapter 4, achieving a constant term  $c$  of approximately 0.7% in the energy resolution of the LAr EM calorimeter requires calibrating the readout electronics with a precision better than 0.25% across the entire energy range. Studies conducted on the existing calibration board in the LAr EM calorimeter have revealed an overall

calibration precision of approximately 0.23%, which satisfies the 0.25% requirement. Furthermore, the main sources of non-uniformity identified are as follows: [33]

- Direct measurements of each line on the calibration board have shown a relative dispersion of 0.19%.
- Measurements on the calibration resistors  $R_0$  have shown a relative dispersion of 0.08% for barrel modules and 0.05% for endcaps.
- Although the average attenuation caused by skin effect<sup>1</sup>, which is proportional to the cable length, has been corrected, a slight relative dispersion of up to 0.1% still remains.

Considering the similarities between the calibration board for the HL-LHC and the existing board, it is reasonable to anticipate similar sources of non-uniformity in the new calibration board as well. Therefore, after accounting for the non-uniformity arising from calibration resistors and cables, the calibration channels in EMB and EMEC must exhibit a uniformity better than 0.2% in order to achieve the overall calibration precision of 0.25%.

The constant term  $c$  in the design energy resolutions of LAr HEC and FCal is higher, at 3% and 10% respectively [35]. Therefore, the requirement for channel uniformity is also higher: at 1% for HEC and 2% for FCal.

## • Stability

- (i) Tolerance to radiation levels expected at the HL-LHC

Table 5.1 presents the radiation tolerance specifications for the calibration board. Since the board is large, it is not feasible to conduct irradiation testing on the entire unit. Instead, the active components in the board need to be individually tested for radiation hardness.

- (ii) Tolerance to magnetic field of few tenths of Gauss expected at the HL-LHC

A high magnetic field will impact the inductance  $L$  on the board, and consequently the decay time of the calibration pulse (see Equation 4.3). Therefore, it is crucial to assess the performance of the inductance in a magnetic environment to ensure accurate calibration measurements.

- (iii) The board should maintain a stability level of less than 0.1% over a year of data-taking and exhibit stability with respect to temperature in the FECs at a rate of less than 0.1% per degree. This requirement is primarily influenced by the stability of the individual components on the calibration board, such as the calibration ASIC and inductance  $L$ .

---

<sup>1</sup> Skin effect is the concentration of alternating current (AC) near the surface of a conductor, occurring at higher frequencies. It causes the majority of the current to flow through the outer layer, reducing current flow in the deeper regions. This increases effective resistance, leading to higher power loss and heating.

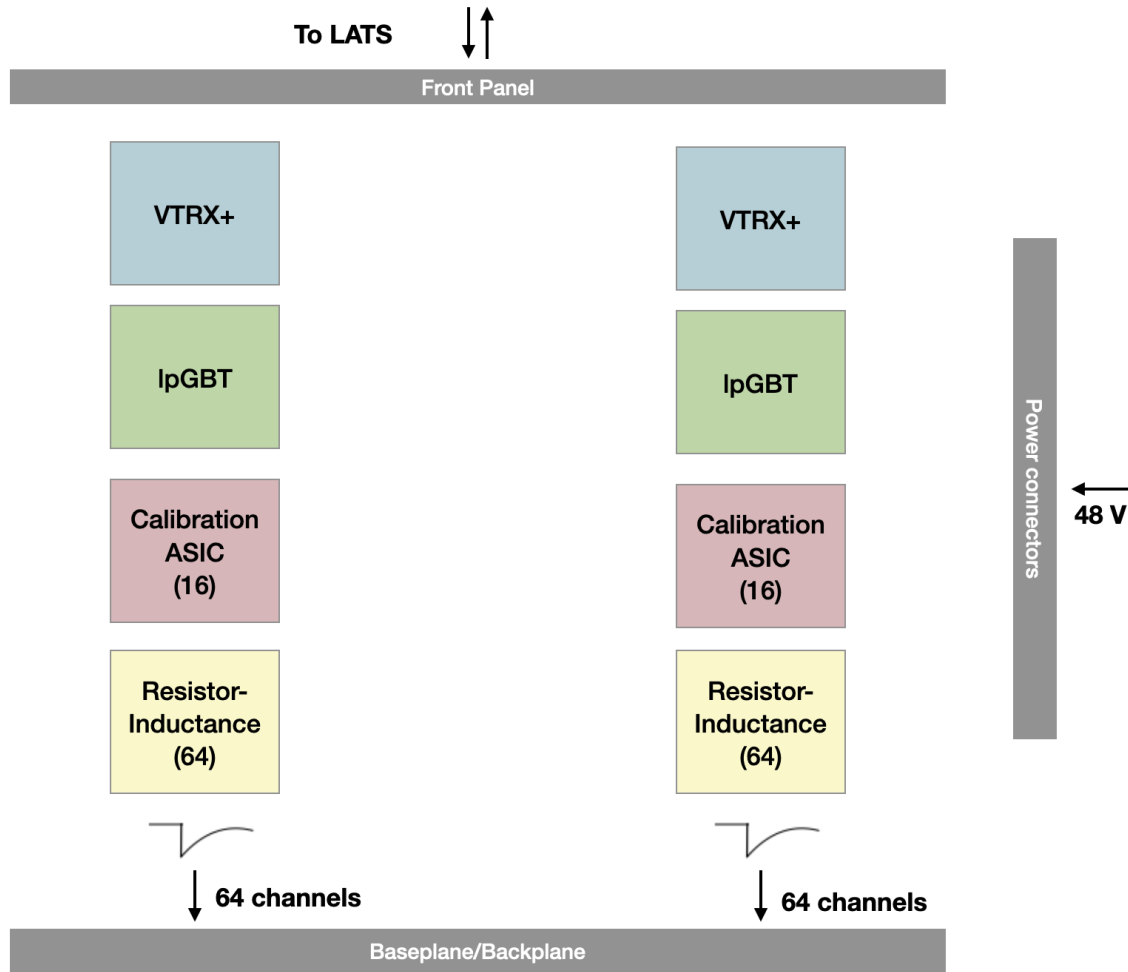


Figure 6.1.: Schematic diagram of the calibration board of the HL-LHC

## 6.2. Design and Components of Calibration Board

### 6.2.1. Layout

The architecture of the calibration board for the HL-LHC is depicted in Figure 6.1. It consists of 32 calibration ASICs, each consisting of 1 DAC and 4 HF switches, as discussed in Section 5.1. Consequently, the board incorporates a network of 128 resistor-inductance ( $R_0 - L$ ) pairs, establishing the 128 calibration channels per board.

The digital section of the board comprises two main components:

- **lpGBT**: Fabricated using TSMC 65nm chip technology, the lpGBT chip facilitates the transfer of clock signals, control signals, and data. The board requires two lpGBT ASICs.
- **VTRx+** [45]: This chip converts the electrical signals from the serial lpGBT output into optical signals. Two VTRx+ modules are needed on the board, one for each lpGBT ASIC.

The HL-LHC calibration boards will be installed within the existing LAr Front End Crates, which means that the mechanical constraints for the boards will remain unchanged from the current setup. This encompasses the board dimensions as well as the placement and type of connectors. Furthermore, since the positioning of the  $R_0 - L$  circuit in the original board (see Figure 4.4) was optimised to minimise cross-talk and the impact of magnetic fields, a similar layout will be maintained for the  $R_0 - L$  circuit in the upcoming board. However, due to the re-designed calibration ASICs, a complete redefinition of their layout is necessary. Specifically, while the original board had a single DAC commanding 128 pulsers, the upcoming board will feature 32 DACs commanding 128 pulsers.

Lastly, as shown in Figure 6.1, the HL-LHC calibration board will receive 48V power on its upper side. However, the required voltages for the different ASICs (5V, 2.5V, 1.2V) are significantly lower than this input voltage. Therefore, a dedicated power distribution network with DC-DC convertors needs to be designed on the calibration board to ensure appropriate voltage levels. In addition to power supply, the board will also transmit calibration pulses on the back side (backplane) and exchange optical signals with the Liquid Argon Timing System (LATS) on the front side. [38]

### 6.2.2. Specifications

From equation 4.3, the decay time of the pulse  $\tau_{\text{cal}}$  and pulse amplitude  $I_{\text{cal}}$  can be written as:

$$\tau_{\text{cal}} = L/R_{\text{eff}} \quad (6.1)$$

$$I_{\text{cal}} \propto R_0(1 - f_{\text{step}})e^{-\frac{t}{\tau_{\text{cal}}}} \quad (6.2)$$

where  $r$  is the internal resistance of the inductance  $L$ ,  $R_{\text{eff}} = r + \frac{R_0}{2}$  is the effective resistance, and  $f_{\text{step}} = r/R_{\text{eff}}$ ,  $f_{\text{step}} \in [0, 1]$ .

Equation 6.1 shows that the values of  $R_0$ ,  $L$  and  $r$  play a critical role in determining the decay time and consequently the shape of the calibration pulse. Hence, it is of utmost importance to meticulously choose their values to achieve a close resemblance between the exponential calibration pulse and the triangular physics ionisation pulse. In case of the EM calorimeter, the optimal values are  $R_0 = 50\Omega$ ,  $L = 12\mu\text{H}$  and  $r = 2.5\Omega$ .

Furthermore, the need for uniformity among all channels of the board (as discussed in Section 6.1) has implications for the design and choice of components in the calibration board, which are highlighted below [44]:

- (i) The calibration board should not degrade the standalone performance of the calibration ASICs. Thus, the calibration board should be routed and fabricated in a way that the cross-talk between channels, which refers to undesired signals in channels other than the one being pulsed, should be below 0.1% of the signal pulse amplitude.
- (ii) The pulse generated by each channel should exhibit high uniformity across all channels. This places the following constraints:
  - 0.1% resistor  $R_0$ : Equation 6.2 shows that the pulse amplitude is directly proportional to  $R_0$ . Thus, a resistor  $R_0$  with a precision of 0.1% is required to ensure a high uniformity of 0.1% in pulse amplitudes.

- 1% internal resistance  $r$ : Equations 6.1 and 6.2 show that  $r$  affects both the decay time and amplitude of the calibration pulse. Thus, to ensure minimum dispersion in pulse properties,  $r$  should be uniform at 1% level.
- 5% inductance  $L$ : Equation 6.1 shows that inductance  $L$  affects the decay time of the pulse. Thus, to ensure 2% uniformity in pulse decay times, the precision/tolerance of the inductance should be 2% too.<sup>2</sup> However, it is worth noting that the current electronic calibration procedure compensates for this effect by directly measuring parameters such as  $\tau_{\text{cal}}$  and  $f_{\text{step}}$ . Therefore, in principle, inductances with a tolerance upto 5% can be used.
- The synchronisation between the physics ionisation pulse and the calibration pulse should be within 2 ns to ensure high uniformity in the peaking time<sup>3</sup> of the pulse.
- As discussed earlier in Section 5.1, the design of the HF switch is a critical factor in determining the rise time of the calibration pulse. Therefore, achieving uniformity in the pulse rise times relies on the precise performance of the HF switch.

### 6.2.3. Calibration Run Patterns

To achieve simultaneous calibration of multiple detector cells and minimise the duration of calibration runs, it is necessary for the board to be able to pulse multiple channels concurrently. However, limitations in power consumption prevent the simultaneous pulsing of all 128 channels of the calibration board at a high current. Additionally, the design of the calibration ASIC allows only one channel per ASIC to be pulsed at the maximum current. If simultaneous pulsing of multiple channels within an ASIC is required, it can only be achieved by operating at a reduced current whose limit is given by:

$$I_{DAC} = I_{DAC}^{max}/N_{ch} \quad (6.3)$$

where  $I_{DAC}^{max}$  is the maximum current of 300 mA and  $N_{ch}$  represents the number of channels to be pulsed in an ASIC, which can range from 1 to 4.

The existing calibration system incorporates an optimised calibration pattern<sup>4</sup> that places a strong emphasis on minimizing cross-talk and conserving power. As a result, this well-designed calibration pattern will be retained in the upcoming calibration system. Within this pattern, it is not necessary to pulse more than 16 channels simultaneously at maximum current. Additionally, the pattern does not require the simultaneous pulsing of four channels within the same ASIC at high current levels. Instead, the pulsing of four channels within the same ASIC only occurs when operating at low current ranges. This particular characteristic is deemed manageable for the upcoming system, as demonstrated by Equation 6.3.

However, for specific calibration runs targeting LATOME and L1Calo, a necessity arises to pulse multiple channels within a single ASIC simultaneously at the maximum current. To address these challenges, active research is currently being conducted to explore and develop appropriate solutions within the design of the calibration board.

<sup>2</sup> Given that  $R_0$  is 0.1% precise and  $r$  is 1% precise, in order to obtain a precision of 2% on  $\tau_{\text{cal}}$ , the precision of  $L$  has to be 2% too.

<sup>3</sup> Peaking time is the time of maximum amplitude of the pulse after shaping

<sup>4</sup> A calibration pattern denotes which calibration channels are pulsed simultaneously in a calibration run

### 6.3. Test of CABANON Prototype

As the development of calibration ASIC prototypes progresses, it is important to focus on the development of prototypes for the calibration board too. This parallel effort ensures comprehensive progress in the overall development of the calibration system. In accordance with this approach, the first calibration board prototype, named CABANON (CALibration Board with 32-chANnels for demonstratiON), was designed and implemented in 2020.

The CABANON prototype incorporated 32 channels and included 8 CLAROCv2 ASICs. However, as mentioned earlier in Section 5.2, the CLAROCv2 ASICs do not meet the specifications for the HL-LHC. Furthermore, the board prototype employed a Serial Peripheral Interface (SPI) communication environment instead of the necessary lpGBT protocol for communicating with the ASICs. Despite these limitations, analysing the CABANON prototype has yielded valuable insights that will be beneficial in designing the ultimate 128-channel calibration board.

The following sections present an overview of the design of CABANON, the tests developed based on its design, and the corresponding test bench setup employed in the CABANON studies conducted in 2021.

#### 6.3.1. Description

As mentioned in Section 6.2, the upcoming calibration board for the HL-LHC will maintain the  $R_0 - L$  circuit from the original board, but a new layout for the calibration ASICs is necessary. Therefore, a primary objective of the CABANON study was to determine the optimal layout of calibration ASICs. To achieve this goal, various board prototypes, each sized at  $410 \times 490$  mm<sup>2</sup> (representing a full-sized board for the FEC), were designed with distinct ASIC positions. These prototypes feature 8 ASICs, but the final calibration board will integrate 32 ASICs spanning the entire board. Hence, the rationale for developing prototype boards with diverse ASIC placements is to ensure result consistency across the entire calibration board.

Additionally, the focus was on identifying the most suitable components for the board. To achieve this, the board prototypes incorporated different types of inductance.

A summary of the distinctions among the board prototypes is provided in Table 6.1. Specifically:

- Inductance: all board prototypes use a shielded  $12\mu\text{H}$  inductance, as specified in Section 6.2. However, there are differences in the specific types of inductance used for each board. Board 1 and Board 3 incorporate the ISC1210ER120J [46] inductance, denoted as L1. This inductance is used in existing ATLAS calibration boards and has a tolerance of 5%. On the other hand, Board 2 utilises the S1812R-123G [47] inductance, referred to as L2. It is a new type of inductance and has a tolerance of 2%.
- Position of calibration ASICs: each board consists of 8 calibration ASICs, with 4 located on the top and 4 on the bottom of the board. Boards 1 and 2 share the same layout, positioning all ASICs in the middle sector. In contrast, Board 3 arranges all ASICs on the upper half of the board. These layouts can be observed in Figure 6.2.

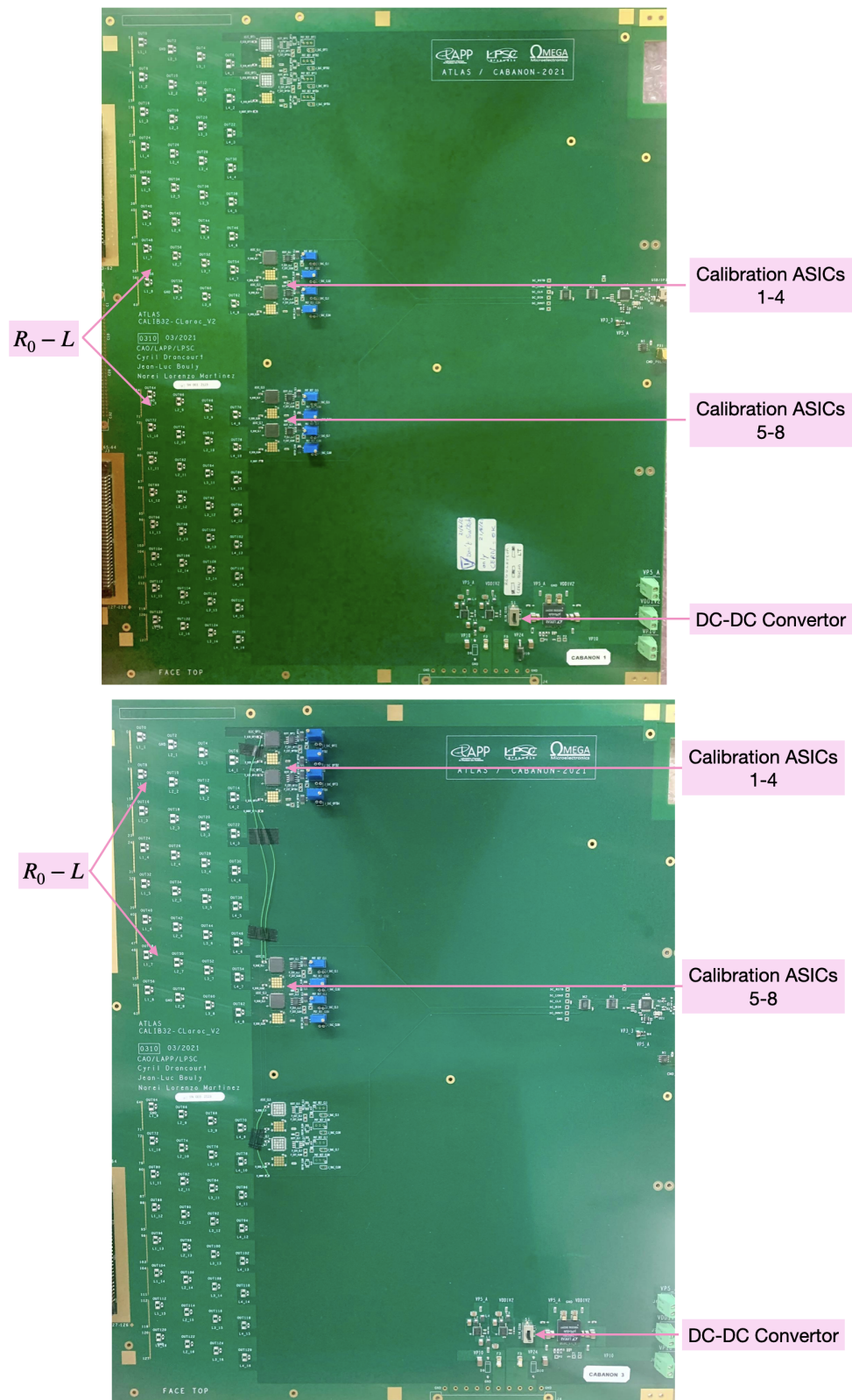


**Figure 6.2.:** Above: CABANON Board 1. A similar layout of calibration ASICs is also in Board 2. Below: CABANON Board 3. In all boards, 8 ASICs are on the top side of the board, and the other 8 on the bottom.

CABANON	Inductance	Position of ASICs
Board 1	L1	Middle sector of board
Board 2	L2	Middle sector of board
Board 3	L1	Only upper half of board

**Table 6.1.:** A comparison of the three CABANON prototypes. L1 denotes inductance ISC1210ER120J and L2 refers to inductance S1812R-123G.

Each board is equipped with a bPOL12V [48] DC-DC convertor to lower the 48V input voltage to the specific voltages required by the different ASICs on the board. This custom convertor, developed by CERN, has successfully fulfilled the radiation requirements for the HL-LHC. Additionally, Boards 2 and 3 offer the flexibility to incorporate an alternative DC-DC convertor called LTM4619 [49]. This commercial component has undergone extensive evaluation by the ATLAS R&D teams and meets the necessary radiation specifications for LHC Run 3. However, further testing is needed to assess its performance under the expected radiation conditions at the HL-LHC. Nevertheless, conducting studies on both types of convertors will facilitate the selection of the most optimal option.

### 6.3.2. Test Objectives

The main objectives of the tests conducted on the CABANON prototype were: i) to evaluate the functionality of the board and ensure its proper operation, ii) to identify and examine any non-uniformity within the board, iii) to ensure consistency in results despite variations in calibration ASIC placements and, iv) to select the most suitable inductance and DC-DC convertor components.

To achieve these objectives, the following tests were performed:

- Testing the functionality of calibration ASICs and DC-DC convertors
- Verifying the board's ability to simultaneously pulse multiple channels.
- Evaluating the additional non-linearity introduced by the board compared to the standalone calibration ASIC non-linearity.
- Measuring the crosstalk between all channels of the board.
- Evaluating the uniformity of maximum pulse amplitude and peaking time across all channels of the board.
- Comparing different boards and investigating how the test results are affected by the placement of ASICs, inductance, and/or convertors

### 6.3.3. Test Bench Setup

In order to perform the tests mentioned above, a test bench setup (refer to Figure 6.3) was established at LAPP consisting of the following components:

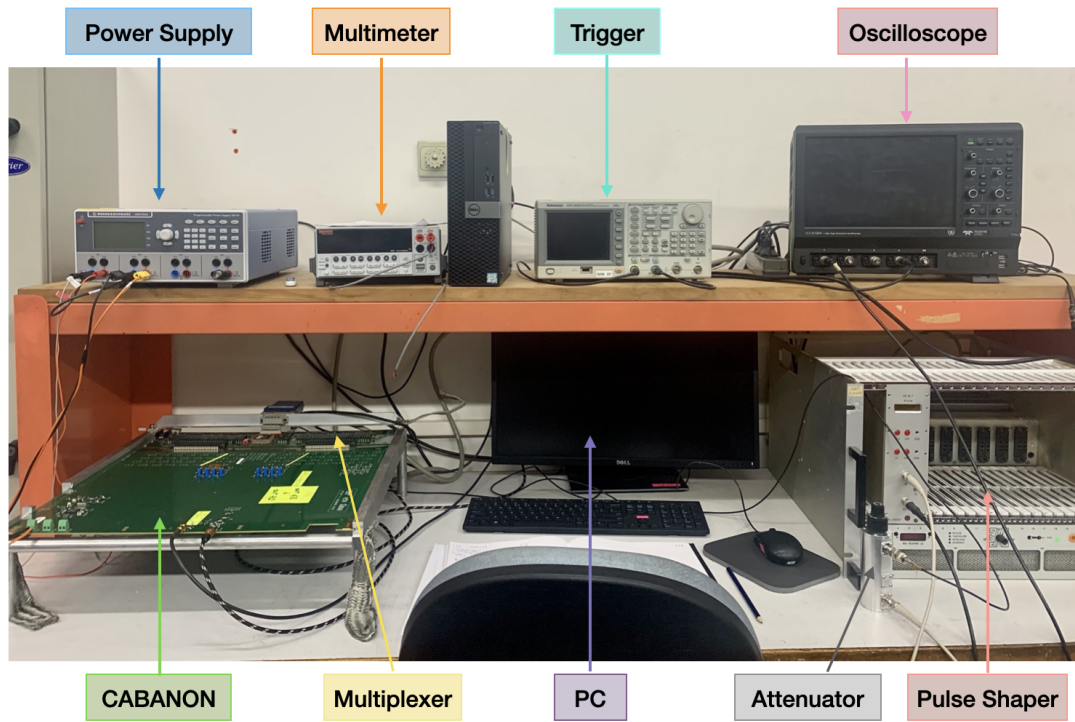


**Figure 6.3.:** Test bench setup at LAPP to conduct tests on CABANON

1. CABANON: It refers to the 32-channel calibration board prototype that is currently under study.
2. Power Supply: It supplies the necessary power to the board.
3. Multimeter: It is utilised for measuring currents and voltages within the circuit.
4. Oscilloscope: It is employed to visualise and analyse signal pulses.
5. Multiplexer: Since there is only one oscilloscope and multimeter available, the multiplexer is required to selectively route multiple inputs to a single output line. It allows the examination of one channel of the board at a time and was designed to study the existing calibration board.
6. Trigger: It generates the *command pulse* for the calibration ASIC on the board. It also ensures the stability and synchronisation of the signal pulse on the oscilloscope's screen.
7. Attenuator: It is employed to reduce the amplitude of the signal pulse, enabling precise measurements within the dynamic range of the oscilloscope.
8. Pulse Shaper: A  $50\text{ns CR-RC}^2$  pulse shaper is employed to shape the signal pulse and minimise the impact of electronic noise. This was also designed to study the existing calibration board.
9. PC: It hosts the LabVIEW [50] programs responsible for controlling the board, providing the user interface, and storing data. These programs were written by the author. A snapshot of one of the programs to control the data provided to the board is shown in Figure 6.4.

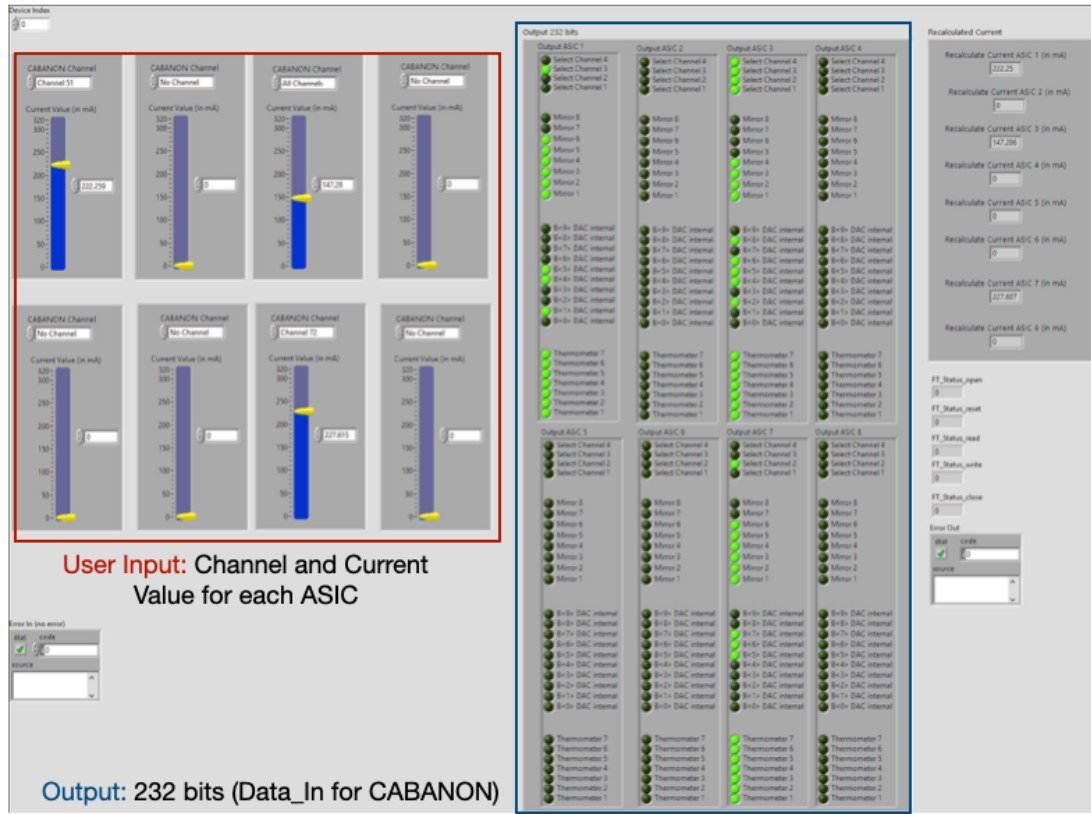


**Figure 6.4.:** This LabVIEW program enables control of the data sent to the CABANON board. Users can input the desired current value (in mA) and select the ASIC channel (1-4) within the red box. The program's output, displayed in the blue box, consists of 232 bits. Specifically, programming a single CLAROC v2 chip requires 29 bits (25 for the current value and 4 for channel selection). Consequently, to program the entire CABANON board, a total of  $8 \times 29 = 232$  bits is needed. This data is then supplied to the CABANON board for further testing as necessary.

The arrangement of the test bench is tailored to the specific test being conducted. For instance, the schematic in Figure 6.5 showcases the configuration of the test bench setup aimed at investigating the calibration pulse. In this arrangement, the *LabVIEW* program, the *trigger*, and the *power supply* serve as inputs to the *CABANON* board to generate the desired signal pulse. The *multiplexer* selects the output channel where the signal pulse will be measured. The generated pulse then passes through an *attenuator*, followed by the *pulse shaper*, and finally, it is captured and observed on an *oscilloscope*. It is important to note that the oscilloscope also requires a trigger command for proper operation. Ultimately, the shaped pulse is routed back to the LabVIEW program for storage and analysis purposes.

## 6.4. Results of CABANON Prototype

This section presents the results obtained from the tests described in Section 6.3.

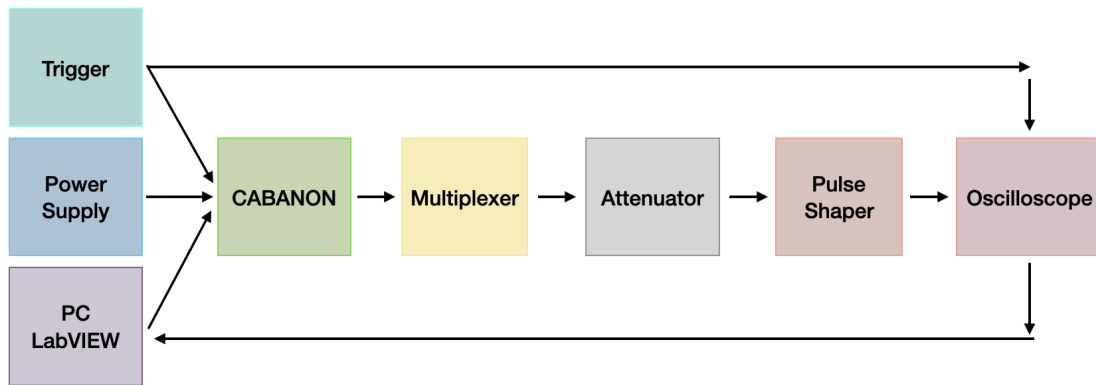


**Figure 6.5.:** Schematic of test bench configuration to study the calibration pulse

#### 6.4.1. Operation of Components

Thorough examinations were conducted to verify the proper operation of the calibration ASICs and DC-DC converters. The outcomes obtained are as outlined below:

- Calibration ASIC

The calibration ASICs revealed defects in certain channels. The defective channels identified were as follows:

- Board 1: All channels of ASIC 3
- Board 2: ASIC 6 Channel 1
- Board 3: ASIC 8 Channel 3, all channels of ASIC 6

Specifically, Board 1 ASIC 3 and Board 3 ASIC 6 were found to be short-circuited. The defects in Board 2 ASIC 6 Channel 1 and Board 3 ASIC 8 Channel 3 were investigated by the cabling team, but a conclusive result could not be obtained. This suggests that the defect could potentially lie in the ASIC itself and/or its packaging.

These defective channels have not been included in the CABANON studies. However, for the final calibration board, thorough checks will be conducted on each calibration ASIC before incorporating it onto the board, which was not performed for CABANON.

- DC-DC Convertor

To evaluate the performance of the two convertors under study, voltage measurements were conducted at the 1.2V and 5V points on CABANON boards 2 and 3. These specific boards were chosen for the comparative analysis since they are the ones equipped with both convertors, as mentioned in Section 6.2. The results, presented in Table 6.2, indicate significant deviations in the measured voltage for the bPOL12V convertor compared to the input voltage on both boards. Additionally, the performance of the bPOL12V convertor deteriorates noticeably when subjected to higher injected currents, such as 300 mA. Furthermore, this deterioration is particularly prominent in Board 3. On the other hand, the LTM4619 convertor demonstrates stable performance.

The poor performance of the bPOL12V convertor can be attributed to a failure to adhere to low noise design rules during the development of the board prototype. Ensuring compliance with specific layout requirements when integrating the DC-DC convertor is essential to minimise noise emissions. Consequently, the next version of the calibration board prototype will receive increased attention in its design phase to effectively address this issue.

CABANON	Input Current	Voltage	Measured Voltage bPOL12V	Measured Voltage LTM4619
Board 2	0	1.2 V	1.2304 V	1.1994 V
	0	5 V	4.8721 V	4.9882 V
	300 mA	1.2 V	1.2305 V	1.1994 V
	300 mA	5 V	4.8719 V	4.9881 V
Board 3	0	1.2 V	1.1955 V	1.1994 V
	0	5 V	4.7974 V	4.9931 V
	300 mA	1.2 V	1.1952 V	1.1994 V
	300 mA	5 V	4.3626 V	4.9845 V

**Table 6.2.:** Measured voltages at 1.2V and 5V points using bPOL12V and LTM4619 DC-DC converters. These measurements were conducted on CABANON boards 2 and 3, considering low (0 mA) and high (300 mA) input currents.

#### 6.4.2. Simultaneous Pulsing of Multiple Channels

As stated earlier, the simultaneous pulsing of multiple channels is a crucial requirement for calibration runs, as discussed in Section 6.2. Thus, in this study, the objective was to simultaneously pulse multiple calibration channels on a board in order to analyse the characteristics of the output pulse produced.

It is important to note that this study was performed exclusively on Board 2. Furthermore, it should be noted that this study aimed to gain a general understanding of the trends, and the measurements obtained were not highly precise. Accordingly, the following tests were carried out:

- pulsing all channels of a calibration ASIC simultaneously

For this test, a 20 mA current was injected into ASIC 1 channel 2. The maximum pulse amplitude measured in ASIC 1 channel 2 was 0.4 in arbitrary units (a.u.). When the same current was injected into all channels of ASIC 1, the maximum amplitude measured in ASIC 1 channel 2 was 0.11 a.u. This test was repeated with other ASICs, yielding the same results. Thus, it can be concluded that the injected current is divided among the four channels within the ASIC, as expected from Equation 6.3.

- pulsing one channel per calibration ASIC simultaneously

In this task, channel 2 of all ASICs was injected with a 20 mA current individually. When the output pulse was measured at channel 2 of any ASIC (e.g. ASIC 1 channel 2, ASIC 4 channel 2, etc.), the maximum amplitude measured was 0.4 a.u. This implies good compatibility across all ASICs of the board.

On the other hand, when the output pulse was measured at any other channel apart from channel 2 (e.g. ASIC 2 channel 4, ASIC 8 channel 1, etc.), only noise was observed. Consequently, as expected, the injected current is not divided within the ASICs when only one channel per ASIC is pulsed.

- pulsing all 32 channels of a board simultaneously

In this test, a 20 mA current was injected into every channel of every calibration ASIC. When measuring the output pulse at any channel, the maximum amplitude observed was 0.11 a.u., indicating that the injected current is distributed among all channels of the ASIC according to Equation 6.3. Once again, uniformity across all channels on the board was observed.

In conclusion, the calibration board prototype behaves as expected when multiple channels are pulsed.

### 6.4.3. DAC Linearity

As mentioned earlier in Section 6.2, it is important to ensure that the calibration board does not compromise the standalone performance of the calibration ASICs. Thus, in this study, the DAC Integral Non-Linearity (INL) results of the CABANON boards were compared to the test results of the standalone CLAROCv2, with the aim of identifying any non-linearity that cannot be attributed to the calibration ASIC itself.

Before soldering the  $R_0 - L$  on the CABANON boards, the linearity between the measured and injected DAC currents was examined. This measurement was conducted using a multimeter in three different input ranges:  $5\mu\text{A}$ -5 mA (with 0.1 mA steps),  $5\mu\text{A}$ -40 mA (with 0.5 mA steps), and  $5\mu\text{A}$ -320 mA (with 5 mA steps), corresponding to 10-bit, 13-bit, and 16-bit DAC configurations, respectively.

As a reminder, CLAROCv2 incorporated four separate HF switches to determine the most optimal design for the final calibration ASIC. (see Section 5.2). Among these switches, Channel 4 of each ASIC was selected as the baseline architecture due to its favorable INL results. Therefore, this study specifically presents the results obtained from Channel 4 of each ASIC. Furthermore, it is important to note that the CABANON setups in this study utilised the bPOL12V convertor.

The following observations were made for each DAC configuration:

- 10-bit: Figure 6.6 illustrates the DAC INL of all functional ASICs for all three boards. In the CLAROCv2 studies, the INL remained within 0.1%, while the DAC linearity in the CABANON setup deteriorated to approximately 0.3%.
- 13-bit: Figure 6.7 shows the DAC INL of all functional ASICs for all three boards, as well as that of the standalone CLAROCv2. In all cases, the INL remained within 0.3%.

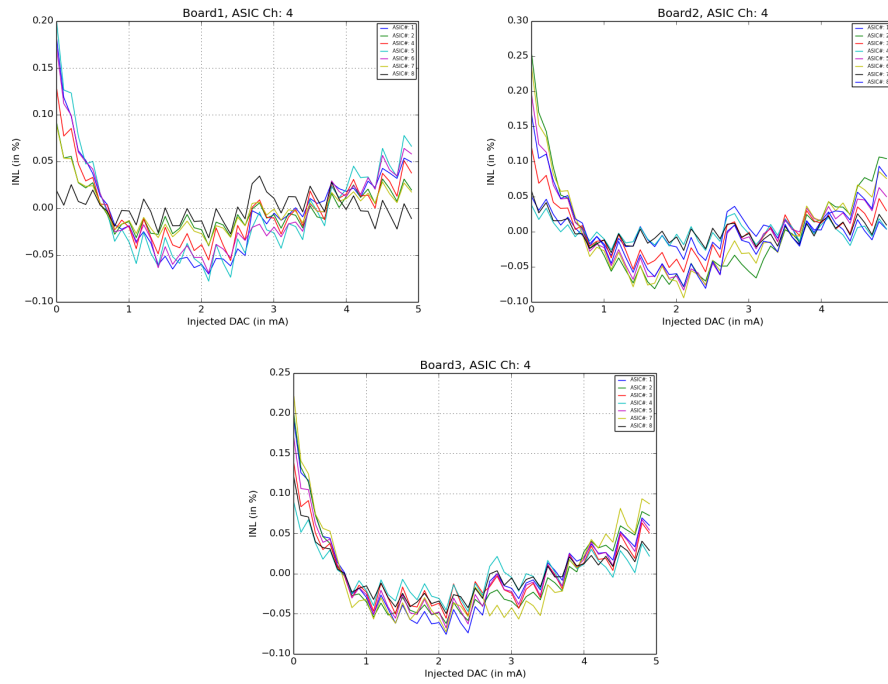


**Figure 6.6.:** DAC INL in 10-bit range for Channel 4 in Board 1 (top left), Board 2 (top right) and Board 3 (bottom)

Additionally, it is worth noting that the large steps in the plot every 5 mA correspond to the addition of a thermometer bit (see 5.2)

- 16-bit: Figure 6.8 displays the DAC INL results of all functional ASICs for all three boards, along with the standalone CLAROCv2. As observed in previous studies, the deteriorating behaviours for large injected DAC values can be attributed to the grid cascode voltage, while the up/down variations in the INL curve are due to a dispersion of the current mirrors. In all cases, a degradation in DAC linearity compared to the standalone CLAROCv2 was observed.

To summarise, the comparison between the CABANON setup and standalone CLAROCv2 reveals the presence of additional non-linearity in the CABANON setup, likely attributed to the unstable performance of the bPOL12V convertor.

It is important to highlight that the DAC INL results show uniformity within a single board. However, significant differences are observed when comparing the results across different boards. Specifically, Board 3 exhibits a more pronounced degradation in DAC linearity, as previously mentioned. Therefore, special attention will be given to the implementation of the convertor chosen in the development of the next calibration board prototype in order to address these issues effectively.

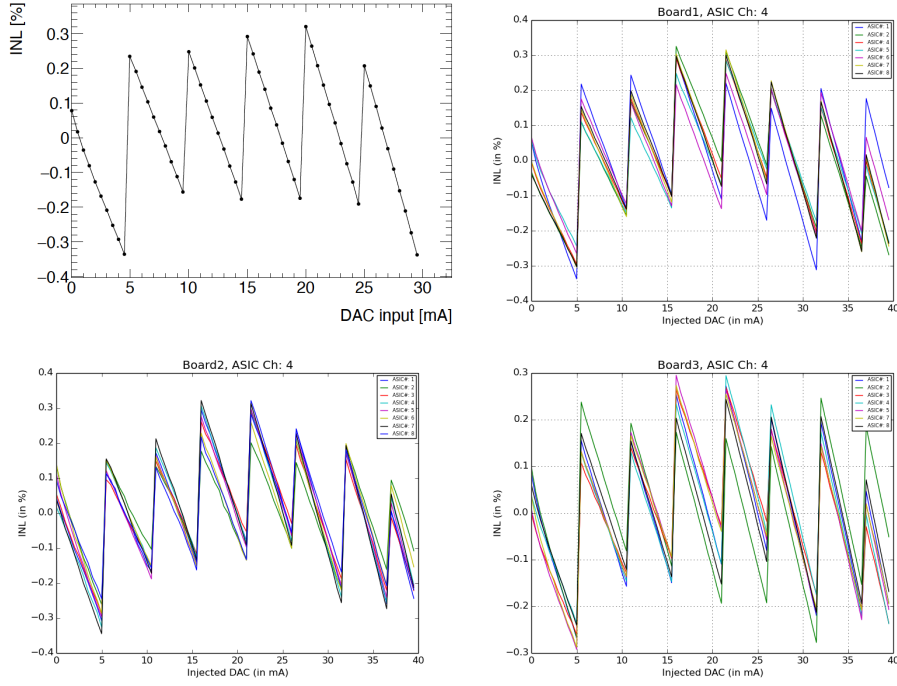


**Figure 6.7.:** DAC INL in 13-bit range for Channel 4 in standalone CLAROCv2 (top left), Board 1 (top right), Board 2 (bottom left) and Board 3 (bottom right)

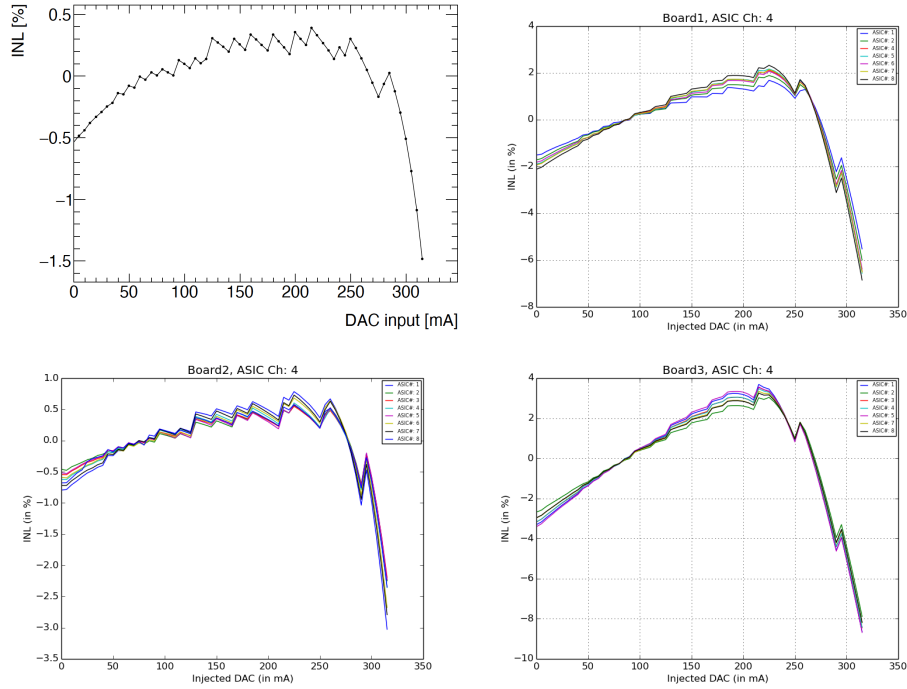


**Figure 6.8.:** DAC INL in 16-bit range for Channel 4 in standalone CLAROCv2 (top left), Board 1 (top right), Board 2 (bottom left) and Board 3 (bottom right)

#### 6.4.4. Pulser Linearity

The linearity of the pulser was evaluated by measuring the maximum pulse amplitude at different DAC currents, following the schematic shown in Figure 6.5. Once again, three distinct input ranges were examined:  $5\mu\text{A}$ -5 mA (with 0.1 mA increments),  $5\mu\text{A}$ -40 mA (with 0.5 mA increments), and  $5\mu\text{A}$ -320 mA (with 5 mA increments), corresponding to 10-bit, 13-bit, and 16-bit DAC configurations, respectively.

In this study, the obtained results were compared to previous studies conducted on CLAROCv2 in order to identify any variations that are not attributable to the calibration ASIC itself. Furthermore, the performance of the LTM4619 convertor was investigated by comparing its outcomes with those of the bPOL12V convertor. These comparative analyses were specifically carried out on Boards 2 and 3, as they are the only boards that have both convertors installed, as mentioned earlier.

Once again, this study specifically focuses on presenting the results obtained from Channel 4 of each ASIC, which represents the HF switch in CLAROCv2 with the baseline architecture.

The following observations were made for each DAC configuration:

- 10-bit: Figure 6.9 displays the pulser INL of all functional ASICs in Boards 2 and 3, after applying the fixed-time correction for injected current as described in Section 5.1. The results of studies with the bPOL12V convertor are shown in blue, while studies with the LTM4619 convertor are shown in red. The figure also includes the pulser INL for standalone CLAROCv2, after applying the fixed-time correction.

In CLAROCv2 studies, the INL remained within 0.1%, while the pulser linearity in the CABANON setup for most ASICs is around 0.2%.

- 13-bit: Figure 6.10 illustrates the pulser INL for all functional ASICs in Boards 2 and 3, along with the standalone CLAROCv2. It is evident that the INL of the pulser is primarily influenced by the non-linearity of the thermometer DAC, which exhibits steps every 5 mA.

In the CLAROCv2 studies, the INL was within 0.4%. The pulser linearity for the CABANON setups also remained relatively similar.

- 16-bit: Figure 6.11 showcases the pulser INL for all functional ASICs in Boards 2 and 3, as well as the standalone CLAROCv2. The dominant factors contributing to the INL of the pulser are once again the non-linearity of the DAC, including thermometer steps, mirror dispersion, and grid cascode voltage at very high currents.

In the case of CLAROCv2, the INL remained within 2.5%. Similarly, for the LTM4619 setup, the INL was within 2.5% for both boards. However, the pulser INL for the bPOL12V setup significantly degraded compared to the CLAROCv2 studies, particularly in board 3. This degradation could be attributed to the unstable performance of the bPOL12V convertor, especially at high currents in board 3, as mentioned earlier.

To summarise, the evaluation indicates that at larger currents, the CABANON setups exhibit increased non-linearity specifically with the bPOL12V convertor, while the LTM4619 convertor maintains stable performance. It is worth emphasising that the INL results demonstrate consistency within a single board. However, notable differences emerge when comparing the results across different boards. Notably, Board 3 displays a more significant degradation

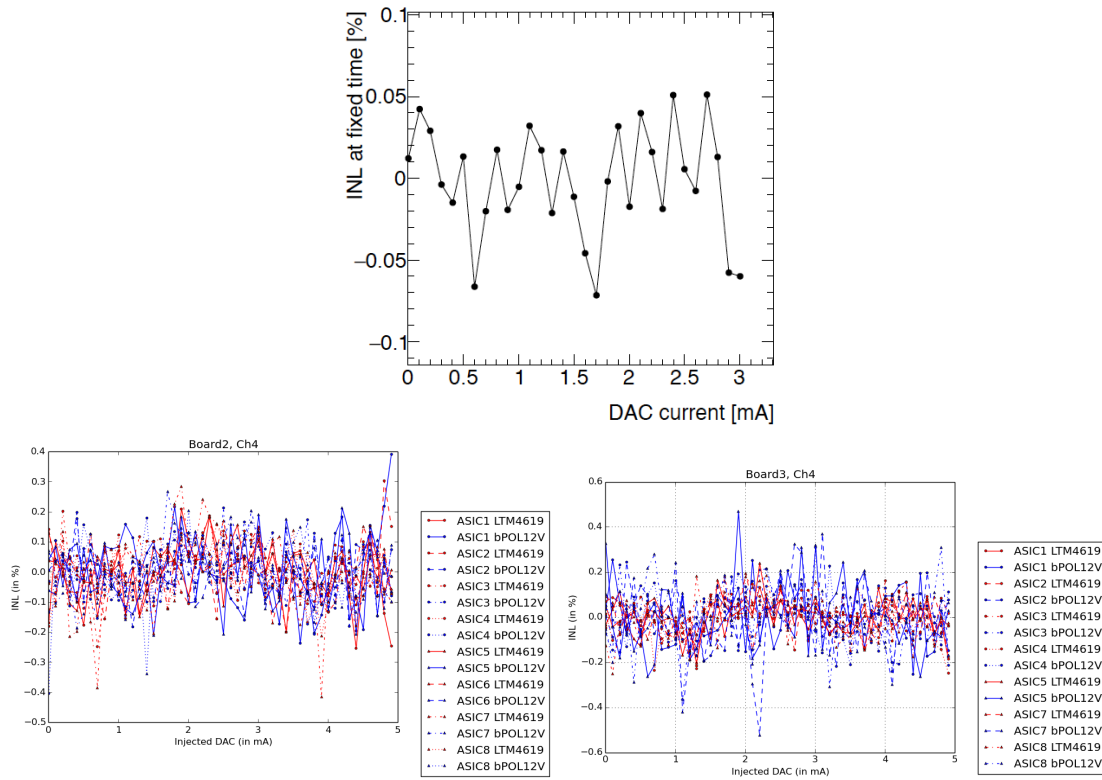


**Figure 6.9.:** Pulser INL (after applying fixed-time correction) in 10-bit range for Channel 4 in standalone CLAROCv2 (top), Board 2 (bottom left) and Board 3 (bottom right). For the boards, bPOL12V results are shown in blue, and LTM4619 results are shown in red.

in linearity, primarily due to the inferior performance of the bPOL12V convertor in that particular board, as previously discussed. Another key finding is that using a stable convertor (such as LTM4619) allows for the recovery of standalone chip performance, highlighting the successful board design.

Consequently, as mentioned earlier, the development of the next calibration board prototype will carefully consider the implementation of the chosen convertor to effectively address these issues.

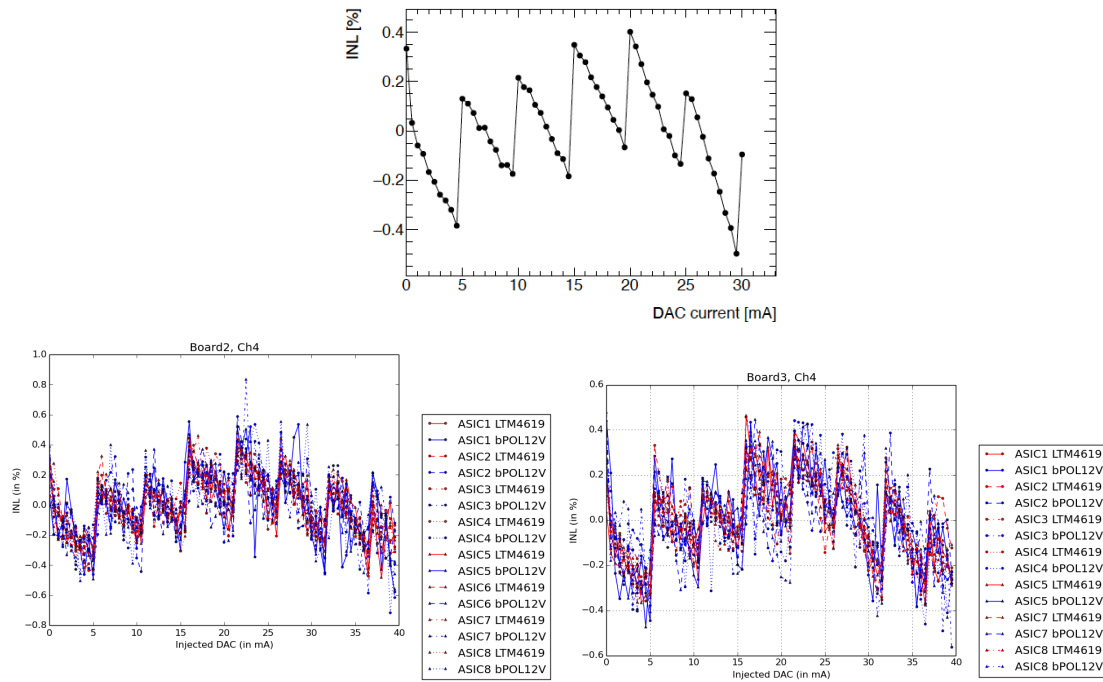


**Figure 6.10.:** Pulser INL in 13-bit range for Channel 4 in standalone CLAROCv2 (top), Board 2 (bottom left) and Board 3 (bottom right). For the boards, bPOL12V results are shown in blue, and LTM4619 results are shown in red.

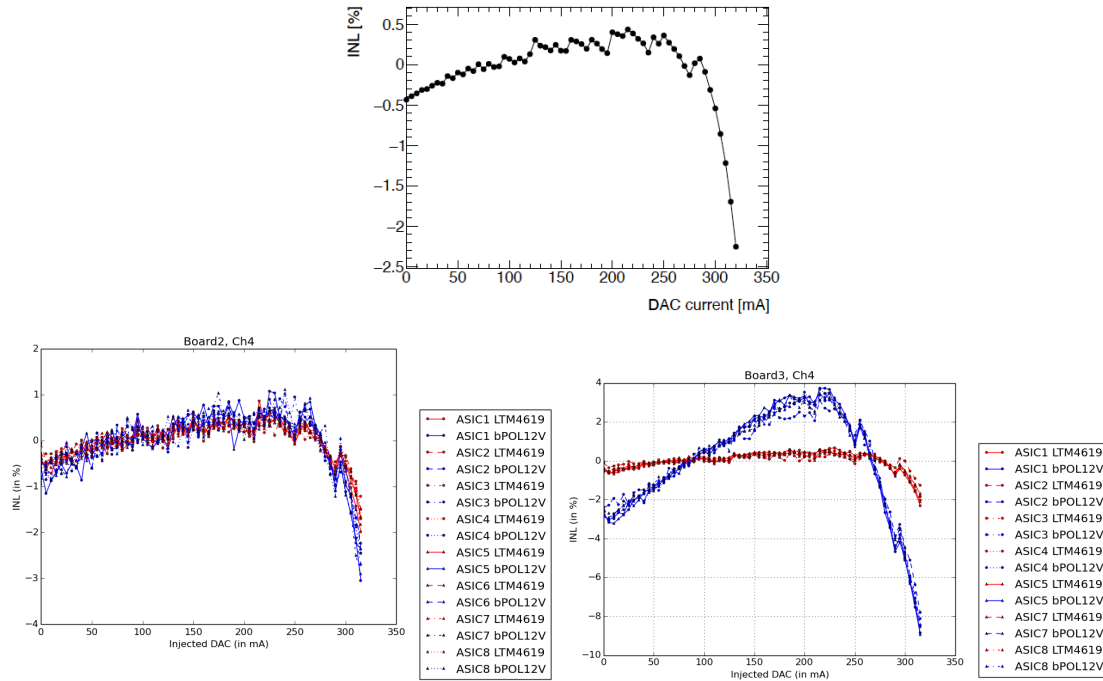


**Figure 6.11.:** Pulser INL in 16-bit range for Channel 4 in standalone CLAROCv2 (top), Board 2 (bottom left) and Board 3 (bottom right). For the boards, bPOL12V results are shown in blue, and LTM4619 results are shown in red.

### 6.4.5. Crosstalk

Crosstalk refers to the undesired signal present in a channel other than the one that was pulsed, leading to non-uniformity on a board. This study focused on analysing crosstalk by injecting a 300 mA pulse into a single channel and measuring the resulting crosstalk pulse in the remaining 31 channels of the board.

The study involved the following tests for each board:

1. Analysis of crosstalk shape
2. Evaluation of crosstalk based on the position of the calibration ASICs

Furthermore, to compare the crosstalk behaviours across different boards, the following studies were conducted:

1. Assessment of the maximum crosstalk amplitude
2. Analysis of crosstalk at the peak of the injected pulse

The subsequent sections provide detailed explanations of the tests performed and present the corresponding test results.

#### 6.4.5.1. Shape of Crosstalk

Figure 6.12 illustrates the shape of the 300 mA current injected into ASIC 1 channel 1 (shown in blue), along with the shape of the maximum crosstalk pulse measured in ASIC 1 channel 3 (shown in green) on board 3. As expected, the crosstalk pulse closely resembles the derivative of the injected pulse.

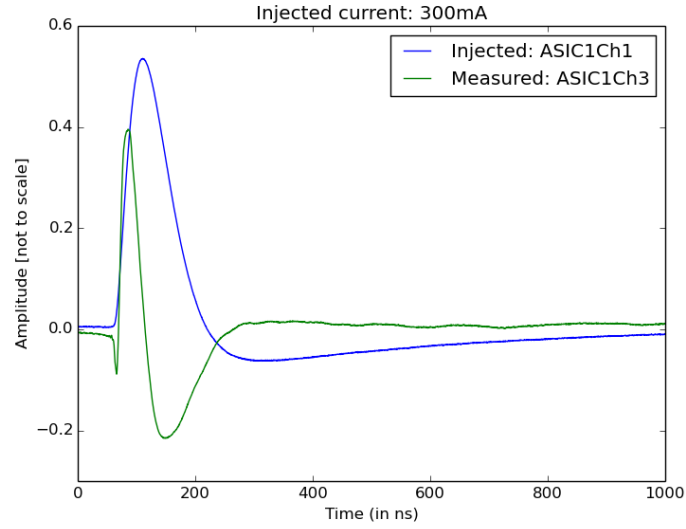
It is important to note that the amplitudes of the pulses in the figure are not represented to scale, as the injected pulse was attenuated while the crosstalk pulse was not. In reality, the maximum crosstalk pulse is relatively small, accounting for approximately 0.1% of the amplitude of the injected pulse.

The measurement was repeated for all channels and in all boards, and no obvious differences in shape were observed for crosstalk pulses.

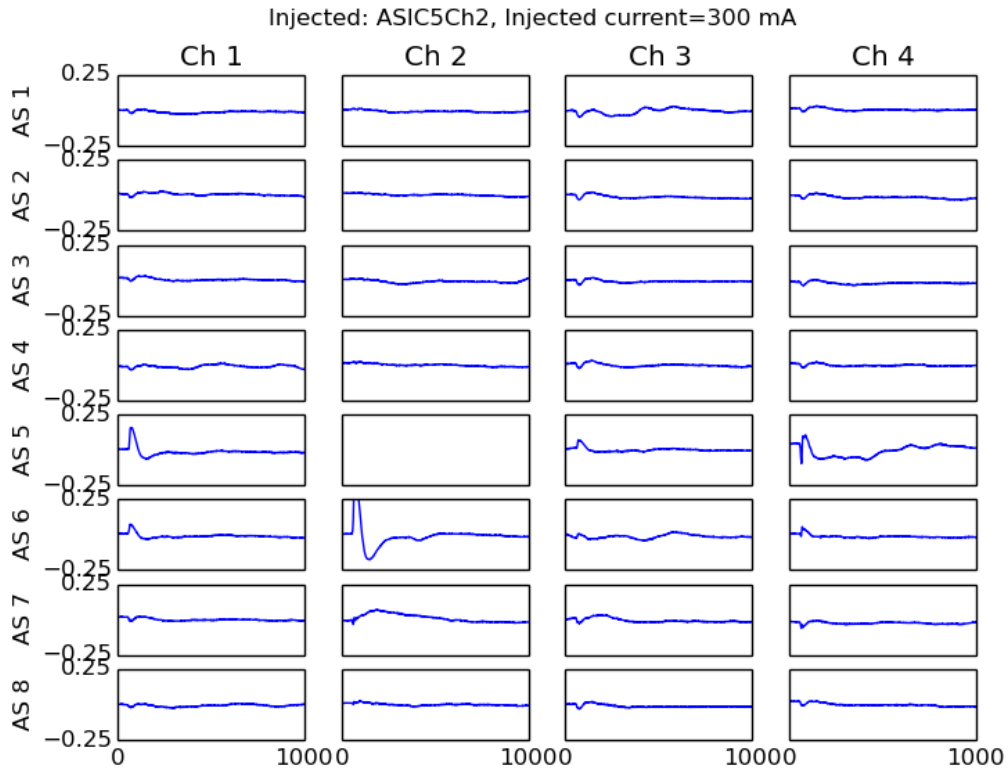
#### 6.4.5.2. Crosstalk based on Position of Calibration ASICs

Figure 6.13 illustrates the crosstalk pulse in the remaining 31 channels when a 300 mA pulse was applied to ASIC 5 channel 2 of board 2. The vertical arrangement of the ASICs corresponds to their positions on the board.

The figure provides clear evidence that ASICs situated closer to the injected channel exhibit elevated levels of crosstalk, whereas the ASICs positioned further away primarily exhibit electronic noise. This observation remained consistent across all tested channels and boards.



**Figure 6.12.:** Shape of injected pulse in channel 1 (blue) and maximum crosstalk pulse measured in change 3 (green) for board 3 ASIC 1. Here, the injected pulse is attenuated by a factor 1000, whereas the crosstalk pulse is not.



**Figure 6.13.:** Crosstalk pulse shapes when a 300 mA pulse was injected in board 2 ASIC 5 channel 2

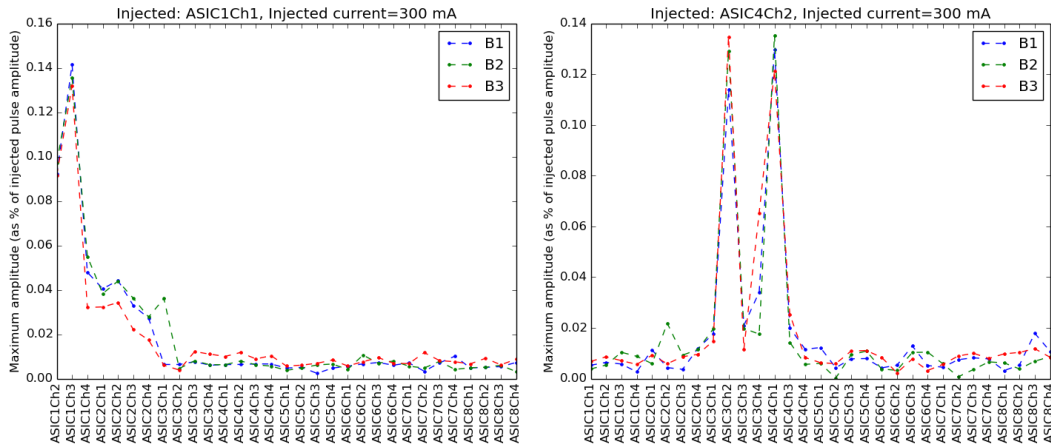


**Figure 6.14.:** Maximum crosstalk (as % of injected pulse amplitude) in each channel when a 300 mA current is injected in i) ASIC 1 channel 1 (left) and ii) ASIC 4 channel 2 (right). Results for boards 1, 2 and 3 are shown in red, blue and green respectively.

#### 6.4.5.3. Comparison of Boards: Peak of Crosstalk

The objective of this study was to compare the maximum crosstalk amplitudes among different boards.

Figure 6.14 illustrates the maximum crosstalk amplitudes in the channels when a 300 mA pulse is injected into i) ASIC 1 channel 1 (left) and ii) ASIC 4 channel 2 (right). The results for board 1, board 2, and board 3 are represented by the colours blue, green, and red, respectively. It is evident that the trends observed in all three boards are quite similar. Additionally, the maximum crosstalk amplitude amounts to approximately 0.14% of the injected pulse amplitude of 300 mA. This aligns with the specified requirement of the maximum crosstalk being around 0.1% of the maximum pulse amplitude, as discussed in Section 6.2.

The same measurement was repeated for all other injected channels, and no discernible differences were observed.

#### 6.4.5.4. Comparison of Boards: Crosstalk at Peak of Injected Pulse

In this study, a comparison of different boards was conducted by analysing the crosstalk at the peak of the injected pulse, which ideally should be zero since the crosstalk pulse is a derivative of the injected pulse.

Figure 6.15 presents the crosstalk at the peak of the injected pulse in all channels when a 300 mA pulse was injected into i) ASIC 1 channel 1 (left) and ii) ASIC 7 channel 3 (right). The results for board 1, board 2, and board 3 are represented by the colours blue, green, and red, respectively. It can be seen that the crosstalk at the peak of the injected pulse is nearly zero.

The same measurement was repeated for all other injected channels and no noticeable differences were observed among the different boards.

In summary, crosstalk was observed in adjacent channels. However, the maximum crosstalk amplitude was minimal, constituting approximately 0.1% of the injected pulse amplitude of

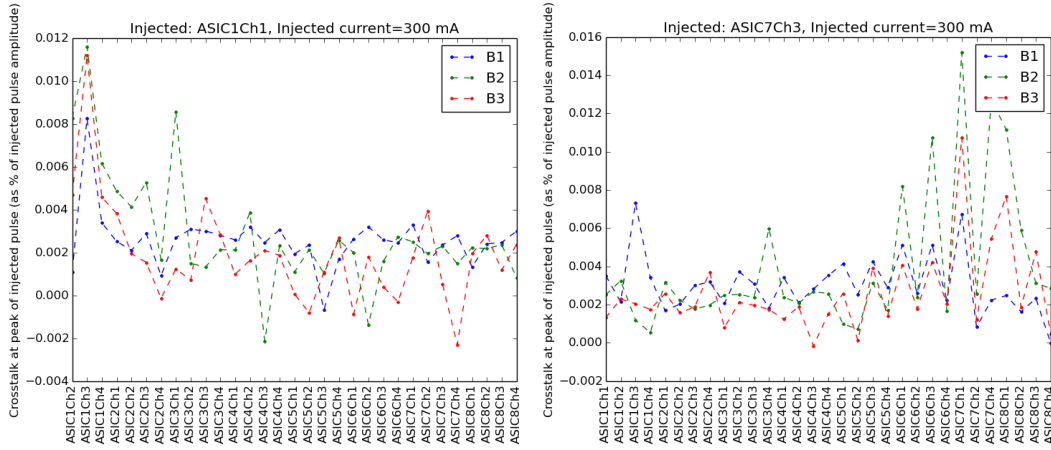


**Figure 6.15.:** Crosstalk at peak of injected pulse (as % of injected pulse amplitude) in each channel when a 300 mA current is injected in i) ASIC 1 channel 1 (left) and ii) ASIC 7 channel 3 (right). Results for boards 1, 2 and 3 are shown in red, blue and green respectively.

300 mA, thus meeting the specified requirement. Furthermore, as anticipated, no crosstalk was observed at the peak of the injected pulse. These consistent results were observed across all boards and channels, indicating a high level of uniformity despite different ASIC placements. Lastly, there was no evident dependence on the type of inductance used, prompting the need for additional magnetic tests to identify the optimal inductor. Based on these findings, it is recommended to adopt a similar routing circuit for the calibration board in the next prototype.

#### 6.4.6. Uniformity

This study aimed to examine the uniformity across all channels of a given board in terms of the maximum pulse amplitude and peaking time. It is important to note that although each channel in CLAROCv2 behaves slightly differently due to its design with 4 different HF-switches, all channels were analysed together to ensure statistical relevance.

The tests were conducted using the bPOL12V convertor for all boards. Additionally, Boards 2 and 3, which were equipped with the LTM4619 convertor, underwent the same tests using this specific convertor. This approach allows for a comparison of both the performance of the convertors and the boards themselves.

Three different injected DACs were used in the tests, specifically: low current (20 mA), intermediate current (185 mA), and high current (310 mA). The corresponding results for each DAC can be observed in Figures 6.16, 6.17, and 6.18, respectively.

The data was analysed by fitting Gaussian curves, and the resulting relative standard deviations<sup>5</sup> and means are presented in Tables 6.3 and 6.4 for the bPOL12V and LTM4619 convertors, respectively. The following conclusions can be drawn:

<sup>5</sup> The relative standard deviation is denoted as  $\frac{\sigma}{\mu}$ , represents the standard deviation ( $\sigma$ ) divided by the mean ( $\mu$ )

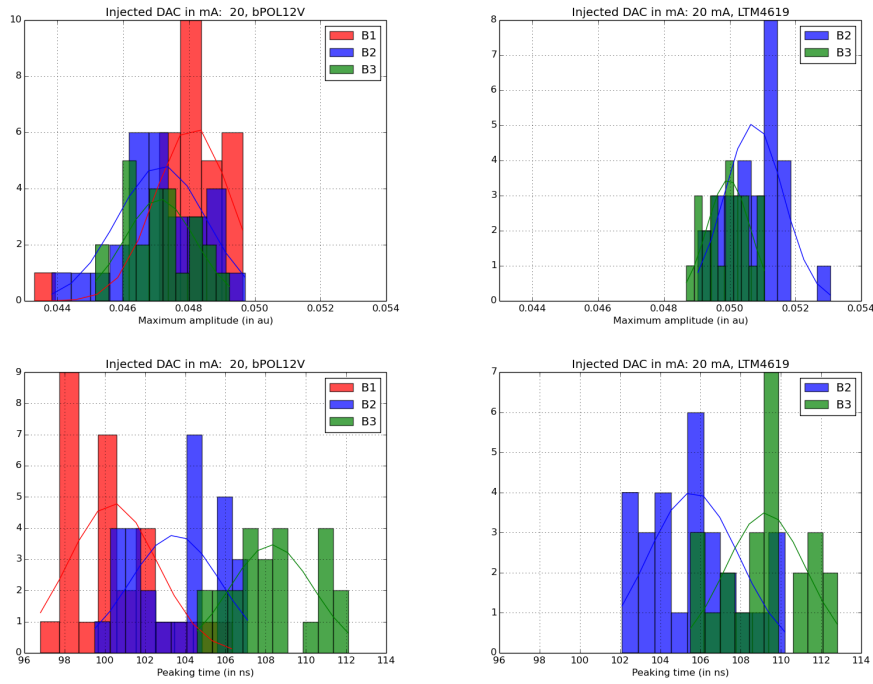


**Figure 6.16.:** Maximum amplitude (top row) and peaking time (bottom row) across all functioning channels. Left column: bPOL12V convertor. Right column: LTM4619 convertor. Boards 1, 2, and 3 depicted in red, blue, and green respectively. Injected DAC: 20 mA.

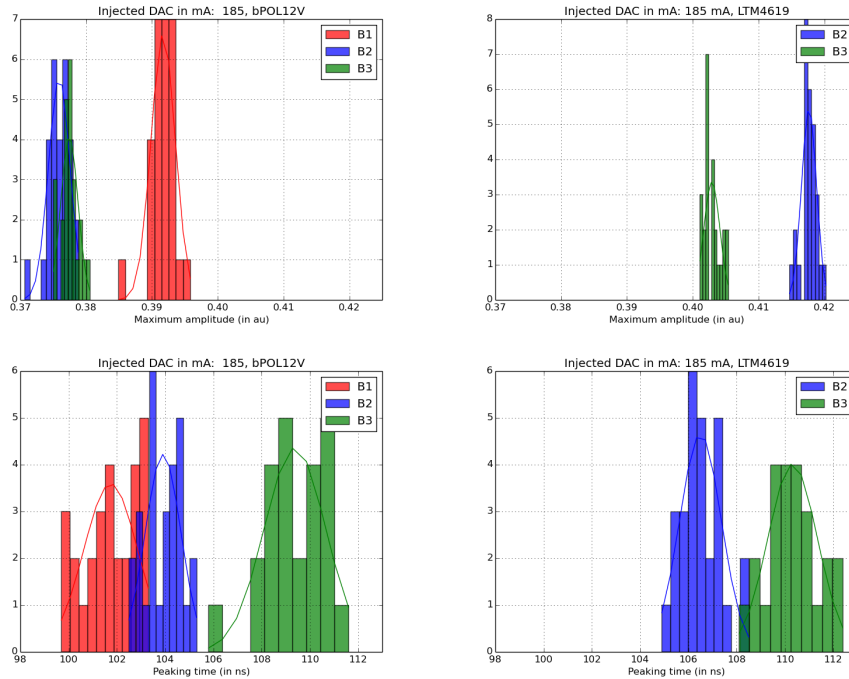


**Figure 6.17.:** Maximum amplitude (top row) and peaking time (bottom row) across all functioning channels. Left column: bPOL12V convertor. Right column: LTM4619 convertor. Boards 1, 2, and 3 depicted in red, blue, and green respectively. Injected DAC: 185 mA.

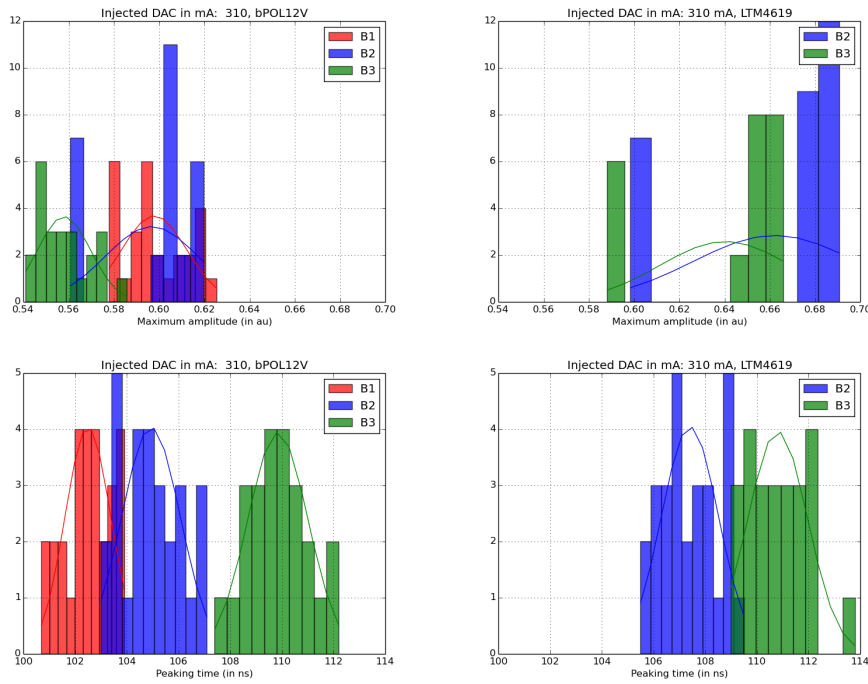


**Figure 6.18.:** Maximum amplitude (top row) and peaking time (bottom row) across all functioning channels. Left column: bPOL12V convertor. Right column: LTM4619 convertor. Boards 1, 2, and 3 depicted in red, blue, and green respectively. Injected DAC: 310 mA.

- **Uniformity Requirement:** None of the boards, tests, or convertor setups meet the specified uniformity requirement of 0.2% for the EMB and EMEC (Section 6.1). Specifically, the obtained relative standard deviations exceed the desired level.
- **Comparison of Boards:**
  - The relative standard deviations are fairly similar across all boards for a given test, convertor setup, and injected current range. This aligns with the desired goal of maintaining consistency despite variations in ASIC placements. Again, the choice of inductance does not have a significant impact on the uniformity of calibration channels. Therefore, additional magnetic tests are needed to further explore this aspect.
  - The mean values for the maximum amplitude demonstrate consistency across all boards for a given injected current range and convertor setup, indicating high uniformity in terms of the mean values of the maximum amplitude.
  - The mean peaking time varies among boards for a given injected current range and convertor setup, suggesting some level of non-uniformity in this parameter. Notably, board 3 exhibits the highest mean peaking time compared to the other boards. Since board 3 has the ASICs situated on top of the board, it could be that the longer length of the electric cables cause a delay in timing pulses.

Injected DAC	Test	Relative Standard Deviation			Mean		
		Board 1	Board 2	Board 3	Board 1	Board 2	Board 3
20 mA	Max amp	2.35%	2.88%	2.28%	0.048 au	0.047 au	0.047 au
	Peak time	2.20%	2.17%	1.91%	100.39 ns	103.5 ns	108.3 ns
185 mA	Max amp	0.47%	0.43%	0.34%	0.39 au	0.38 au	0.38 au
	Peak time	1.1%	0.71%	1.16%	101.7 ns	103.9 ns	109.4 ns
310 mA	Max amp	2.4%	3.42%	2.11%	0.6 au	0.6 au	0.56 au
	Peak time	0.86%	1.08%	1.06%	102.5 ns	104.9 ns	109.8 ns

**Table 6.3.:** Relative standard deviation and mean value for each board and uniformity test across three injected DAC values. Results shown for bPOL12V convertor.

Injected DAC	Test	Relative Standard Deviation		Mean	
		Board 2	Board 3	Board 2	Board 3
20 mA	Max amp	1.75%	1.32%	0.05 au	0.05 au
	Peak time	2.14%	1.83%	105.6 ns	109.2 ns
185 mA	Max amp	0.27%	0.30%	0.42 au	0.4 au
	Peak time	0.81%	0.93%	106.5 ns	110.3 ns
310 mA	Max amp	5.48%	4.51%	0.66 au	0.64 au
	Peak time	1.03%	1.05%	107.4 ns	110.8 ns

**Table 6.4.:** Relative standard deviation and mean value for each board and uniformity test across three injected DAC values. Results shown for LTM4619 convertor.

Additionally, the uniformity across all channels of board 2 was examined to compare the performance of two convertors. It is important to mention that the studies were specifically conducted using board 2 since the bPOL12V setup of board 3 is more prone to malfunction, as mentioned earlier. The results of this comparison are presented in Table 6.5, and the following conclusions can be drawn:

- Comparison of Convertors:
  - Both convertors exhibit a similar relative standard deviation for peaking time, indicating a comparable level of uniformity in this parameter.
  - The LTM4619 convertor shows better relative standard deviation outcomes for maximum amplitude at low currents compared to the bPOL12V convertor, while its performance diminishes at high currents. This suggests that the uniformity of maximum amplitude varies depending on the current range and the specific convertor used.
  - The mean values for the maximum amplitude remain consistent across all convertors for a given injected current range, indicating a good level of uniformity in this parameter.
  - The mean peaking time is consistently larger for the LTM4619 convertor across all current ranges. This indicates that the LTM4619 may introduce a time delay while converting the current. This has to be confirmed with more studies.

Injected DAC	Test	Relative Standard Deviation		Mean	
		bPOL12V	LTM4619	bPOL12V	LTM4619
20 mA	Max amp	2.88%	1.75%	0.047 au	0.05 au
	Peak time	2.17%	2.14%	103.5 ns	105.6 ns
185 mA	Max amp	0.43%	0.27%	0.38 au	0.42 au
	Peak time	0.71%	0.81%	103.9 ns	106.5 ns
310 mA	Max amp	3.42%	5.48%	0.6 au	0.66 au
	Peak time	1.08%	1.03%	104.9 ns	107.4 ns

**Table 6.5.:** Relative standard deviation and mean value for each convertor setup and uniformity test across three injected DAC values. Results shown for Board 2.

In summary, none of the boards achieved the desired level of uniformity, which was set at 0.2% across all channels. Although certain dependencies were observed concerning the selection of convertors and/or boards, additional statistical analysis and tests are needed to validate these findings. Furthermore, the failure to meet the uniformity requirement can be attributed to the following key factors:

- A large non-linearity is already present in both the calibration ASICs and the boards themselves.

- In this study, precise adjustment of reference voltages in the calibration ASICs was not achievable, resulting in a significant dispersion among ASIC results. However, this issue will be addressed and resolved in the next calibration prototype.
- The calibration ASIC used in the study has four different channels. However, in the final calibration board, all channels will be identical, thereby improving uniformity.
- The study was limited to only 32 channels, and obtaining a larger dataset would greatly contribute to obtaining more comprehensive and robust results.

## 6.5. Current Status of Calibration Board Prototype

The tests conducted on the CABANON prototype have yielded valuable insights for the development of the next calibration board prototype. They can be summarised as follows:

- No obvious dependence was observed on the placement of ASICs. This suggests consistent results across an entire board.
- The LTM4619 DC-DC convertor demonstrated a superior performance compared to the bPOL12V convertor. The poor performance of the bPOL12V convertor was attributed to the failure to adhere to low noise design rules during its development. Consequently, greater emphasis will be placed on addressing this issue in the design phase of the next calibration board prototype. Furthermore, the choice of convertor will be determined by further tests on radiation tolerance, voltage conversion efficiency, and temperature losses.
- Both the S1812R-123G and ISC1210ER120J inductances showed similar performance. Since the S1812R-123G is no longer in production, the newer ISC1210ER120J inductance will be selected for the next calibration board prototype, pending successful completion of the magnetic tests.
- Cross-talk was detected at a level of 0.1% of the signal in channels where it was present. Notably, only a small subset of channels (approximately 5-10) surrounding the signal channel experienced cross-talk, while the remaining channels primarily exhibited electronic noise. These findings support the implementation of a similar positioning and routing approach for the calibration ASICs and  $R_0 - L$  circuit in the next calibration board prototype.
- The CABANON prototype did not meet the uniformity requirement. One of the contributing factors was the inability to fine-tune the reference voltages in the calibration ASICs. This issue will be addressed in the next version of the calibration board prototype.

Based on these findings, the design of the first full 128-channel calibration board prototype is currently underway, with plans for fabrication scheduled for summer/autumn 2023.

## Part II.

## Chapter 7.

# Vector Boson Scattering at LHC

A typical VBS interaction at the LHC is shown in Figure 7.1. In this process, two vector bosons are emitted by the quarks in the colliding beams. These vector bosons then interact with each other, leading to the production of two additional vector bosons, which may differ from the initial ones. The quarks involved in the interaction are subsequently deflected and emitted as forward-backward jets<sup>1</sup>. Therefore, VBS processes at the LHC are characterised by the presence of two vector bosons accompanied by two jets with large pseudorapidity difference between them. In fact, they are commonly denoted as EW- $VVjj$ <sup>2</sup> processes. The interaction between the two vector bosons, represented by the circle in Figure 7.1, involves contributions from both the self-couplings of the gauge bosons and the couplings of the Higgs boson to gauge bosons (as discussed previously in Section 2.2).

Figure 7.2 presents an overview of cross-section measurements obtained with the ATLAS detector, focusing on processes allowed by the Standard Model. Among these measurements, the production cross-section for VBS processes, indicated by the EWK- $Z\gamma jj$  and EWK- $VVjj$  labels in Figure 7.2, is found to be approximately  $O(10^{-3})$  pb. This relatively low cross-section poses a significant challenge for experimental studies on VBS. In fact, historically, studies on VBS have been restricted by limited statistics. However, the advent of the LHC Run-2 data sets, distinguished by their unparalleled energy scale and integrated luminosity, has ushered in a new era of exploration and provided opportunities to investigate these rare processes in greater detail.

Now, VBS processes at the LHC [52] can be categorised into different channels and final states based on the types of vector bosons involved and their decay modes, as presented in Table 7.1. Each channel and final state exhibits distinct characteristics. The fully leptonic channel offers a clean signal with minimal background contamination, but it has a lower yield in terms of signal events. On the other hand, the hadronic channel provides the highest signal yield, but it is accompanied by a larger background contribution<sup>3</sup>. The semi-leptonic final state strikes a balance between these two channels, providing a cleaner reconstruction of bosons from leptons and higher yields from bosons decaying into hadrons. Additionally, the photonic channels, which involve the presence of at least one photon, exhibit relatively higher production cross-sections in the measurement phase space, as evidenced by the labels  $Z\gamma jj$  and  $VVjj$  in Figure 7.2.

---

<sup>1</sup> Jets refer to collimated bunches of particles that result from the interaction of quarks and gluons produced in high-energy collisions

<sup>2</sup>  $V$  refers to electroweak vector bosons, and  $j$  denotes jets

<sup>3</sup> In particle physics, the term "signal" refers to the specific process of interest, while "background" describes any physics process resembling the signal and producing a similar detector signature.

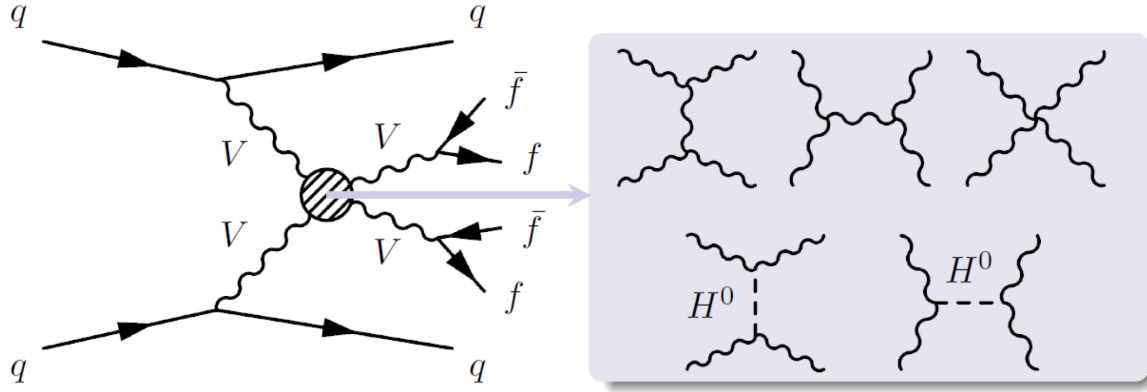


Figure 7.1.: VBS process at the LHC

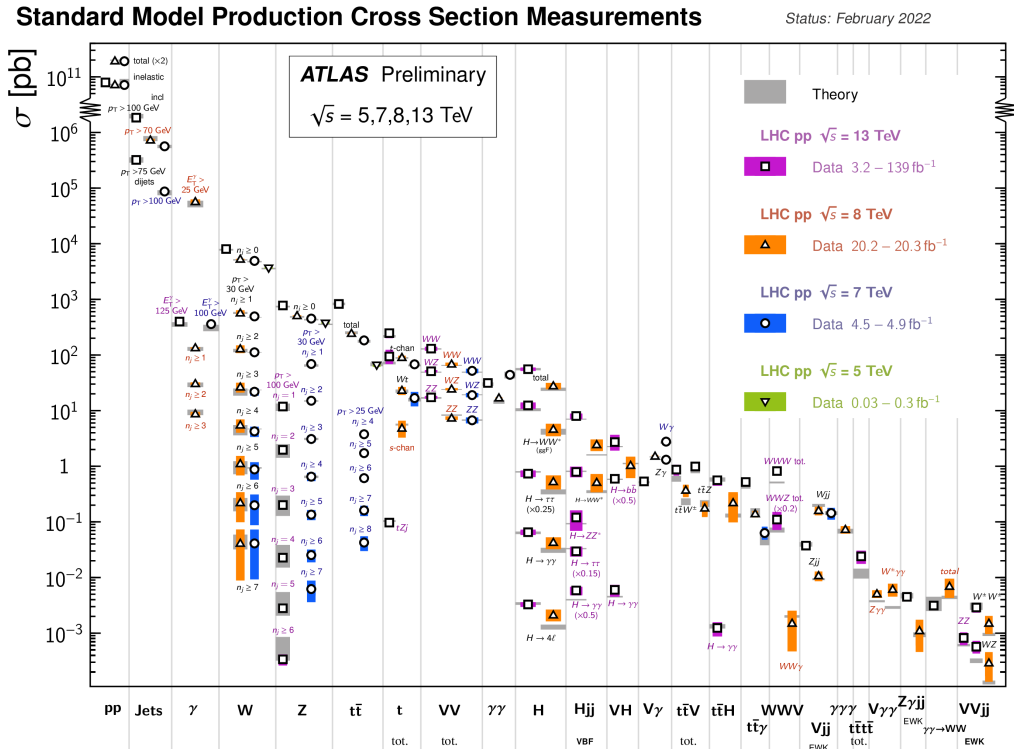


Figure 7.2.: Standard Model production cross section measurements by the ATLAS experiment [51]

Channel	Fully Leptonic	Semi Leptonic	Hadronic	Photonic
Final State	$W^\pm W^\pm \rightarrow l^\pm \nu l^\pm \nu$	$ZV \rightarrow 2l2q$	$VV \rightarrow 4q$	$Z\gamma \rightarrow l^\pm l^\mp \gamma$
	$W^\pm W^\mp \rightarrow l^\pm \nu l^\mp \nu$	$WV \rightarrow l\nu 2q$	$ZV \rightarrow 2\nu 2q$	$Z\gamma \rightarrow 2\nu \gamma$
	$WZ \rightarrow 3l\nu$			$W\gamma \rightarrow l\nu \gamma$
	$WZ \rightarrow l3\nu$			$V\gamma \rightarrow 2q\gamma$
	$ZZ \rightarrow 4l$			$\gamma\gamma$
	$ZZ \rightarrow 2l2\nu$			
	$ZZ \rightarrow 4\nu$			

**Table 7.1.:** The list of all possible VBS channels and final states, categorised by vector bosons engaged in the interactions:  $W, Z$  boson or photon  $\gamma$ , and their decay modes to charged leptons  $l$ , neutrinos  $\nu$ , and/or to quarks  $q$ .  $V = W, Z$ .

The main focus of this thesis is to investigate the photonic  $Z\gamma$  VBS process using the full Run-2 data obtained by the ATLAS detector. The motivation for studying this process is discussed in Section 7.1, while its experimental signature is described in Section 7.2. Lastly, Section 7.3 provides an overview of the objectives pursued in this study.

## 7.1. Motivation

In Section 2.2, it was discussed that VBS studies are important for constraining dimension-6 and dimension-8 Wilson coefficients. However, dimension-6 operators, which modify triple gauge couplings, are better constrained by other non-VBS processes with higher cross-sections at the LHC, such as vector boson production with jets (labeled  $Vjj$  in Figure 7.2). On the other hand, dimension-8 operators, which specifically affect the quartic gauge coupling, can only be constrained through VBS and triple vector boson production. Therefore, investigating VBS processes at the LHC plays a pivotal role in constraining dimension-8 Wilson coefficients. The primary motivation for studying the  $Z\gamma$  VBS process is to explore anomalies in the quartic  $WWZ\gamma$  coupling and search for the presence of neutral quartic gauge couplings, such as  $ZZZ\gamma$ ,  $ZZ\gamma\gamma$ , and  $Z\gamma\gamma\gamma$ , which are not allowed within the Standard Model framework (as discussed in Section 2.1.2).

It is worth noting that other VBS processes, such as  $ZZ$  and  $\gamma\gamma$ , also involve neutral gauge couplings. However,  $ZZ$  has a lower cross-section as it is a non-photonic channel and  $\gamma\gamma$  is more susceptible to a larger background from misidentified photons. Hence, the  $Z\gamma$  VBS process is considered the optimal choice for investigating neutral quartic gauge couplings.

The  $Z\gamma$  VBS process can result in various final states depending on the decay of the  $Z$  boson. As shown in Table 7.1, the final state can involve charged leptons ( $Z\gamma \rightarrow l^\pm l^\mp \gamma$ ), neutrinos ( $Z\gamma \rightarrow 2\nu \gamma$ ), or quarks ( $Z\gamma \rightarrow 2q\gamma$ ). The hadronic final states tend to have larger backgrounds, while neutrinos, being weakly interacting particles, escape the detector without leaving a detectable signal. In contrast, charged leptons can be accurately detected and measured in the detector, providing clean signals. Hence, in this analysis, the chosen final state for the  $Z\gamma$  VBS process is  $l^\pm l^\mp \gamma$ , where  $l$  represents either an electron or a muon.

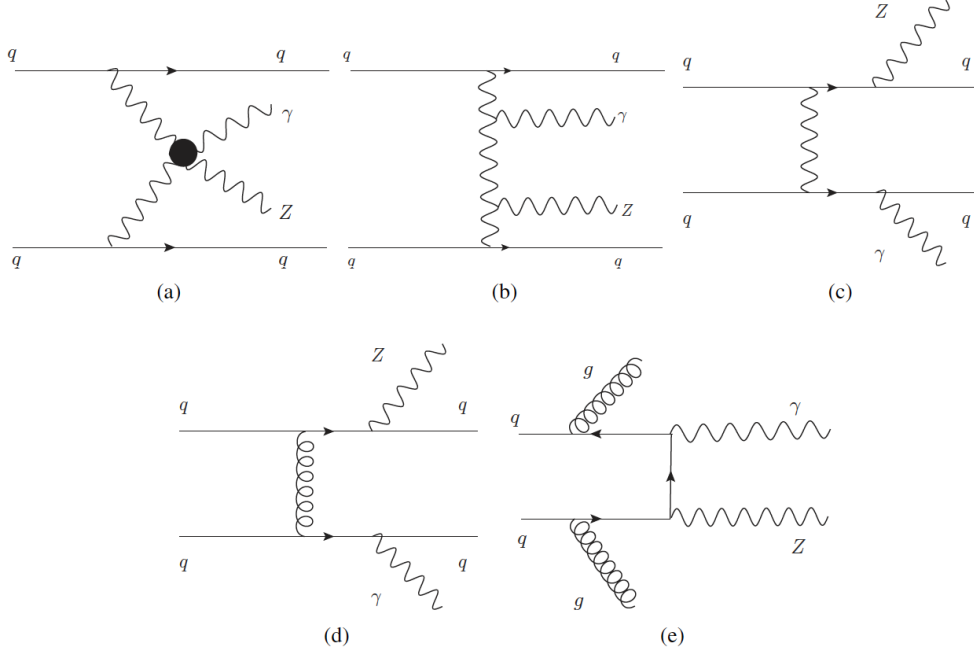


**Figure 7.3.:** Representative Feynman diagrams of the processes relevant to the  $Z\gamma jj$  analysis: (a) quartic gauge coupling VBS, (b) triple gauge coupling VBS, (c) electroweak non-VBS; QCD-induced process with (d) gluon exchange or (e) gluon radiation.[53]

It is important to note that, due to lepton universality in the weak interaction [1],  $Z$  decaying to tau leptons is as prevalent as  $Z$  decaying to electrons and muons. Moreover, if the  $\tau$  decays leptonically<sup>4</sup>, the final state of  $Z \rightarrow \tau\tau$  closely resembles that of  $Z \rightarrow ee$  or  $Z \rightarrow \mu\mu$  processes, since neutrinos from the  $\tau$  decay do not leave a detectable signal in the detector. In this analysis, the  $p_T$  cut for the leading lepton<sup>5</sup> from the  $Z$  decay has been set above the lowest unprescaled lepton trigger threshold (see Chapter 11). Thus, a very small fraction of  $Z \rightarrow \tau\tau$  events survive<sup>6</sup>. In fact, in a separate study, a limited number ( $<10$ ) of events involving  $\tau$  leptons satisfied the  $Z\gamma$  analysis criteria, in contrast to the approximately 260 signal events involving electrons and muons. Consequently, tau leptons have been disregarded in this analysis due to their negligible contribution.

## 7.2. Experimental Signature

As mentioned earlier, the  $Z\gamma$  VBS process at the LHC is characterised by the final state of  $Z\gamma jj$ . However, there are additional processes that contribute to the same final state, as depicted in Figure 7.3. Specifically, the top row illustrates the electroweak production of  $Z\gamma$  in association with two jets. Among these diagrams, Figures (a) and (b) correspond

<sup>4</sup>  $\tau \rightarrow l\nu_l\nu_\tau$ , where  $l$  is  $e$  or  $\mu$

<sup>5</sup> Leading lepton is the lepton with the highest  $p_T$

<sup>6</sup> The rationale is that electrons or muons originating from tau decays exhibit lower energy due to some being carried away by neutrinos. Consequently, low- $p_T$  electrons or muons resulting from  $\tau$  decays fail to pass the high lepton  $p_T$  cut.

to VBS processes with triple and quartic gauge couplings, while Figure (c) does not. It is important to emphasise that since all these processes are generated at  $O(\alpha_{EW}^4)$ , where  $\alpha_{EW}$  represents the electroweak gauge coupling, they cannot be disentangled based on the principle of gauge invariance. Therefore, the study of the  $Z\gamma$  VBS process at the LHC necessitates an investigation of the complete electroweak production of  $Z\gamma$  pairs in association with two jets, referred to as EW- $Z\gamma jj$  production.

Additionally, there are other processes involving Quantum Chromodynamics (QCD)<sup>7</sup> radiation of partons that also contribute to the  $Z\gamma jj$  final state at  $O(\alpha_S^2\alpha_{EW}^2)$ , where  $\alpha_S$  represents the strong interaction coupling constant. These processes, depicted in the bottom row of Figure 7.3, form an irreducible background<sup>8</sup> to the measurements of the EW- $Z\gamma jj$  production and are referred to as QCD- $Z\gamma jj$ .

Lastly, the interference between EW- $Z\gamma jj$  and QCD- $Z\gamma jj$  processes, generated at  $O(\alpha_S\alpha_{EW}^3)$ , is small. Consequently, it can be treated as a theoretical uncertainty for EW- $Z\gamma jj$  measurements, as discussed later in Chapter 10.

### 7.3. Measurement Objectives

Previous experimental studies on the production of EW- $Z\gamma jj$  have been conducted by the ATLAS [54] and CMS [55] collaborations using data collected at  $\sqrt{s} = 8$  TeV, yielding no evidence at that time. However, both experiments reported evidence of the process based on partial data sets collected at  $\sqrt{s} = 13$  TeV with an integrated luminosity of  $36 \text{ fb}^{-1}$  [56] [57]. Furthermore, ATLAS and CMS observed the process using the full Run-2 data sample [53] [58]. This thesis describes the analysis that led to observation and production cross-section measurement of the EW- $Z\gamma jj$  process using the complete Run-2 dataset recorded by the ATLAS detector.

As mentioned in Section 2.2, the presence of new physics can be observed through deviations in cross-sections. Figure 7.4 illustrates that these deviations are most pronounced around the energy scale associated with new physics. By performing precise measurements of the tails of the distributions, it becomes possible to establish limits on the Wilson coefficients. Thus, another objective of this analysis is to conduct differential cross-section measurements of the EW- $Z\gamma jj$  process, focusing on variables that are highly sensitive to anomalous quartic gauge couplings in the high-value tail regions.

Moreover, as stated in the next chapter, simulation of physics processes is crucial in particle physics. Thus, this analysis also provides differential cross-section measurements of various EW- $Z\gamma jj$  variables to improve their modelling.

Finally, this analysis includes measurements of the overall  $Z\gamma jj$  process, encompassing contributions from EW- $Z\gamma jj$ , QCD- $Z\gamma jj$ , and interference terms. It is important to highlight that ATLAS recently reported cross-section measurements for the  $Z\gamma$ +jets process [59]. Therefore, the results presented in this thesis complement the aforementioned study by providing a measurement of the total  $Z\gamma jj$  in a VBS-like region. This measurement is crucial

<sup>7</sup> QCD is the gauge theory for strong interactions in the SM

<sup>8</sup> In particle physics analyses, there are two types of backgrounds: reducible and irreducible. Reducible backgrounds occur when particles imitate the particles of interest, such as jets resembling high-energy photons. Irreducible backgrounds, on the other hand, consist of particles that are of the same type as the particles being studied.

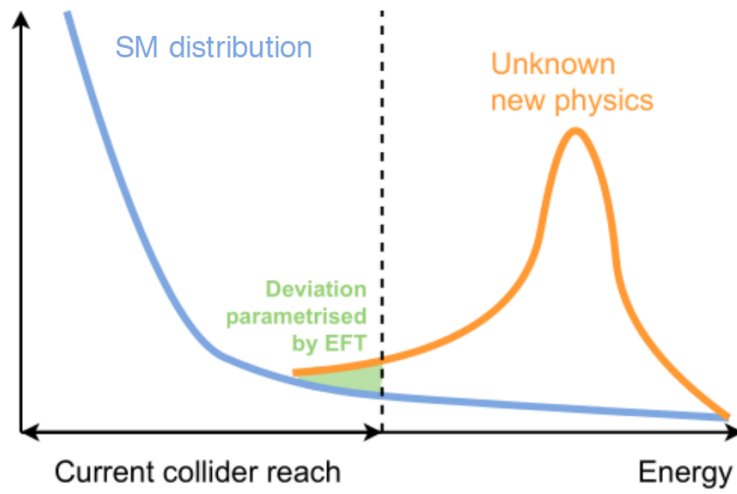


**Figure 7.4.:** A diagram showing possible measurable effects in the tails of current energy reaches, due to new physics present beyond current accessible scales.

for achieving a comprehensive characterization of this process in a region highly sensitive to new physics.

## Chapter 8.

# Simulation

The primary purpose of the ATLAS detector is to accurately detect and record the particles produced from collisions occurring at the LHC. However, to fully comprehend the observed outcomes, a deep understanding of the complete kinematics of proton-proton ( $pp$ ) collisions and the detector's response to the resulting particles is essential. Due to the intricate nature of these processes, it is not feasible to analyse them analytically. Hence, modelling or simulation techniques must be employed.

In the field of particle physics, where stochastic processes govern particle production and decays, the *Monte Carlo (MC) method* is the most suitable choice for simulations. This method involves generating a large number of random events based on theoretical predictions and established physical laws, using specialised software tools called MC generators.

Section 8.1 provides an overview of the MC simulation utilised in analyses at proton colliders, while Section 8.2 focuses specifically on the MC samples related to the  $Z\gamma jj$  analysis.

### 8.1. Simulation of Proton Collisions

Simulations performed at proton colliders consist of two primary components: *event generation* and *detector simulation*. Event generation simulates the physics processes that occur during collisions, providing valuable information about particle types, energies, and momenta. On the other hand, detector simulation focuses on modelling how the detector responds to the produced particles, considering its geometry and response functions. By combining event generation and detector simulation, it becomes possible to simulate the entire process from collisions to recorded signals.

#### 8.1.1. Event Generation

Figure 8.1 shows the diagram of a  $pp$  collision. Event generation tries to mimic the process, resulting in the following key steps [60] [61]:

- **Hard scattering:** The highest energy interaction in a proton collision is the hard scattering process, involving the collision of partons within the protons. The likelihood of this

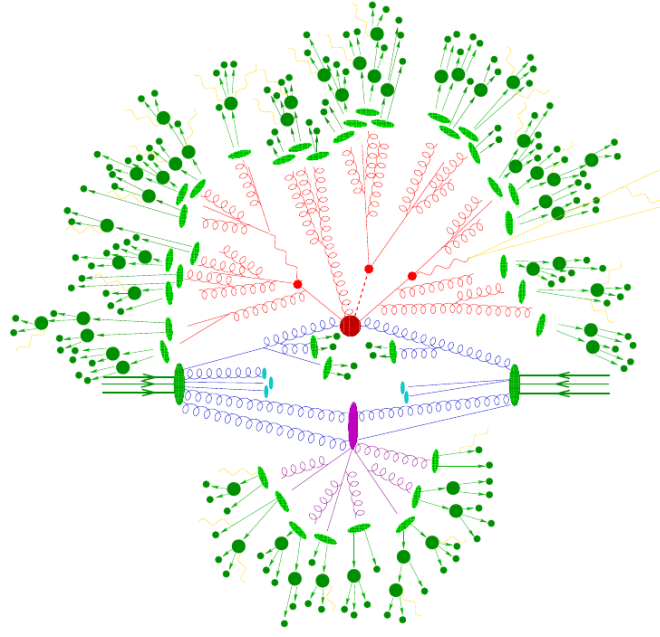


**Figure 8.1.:** A  $pp$  collision with distinct stages: hard scattering (dark red circle), parton shower (red), hadronisation (green), and underlying event (blue,purple).[60]

process, represented by its cross-section, can be calculated perturbatively<sup>1</sup> using *matrix element generators*, typically at leading order (LO) or next-to-leading order (NLO)<sup>2</sup>.

- **Parton Shower:** During the hard scattering process, energetic partons produced in the initial and final states can emit additional partons through successive branching processes. These emissions account for higher-order perturbative contributions beyond LO or NLO. However, calculating the exact outcomes of these emissions from first principles would be computationally intensive. To address this, a simplified probabilistic method known as parton shower is used to simulate the parton emissions, taking into account the kinematics and probabilities of each emission.
- **Hadronisation:** As the parton shower progresses, the partons gradually lose energy until they reach energy levels where they can no longer exist as isolated particles. At this stage, the partons undergo a process known as hadronisation, wherein they combine to form bound states called hadrons. Due to the complex nature of QCD processes at low energy scales, hadronisation cannot be modelled using perturbation theory<sup>3</sup> and require empirical modelling.
- **Underlying Event:** Lastly, partons that are not directly involved in the hard scattering process can also interact with each other resulting in additional hadrons, such as pileup. This phenomenon, known as underlying event, is simulated separately and incorporated into the final model at a later stage of the simulation process.

<sup>1</sup> Perturbative QCD is a theoretical approach that uses series expansions based on small parameters, such as the strength of the strong coupling constant, to study the interactions of quarks and gluons.

<sup>2</sup> LO and NLO refer to different levels of approximations perturbative expansion. LO represents the dominant contribution, while NLO includes the LO term and the first-order correction, resulting in improved accuracy.

<sup>3</sup> Perturbative QCD is particularly useful for high-energy processes where the coupling constant is small, but other techniques are needed for low energies.

All simulation stages which require approximate modelling (i.e. parton shower, hadronisation, underlying event simulation) involve free parameters in the modelling descriptions. The optimised sets of the free parameters, called *tunes*, are taken as input by the MC generators.

General-purpose MC event generators are versatile software packages that handle all aspects of the event generation procedure. Examples of such generators include **PYTHIA**, **HERWIG**, and **SHERPA**. On the other hand, there are dedicated matrix element generators such as **MADGRAPH** and **POWHEG** that specifically focus on generating matrix elements. Since they do not perform parton showering and hadronisation, they are typically interfaced with general-purpose generators. [62]

It should be noted that different generators employ different phenomenological models, thereby making it important to test multiple generators for analysing physics processes. Moreover, to ensure accuracy and avoid double counting of emissions, it is crucial to match or merge the order at which the matrix element is generated with the order used for the parton shower. *Matching* entails the computation of higher-order matrix elements for emissions, which are then harmonised with the outcomes obtained from the parton shower. On the contrary, *merging* involves the introduction of a threshold scale. Partons generated above this scale are derived using a higher-order matrix element, whereas those generated below the scale are simulated via the parton shower. [61]

### 8.1.2. Detector Simulation

The final step in producing simulated events is to model the interaction between stable particles and the detector hardware so that simulation can be compared directly to data. The **GEANT4** framework is used for most detector simulation within ATLAS. It utilises MC simulation techniques to individually simulate the trajectory of each particle as it passes through the detector hardware. This approach provides a highly accurate approximation of the detector response.

## 8.2. Simulated Samples

This section provides information about the MC samples used to simulate the signal and background processes in the  $Z\gamma jj$  analysis. These simulated samples play a critical role in optimising analysis techniques, estimating backgrounds, and comparing experimental data with theoretical predictions.

### 8.2.1. Signal Sample

In this particular analysis, the process of interest is EW- $Z\gamma jj$ . The corresponding sample was generated with **MADGRAPH5\_AMC@NLO** 2.6.5 [63] at LO QCD with the NNPDF3.1 parton distribution function<sup>4</sup> (PDF) [64] set. The sample was interfaced with **PYTHIA** 8.240 [65] for parton showering, hadronisation and underlying event with the **A14** tune [66].

---

<sup>4</sup> A parton distribution function (PDF) describes the distribution of partons within a proton or other hadron. PDFs provide information about the likelihood of finding a parton with a specific momentum at a given energy scale. They are crucial for calculating cross-sections and making predictions for high-energy physics processes.

Process	Matrix Element (ME)	Parton Shower	ME $\mathcal{O}(\alpha_S)$
EW- $Z\gamma jj$	MADGRAPH	PYTHIA	LO
QCD- $Z\gamma jj$	SHERPA	SHERPA	NLO
$Z$ +jets	POWHEG	PYTHIA	NLO
$t\bar{t}\gamma$	MADGRAPH	PYTHIA	LO
QCD- $WZjj$	SHERPA	SHERPA	NLO
EW- $WZjj$	MADGRAPH	PYTHIA	LO

**Table 8.1.:** List of nominal MC samples used in the  $Z\gamma jj$  analysis. The table provides information on the MC generators used for matrix element and parton showers. It also provides the accuracy of the simulation at the matrix-event level.

### 8.2.2. Background Samples

In the cross-section measurements of EW- $Z\gamma jj$ , the primary background is the QCD- $Z\gamma jj$  process<sup>5</sup>. Two sets of MC samples were used to model this final state:

- i The nominal sample was generated with SHERPA 2.2.11 [67] [68] at NLO QCD with the NNPDF3.0 PDF set. The matching and merging was performed using MEPS@NLO [69] [70] prescription. In this sample, the matrix element included up to one additional parton at NLO and up to three additional partons at LO.
- ii The alternative sample, used for cross-checks, was generated with MADGRAPH5\_AMC@NLO 2.3.3 at NLO QCD with the NNPDF3.0 PDF set. It was interfaced with PYTHIA. In this sample, the matrix element included up to one additional parton at NLO and up to two additional partons at LO.

The second-largest background arises from the  $Z$ +jets process, with one of the jets misidentified as a photon. This sample was generated with POWHEG BOX v1 [71] [72] [73] at NLO QCD with the CT10 [74] PDF set. The sample was interfaced with PYTHIA 8.210 for parton showering, hadronisation and underlying event with the ANZLO tune.

The third largest background originates from  $t\bar{t}\gamma$  process. This sample was generated with MADGRAPH5\_AMC@NLO at LO QCD with the NNPDF 2.3 PDF [75] set. The sample was interfaced with PYTHIA 8.212 with the A14 tune.

The smallest background contribution was evaluated from the  $WZjj$  process. The QCD- $WZjj$  sample was generated with Sherpa 2.2.2 at NLO QCD with the NNPDF3.0 PDF set. The EW- $WZjj$  sample was generated with MADGRAPH5\_AMC@NLO 2.6.2 at LO QCD with the NNPDF3.0 PDF set. It was interfaced with PYTHIA 8.235.

A summary of the nominal MC samples used in the analysis is shown in Table 8.1. All simulated samples were passed through the ATLAS detector simulation based on GEANT4.

<sup>5</sup> It should be noted that in the analysis of  $Z\gamma jj$  process, QCD- $Z\gamma jj$  is the signal too

## Chapter 9.

# Object Reconstruction

The primary goal of the ATLAS detector is to identify and detect particles produced in collisions. Figure 9.1 provides a visual representations of the paths taken by different particles as they traverse the ATLAS detector. However, instead of directly detecting particles, the ATLAS detector operates by capturing and analysing electrical signals generated by its sub-detector systems. As a result, these signals need to be combined in order to create meaningful physics objects, a process referred to as *object reconstruction*.

Different technologies are employed in the sub-detectors, but the resulting measurements can be broadly classified as either spatial hits or energy deposits. This distinction gives rise to four fundamental *low-level objects*: tracks formed from spatial hits, topological clusters or *topo-clusters* formed from energy deposits, vertices constructed by combining tracks, and *particle-flow* objects generated by combining tracks and topo-clusters. The *high-level objects* used in physics analyses, such as electrons or jets, are then formed by combining these low-level objects in various ways.

In this chapter, Section 9.1 provides a description of the reconstruction process for low-level objects, while Section 9.2 delves into the reconstruction of high-level objects specifically

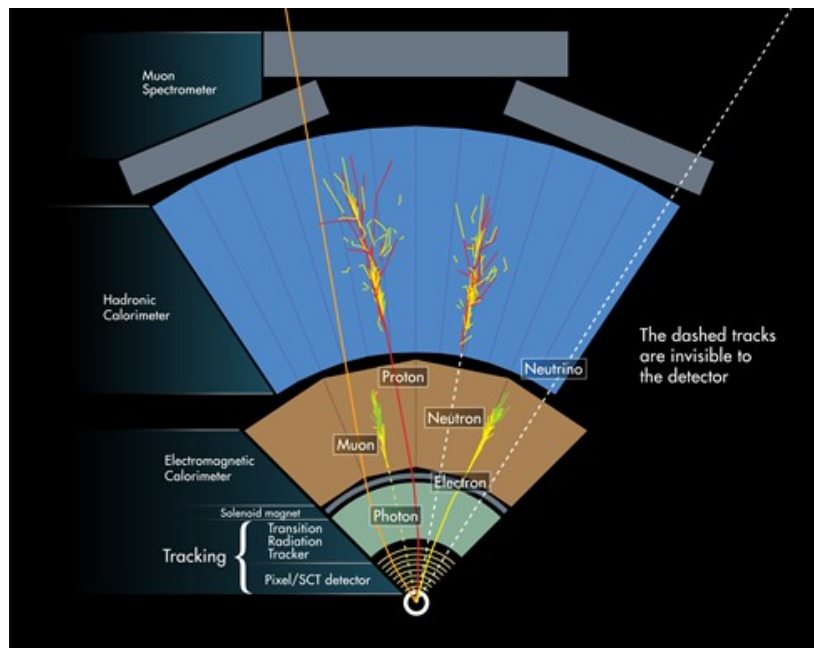


**Figure 9.1.:** Schematic representation of interactions of particles in the ATLAS detector[76]

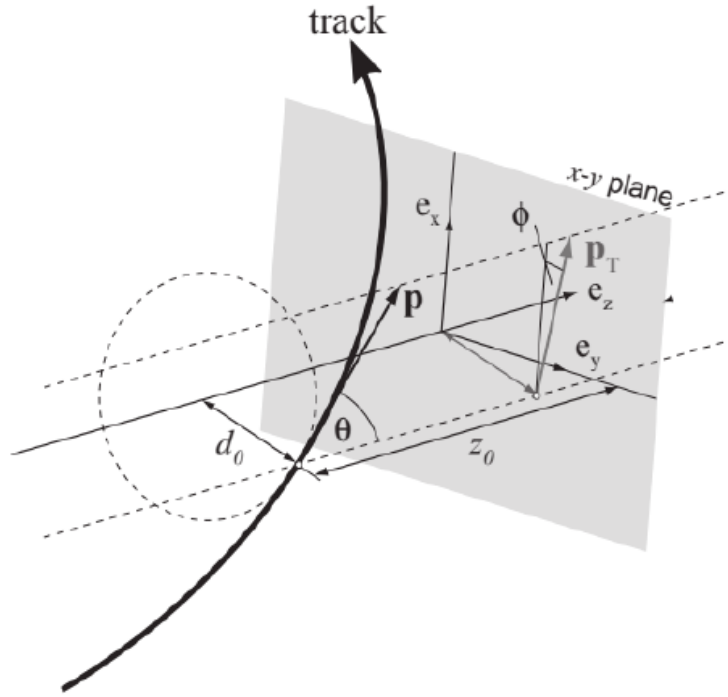


**Figure 9.2.:** The perigee representation of a track in ATLAS

relevant to the  $Z\gamma jj$  analysis. Lastly, Section 9.3 outlines the selection criteria used to identify high-quality objects in the analysis.

## 9.1. Low-Level Objects

### 9.1.1. Tracks

Track reconstruction in the ATLAS detector primarily relies on information obtained from the Inner Detector (ID). Two main tracking algorithms are employed: [77]

- The *inside-out* algorithm starts by identifying hits in the innermost layers of the ID. It then extends the tracks outward into the TRT if consistent hits are found. This algorithm is the default choice for reconstructing high-quality tracks originating from primary interactions in  $pp$  collisions.
- The *outside-in* algorithm is designed to improve the detection efficiency for particles produced farther from the beamline, such as electrons resulting from photon conversion in the detector material. It begins with hits in the TRT and works backward, matching them with Pixel+SCT hits that were not utilized in the inside-out track reconstruction.

Tracks are commonly described using the *perigee representation*, which employs five parameters ( $d_0$ ,  $z_0$ ,  $\phi$ ,  $\theta$ ,  $q/p$ ), as depicted in Figure 9.2. These parameters, determined at the point on the track closest to the interaction vertex, provide important information about the tracks: transverse impact parameter  $d_0$  that represents the distance to the vertex in the  $x - y$  plane, longitudinal impact parameter  $z_0$  that represents the distance to the vertex in the  $z$  plane,

azimuthal angle  $\phi$  and polar angle  $\theta$  of the track, and factor  $q/p$  that denotes the ratio of the particle's electric charge  $q$  to the magnitude of its momentum  $p$ .

### 9.1.2. Vertices

By extrapolating reconstructed tracks, it is possible to identify locations where multiple tracks converge, which are referred to as vertices. There are two types of vertices: *primary vertices* and *secondary vertices*. [77]

Primary vertices (PVs) are defined as the points in space where  $pp$  interactions have taken place. In each bunch crossing, there are typically multiple PVs originating from both the collision of interest and pileup events. The primary vertex associated with the collision of interest is referred to as the *hard-scatter* primary vertex. It is determined by selecting the PV with the highest  $\Sigma p_T^2$  of the associated tracks. This vertex corresponds to the position where the largest momentum transfer occurs, indicating the likely creation point of particles of interest.

On the other hand, secondary vertices arise from the decays of primary particles or interactions with detector material. These vertices are generally located farther away from the primary vertices.

### 9.1.3. Topological Clusters

Topological clusters [78], also referred to as topo-clusters, are formed by grouping together adjacent calorimeter signal cells in three dimensions based on the significance of their energy content relative to the background noise. These clusters are crucial for reconstructing various physics objects like jets, electrons and photons.

It is important to note that individual topo-clusters are not expected to exclusively capture the complete energy deposit of a single particle at all times. Rather, they can represent a partial energy deposit from a single particle, a combined energy deposit from multiple particles, or a combination of both cases. Therefore, the primary aim of the topological clustering algorithm is not to differentiate between energy deposits originating from different particles. Rather, it aims to separate continuous energy deposits and mitigate the impact of noise. Furthermore, the algorithm takes into account the spatial distribution of the cell signals in all three dimensions to determine the directions of the incoming particles as well.

### 9.1.4. Particle-Flow Objects

In Run 1 of the LHC, ATLAS used either the calorimeter or the tracker to reconstruct hadronic jets. However, in Run 2, an enhanced method called particle-flow (PFlow) [79] was introduced which simultaneously combines measurements from both the tracker and calorimeter, taking advantage of their individual strengths. Specifically, the tracker provides improved angular resolution, while the calorimeter offers superior energy resolution. Moreover, the tracker demonstrates better momentum resolution for low-energy charged particles, whereas the calorimeter excels in high-energy particle momentum resolution. As a result, a combination of both subsystems is preferred for optimal jet reconstruction.

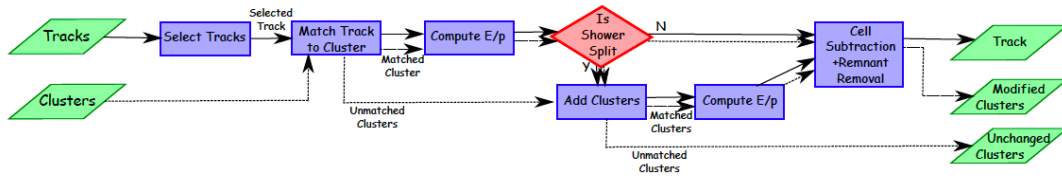


Figure 9.3.: A flow chart of the particle-flow algorithm [79]

Figure 9.3 depicts the schematic of the particle-flow algorithm. First, the algorithm matches a well-measured track to a single topo-cluster. Using the topo-cluster position and the track momentum, the algorithm estimates the expected energy deposited by the particle associated with the track in the calorimeter. However, as mentioned before, it is possible for a single particle to deposit its energy into multiple topo-clusters. Thus, depending on the probability of the energy being distributed among multiple topo-clusters, the algorithm determines whether additional topo-clusters should be added to the track/topo-cluster system to accurately reconstruct the entire particle energy. Subsequently, the expected energy deposited in the calorimeter by the particle that produced the track is subtracted cell-by-cell from the set of matched topo-clusters. Finally, if the remaining energy in the system aligns with the expected fluctuations of a particle’s energy, the remnants of the topo-clusters are eliminated. This last step of cell subtraction and remnant removal ensures that energy information is not double-counted between tracks and topo-clusters.

The output of the algorithm can consist of various particle-flow objects: i) high-quality tracks, which represent charged particles with all their energy deposited in a single topo-cluster, ii) modified clusters, which represent charged particles with their energy spread across multiple topo-clusters, and iii) unchanged clusters, which are not associated with any track and represent neutral particles. These particle-flow objects are used as inputs for jet reconstruction.

## 9.2. High-Level Objects

### 9.2.1. Electrons and Photons

The reconstruction processes for electrons and photons are closely intertwined due to their interactions with the detector material [80]. In particular, electrons can emit bremsstrahlung photons in the ID, while photons can form electron-positron pairs within the ID (*converted photons*). Thus, to handle these interactions, the reconstruction algorithm for electrons and photons combines information from topo-clusters<sup>1</sup> in the calorimeter as well as tracking information from the ID.

A crucial aspect of the reconstruction algorithm is the construction of *superclusters* that encompass the energy cluster of primary electrons/photons and their associated secondary particles. Figure 9.4 illustrates an example of a supercluster, where an electron emits a bremsstrahlung photon due to interactions with the ID material. Thus, the algorithm aims to

<sup>1</sup> A key reason for utilising topo-clusters is their capability to detect and reconstruct low-energy particles, such as bremsstrahlung photons

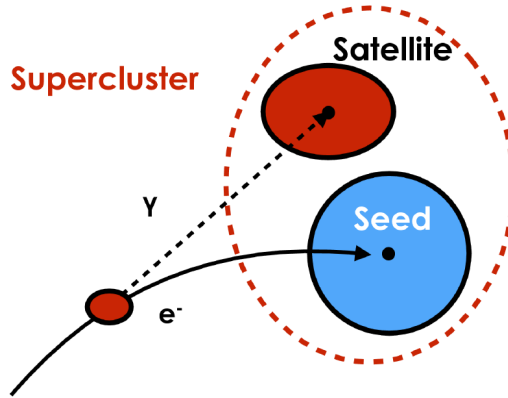


**Figure 9.4.:** A schematic depiction of a supercluster consisting of the seed and a satellite topoclusters originating from an electron and a bremsstrahlung photon, respectively[80]

find and connect the primary topo-cluster from the electron shower (*seed cluster*) with the nearby secondary topo-cluster from the photon shower (*satellite cluster*).

In the final stage of the algorithm, an electron is defined as an object consisting of a supercluster matched to a track, a converted photon is identified by a calorimeter cluster matched to a conversion vertex<sup>2</sup> and an unconverted photon refers to a cluster that does not match either an electron track or a conversion vertex.

### Electron and Photon Calibration

The reconstructed electron and photon candidates are calibrated to compensate for energy losses upstream of the calorimeter, in neighbouring cells of the supercluster, and beyond the LAr calorimeter. A multivariate regression algorithm trained on MC samples is employed for this calibration. However, despite this calibration, discrepancies between data and simulation may persist. To address these differences, an additional calibration step is performed using  $Z \rightarrow ee$  events<sup>3</sup>. Ultimately, the calibration procedure adjusts the energy scale and resolution of electron and photon candidates. [81]

### Electron and Photon Identification

Reconstructed electron candidates suffer large backgrounds from three main sources: misidentified hadrons, photon conversions, and heavy hadron decays. In the case of photon conversions and heavy hadron decays, an actual electron is present in the final state. These electrons are still considered background in the sense that they are not produced in the primary interaction, and are referred to as *non-prompt* electrons.

A likelihood-based identification is used to assess the quality of the reconstructed electron candidate. This likelihood discriminant is built from quantities measured in the ID and calorimeter that assist in distinguishing signal (prompt electrons) from background. From this

<sup>2</sup> A conversion vertex refers to a vertex in the detector where a photon undergoes conversion into an electron-positron pair

<sup>3</sup> The same corrections can be applied to photons. The accuracy of these corrections is confirmed by analysing photons from radiative Z boson decays in the electron and muon channels, and the results exhibit compatibility

discriminant, three *working points* (WPs) of increasing background rejection and decreasing efficiency are designed: **Loose**, **Medium** and **Tight**. The **Medium** WP includes a subset of objects that meet the requirements of the **Loose** WP, while the **Tight** WP comprises a subset of objects that satisfy the criteria of the **Medium** WP. [81]

Similarly, reconstructed photon candidates face backgrounds primarily from non-prompt photons in hadronic jets with a significant electromagnetic (EM) fraction, such as  $\pi^0 \rightarrow \gamma\gamma$  decays. Thus, additional identification requirements are imposed on photon candidates to enhance their purity. This identification process involves placing cuts on calorimeter shower shape variables that can distinguish signal (prompt photons) from background. Similar to electrons, working points are defined for photon identification too. [81]

### Electron and Photon Isolation

In addition to imposing identification requirements, background can be further reduced by using isolation requirements. Prompt electrons/photons can be discriminated from electrons/photons of secondary sources by measuring the amount of hadronic activity around them. They are well-separated without any particles in the vicinity, i.e. are more isolated, compared to non-prompt electrons/photons which are surrounded by jet constituents.

Isolation can be measured using either ID tracks or calorimeter clusters. Track-based isolation sums the  $p_T$  of ID tracks within a cone of size  $\Delta R$  around the electron or photon candidate. Calorimeter-based isolation sums the transverse energy of topoclusters within a cone of size  $\Delta R$  around the candidate. Typically,  $\Delta R = 0.2$  is used for electrons, while  $\Delta R = 0.2$  or  $0.4$  is common for photons. The contributions from the candidates themselves are excluded in both cases. Additionally, calorimeter isolation is corrected for underlying event and pileup contributions. As is customary, various isolation WPs with different efficiencies are defined. [81]

### 9.2.2. Muons

The reconstruction and identification of muons rely on data from all subsystems. Initially, tracks in the Muon Spectrometer (MS) are reconstructed, and their compatibility with the interaction point is verified. Subsequently, a global muon reconstruction is performed, incorporating information from the ID and calorimeters. This results in five distinct reconstruction strategies and muon types [82]:

- **Combined (CB) muons:** CB muons are identified by matching MS tracks to ID tracks and conducting a combined track fit using hits from both the ID and MS. The energy loss in the calorimeters is taken into account during this process.
- **Inside-Out (IO) muons:** IO muons are reconstructed by extrapolating ID tracks to the MS and searching for at least three loosely-aligned MS hits. The ID track, energy loss in the calorimeters, and MS hits are combined in a track fit. This approach recovers efficiency in regions with limited MS coverage and for low- $p_T$  muons.
- **Muon Spectrometer Extrapolated (ME) muons:** ME muons are reconstructed when an MS track cannot be matched to an ID track. This reconstruction strategy enables the reconstruction of muons outside the ID acceptance region. In such cases, the parameters of the MS track are extrapolated to the beamline to determine the muon's properties.

- Segment-Tagged (ST) muons: ST muons are identified by requiring that an ID track matches at least one track segment in the MS. In these cases, the muon parameters are directly obtained from the ID track fit.
- Calorimeter-Tagged (CT) muons: CT muons are identified by extrapolating ID tracks through the calorimeters and searching for energy deposits consistent with those produced by minimum-ionising particles. Similar to ST muons, the muon parameters are directly derived from the ID track fit.

### Muon Identification and Isolation

To select high-quality prompt muons and mitigate backgrounds from non-prompt muons in hadronic decays, reconstructed muon candidates are subjected to identification and isolation requirements. [82]

Non-prompt muons from light hadron decays exhibit poor-quality tracks due to trajectory changes caused by in-flight decay. Consequently, the muon identification algorithm relies on the track quality of muons to differentiate prompt muons from non-prompt ones originating in light hadrons. The algorithm provides different working points with varying efficiencies.

Prompt muons originating from heavy-flavor decays, such as bottom and charm hadrons, possess high-quality tracks that cannot be suppressed using muon identification alone. In such cases, muon isolation plays a crucial role. Isolation can be measured using the inner detector (ID) tracks or calorimeters, with track-based and calorimeter-based isolation defined similarly to electrons and photons. Typically, a radius of  $\Delta R = 0.2$  or  $0.3$  around the muon candidate is used for these isolation variables.

Combining track-based and calorimeter-based isolation tends to yield better results compared to using either one alone, as these variables offer complementary information. Track-based isolation provides higher resolution and is less affected by pileup, while calorimeter-based isolation captures details about neutral particles that track isolation may miss. However, both track and calorimeter isolation redundantly measure hadronic activity due to the detection of charged particles by both systems. To address this redundancy, the particle-flow algorithm is employed to eliminate overlapping contributions and decrease their correlation. The resulting particle-flow-based isolation is obtained by summing track-based isolation and *neutral particle-flow* isolation. Neutral particle-flow isolation involves summing the transverse energy of neutral particle-flow objects within a cone of radius  $\Delta R = 0.2$  around the muon candidate. Additionally, corrections are applied to account for underlying event and pileup contributions.

As with identification, various working points are established for each isolation variable.

### Muon Calibration

Muon momentum depends significantly on various factors, including the alignment of the ID and MS, the distribution and composition of material within the tracking volume, and the accuracy of the magnetic field knowledge. While dedicated procedures are applied to correct the detector alignment, residual misalignments may introduce a bias in the momentum measurement. To account for and rectify this bias, extensive samples of  $Z \rightarrow \mu\mu$  decays are utilised. Despite these calibration efforts, discrepancies between the observed data and theoretical simulation may persist. To address these discrepancies, an additional calibration step is conducted, employing  $Z \rightarrow \mu\mu$  and  $J/\Psi \rightarrow \mu\mu$  events. Only CB muons are utilised to

extract the necessary calibration parameters. Ultimately, the calibration procedure adjusts the momentum scale and resolution of muon candidates. [83]

### 9.2.3. Jets

According to QCD, particles such as quarks and gluons, which carry color charge, cannot be observed isolated. Instead, they undergo hadronisation and convert into color-neutral hadrons. These hadrons then decay and break apart into multiple particles that are tightly concentrated in a narrow cone aligned with the original parton direction. In experimental physics, these collimated particle sprays are reconstructed as composite structures called *jets*.

Jet reconstruction algorithms are designed to group together the particles produced during the hadronisation process and extract information about the properties of the initial parton. These algorithms utilise specialized clustering techniques that must meet the criteria of being both infrared and collinear (IRC) safe. Infrared safety ensures that the algorithm remains unchanged when additional soft<sup>4</sup> radiation, such as a low- $p_T$  particle, is added. Collinear safety ensures that the reconstruction of a jet is not affected by the inclusion of a particle closely aligned with the jet's direction.

In this analysis, the anti- $k_T$  algorithm [84] [85] is employed to reconstruct the jets. The input to the algorithm consists of particle-flow objects. The algorithm relies on the following defined quantities:

$$d_i = \frac{1}{p_{Ti}^2} \quad \text{and} \quad d_{ij} = \min \left( \frac{1}{p_{Ti}^2}, \frac{1}{p_{Tj}^2} \right) \frac{\Delta R_{ij}^2}{R^2} \quad (9.1)$$

Here,  $i$  and  $j$  represent indices of particle-flow objects,  $\Delta R_{ij}^2 = \Delta\phi_{ij}^2 + \Delta y_{ij}^2$ , and  $R$  denotes a fixed parameter known as the jet radius. Typically,  $R = 0.4$  is used for quark and gluon jets, while  $R = 1.0$  is used for jets from hadronically decaying massive particles. The algorithm initiates by identifying all possible pairs of input objects and their distances computed based on the aforementioned metrics. If  $d_{ij} < d_i$ , the objects  $i$  and  $j$  are combined and removed from the input collection, while the combined object is added as a new input. Conversely, if  $d_{ij} > d_i$ , the object  $i$  is selected as a jet and removed from the input collection. This iterative process continues, recomputing distances  $d_{ij}$  and  $d_i$  at each step, until no further combinations are possible.

### Jet Calibration

Reconstructed jet candidates undergo calibration to address detector effects and minimise pileup contamination. The calibration process involves multiple steps<sup>5</sup>, starting with pileup correction using an area-based subtraction method. Subsequently, an MC-based calibration is employed to align the energy and  $\eta$  of reconstructed jet candidates with those of truth-level jets<sup>6</sup>. This calibration compensates for various effects, such as energy losses in inactive detector regions, incomplete energy reconstruction in the calorimeters and biases in  $\eta$  reconstruction caused by transitions between different calorimeter technologies and changes in calorimeter

<sup>4</sup> In QCD, soft interactions occur at low energies with low-momentum exchanges, while hard interactions occur at high energies with high-momentum exchanges.

<sup>5</sup> The calibration procedure described in this thesis is applicable to jets with  $R = 0.4$

<sup>6</sup> Truth-level jets refer to the simulated jets in which detector effects are not taken into account

granularity. Despite these calibrations, the jet response<sup>7</sup> remains influenced by factors such as shape, flavor, and quark-gluon distinctions. Thus, multiplicative corrections are applied to mitigate these dependencies. This step is known as Global Sequential Calibration (GSC). Additionally, an in-situ calibration using  $Z$ +jet,  $\gamma$ +jet, and multi-jet events is performed to further account for discrepancies between data and simulation. Ultimately, the calibration procedure adjusts the jet energy scale (JES) and jet energy resolution (JER). [86]

### Jet Cleaning

Reconstructed jet candidates undergo *jet cleaning* to differentiate jets produced in proton-proton collisions from background. The primary sources of background for collision jets include beam-induced background resulting from proton losses before the interaction point, cosmic-ray showers that coincide with collisions, and calorimeter noise.

Jet cleaning algorithms utilise three categories of variables to discriminate between collision jets and background. These categories are based on electronic signal pulse shape in the LAr calorimeters, energy ratio variables, and track-based variables. Pulse shape variables are effective in distinguishing noise in the LAr calorimeters. The energy ratio variable and track-based variables are able to reject calorimeter noise in the LAr and Tile calorimeters, as well as mitigating beam-induced background and cosmic muon showers. The algorithms provide various working points which correspond to different levels of background rejection. [87]

#### 9.2.3.1. Jet Vertex Tagger

In the process of calibrating jets, the average energy from pileup interactions is subtracted using the jet area. However, variations in local pileup can still create spurious jets. To minimise the impact of pileup interactions, the *Jet Vertex Tagger* (JVT) is applied to reconstructed jet candidates. JVT utilises a likelihood discriminant that analyses the tracks linked to the jets, differentiating between jets originating from the hard scatter process and those from pileup. It provides multiple working points for optimisation purposes. [88]

Since JVT relies on tracks, it can only be used for jets within the acceptance of the inner detector. Therefore, to handle pileup jets in the forward regions, the *Forward Jet Vertex Tagger* (fJVT) is employed. The reconstruction of jets affected by pileup involves two types: QCD jets, originating from a single pileup interaction, and stochastic jets, formed by combining particles from multiple vertices. In the forward region, QCD pileup jets are prevalent and tend to occur in pairs with opposite directions in the transverse plane due to the conservation of transverse momentum. Exploiting this dijet correlation enables the identification of QCD pileup jets, which forms the basis of the fJVT algorithm. [89]

In order to account differences in data and simulation, the hard-scatter jet efficiency for both JVT and fJVT is calibrated using  $Z(\rightarrow \mu\mu)$ +jets events.

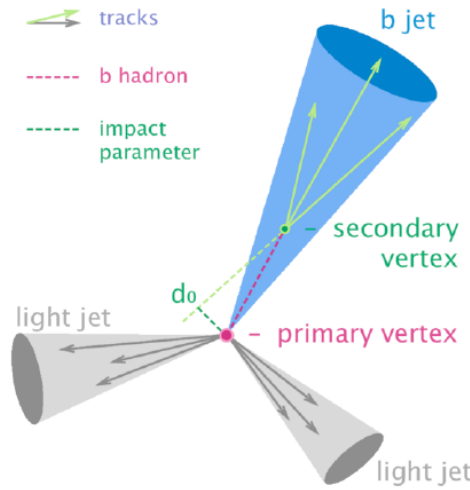


**Figure 9.5.:** A diagram showing the distinct decay geometry of a  $b$ -jet.

### 9.2.3.2. $b$ -Tagger

Jets that contain  $b$ -hadrons are referred to as  $b$ -jets, and the process of identifying them is called  $b$ -tagging.  $b$ -tagging algorithms exploit the distinctive experimental properties of  $b$ -hadrons, as seen in Figure 9.5. These particles have a relatively long lifetime, leading to the presence of secondary vertices and tracks with high impact parameters.  $b$ -hadrons also possess a larger mass, resulting in wider and heavier jets compared to jets originating from light-flavor particles. Additionally, the decay properties of  $b$ -hadrons increase the probability of detecting muons within the jet.

The  $b$ -tagging process involves two steps. Initially, low-level algorithms based on track impact parameters, displaced vertices or reconstruction of the  $b$ -hadron decay chain are employed. The outputs of these algorithms serve as inputs for high-level algorithms, which employ multivariate techniques like boosted decision tree or deep feed-forward neural network algorithms. These multivariate algorithms classify reconstructed jet candidates as  $b$ -jets,  $c$ -jets, or light-flavor jets, with various working points available to achieve different efficiencies in  $b$ -tagging. [90]

### $b$ -Tagging Calibration

Discrepancies in the efficiency of  $b$ -tagging between data and simulation can stem from challenges in theoretical and detector modeling. To address this, the  $b$ -tagging efficiency is calibrated by utilizing leptonic decays of  $t\bar{t}$ , which are known to contain a higher number of  $b$ -jets. In a similar manner, the mis-tagging rates of  $c$ -jets and light-flavor jets also require calibration. The mis-tagging rate of  $c$ -jets is calibrated using semi-leptonic decays of  $t\bar{t}$ , while the mis-tagging rate of light-flavor jets is calibrated using  $Z$ +jets events. [91]

<sup>7</sup> The jet response is typically quantified by comparing the energy or  $\eta$  of a reconstructed jet to that of a truth-level jet

### 9.3. Object Selection

In 2021, the ATLAS collaboration released fiducial cross-section measurements for the EW- $Z\gamma jj$  and total  $Z\gamma jj$  processes, utilising the complete Run-2 dataset [92]. This current analysis replicates the same task, incorporating enhanced Monte Carlo samples and refined analysis techniques to improve measurement accuracy and precision. As a result, the object selection criteria in this analysis draw inspiration from those applied in [92].

This section delineates the object selection criteria optimised for the current analysis. It is important to note that both data and detector-level Monte Carlo simulation samples are subject to the same object selection criteria.

The selection criteria for lepton and photon candidates in the analysis are presented in Table 9.1. Both converted and unconverted photons are considered for photon candidates. Notably, electron and photon candidates are excluded from the transition region between the barrel and endcap electromagnetic calorimeters ( $1.37 < |\eta| < 1.52$ ). Additionally, electron and muon candidates, being prompt particles, are required to originate from the hard-scatter primary vertex, leading to constraints on their transverse  $d_0$  and longitudinal  $z_0$  impact parameters.

In terms of isolation criteria, electron and photon candidates are evaluated using the working points [81] defined in Table 9.2. For muon candidates, the particle-flow-based isolation method described in Section 9.2 is utilised, and the corresponding working point [82] is defined in Table 9.3.

Efficiency studies reveal the performance of the candidate selection. Figure 9.6 shows that the isolation efficiency of electron candidates with **Medium** ID WP, for  $p_T > 20$  GeV, exceeds 95% (indicated by the green line). Similarly, Figure 9.7 demonstrates that the efficiency of photon candidates with **Tight** ID WP, for  $p_T > 25$  GeV, is above 85%. Additionally, Figure 9.8 highlights that the efficiency of muon candidates with **Medium** ID WP, for  $p_T > 20$  GeV, surpasses 90%.

The selection criteria for jet candidates are provided in Table 9.4. They are clustered using the anti- $k_T$  algorithm with a radius parameter of  $\Delta R = 0.4$ . Jet candidates with  $p_T < 60$  GeV and  $|\eta| < 2.4$  are required to originate from the hard-scatter primary vertex. To ensure this, the **Tight** working point [93] of the jet vertex tagging (JVT) algorithm is employed in this analysis. Additionally, jet candidates must satisfy the *LooseBad* jet cleaning criteria [87]. Furthermore, jet candidates in the central region ( $|\eta| < 2.5$ ) that contain  $b$ -hadrons are identified using the **DL1r** deep neural network discriminant with a 70%  $b$ -tagging efficiency working point [90].

	Electrons	Photons	Muons
$p_T$	$>20$ GeV	$>25$ GeV	$>20$ GeV
$ \eta $	$<2.47$	$<2.37$	$<2.5$
	veto transition region	veto transition region	
Impact Parameter	$d_0/\sigma(d_0) < 5$		$d_0/\sigma(d_0) < 3$
	$ z_0 \sin\theta  < 0.5$ mm		$ z_0 \sin\theta  < 0.5$ mm
Identification	Medium	Tight	Medium
Isolation	Loose	Loose	PflowLoose

**Table 9.1.:** Object selection criteria for leptons and photons

Working Point	Calorimeter Isolation	Track Isolation
Electron Loose	$E_T^{cone20}/p_T < 0.20$	$p_T^{cone20}/p_T < 0.15$
Photon Loose	$E_T^{cone20}/E_T < 0.065$	$p_T^{cone20}/E_T < 0.05$

**Table 9.2.:** Definition of photon and electron isolation working points [81] Here, *cone20* corresponds to cone of  $\Delta R = 0.2$  around the candidate.

Working Point	Definition	Track $p_T$
PflowLoose	$(p_T^{varcone30} + 0.4 \cdot E_T^{neflow20}) < 0.16 \cdot p_T^\mu$	$p_T > 500$ MeV

**Table 9.3.:** Definition of muon isolation working point [82] Here, *cone30* corresponds to cone of  $\Delta R = 0.3$  around the candidate, and *neflow20* is a cone of neutral particle-flow objects of  $\Delta R = 0.2$ .

	Jets
$p_T$	$>25$ GeV
$ \eta $	$<4.4$
Jet Cleaning	LooseBad
JVT	Tight for jets in $ \eta  < 2.4$ and $p_T < 60$ GeV
$b$ -tagging	DL1r, $\epsilon_b = 70\%$ for jets with $ \eta  < 2.5$

**Table 9.4.:** Object selection criteria for jets

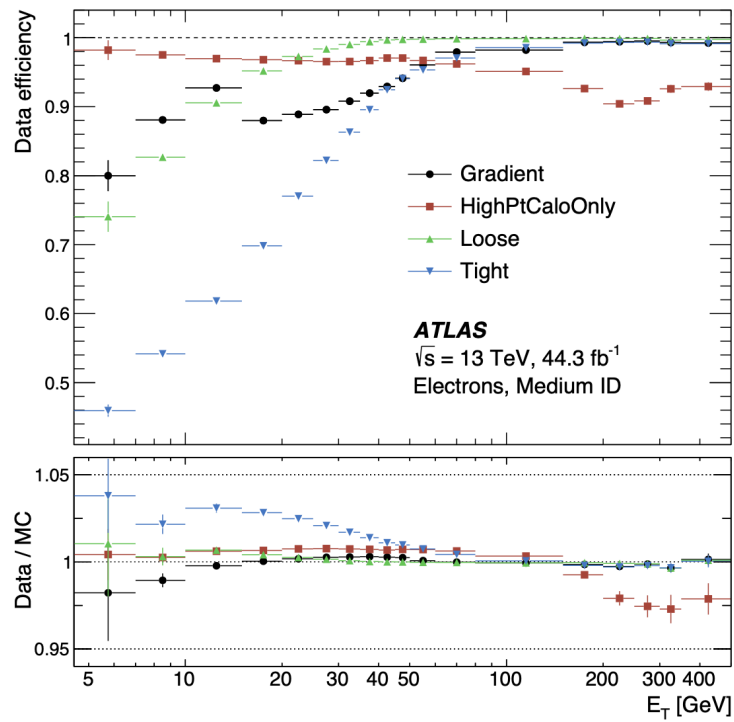


**Figure 9.6.:** Efficiency of the different isolation working points for electrons from inclusive  $Z \rightarrow ee$  events as a function of the electron transverse energy  $E_T$ . The electrons are required to fulfil the **Medium** selection from the likelihood-based electron identification. The lower panel shows the ratio of the efficiencies measured in data and in MC simulations. The total uncertainties are shown, including the statistical and systematic components.[81]

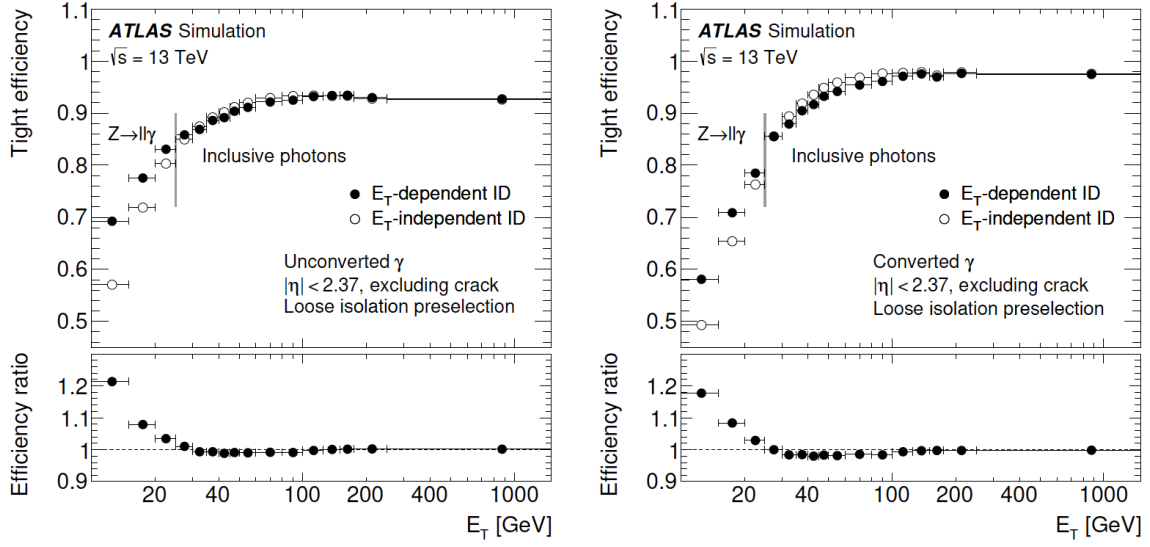


**Figure 9.7.:** Efficiencies of the **Tight** photon identification for unconverted (left) and converted (right) signal photons, plotted as a function of photon  $E_T$ . The signal events are taken from the sample of  $Z \rightarrow ll\gamma$  photons with  $E_T < 25$  GeV, and from inclusive-photon production above 25 GeV. In each case, the  $E_T$ -independent and  $E_T$ -dependent selections are compared. The **Loose** isolation is applied as a preselection. For both plots, the bottom panel shows the ratios between the  $E_T$ -dependent and  $E_T$ -independent identification efficiencies.[81]

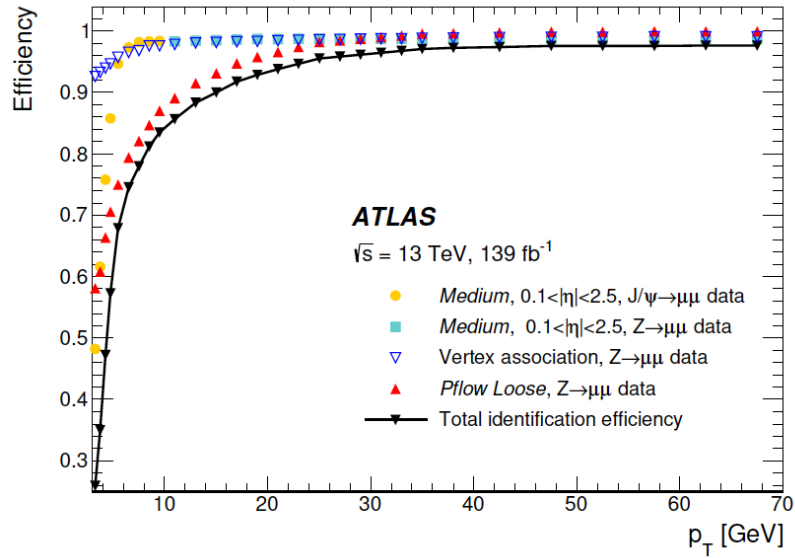


**Figure 9.8.:** Overall efficiency measured in data with  $Z \rightarrow \mu\mu$  and  $J/\psi \rightarrow \mu\mu$  decays. The total efficiency for satisfying simultaneously the **Medium** identification, **PflowLoose** isolation and vertex association criteria (black line) is shown together with its separate components (coloured markers). Here, vertex association criteria refers to the requirements imposed on the impact parameters to reject muons not originating from the hard-scatter primary vertex.[82]

It is possible that the tracks or energy deposits from a single particle can be reconstructed as two different objects. Thus, an overlap removal procedure is implemented to avoid the double-counting of analysis objects. In all cases, the object reconstructed with a poorer efficiency is removed as follows:

- If a jet and an electron are reconstructed within a distance of  $\Delta R = 0.2$  from each other, the jet is removed.
- If a jet and a photon are reconstructed within  $\Delta R = 0.4$  of each other, the jet is removed.
- If a lepton (electron or muon) and a jet are reconstructed within  $\Delta R = 0.4$  of each other, the lepton is removed.
- If a photon and a lepton (electron or muon) are reconstructed within  $\Delta R = 0.4$  of each other, the photon is removed.
- If a muon and an electron are reconstructed within  $\Delta R = 0.2$  of each other, the electron is removed.

# Chapter 10.

## Uncertainties

Every measurement is subject to two types of uncertainties: statistical and systematic. Statistical uncertainties arise from the limited size of the datasets and are associated with the inherent randomness in the observed events. These uncertainties are quantified by the standard error of a Poisson distribution, reflecting the fluctuations in the data.

In contrast, systematic uncertainties encompass various sources of uncertainty in the analysis that are not due to statistical fluctuations. These uncertainties can manifest at different stages of the analysis process, including the use of theoretical models in simulations (commonly referred to as *theoretical uncertainty*) and the reconstruction of objects and calibration of the detector (referred to as *experimental uncertainty*). Furthermore, systematic uncertainties can also arise due to the finite number of events available in simulations.

In this chapter, Section 10.1 provides an overview of the experimental systematic uncertainties, while Section 10.2 discusses the theoretical systematic uncertainties specifically related to the  $Z\gamma jj$  process. It is important to highlight that the uncertainties detailed in this chapter, along with their naming convention, adhere to ATLAS-wide guidelines.

### 10.1. Experimental Uncertainties

A description of experimental uncertainties is summarised below:

- **Luminosity** Dedicated detectors like LUCID-2 measure the LHC’s instantaneous luminosity during data-taking. To achieve absolute luminosity, an annual van der Meer beam separation scan is performed, where proton beams are deliberately displaced from their normal position in the horizontal and vertical planes. This method led ATLAS to determine the integrated luminosity for the Run 2 dataset as  $140 \text{ fb}^{-1}$  with an uncertainty of 0.83% [94], establishing the most precise luminosity measurement at a hadron collider to date. This is vital for achieving high precision in production cross-section studies.
- **PRW\_DATASF** The distribution of the proton-proton collisions per bunch crossing is modelled in the simulation and needs to be corrected to match the data. The pileup re-weighting procedure determines scale factors to account for these differences, and the associated uncertainty is provided by the ATLAS PileupReweighting analysis tool [95]. In this analysis, the relative uncertainty<sup>1</sup> is about 2% for the EW- $Z\gamma jj$  and QCD- $Z\gamma jj$  samples.

---

<sup>1</sup> Relative uncertainty = (systematic-nominal)/nominal  $\times 100$

- 1. **EG** These uncertainties arise from the calibration of electrons and photons, encompassing uncertainties in the energy scale and resolution [81]. The names and sources of these uncertainties are presented in Table 10.1.
- 2. **EL\_EFF** These uncertainties are associated with the trigger, reconstruction, identification, and isolation efficiencies of electrons [81], as depicted in Table 10.1.
- 3. **PH\_EFF** These uncertainties are associated with the trigger, identification, and isolation efficiencies of photons [81], as illustrated in Table 10.1.

These uncertainties have been grouped and depicted in red in Figure 10.1.

- **MUON** These uncertainties stem from the muon reconstruction, identification, isolation, and calibration [82]. They are detailed in Table 10.2 and represented in blue in Figure 10.1.
- **JET** These uncertainties arise from the reconstruction and calibration of jets. They encompass the uncertainties in the jet energy scale (JES) and jet energy resolution (JER) [86]. The details are presented in Table 10.3 and portrayed in pink in Figure 10.1. It can be seen that jet-related uncertainties are the largest source of experimental systematic in this analysis.
- **FT\_EFF** These uncertainties pertain to the reconstruction and calibration of  $b$ -jets. They include the uncertainties in the  $b$ -tagging efficiency and the mis-tag rate [90]. The specifics are outlined in Table 10.4 and represented in green in Figure 10.1.

It should be noted that **Luminosity** affects all signal and background processes, while the rest of the experimental systematic uncertainties affect EW- $Z\gamma jj$  and QCD- $Z\gamma jj$  processes only.

## 10.2. Theoretical Uncertainties

The theoretical uncertainties affecting the EW- $Z\gamma jj$  process are summarised as follows:

- **SCALE\_EW** The theoretical cross section depends on the renormalisation ( $\mu_R$ ) and factorisation ( $\mu_F$ ) scales.<sup>2</sup> To evaluate the uncertainty associated with these scales, the  $\mu_R$  and  $\mu_F$  parameters of the nominal MADGRAPH5\_AMC@NLO 2.6.5 sample were modified by factors of 0.5 and 2.0, while adhering to the constraint  $0.5 \leq \mu_R/\mu_F \leq 2$ . The scale uncertainty was assessed by considering the maximum change in the distribution shapes.
- **PDF\_EW** The theoretical cross section depends on parton distribution functions (PDFs), which describe the momentum fraction carried by partons in the proton. To quantify the uncertainty arising from the choice of the nominal NNPDF3.1 PDF set, predictions from various PDF sets were compared following the PDF4LHC guidelines [96].
- **PS and UE** The choice of the parton showering model, such as PYTHIA 8.240 in the nominal sample, introduces an uncertainty. To estimate this uncertainty, an alternative sample was generated using the HERWIG ++ 2.7.1 [97] [98] showering algorithm

<sup>2</sup> According to the factorization theorem in QCD, the theoretical cross section can be split into perturbative and non-perturbative parts. Perturbative calculations use perturbation theory, while non-perturbative effects are described by PDFs. The factorization scale sets the boundary between these two components. Additionally, the renormalization scale is used to address divergences in perturbative QCD calculations.

while keeping the `MADGRAPH5_AMC@NLO 2.6.5` matrix element generator constant. The uncertainties associated with parton showering and underlying events are considered uncorrelated.

- **INT** The interference between the  $\text{EW-}Z\gamma jj$  and  $\text{QCD-}Z\gamma jj$  processes was evaluated at LO precision using the `MADGRAPH5_AMC@NLO 2.3.3` event generator with the `NNPDF3.0` LO PDF set. This computation included all relevant diagrams at order  $\alpha_S \alpha_{EW}^3$ . The resulting interference effects were found to be positive and contributed approximately 7% [99] to the  $\text{EW-}Z\gamma jj$  cross-section within the studied phase space. Consequently, this effect was incorporated as a systematic uncertainty in the  $\text{EW-}Z\gamma jj$  prediction.

Figure 10.2 provides a visualisation of all the uncertainties discussed above. It can be seen that the most significant source of theoretical systematic uncertainty for the  $\text{EW-}Z\gamma jj$  process in the signal region of this analysis is the EW scale uncertainty.

The theoretical uncertainties affecting the  $\text{QCD-}Z\gamma jj$  process are summarised as follows:

- **SCALE\_QCD** Similar to the  $\text{EW-}Z\gamma jj$  signal sample, uncertainties related to the choice of  $\mu_R$  and  $\mu_F$  parameters of the nominal `Sherpa 2.2.11` sample were assessed by varying them within a reasonable range.
- **PDF\_QCD** The uncertainty associated with the selection of the nominal `NNPDF3.0` PDF set was estimated by comparing predictions obtained from different PDF sets according to the standard `PDF4LHC` prescription.
- **CKKW and QSF** To account for uncertainties arising from the matching between matrix elements and the parton shower, variations in the merging (CKKW) and resummation (QSF) scales were considered. The nominal sample, which uses the `Sherpa 2.2.11` generator and the `NNPDF3.0` PDF set, employed a CKKW merging cut (QCUT<sup>3</sup>) of 20 GeV and a resummation scale QSF<sup>4</sup> of 1. Additional samples, also generated with the `Sherpa 2.2.11` generator and the `NNPDF3.0` PDF set, were created with QCUT values of 15 GeV and 30 GeV for merging variations, and QSF values of 0.25 and 4 for resummation scale variations.

Again, all these uncertainties are illustrated in Figure 10.3, with the QCD scale uncertainty being the most significant source for the  $\text{QCD-}Z\gamma jj$  process in this analysis.

<sup>3</sup> QCUT indicates the scale for the calculation of the overlap between jets from the matrix element and the parton shower

<sup>4</sup> QSF represents the scale used for the resummation of the soft gluon emissions

Uncertainty	Description
EG_SCALE_ALL	Electron/photon energy scale
EG_SCALE_AF2	Electron/photon energy scale
EG_RESOLUTION_ALL	Electron/photon resolution
EL_EFF_Trigger_TOTAL_1NPCOR_PLUS_UNCOR	Electron trigger efficiency
EL_EFF_TriggerEff_TOTAL_1NPCOR_PLUS_UNCOR	Electron trigger efficiency
EL_EFF_Reco_TOTAL_1NPCOR_PLUS_UNCOR	Electron reconstruction efficiency
EL_EFF_ID_TOTAL_1NPCOR_PLUS_UNCOR	Electron identification efficiency
EL_EFF_Iso_TOTAL_1NPCOR_PLUS_UNCOR	Electron isolation efficiency
PH_EFF_TRIGGER_Uncertainty	Photon trigger efficiency
PH_EFF_ID_Uncertainty	Photon identification efficiency
PH_EFF_ISO	Photon isolation efficiency

**Table 10.1.:** Electron and photon experimental uncertainties [81]

Uncertainty	Description
MUON_SCALE	Muon momentum scale
MUON_SAGITTA_RHO	Muon momentum scale
MUON_SAGITTA_RESBIAS	Muon momentum scale
MUON_ID	Muon resolution
MUON_MS	Muon resolution
MUON_EFF_TrigStatUncertainty	Muon trigger efficiency
MUON_EFF_TrigSystUncertainty	Muon trigger efficiency
MUON_EFF_RECO_STAT	Muon reconstruction efficiency
MUON_EFF_RECO_STAT_LOWPT	Muon reconstruction efficiency
MUON_EFF_RECO_SYS	Muon reconstruction efficiency
MUON_EFF_RECO_SYS_LOWPT	Muon reconstruction efficiency
MUON_EFF_ISO_SYS	Muon isolation efficiency
MUON_EFF_ISO_STAT	Muon isolation efficiency
MUON_EFF_TTVA_STAT	Muon track-to-vertex association efficiency
MUON_EFF_TTVA_SYS	Muon track-to-vertex association efficiency

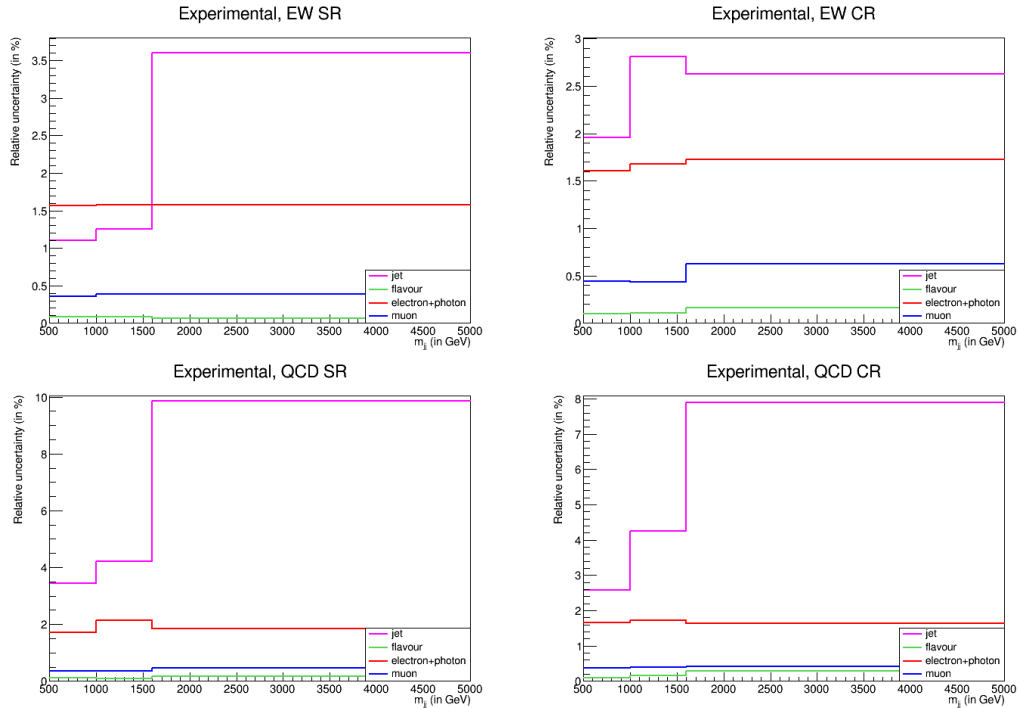
**Table 10.2.:** Muon experimental uncertainties [82]

<sup>5</sup>Punch-through jets are jets whose showers extend beyond the calorimeters

Uncertainty	Description
JET_EffectiveNP_1	Jet Energy Scale
JET_EffectiveNP_2	Jet Energy Scale
JET_EffectiveNP_3	Jet Energy Scale
JET_EffectiveNP_4	Jet Energy Scale
JET_EffectiveNP_5	Jet Energy Scale
JET_EffectiveNP_6	Jet Energy Scale
JET_EffectiveNP_7	Jet Energy Scale
JET_EffectiveNP_8restTerm	Jet Energy Scale
JET_EtaIntercalibration_Modelling	Jet Energy Scale ( $\eta$ calibration)
JET_EtaIntercalibration_TotalStat	Jet Energy Scale ( $\eta$ calibration)
JET_EtaIntercalibration_NonClosure_highE	Jet Energy Scale ( $\eta$ calibration)
JET_EtaIntercalibration_NonClosure_negEta	Jet Energy Scale ( $\eta$ calibration)
JET_EtaIntercalibration_NonClosure_posEta	Jet Energy Scale ( $\eta$ calibration)
JET_EtaIntercalibration_NonClosure_2018data	Jet Energy Scale ( $\eta$ calibration)
JET_Pileup_OffsetMu	Jet Energy Scale (pileup)
JET_Pileup_RhoTopology	Jet Energy Scale (pileup)
JET_Pileup_OffsetNPV	Jet Energy Scale (pileup)
JET_Pileup_PtTerm	Jet Energy Scale (pileup)
JET_Flavor_Composition	Jet Energy Scale (jet flavor)
JET_Flavor_Response	Jet Energy Scale (jet flavor)
JET_BJES_Response	Jet Energy Scale ( $b$ -jet flavour)
JET_JvtEfficiency	Jet Energy Scale (JVT)
JET_fJvtEfficiency	Jet Energy Scale (fJVT)
JET_SingleParticle_HighPt	Jet Energy Scale (single-particle high $p_T$ )
JET_PunchThrough_MC16	Jet Energy Scale (punch-through <sup>5</sup> )
JET_JER_EffectiveNP_1	Jet Energy Resolution
JET_JER_EffectiveNP_2	Jet Energy Resolution
JET_JER_EffectiveNP_3	Jet Energy Resolution
JET_JER_EffectiveNP_4	Jet Energy Resolution
JET_JER_EffectiveNP_5	Jet Energy Resolution
JET_JER_EffectiveNP_6	Jet Energy Resolution
JET_JER_EffectiveNP_7restTerm	Jet Energy Resolution
JET_JER_DataVsMC_MC16	Jet Energy Resolution

Table 10.3.: JES and JER experimental uncertainties [86]

Uncertainty	Description
FT_EFF_Eigen_Light_0	$b$ -tagging efficiency (light flavour jet)
FT_EFF_Eigen_Light_1	$b$ -tagging efficiency (light flavour jet)
FT_EFF_Eigen_Light_2	$b$ -tagging efficiency (light flavour jet)
FT_EFF_Eigen_Light_3	$b$ -tagging efficiency (light flavour jet)
FT_EFF_Eigen_Light_4	$b$ -tagging efficiency (light flavour jet)
FT_EFF_Eigen_C_0	$b$ -tagging efficiency ( $c$ -jet)
FT_EFF_Eigen_C_1	$b$ -tagging efficiency ( $c$ -jet)
FT_EFF_Eigen_C_2	$b$ -tagging efficiency ( $c$ -jet)
FT_EFF_Eigen_C_3	$b$ -tagging efficiency ( $b$ -jet)
FT_EFF_Eigen_B_0	$b$ -tagging efficiency ( $b$ -jet)
FT_EFF_Eigen_B_1	$b$ -tagging efficiency ( $b$ -jet)
FT_EFF_Eigen_B_2	$b$ -tagging efficiency ( $b$ -jet)
FT_EFF_extrapolation	$b$ -tagging efficiency (high $p_T$ jet)
FT_EFF_extrapolation_from_charm	$b$ -tagging efficiency ( $\tau$ jet)

Table 10.4.:  $b$ -tagging efficiency experimental uncertainties [90]Figure 10.1.: Experimental uncertainties for the EW- $Z\gamma jj$  process (left) and QCD- $Z\gamma jj$  process (right) as a function of the mass of the two tagging jets. The top row represents the relative uncertainty in the signal region, while the bottom row corresponds to the control region for the EW- $Z\gamma jj$  analysis.

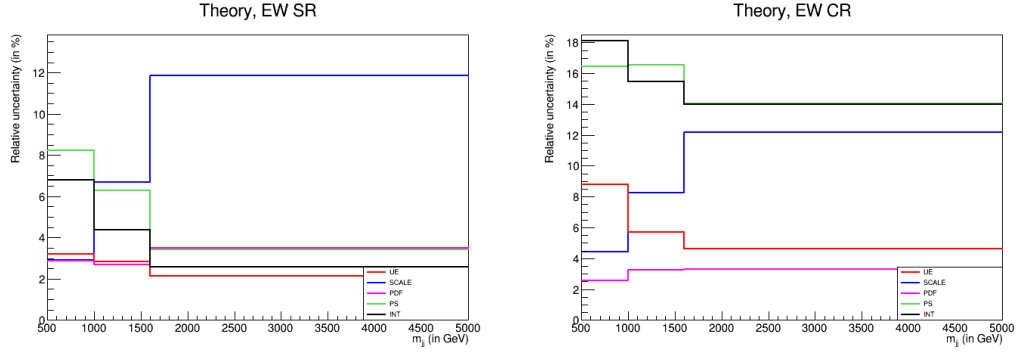


**Figure 10.2.:** Theoretical uncertainties for the EW- $Z\gamma jj$  process as a function of the mass of the two tagging jets. The left plot represents the relative uncertainty in the signal region, while the right plot corresponds to the control region for the EW- $Z\gamma jj$  analysis.

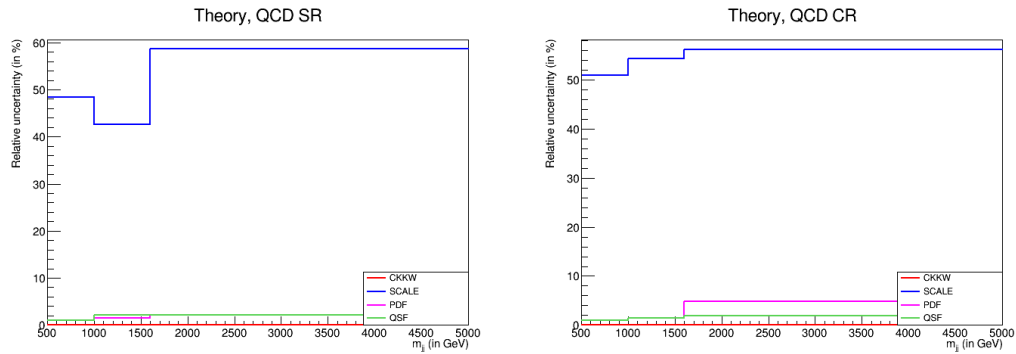


**Figure 10.3.:** Theoretical uncertainties for the QCD- $Z\gamma jj$  process as a function of the mass of the two tagging jets. The left plot represents the relative uncertainty in the signal region, while the right plot corresponds to the control region for the EW- $Z\gamma jj$  analysis.

# Chapter 11.

## Analysis Strategy

As discussed in Section 7.3, the main objective of this analysis is to observe the  $\text{EW-}Z\gamma jj$  process, with a focus on maximising the signal-to-background ratio. Therefore, the main strategies implemented in this analysis are centred around minimising the contribution of background events.

The first step employed to reduce background involves applying specific selection criteria to the collision events that favour the signal, as explained in Section 11.1.

While MC simulations are utilised to estimate the contributions from background events (as stated in Section 8.2), the shape and size of the predicted distributions and their associated modelling uncertainties are significant and not entirely reliable on their own. As a result, alternative methods are employed to extract the main backgrounds directly from the experimental data itself, since they offer a more robust estimation. Thus, the second step involves estimating the backgrounds, as elaborated in Section 11.2. This section also discusses the background systematic uncertainties.

It should be noted that the implementation of event selection and background estimation techniques aligns with those used in the earlier ATLAS analysis [92], but adapted to the updated MC samples.

The final step involves a meticulous choice of measurement regions, considering both background modelling and the signal-to-background ratio. This process, detailed in Section 11.3, was developed in this thesis work.

### 11.1. Event Selection

As described in Section 3.2, due to the impracticality of storing all recorded events from collisions, ATLAS employs various triggers to select specific final state objects. In this analysis, the focus is on the final state with two leptons. Therefore, un-prescaled single and di-lepton triggers were utilised to record the collision events [100] [101].

These triggers, with transverse momentum thresholds dependent on lepton flavor and running period, are outlined in Table 11.1. Specifically, in 2015, the transverse momentum ( $p_T$ ) thresholds for single electron and muon triggers were set at 24 GeV and 20 GeV, respectively. In subsequent years, these thresholds were adjusted to 26 GeV for both lepton flavors. To enhance data-taking efficiency, additional single-lepton triggers with higher  $p_T$  thresholds but more relaxed identification criteria were also incorporated. Additionally, in 2015, events with a pair of electron candidates with  $p_T > 12$  GeV, or a pair of muon candidates meeting  $p_T >$

18 GeV for the leading muon and  $p_T > 8$  GeV for the subleading muon, were selected at the trigger level. In the following years, these dilepton trigger thresholds were increased to 24 GeV for dielectron events and 22 GeV for the leading muon and 8 GeV for the subleading muon in dimuon events. The trigger efficiency for events satisfying all the described selection criteria is approximately 99%.

Trigger	2015	2016-2018
Single Electron	HLT_e24_lhmedium_L1EM20VH	HLT_e26_lhtight_nod0_ivarloose
	HLT_e60_lhmedium	HLT_e60_lhmedium_nod0
	HLT_e120_lhloose	HLT_e140_lhloose_nod0
Di-Electron	HLT_2e12_lhloose_L12EM10VH	HLT_2e17_lhvloose_nod0
		HLT_2e24_lhvloose_nod0
Single Muon	HLT_mu20_iloose_L1MU15	HLT_mu26_ivarmedium
	HLT_mu50	HLT_mu50
Di-Muon	HLT_mu18_mu8noL1	HLT_mu22_mu8noL1

**Table 11.1.:** List of lepton high level triggers (HLT) used in the analysis [100] [101]

The specific final state targeted in this analysis is  $l^+l^-\gamma jj$ , where  $l = e, \mu$ . Consequently, collision events should contain a minimum of two leptons with the same flavor but opposite charge, at least one photon, and at least two jets. These objects must satisfy the object selection requirements outlined in Section 9.3. Additionally, in case of single-lepton triggered events, it is necessary for one of the electrons or muons in the lepton pair to be matched to the lepton that triggered the event.

Furthermore, the leading lepton must have a minimum value of 30 GeV<sup>1</sup>. Similarly, the photon candidate with the highest  $p_T$  in the event is selected. To proceed with the analysis, at least one primary vertex needs to be reconstructed in the event. The hard-scatter primary vertex is determined by selecting the vertex candidate with the highest sum of the squared transverse momenta ( $p_T^2$ ) of the associated tracks.

To minimise the contribution from non-electroweak  $Z\gamma jj$  processes, events are selected based on typical VBS topology, as depicted in Figure 11.1. Its key characteristics are as follows [102]:

- Two high-energy jets with a wide rapidity separation and a large invariant mass. These jets originate from the incoming quarks which emit the scattering vector bosons. Thus, they carry a high fraction of the momentum of the incoming protons. They are known as *tagging jets*.

In this analysis, the two jet candidates with the highest  $p_T$  are designated as the tagging jets. They must have an energy greater than 50 GeV, and the difference in rapidity between them ( $|\Delta y|$ ) must be greater than 1. Additionally, the invariant mass of the jet pair ( $m_{jj}$ ) must be above 150 GeV, in order to reduce the number of events with three bosons in the final state where a boson can decay to two jets.

<sup>1</sup> As a reminder, this cut on lepton  $p_T$  reduces  $Z \rightarrow \tau\tau$  events

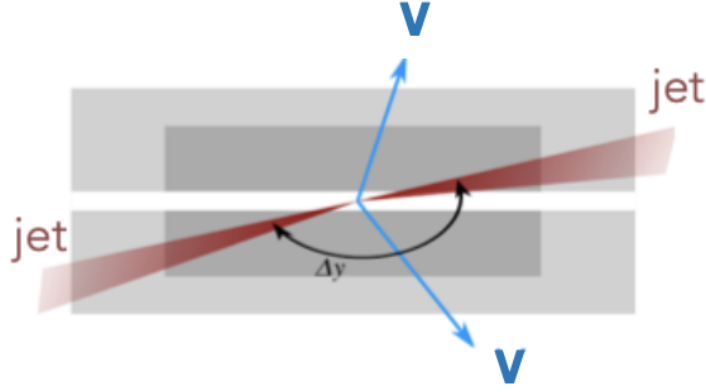


**Figure 11.1.:** Topology of a VBS event. Here  $V$  refers to the vector boson and jet is the tagging jet.

- Suppression of hadronic activity between the two tagging jets, resulting from the absence of color flow between the incoming quarks.

In this analysis, events with additional jets of  $p_T > 25$  GeV in the rapidity gap between the two VBS tagging jets are excluded. In other words, the number of jets in the gap ( $N_{gap}^{jets}$ ) should be zero.

- Centrally located pair of vector bosons with respect to the tagging jets. The centrality is measured by the variable  $\zeta$ , defined as follows:

$$\zeta = \left| \frac{y_{VV} - (y_{j1} + y_{j2})/2}{y_{j1} - y_{j2}} \right| \quad (11.1)$$

where  $y_{j1}$  and  $y_{j2}$  represent the rapidities of the tagging jets, and  $y_{VV}$  represents the rapidity of the diboson system.

In this analysis, the value of  $\zeta(Z\gamma)$  should be less than 5. Additionally, it plays a crucial role in distinguishing events originating from EW- $Z\gamma jj$  and QCD- $Z\gamma jj$  processes, as described in the next section.

Furthermore, to suppress events originating from leptonic  $Z$  decays where one of the leptons has radiated a photon, the sum of  $m_{ll}$  and  $m_{ll\gamma}$  must be greater than 182 GeV. This selection is akin to a  $Z$  mass window cut. Also,  $m_{ll}$  must exceed 40 GeV. Finally, to remove background from  $t\bar{t}\gamma$  processes, events with  $b$ -jets (identified by  $b$ -tagging algorithm described in Table 9.4) are vetoed. A summary of the event selection criteria is shown in Table 11.2.

## 11.2. Background Estimation

In particle physics, it is common to estimate backgrounds using *control regions*. These regions are carefully defined in the phase space to primarily consist of contributions from the background process under investigation. It is crucial that these regions are uncorrelated with the *signal region*, which is the region where the signal process is expected to be dominant. Furthermore, it is important to ensure a sufficient number of events in the control region to achieve statistical precision. The main idea is to gather information about the background

Event Selection	
Lepton	$N_l \geq 2$
	$p_T^l > 20, 30 \text{ GeV}$
Photon	$N_\gamma \geq 1$
	$p_T^\gamma > 25 \text{ GeV}$
Jet	$N_j \geq 2$
	$p_T^j > 50 \text{ GeV}$
Event	$m_{jj} > 150 \text{ GeV}$
	$ \Delta y  > 1$
	$m_{ll} > 40 \text{ GeV}$
	$m_{ll} + m_{ll\gamma} > 182 \text{ GeV}$
	$N_{gap}^{jets} = 0$
	$b\text{-jet veto}$
	$\zeta(Z\gamma) < 5$

**Table 11.2.:** Summary of baseline event selection criteria. The objects (lepton, photon, jet) must also satisfy the object selection criteria described in Section 9.3.

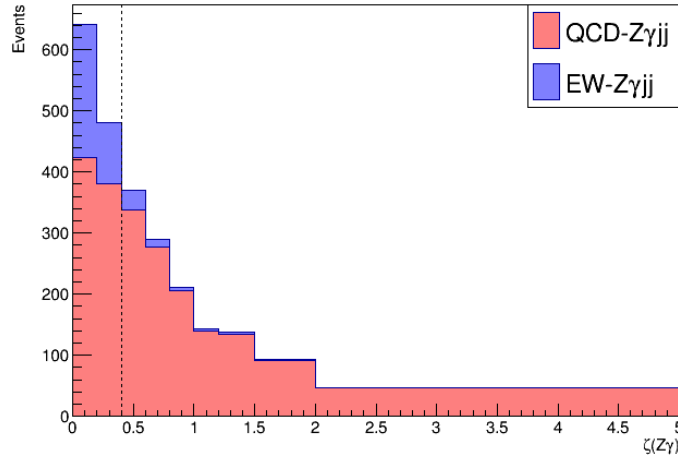


**Figure 11.2.:** Stacked histogram showing the centrality ( $\zeta(Z\gamma)$ ) distribution for QCD- $Z\gamma jj$  (in red) and EW- $Z\gamma jj$  (in blue) detector-level MC samples that fulfill the baseline event selection criteria. The dotted vertical line corresponds to  $\zeta(Z\gamma)=0.4$ .

from the control regions and extrapolate it to the signal region. In this analysis, this approach has been adopted to estimate most of the backgrounds, as outlined below.

### 11.2.1. QCD- $Z\gamma jj$

As discussed in Section 7.2, the primary background for the EW- $Z\gamma jj$  final state is the QCD-induced  $Z\gamma jj$  process. However, it has been observed that this background is not well modelled in MC simulations. To address this issue, the baseline event phase-space is divided into two distinct regions based on simulation studies, as illustrated in Figure 11.2. The first region is the signal region, which is enriched with the EW- $Z\gamma jj$ . This region is defined by  $\zeta(Z\gamma) < 0.4$ . The second region is the QCD-enriched control region, which is orthogonal to the signal region. In this control region, the primary contribution comes from QCD- $Z\gamma jj$  events, and it is defined by  $\zeta(Z\gamma) > 0.4$ .

In this analysis, when determining the production cross-section of the EW- $Z\gamma jj$  process, the shape of the QCD- $Z\gamma jj$  background is estimated using MC simulation, while its normalisation is corrected with a data-driven fit in both the signal and control regions (see Chapter 12). For computing the differential cross-sections, the shape of the QCD- $Z\gamma jj$  background is determined by a simultaneous fit in both regions, and the normalisation is estimated using simulation. In other words, for the differential studies, the normalisation of the QCD- $Z\gamma jj$  background is constrained bin-by-bin simultaneously in signal and control regions, but the total QCD- $Z\gamma jj$  normalisation from simulation remains constant (see Chapter 13).

Lastly, uncertainties related to QCD- $Z\gamma jj$  process have already been discussed in Chapter 10.

### 11.2.2. $Z$ +jets

In order to estimate the background from events involving a  $Z$ -boson and a jet misidentified as a photon, the data-driven *two-dimensional sideband* method is employed. This method makes use of two variables that are nearly uncorrelated: the calorimeter-based isolation and the photon identification criteria. These variables define four distinct regions: a signal region A enriched in prompt photons, and three control regions B, C, and D enriched in fake photons resulting from jets misidentified as photons. The ratio of event counts in these regions follows the relation:

$$\frac{N_A}{N_B} = R \cdot \frac{N_C}{N_D} \quad (11.2)$$

Here,  $R$  accounts for the correlation between the isolation and identification variables. This equality is then utilised to estimate the fake photon background by extrapolating information obtained from the control regions.

To implement this method, the baseline event selection criteria (outlined in Table 11.2) are applied to data, with the exception of the calorimeter-based isolation and the photon identification criteria. The phase space is subsequently divided into four regions, as shown in Figure 11.3, as follows:

- Signal Region A: This region comprises events with isolated photon candidates ( $E_T^{\text{cone20}}/E_T < 0.065$ ) that satisfy the **Tight** identification criteria.
- Control Region B: This region consists of events with non-isolated photon candidates ( $E_T^{\text{cone20}}/E_T > 0.065$ ) that meet the **Tight** identification criteria.

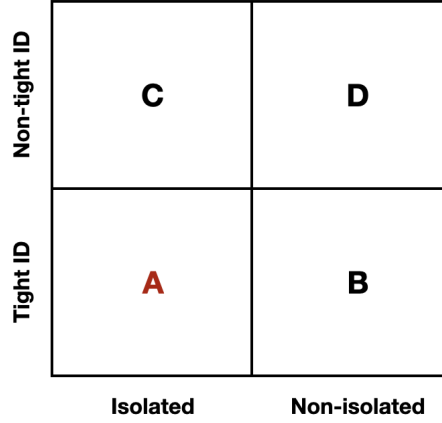


**Figure 11.3.:** Graphic illustration of the ABCD regions in the two-dimensional plane. Region A is the signal region enriched in prompt photons, and regions B, C and D are the background control regions.

- Control Region C: This region consists of events with isolated photon candidates that satisfy the *anti-Tight* identification criteria. The anti-Tight selection is achieved by relaxing the requirements on four of the nine EM calorimeter shower shape variables that are necessary for **Tight** photons. Specifically, the four variables with the least correlation to isolation energy are removed.
- Control Region D: This region comprises events with non-isolated photon candidates that satisfy the anti-Tight selection criteria.

It is important to note that when estimating fake photons, prompt photons are considered as signal, regardless of their origin from either the EW- $Z\gamma jj$  or QCD- $Z\gamma jj$  process. Consequently, region A considers all  $Z\gamma jj$  events as signal.

The number of events in each region is given by:

$$N_A = N_A^{Z\gamma jj} + N_A^{Z+jets} + N_A^{bkg} \quad (11.3)$$

$$N_B = c_B \cdot N_A^{Z\gamma jj} + N_B^{Z+jets} + N_B^{bkg} \quad (11.4)$$

$$N_C = c_C \cdot N_A^{Z\gamma jj} + N_C^{Z+jets} + N_C^{bkg} \quad (11.5)$$

$$N_D = c_D \cdot N_A^{Z\gamma jj} + N_D^{Z+jets} + N_D^{bkg} \quad (11.6)$$

where

- $N_X$  represents the number of events in data for region  $X$  ( $=A, B, C, D$ ).
- $N_A^{Z\gamma jj}$  represents the number of  $Z\gamma jj$  events in Region A, which corresponds to the signal prompt photons.
- $c_X = \frac{N_X^{Z\gamma jj}}{N_A^{Z\gamma jj}}$  denotes the *signal leakage coefficients*, indicating the fraction of prompt photons in region  $X$  ( $=B, C, D$ ).
- $N_X^{Z+jets}$  represents the number of  $Z$ +jets events in region  $X$  ( $=A, B, C, D$ ), which correspond to the fake photons background of interest.

- $N_X^{bkg}$  denotes the number of events originating from background processes such as  $t\bar{t}\gamma$  and  $WZjj$  in region  $X$  ( $=A, B, C, D$ ). These account for other minor background sources of prompt photons and fake photons.

The quantities  $N_X$  are measured directly from the data, while  $c_X$  and  $N_X^{bkg}$  are estimated from MC simulations since they do not involve estimating the fake photon probability<sup>2</sup>. Table 11.3 shows the estimates of the signal leakage coefficients.

Parameter	Value
$c_B$	$0.057 \pm 0.005$
$c_C$	$0.056 \pm 0.003$
$c_D$	$0.007 \pm 0.001$

**Table 11.3.:** Signal leakage coefficients derived from nominal EW- $Z\gamma jj$  (MADGRAPH) and QCD- $Z\gamma jj$  (SHERPA) samples, including associated systematic uncertainty from variations in the EW fraction and the use of an alternative QCD- $Z\gamma jj$  (MADGRAPH) sample.

Following equation 11.2, the residual correlation between the photon identification and isolation is quantified by the *correlation factor*  $R$ , given by

$$R = \frac{N_A^{Z+jets} \cdot N_D^{Z+jets}}{N_B^{Z+jets} \cdot N_C^{Z+jets}} \quad (11.7)$$

While complete uncorrelation would result in  $R = 1$ , the value of  $R$  is estimated from MC simulation as well as a data control region where the photons fail track isolation. The estimated value of  $R$  is  $1.19 \pm 0.14$ . The correlation is also estimated in data using a control region where the photon fails track isolation and the difference between the MC and data results are included in the systematic uncertainty.

Finally, the number of  $Z$ +jets events in Signal Region A can be calculated as follows:

$$\begin{aligned} N_A^{Z+jets} &= R \cdot N_B^{Z+jets} \cdot \frac{N_C^{Z+jets}}{N_D^{Z+jets}} \\ &= R \cdot \frac{(N_B - c_B \cdot N_A^{Z\gamma jj} - N_B^{bkg}) \cdot (N_C - c_C \cdot N_C^{Z\gamma jj} - N_C^{bkg})}{N_D - c_D \cdot N_D^{Z\gamma jj} - N_D^{bkg}} \end{aligned} \quad (11.8)$$

The estimated value of  $N^{Z+jets}$  in Signal Region A, along with its statistical and systematic uncertainties, is presented in Table 11.4. The results are provided separately for the sub-regions of Signal Region A based on the centrality variable  $\zeta(Z\gamma)$ .

In this analysis, the two-dimensional sideband method is used only to determine the size of the  $Z$ +jets background, while its shape is obtained from control regions C and D that are rich in  $Z$ +jets events. In particular, the event selection criteria are applied to both data and  $Z + jets$  background MC samples (i.e.  $t\bar{t}\gamma$ ,  $WZjj$ , EW- $Z\gamma jj$  and QCD- $Z\gamma jj$ ) in the anti-Tight region, and the difference in shape represents the shape of the  $Z$ +jets component.

<sup>2</sup>  $N_X^{bkg}$  includes a contribution of fake photons from  $WZjj$  events, but it is typically very small

Signal Region A	$N^{Z+jets}$
$\zeta(Z\gamma) < 0.4$	$77 \pm 25(\text{stat}) \pm 16(\text{sys})$
$\zeta(Z\gamma) > 0.4$	$130 \pm 35(\text{stat}) \pm 24(\text{sys})$

**Table 11.4.:** Estimated number of  $Z$ +jets events in  $\zeta(Z\gamma) < 0.4$  and  $\zeta(Z\gamma) > 0.4$  sub-regions of Signal Region A

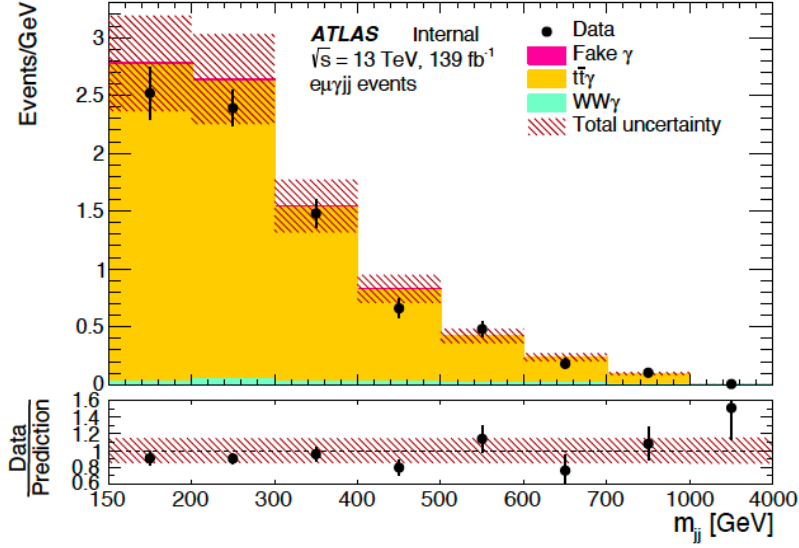


**Figure 11.4.:** Di-jet invariant mass distribution for  $e\mu\gamma$  events, without requirement on  $b$ -jet veto[53]

The uncertainty on the normalisation of the  $Z$ +jets background is already presented in Table 11.4. Its statistical component dominates at 32% (26%) in  $\zeta < 0.4$  ( $\zeta > 0.4$ ). The systematic component, which encompasses uncertainties related to the correlation factor, signal leakage coefficients, and background subtraction, amounts to 21% (18%) in  $\zeta < 0.4$  ( $\zeta > 0.4$ ). Additionally, a minor uncertainty arises from assessing the background shape of the  $Z$ +jets process.

### 11.2.3. $t\bar{t}\gamma$

The  $t\bar{t}\gamma$  background is estimated using MC simulation and validated in a control region enriched with  $t\bar{t}\gamma$  events. This control region is constructed by selecting  $e\mu\gamma$  events from data that meet the baseline event selection criteria.

A small fraction of the selected  $e\mu\gamma jj$  events originate from the  $WW\gamma$  process, and its contribution is estimated using MC simulation. Additionally, jet-faking-photon events yield the same signature and its contribution is estimated using a similar two-dimensional sideband method as described earlier.

Figure 11.4 depicts the distribution of the dijet invariant mass of the  $e\mu\gamma$  events in data, compared to the MC predictions for  $t\bar{t}\gamma$ ,  $WW\gamma$ , and fake photon background events. To

examine any discrepancies in the mass spectrum, a sufficient amount of statistics is required, hence no requirement is imposed on the  $b$ -jets. The same study has also been conducted with a  $b$ -jet veto. In both cases, it is observed that the predictions need to be scaled by an NLO  $k$ -factor<sup>3</sup> of  $1.44 \pm 0.22$  to accurately describe the data, consistent with previous studies[103]. This band of  $\pm 15\%$  to cover for the data/MC discrepancy is taken as an uncertainty on  $t\bar{t}\gamma$  estimate.

#### 11.2.4. Other

The background contribution due to  $WZjj$  events is minor and it is evaluated from simulation. It is assigned an overall normalisation uncertainty of 20%. Other background processes, such as  $tW\gamma$ ,  $ZZ$ ,  $Z(\tau\tau)\gamma$  and pileup, have been found to be negligible.

### 11.3. Measurement Regions

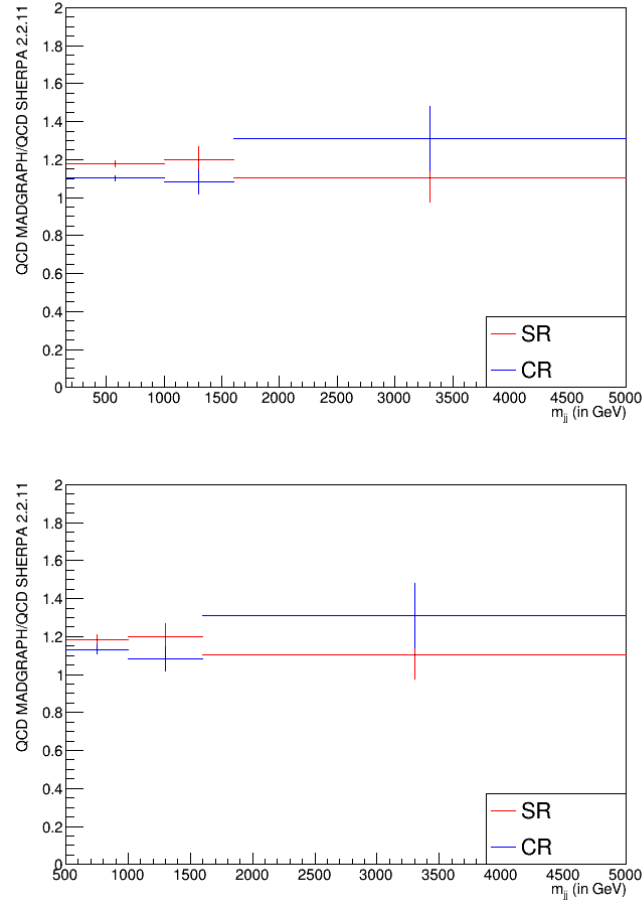
As discussed in Section 11.2, the shape (or bin-by-bin normalisation) of the QCD- $Z\gamma jj$  background is estimated by performing a simultaneous fit in both the EW- $Z\gamma jj$  SR ( $\zeta(Z\gamma) < 0.4$ ) and the QCD- $Z\gamma jj$  enriched CR ( $\zeta(Z\gamma) > 0.4$ ) when calculating the differential cross-sections. Since the QCD- $Z\gamma jj$  contribution is significantly larger in CR than in SR, the shape of the QCD- $Z\gamma jj$  distribution is primarily extrapolated from the CR. To ensure the accuracy of this extrapolation, it is crucial that any discrepancies in the shape of the QCD- $Z\gamma jj$  background among different MC simulations are not dependent on the region being studied. If the shape difference for different MC simulations remains consistent between SR and CR, then it can be assumed that a shape difference observed in the data and CR can be correctly extrapolated to a difference in SR.

Figure 11.5 presents the ratio between the alternative QCD- $Z\gamma jj$  MC sample (MADGRAPH) and the nominal QCD- $Z\gamma jj$  MC sample (SHERPA 2.2.11) at the detector-level in both the SR and CR. The ratio is plotted as a function of the invariant mass of the two tagged jets in the event. This is because  $m_{jj}$  and  $\zeta(Z\gamma)$  are uncorrelated variables. The top plot corresponds to the baseline event selection criteria, while the bottom plot includes an increased  $m_{jj}$  cut of 500 GeV.

The top plot demonstrates a non-closure in the first bin, indicating that the discrepancy between the QCD- $Z\gamma jj$  MADGRAPH MC and QCD- $Z\gamma jj$  SHERPA 2.2.11 MC is not the same in SR and CR. However, the bottom plot reveals that the difference between the two MC samples is independent of the centrality cuts. This observation supports the extrapolation of the QCD- $Z\gamma jj$  shape from the CR to the SR.

Furthermore, simulation studies (Figure 11.6) reveal that by implementing a cut at  $m_{jj} = 500$  GeV, the number of QCD- $Z\gamma jj$  events is significantly reduced. This reduction greatly improves the signal-to-background ratio, facilitating the measurement of EW- $Z\gamma jj$  signal processes.

<sup>3</sup> The term  $k$ -factor refers to a multiplicative factor used to account for higher-order corrections or additional contributions in theoretical predictions.



**Figure 11.5.:** Ratio of QCD- $Z\gamma jj$  MADGRAPH to SHERPA 2.2.11 MC samples in SR and CR. The top plot corresponds to the dijet invariant mass  $m_{jj}$  range of 150-5000 GeV, while the bottom plot corresponds to the  $m_{jj}$  range of 500-5000 GeV. All overflow events are in last bin. The uncertainties are purely from MC statistics.

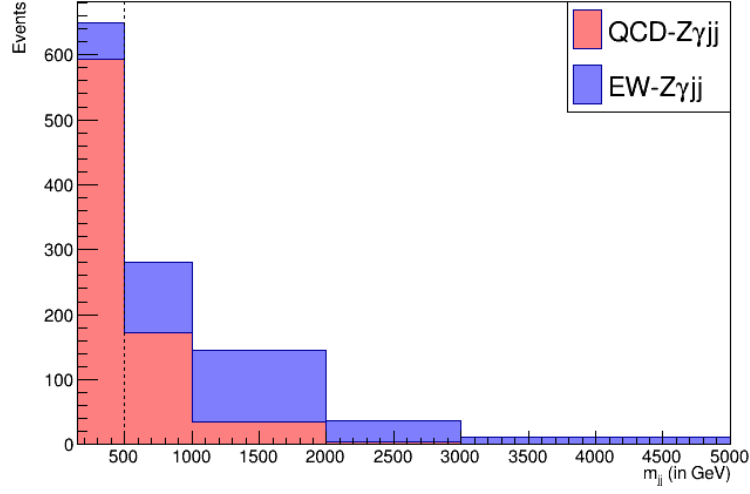


**Figure 11.6.:** Stacked histogram showing the dijet invariant mass ( $m_{jj}$ ) distribution for QCD- $Z\gamma jj$  (in red) and EW- $Z\gamma jj$  (in blue) detector-level MC samples in region  $\zeta(Z\gamma) < 0.4$ . The dotted vertical line corresponds to  $m_{jj}=500$  GeV.

Based on this study, the baseline event phase space is split into two parts, and the following regions are defined for the analysis:

EW- $Z\gamma jj$ Measurements	$Z\gamma jj$ Measurements
$m_{jj} > 500$ GeV	$m_{jj} > 150$ GeV
Signal Region $\zeta(Z\gamma) < 0.4$	Extended Signal Region $\zeta(Z\gamma) < 0.4$
Control Region $\zeta(Z\gamma) > 0.4$	No Control Region

**Table 11.5.:** Measurement Regions

As seen from Table 11.5, studies involving  $Z\gamma jj$  process do not need a QCD-enriched CR since QCD- $Z\gamma jj$  is a part of the signal. Additionally, for more statistics, the  $m_{jj}$  cut is kept at 150 GeV.

# Chapter 12.

## Inclusive Measurements

To determine the EW- $Z\gamma jj$  and  $Z\gamma jj$  production cross sections from experimental data, a profile likelihood fit is performed on the distributions of the invariant mass ( $m_{jj}$ ) of the two tagging jets. A comprehensive explanation of the profile likelihood fit is provided in Section 12.1, while specific details of the fit procedure in this analysis are outlined in Section 12.2. The methodology for measuring the cross-section is described in Section 12.3, and the corresponding results are presented in Section 12.4. All the measurements reported in this chapter have been carried out during this PhD.

### 12.1. Profile Likelihood Fit

The profile likelihood fit [104] [105] is a statistical technique used to estimate parameters of a statistical model based on observed data. It maximises the likelihood function, which measures the probability of observing the data for various parameter values within the model. These parameters include the *parameter of interest* (POI) as well as *nuisance parameters* (NP) that influence the prediction but are not directly of interest.

In this analysis, the model corresponds to the Standard Model theory, and the POI is the *signal strength* parameter  $\mu$ , defined as the ratio of the measured signal cross-section to the predicted Standard Model signal cross-section:

$$\mu = \frac{\sigma_{\text{measured}}^{\text{signal}}}{\sigma_{\text{predicted}}^{\text{signal}}}$$

The fit is performed using the `TRExFitter`[106] software package, which incorporates `HistFactory` [107] tools.

The likelihood function is composed of several components. The first part involves Poissonian probability terms based on the observed events and the SM predicted events in each bin  $i$  of every region of the fit:

$$L(\mu) = \prod_{i \in \text{bins}} \text{Pois}(n_i | \mu s_i + b_i)$$

Here,  $n_i$  represents the observed events from the data histogram, while  $s_i$  and  $b_i$  correspond to the expected number of signal and background events taken from the signal and background MC templates, respectively. The signal prediction is scaled by  $\mu$ , which is the POI to be determined from the fit.

Additionally, in the same way as the POI, unconstrained normalisation factors can be attributed to selected background templates. They are introduced as nuisance parameters  $\vec{k}$  that scale the total background prediction  $\{b_i \rightarrow kb_i\}$ . Then,

$$L(\mu, \vec{k}) = \prod_{i \in \text{bins}} \text{Pois}(n_i | \mu s_i + kb_i)$$

Systematic uncertainties are introduced through nuisance parameters,  $\vec{\theta}$ , which modify the expected signal and background templates:  $\{s_i, b_i\} \rightarrow \{s_i(\vec{\theta}), b_i(\vec{\theta})\}$ . They are implemented as a set of Gaussian constraints  $C(\theta|0, 1)$ , which have a mean value of 0 and standard deviation of 1:

$$L(\mu, \vec{k}, \vec{\theta}) = \prod_{i \in \text{bins}} \text{Pois}(n_i | \mu s_i(\vec{\theta}) + kb_i(\vec{\theta})) \times \prod_{j \in \text{syst}} C(\theta_j | 0, 1)$$

where  $j$  is the number of systematic uncertainties. These systematic uncertainties are estimated from separate auxiliary measurements or theoretical calculations, generating templates for both the nominal ( $\theta = 0$ ) and variation ( $\theta = \pm 1\sigma$ ) cases. To ensure a continuous description of each systematic effect and obtain templates at  $\theta \neq 0, \pm 1\sigma$ , **TRExFitter** utilises interpolation. For this purpose, each NP is divided into two components: a shape component, represented by linear interpolation, and a normalisation component, represented by exponential interpolation. Despite being split, both components share the same Gaussian constraint term, resulting in only one constraint term per NP. Notably, the choice of exponential interpolation for the normalisation component is motivated by its equivalence to a log-normal constraint when combined with the Gaussian term, thereby preventing non-physical negative event yields.

Moreover, to account for the finite MC statistics of the templates used in the fit, an additional set of nuisance parameters  $\vec{\gamma}$  are included in the likelihood function. Each  $\gamma$  parameter is associated with a specific bin and scales the total MC prediction:  $\{s_i(\vec{\theta}), b_i(\vec{\theta})\} \rightarrow \{s_i(\vec{\theta})\gamma_i, b_i(\vec{\theta})\gamma_i\}$ . Thus, unlike the previous nuisance parameters, the nominal value of  $\gamma$  is set to 1. These  $\vec{\gamma}$  parameters are implemented in the likelihood function as a set of Poissonian constraints  $C(\gamma|1, \sigma_\gamma)$ , where the mean value is 1, and the standard deviation  $\sigma_\gamma$  is equal to the statistical uncertainty on the expected total yield for that specific bin. The full likelihood function is then expressed as:

$$L(\mu, \vec{k}, \vec{\theta}, \vec{\gamma}) = \prod_{i \in \text{bins}} \text{Pois}(n_i | (\mu s_i(\vec{\theta}) + kb_i(\vec{\theta}))\gamma_i) \times \prod_{j \in \text{syst}} C(\theta_j | 0, 1) \times \prod_{i \in \text{bins}} C(\gamma_i | 1, \sigma_{\gamma_i}) \quad (12.1)$$

All the nuisance parameters ( $\vec{\theta}$ ,  $\vec{k}$  and  $\vec{\gamma}$ ) are assumed to be uncorrelated in the likelihood, although correlations can be determined during the fit. This is described in detail in the next section.

The fit itself, i.e. maximising the likelihood, is carried out by minimising the negative log-likelihood function using algorithms implemented in **MINUIT**. During the fit, both the nuisance parameters and the parameter of interest are allowed to vary. However,  $\mu$  and  $\vec{k}$  are considered as free-floating parameters in the likelihood, while the other nuisance parameters  $\vec{\theta}$  and  $\vec{\gamma}$  are constrained by their respective constraint terms.

Finally, the fit has the ability to perform the following adjustments to the nuisance parameters:

- *Pull*: It can shift the central value of a nuisance parameter to better align with the observed data and improve the agreement between data and Monte Carlo (MC) predictions
- *Constrain*: It can reduce (or very rarely, increase) the  $\pm 1\sigma$  uncertainty assigned to a nuisance parameter if the initial  $\pm 1\sigma$  band is found to be inconsistent with the observed data.

These parameters provide valuable insights into the modelling of uncertainties and contribute to refining the overall accuracy of the analysis.

## 12.2. Fit Procedure

As mentioned in Chapter 11, the determination of the EW- $Z\gamma jj$  cross section involves conducting a simultaneous fit in both the Signal Region (SR) and Control Region (CR). It should be noted that both electron and muon channels are combined in this fit. The POI in this fit is represented by  $\mu_{EW}$ , given by

$$\mu_{EW} = \frac{\sigma_{\text{measured}}^{\text{EW}-Z\gamma jj}}{\sigma_{\text{predicted}}^{\text{EW}-Z\gamma jj}} \quad (12.2)$$

The fit also constrains the normalisation of the QCD- $Z\gamma jj$  background, represented by  $\mu_{QCD}$ . This normalisation is included as a  $\vec{k}$  nuisance parameter in the likelihood function, and it is correlated between the SR and CR. In contrast, the other background processes are also correlated between regions, but do not involve free-floating normalisation factors. This is due to their small contributions, which are well controlled either in the background control region or through data-driven methods. Moreover, the small number of EW- $Z\gamma jj$  events in the CR (see Table 12.5) is treated as background and is not correlated with the signal EW- $Z\gamma jj$  process in the SR. Notably, the  $\vec{\gamma}$  nuisance parameters are not correlated between the regions of the fit. Further details regarding the  $\vec{\theta}$  NPs are discussed in the next section.

On the other hand, to measure the  $Z\gamma jj$  cross-section, the fit is performed solely in the Extended Signal Region with electron and muon channel combined. In this case, the POI is  $\mu_{Z\gamma jj}$ , defined as

$$\mu_{Z\gamma jj} = \frac{\sigma_{\text{measured}}^{Z\gamma jj}}{\sigma_{\text{predicted}}^{Z\gamma jj}} \quad (12.3)$$

Again, no normalisation factor for the backgrounds is introduced in this particular fit. Details of the  $\vec{\theta}$  NPs are discussed in the subsequent section.

### 12.2.1. Treatment of Systematic Uncertainties

Before performing an actual fit with the observed data, it is vital to validate the fit configuration. One effective way to achieve this is through the *Asimov fit*, where the combination of predicted background and signal is used as pseudo-data for the fit. This proves particularly valuable in systematic studies as it facilitates the assessment of the analysis's sensitivity to various sources of uncertainties. Specifically, by fitting to Asimov data with various systematic variations,

one can explore the impact of these uncertainties on the fit results. This approach provides a proper and unbiased method for handling systematic uncertainties.

In this thesis, the results of the Asimov fit have not been presented<sup>1</sup>. Nevertheless, the key techniques for handling systematic uncertainties are outlined below:

**Symmetrisation:** As previously mentioned, the input systematic templates consist of the nominal ( $\theta = 0$ ) and variation ( $\theta = \pm 1\sigma$ ) cases. These variation templates are commonly referred to as *up* and *down* variations. If either only the up or the down variation is available (eg JER, PS,...), one-sided symmetrisation is applied. In this case, the mirrored distribution of the given up/down variation is used to describe the down/up variation.

It is essential to ensure that the up/down variation histograms represent opposite sides of the nominal histogram, meaning that the ratios (nominal-up)/nominal and (nominal-down)/nominal should not both be positive or negative for the same bin. To address this concern, a corrective step is taken for each systematic uncertainty. When both ratios in a specific bin have the same sign, the sign of the smallest variation is inverted. This ensures that there are always two different signs for the variation, preserving the correct representation of uncertainties during the analysis.

**Smoothing:** To mitigate the influence of statistical fluctuations in the provided systematic uncertainty templates, a *smoothing* technique based on algorithm 353QH [108] as implemented in ROOT is utilised. This method is applied to the (nominal-up)/nominal and (nominal-down)/nominal histograms, helping to improve the stability and accuracy of the analysis.

#### Correlations:

- (i) The systematic uncertainties for the EW- $Z\gamma jj$  fit are correlated across all bins. However, for different regions, the correlations are as follows:
  - The experimental uncertainties discussed in Section 10.1 have the following correlations:
    - The **Luminosity** uncertainty is correlated between SR and CR.
    - All object uncertainties listed in Tables 10.1-10.4 are correlated among the EW- $Z\gamma jj$  and QCD- $Z\gamma jj$  samples and between SR and CR.
  - The theory uncertainties discussed in Section 10.2 have the following correlations:
    - The **SCALE\_EW**, **PDF\_EW**, **PS**, **UE** and **Int** uncertainties are not correlated between SR and CR. This decision is made due to the small number of EW- $Z\gamma jj$  events in the CR that are treated as background in this analysis. As a result, it is appropriate to handle the systematic uncertainties affecting the background and signal separately.
    - The **SCALE\_QCD** and **PDF\_QCD** uncertainties are correlated between SR and CR.
    - The **CKKW** and **QSF** uncertainties are correlated between SR and CR.
  - The uncertainties associated with  $Z$ +jets,  $t\bar{t}\gamma$ , and  $WZjj$ , as described in Section 11.2, are correlated between the SR and CR.

<sup>1</sup> Although the author of the thesis conducted Asimov studies, they are intentionally omitted ensure that the main results of the analysis remain the central focus of the thesis.

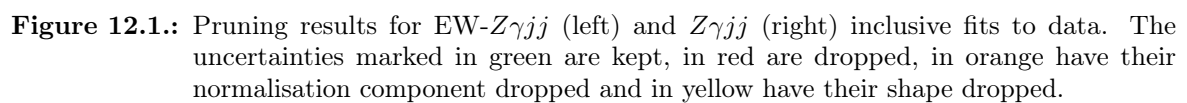
- (ii) The systematic uncertainties for the  $Z\gamma jj$  fit are generally correlated across all bins, except for `SCALE_QCD`. During the Asimov fit, it was noticed that this particular nuisance parameter exhibited a pull and over-constraint issue (see Section 12.4 later). To address this, `SCALE_QCD` is treated as uncorrelated in bin1, bin2, bin3, and "high" bins (bins 4-6). This modification is aimed at reducing the problem of over-constraint observed during the fitting process.

**Subtraction of Normalisation Component:** Before performing the EW- $Z\gamma jj$  fit, the normalisation components related to the `SCALE_EW`, `SCALE_QCD`, `PDF_EW`, and `PDF_QCD` uncertainties are subtracted. This step is essential because their normalisation is already accounted for in the free-floating parameters of the fit, namely  $\mu_{EW}$  and  $\mu_{QCD}$ . Similarly, in the  $Z\gamma jj$  fit, the normalisation components for the `SCALE_EW`, `PDF_EW`, and `PDF_QCD` uncertainties are also subtracted for the same reason. However, it is worth noting that the normalisation component associated with the `SCALE_QCD` uncertainty is not subtracted in the  $Z\gamma jj$  fit. This is because it has been de-correlated among bins, leaving only its normalisation component to vary in the fit.

**Pruning:** To enhance the efficiency and stability of the fit process, a technique called *pruning* is implemented in `TRExFitter`. This method involves excluding systematic uncertainties that have minimal impact on the final results.

For EW- $Z\gamma jj$  measurements, systematic uncertainties with an impact smaller than 0.5% on the normalisation are considered only for the shape effect, while uncertainties with an impact smaller than 0.5% on the shape are considered only for the normalisation effect. If a specific systematic uncertainty has both shape and normalisation effects below these thresholds, it is removed from the fit entirely. Similar considerations apply for  $Z\gamma jj$  measurements, where all thresholds are set to 0.1%. These specific threshold values were chosen after ensuring that the fit produces the same results even when all nuisance parameters are retained.

In Figure 12.1, the results of the pruning technique for both the EW- $Z\gamma jj$  and  $Z\gamma jj$  fits to data are depicted. Notably, the plot for EW- $Z\gamma jj$  also showcases the correlations among regions and samples, as indicated by the NPs with the same name in the fitting tool.



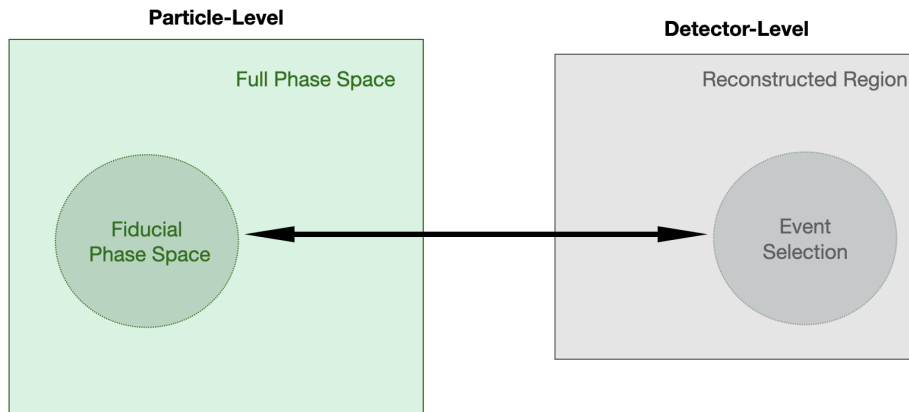


**Figure 12.2.:** Sketch of equivalence between fiducial particle-level phase space and detector-level event phase space

### 12.3. Measurement of Cross Section

The criteria used to define the measurement regions (Table 11.5) rely on objects reconstructed at the detector level. As a result, any cross-section measured within these regions will inherently incorporate detector inefficiencies. Instead, the preferred approach is to obtain a cross-section measurement that is not affected by detector effects, allowing for a direct comparison with theoretical predictions. Consequently, the cross-section should be determined in a *fiducial phase space* at the event-generation or *particle level*, which corresponds to the phase space defined by the event selection criteria at the detector level, as depicted in Figure 12.2.

To obtain the *fiducial cross-section*, the signal strength parameter ( $\mu_{\text{signal}}$ ) from the profile likelihood fit can be used. Specifically, referring to equation 3.2, the measured fiducial cross-section is expressed as:

$$\sigma_{\text{measured}}^{\text{fiducial}} = \frac{N_{\text{measured}}^{\text{signal}}}{C \times L} \quad (12.4)$$

where,  $N_{\text{measured}}^{\text{signal}}$  represents the number of signal events measured in the detector-level phase space,  $C$  denotes the detector acceptance efficiency<sup>2</sup>, and  $L$  stands for the luminosity. Similarly, the predicted fiducial cross-section can be defined as:

$$\sigma_{\text{predicted}}^{\text{fiducial}} = \frac{N_{\text{predicted}}^{\text{signal}}}{C \times L} \quad (12.5)$$

<sup>2</sup> Acceptance efficiency refers to the fraction of particles or events the detector can successfully detect and measure. It relies on various factors, such as the detector's geometry, technology, triggering criteria, and reconstruction algorithms.

where,  $N_{\text{predicted}}^{\text{signal}}$  represents the expected number of signal events in the detector-level phase space obtained from simulation. Thus, combining both equations, we get

$$\begin{aligned}\sigma_{\text{measured}}^{\text{fiducial}} &= \frac{N_{\text{measured}}^{\text{signal}}}{L} \times \frac{L}{N_{\text{predicted}}^{\text{signal}}} \times \sigma_{\text{predicted}}^{\text{fiducial}} \\ &= \frac{\sigma_{\text{measured}}}{\sigma_{\text{predicted}}} \times \sigma_{\text{predicted}}^{\text{fiducial}} = \mu_{\text{signal}} \times \sigma_{\text{predicted}}^{\text{fiducial}}\end{aligned}\quad (12.6)$$

where,  $\sigma_{\text{predicted}}$  and  $\sigma_{\text{measured}}$  are the signal cross-sections at the detector-level.

The measurement of the fiducial cross-section, as evident from 12.6, requires knowledge of the predicted fiducial cross-section. This prediction is established by defining the fiducial phase space, which relies on criteria similar to the detector-level event selection but at the particle-level. Specifically, in this analysis, the fiducial phase space is determined using particle-level objects, which consist of stable particles (with a mean lifetime greater than  $0.3 \times 10^{-10}$  s) generated by the MC event-generator:

- Only prompt electrons and muons are selected, meaning those not originating from hadrons or  $\tau$ -leptons. Additionally, a process known as *dress*ing is performed, summing contributions from photons within  $\Delta R = 0.1$  of a lepton to correct its four-momentum. Dressed leptons account for final-state radiation and photon radiation effects observed at the detector-level.
- Only prompt photons that do not originate from hadron decays are selected. A photon isolation criterion is applied, ensuring that the scalar sum of  $p_T$  for all stable particles (excluding neutrinos, muons, and the photon itself) within a cone of radius  $\Delta R = 0.2$  around the photon (denoted as  $E_T^{\text{cone}20}$ ) is less than 7% of the photon's  $p_T$ . This criterion closely resembles the detector-level photon isolation criteria used in the analysis.
- Jets are reconstructed using the anti- $k_t$  algorithm with a radius parameter of  $R=0.4$ , considering all stable particles (except for neutrinos and prompt photons, electrons, muons) for jet clustering.

Finally, an object overlap removal procedure is implemented:

- if a jet and a lepton are reconstructed within  $\Delta R = 0.3$  from each other, the jet is removed.
- If a jet and a photon are reconstructed within  $\Delta R = 0.4$  of each other, the jet is removed.
- If a photon and a lepton are reconstructed within  $\Delta R = 0.4$  of each other, the photon is removed.

The selection criteria for the fiducial region are specified in Table 12.1. Importantly, the rejection of events containing  $b$ -tagged jets is not applied in the fiducial phase space. This decision is made to avoid reducing the predicted fiducial cross-section. It is based on the assumption that the simulation accurately extrapolates from the reconstructed to the fiducial phase space, enabling the preservation of the predicted fiducial cross-section.

Following the selection criteria of table 11.5, the fiducial phase space can be divided into SR, CR and Extended SR at the particle-level for the EW- $Z\gamma jj$  and  $Z\gamma jj$  measurements.

Selection	
Lepton	$N_l \geq 2,  \eta_l  < 2.5$ dressed $p_T^l > 20, 30 \text{ GeV}$
Photon	$N_\gamma \geq 1,  \eta_\gamma  < 2.37$ $p_T^\gamma > 25 \text{ GeV}$ $E_T^{\text{cone20}} < 0.07 E_T^\gamma$
Jet	$N_j \geq 2,  y_j  < 4.4$ $p_T^j > 50 \text{ GeV}$
Event	$m_{jj} > 150 \text{ GeV}$
	$ \Delta y  > 1$
	$m_{ll} > 40 \text{ GeV}$
	$m_{ll} + m_{ll\gamma} > 182 \text{ GeV}$
	$N_{gap}^{\text{jets}} = 0$ $\zeta(Z\gamma) < 5$

**Table 12.1.:** Summary of fiducial phase space selection criteria.

## 12.4. Results

As mentioned previously, in 2021, the ATLAS collaboration published the first fiducial cross-section measurements of the EW- $Z\gamma jj$  and total  $Z\gamma jj$  processes using the full Run-2 data[92]. In this present analysis, the same measurements have been replicated with the following key distinctions:

- A revised definition of the measurement phase space, as described in Table 11.5, has been implemented.
- Instead of the QCD- $Z\gamma jj$  MADGRAPH MC sample, the QCD- $Z\gamma jj$  SHERPA 2.2.11 sample has been utilised, in accordance with the recommendations from the ATLAS Physics Modelling Group (PMG).
- The TRExFitter fitting tool has been employed in place of HistFactory. To validate this change, the inclusive EW- $Z\gamma jj$  fit was performed using both tools, and comparable results were obtained. This verification process has been documented in Appendix A.

These changes aim to improve the accuracy and precision of the measurements and enhance the understanding of the underlying physical processes. The following sections show the results of the fits with data.

### 12.4.1. EW- $Z\gamma jj$

Figure 12.3 displays the pre-fit and post-fit distributions of the fit to data, and the corresponding event yields are provided in Tables 12.2 and 12.3. By comparing the post-fit distribution/yield to the pre-fit one, one can observe a significant improvement in the agree-

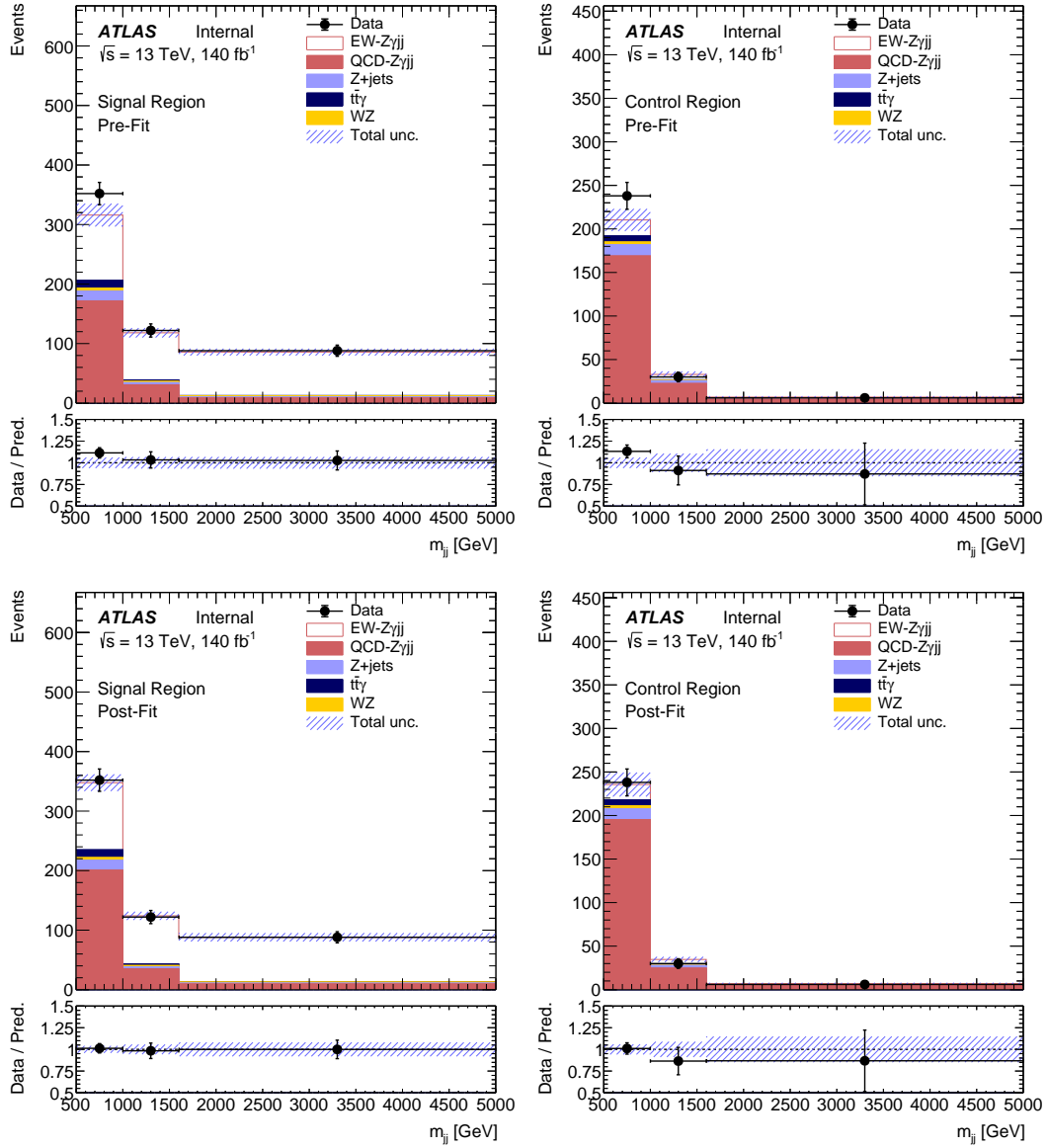


**Figure 12.3.:** Pre-fit (top) and post-fit (bottom) distributions of  $m_{jj}$  in SR (left) and CR (right) for the inclusive EW- $Z\gamma jj$  fit. Electron and muon channels are combined. The total uncertainty is shown. The last bin contains overflow events.

ment with data. Additionally, the total uncertainty is substantially reduced after the fit. This reduction in uncertainty is attributed to the constraints and, particularly, the correlations of all NPs obtained from the fit to data in the post-fit uncertainties. In contrast, the pre-fit uncertainties are based on individual NP variations without considering their interrelations. Overall, the model employed in the fit aptly describes the data within the estimated uncertainties.

	Signal Region	Control Region
EW- $Z\gamma jj$	$262.17 \pm 23.29$	$26.84 \pm 6.64$
QCD- $Z\gamma jj$	$210.63 \pm 14.56$	$195.60 \pm 14.11$
$Z$ +jets	$22.10 \pm 8.83$	$16.25 \pm 5.76$
$t\bar{t}\gamma$	$16.04 \pm 2.62$	$7.49 \pm 1.32$
$WZjj$	$8.75 \pm 1.76$	$3.92 \pm 0.80$
Total	$519.69 \pm 30.53$	$250.11 \pm 16.75$
Data	562	274

**Table 12.2.:** Pre-fit yields of the inclusive EW- $Z\gamma jj$  fit

	Signal Region	Control Region
EW- $Z\gamma jj$	$268.56 \pm 26.88$	$25.49 \pm 6.15$
QCD- $Z\gamma jj$	$244.96 \pm 21.02$	$224.44 \pm 18.46$
$Z$ +jets	$21.49 \pm 8.50$	$15.79 \pm 5.52$
$t\bar{t}\gamma$	$16.08 \pm 2.42$	$7.51 \pm 1.13$
$WZjj$	$8.74 \pm 1.75$	$3.91 \pm 0.78$
Total	$559.83 \pm 22.77$	$277.15 \pm 16.52$
Data	562	274

**Table 12.3.:** Post-fit yields of the inclusive EW- $Z\gamma jj$  fit

The results of the fit are displayed in Figures 12.4-12.7, each plot serving a specific purpose:

- Figure 12.4: This plot shows the best-fit values of the POI  $\mu_{EW}$  and the QCD- $Z\gamma jj$  normalisation factor  $\mu_{QCD}$ , along with their  $\pm 1\sigma$  uncertainties.
- Figure 12.5: Although the parameters of the fit are initially treated as uncorrelated, the fitting process itself introduces correlations between complementary nuisance parameters. Large correlations among nuisance parameters can indicate redundant degrees of freedom, suggesting that certain parameters are already accounted for by others in the fit. Additionally, significant correlations between nuisance parameters and the signal can imply that these parameters share similar characteristics with the signal, potentially leading to a reduced analysis sensitivity.

The correlation matrix of the fit parameters, estimated using the **HESSE** algorithm that is implemented in **TRExFitter**, is presented in this plot. Although some correlations are observed among the nuisance parameters, they are not considerably large. As expected, there is an anti-correlation between the  $\mu_{EW}$  and  $\mu_{QCD}$  parameters, as they both influence the normalisation of the signal and background. For instance, if the signal increases, the background decreases, and vice versa. The major (anti-)correlations for the POI  $\mu_{EW}$  arise from EW theory uncertainties and pileup re-weighting, while the major (anti-)correlations for  $\mu_{QCD}$  are with QCD theory uncertainties.

- Figure 12.6: This plot depicts the pulls of the NPs  $\vec{\theta}$ . It is given by  $(\hat{\theta} - \theta_0)/\Delta\theta$ , where  $\hat{\theta}$  is the best-fit value of the NP,  $\theta_0$  is its nominal value, and  $\Delta\theta$  is the uncertainty on  $\theta_0$ .

Due to the unit Gaussian constraint term, these NPs are expected to be centred around 0 with a  $\sigma$  of  $\pm 1$ . Although a few pulls are observed in the fit, they are not significantly large and remain within their corresponding  $1\sigma$  bands. Notably, the CKKW merging scale parameter exhibits the largest pull among the nuisance parameters. However, given that the over-constraint is not substantial and that the pull can be attributed to the substantial size of the shape variation (as depicted in Figure 12.8), no specific action is taken for this parameter.

- Figure 12.7 illustrates the *impact*  $\Delta\mu$  on the best-fit value of the POI  $\mu_{EW}$ . The pre-fit impact is determined by conducting two additional fits: one with the  $\theta$  fixed to its pre-fit value plus its uncertainty, and another with the  $\theta$  fixed to its pre-fit value minus its uncertainty. The difference in  $\mu_{EW}$  between these fits and the nominal fit provides the pre-fit impacts. Similarly, the post-fit impact is evaluated by performing two additional fits: one with the  $\theta$  fixed to its post-fit value plus its uncertainty, and another with the  $\theta$  fixed to its post-fit value minus its uncertainty. The difference in  $\mu_{EW}$  between these fits and the nominal fit provides the post-fit impacts. For the  $\vec{\gamma}$  NPs (which reflect MC statistical uncertainties) and the  $\mu_{QCD}$  NP, only the post-fit impacts are evaluated, as there is no proper estimation of their pre-fit uncertainties.

The ranking plot indicates that the largest contributors to the uncertainty are primarily related to EW theory uncertainties and pileup reweighting, as expected from the correlation plot.

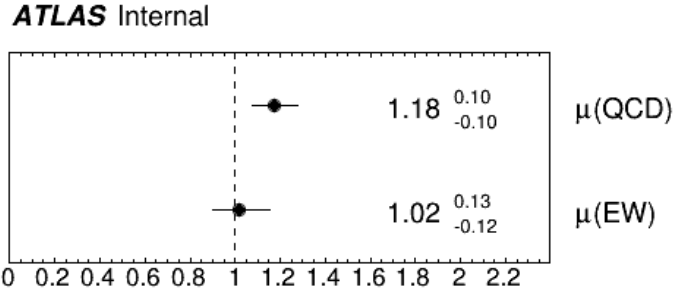


**Figure 12.4.:** Best-fit values of  $\mu_{EW}$  and  $\mu_{QCD}$  along with their  $\pm 1\sigma$  uncertainties in the inclusive EW- $Z\gamma jj$  fit.

**ATLAS Internal**

zjets_stat	100.0	-0.9	-0.4	0.0	0.1	-0.6	-0.1	-0.0	0.7	-0.0	0.0	0.0	0.7	0.0	-0.6	-0.7	1.1	-0.1	-4.4	-24.6
zjets_sys	-0.9	100.0	-0.1	0.0	0.0	-0.3	-0.0	-0.0	0.4	-0.0	-0.0	0.0	0.3	-0.1	-0.3	-0.4	0.5	-0.0	-2.5	-16.1
CKKW	-0.4	-0.1	100.0	0.5	6.2	-2.6	-0.2	-0.6	2.8	0.3	0.4	0.4	2.2	6.6	-2.4	-2.5	4.4	-0.3	10.4	22.7
OTAL_1NPCOR_PLUS_UNCOR	0.0	0.0	0.5	100.0	-0.3	0.2	-0.0	-0.0	-0.1	-0.0	-0.0	-0.0	-0.1	-0.3	0.2	0.2	-0.4	0.0	-6.2	-12.4
Int_CR	0.1	0.0	6.2	-0.3	100.0	1.5	-0.1	-0.2	-1.0	-0.2	-0.2	-0.2	-1.0	-4.4	1.7	1.4	-2.8	0.2	6.0	-15.8
Int_SR	-0.6	-0.3	-2.6	0.2	1.5	100.0	0.0	0.1	1.5	0.0	0.1	0.1	2.0	1.4	-2.8	-2.2	4.5	-0.3	-28.6	-7.4
JET_EtaIntercalibration_Modelling	-0.1	-0.0	-0.2	-0.0	-0.1	0.0	100.0	-0.0	0.1	-0.0	-0.0	-0.0	0.0	-0.1	0.1	-0.1	-0.1	0.0	-6.6	-11.3
JET_Flavor_Composition	-0.0	-0.0	-0.6	-0.0	-0.2	0.1	-0.0	100.0	0.0	-0.0	-0.0	-0.0	-0.1	-0.2	0.3	0.1	-0.4	0.0	-10.8	6.9
JET_Flavor_Response	0.7	0.4	2.8	-0.1	-1.0	1.5	0.1	0.0	100.0	-0.0	-0.0	-0.1	-1.5	-0.9	1.5	1.7	-2.7	0.2	14.1	-3.1
lumi	-0.0	-0.0	0.3	-0.0	-0.2	0.0	-0.0	-0.0	-0.0	100.0	-0.0	-0.0	-0.0	-0.2	0.0	0.0	-0.1	0.0	-6.7	-12.0
PH_EFF_ID_Uncertainty	0.0	-0.0	0.4	-0.0	-0.2	0.1	-0.0	-0.0	-0.0	-0.0	100.0	-0.0	-0.0	-0.3	0.1	0.1	-0.1	0.0	-7.1	-12.5
PH_EFF_ISO	0.0	0.0	0.4	-0.0	-0.2	0.1	-0.0	-0.0	-0.1	-0.0	-0.0	100.0	-0.1	-0.3	0.1	0.1	-0.2	0.0	-6.7	-11.7
PRW_DATASF	0.7	0.3	2.2	-0.1	-1.0	2.0	0.0	-0.1	-1.5	-0.0	-0.0	-0.1	100.0	-0.9	2.2	1.9	-3.7	0.2	22.9	-1.1
PS_CR	0.0	-0.1	6.6	-0.3	-4.4	1.4	-0.1	-0.2	-0.9	-0.2	-0.3	-0.3	-0.9	100.0	1.5	1.3	-2.6	0.2	5.7	-14.4
PS_SR	-0.6	-0.3	-2.4	0.2	1.7	-2.8	0.1	0.3	1.5	0.0	0.1	0.1	2.2	1.5	100.0	-2.4	5.5	-0.4	-38.5	-7.9
QSF	-0.7	-0.4	-2.5	0.2	1.4	-2.2	-0.1	0.1	1.7	0.0	0.1	0.1	1.9	1.3	-2.4	100.0	4.0	-0.3	-9.1	-22.2
SCALE_EW_SR	1.1	0.5	4.4	-0.4	-2.8	4.5	-0.1	-0.4	-2.7	-0.1	-0.1	-0.2	-3.7	-2.6	5.5	4.0	100.0	0.6	-21.0	13.5
UE_SR	-0.1	-0.0	-0.3	0.0	0.2	-0.3	0.0	0.0	0.2	0.0	0.0	0.0	0.2	0.2	-0.4	-0.3	0.6	100.0	-20.6	-0.9
$\mu(EW)$	-4.4	-2.5	10.4	-6.2	6.0	-28.6	-6.6	-10.8	14.1	-6.7	-7.1	-6.7	22.9	5.7	-38.5	-9.1	-21.0	-20.6	100.0	-14.9
$\mu(QCD)$	-24.6	-16.1	22.7	-12.4	-15.8	-7.4	-11.3	6.9	-3.1	-12.0	-12.5	-11.7	-1.1	-14.4	-7.9	-22.2	13.5	-0.9	-14.9	100.0

**Figure 12.5.:** Correlation coefficients of the parameters in the inclusive EW- $Z\gamma jj$  fit. All values are given in percentage. Only nuisance parameters with at least one correlation coefficient above 10% are shown.

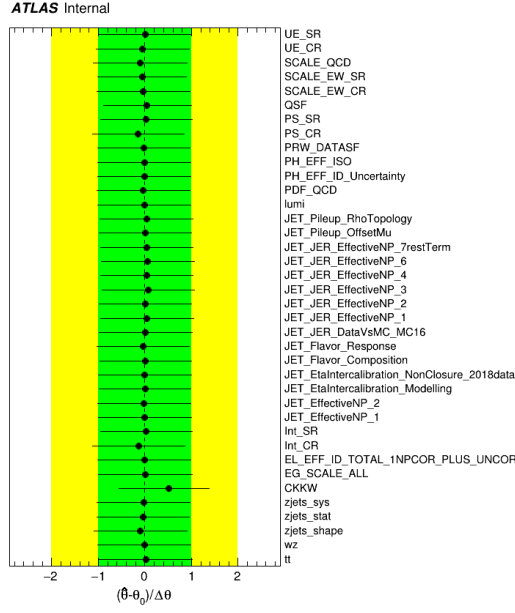


**Figure 12.6.:** Pulls and constraints of all nuisance parameters  $\vec{\theta}$  in the inclusive EW- $Z\gamma jj$  fit. The green (yellow) area represents the  $\pm 1(2)\sigma$  band on the pre-fit systematic uncertainty. The black dots represent the post-fit values of the NPs, the black lines their post-fit uncertainties.

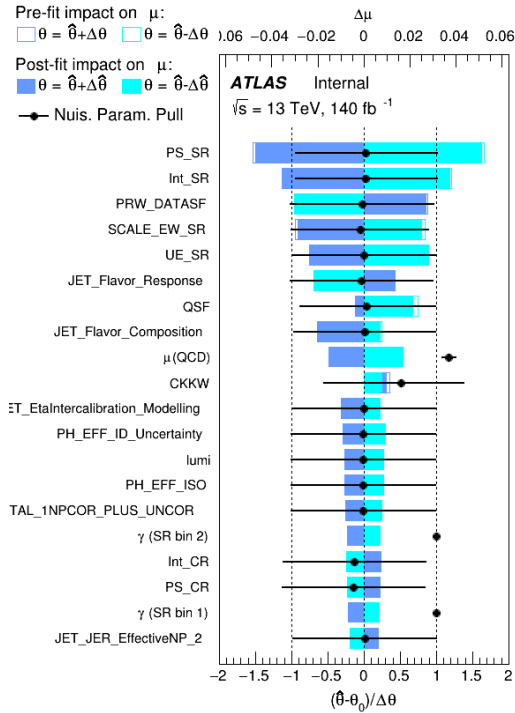


**Figure 12.7.:** Ranking plot showing the impact of each NP on  $\mu_{EW}$  in the inclusive EW- $Z\gamma jj$  fit. The empty/full boxes show the pre-/post-fit impacts. Only the 20 NPs with the highest post-fit impacts are displayed. The black dots/lines represent the post-fit values/uncertainties of all NPs.

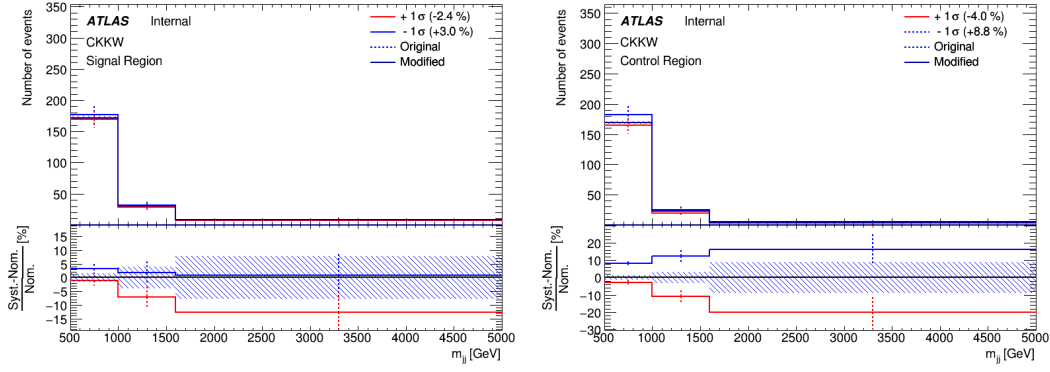


**Figure 12.8.:** The upper plot presents the nominal (both original and modified after smoothing/symmetrisation) along with the variation templates of the CKKW systematic in the inclusive EW- $Z\gamma jj$  fit, plotted as functions of  $m_{jj}$  for SR (left) and CR (right). The lower plot displays the ratio of (systematic-nominal)/nominal in percentage.

An additional method for assessing the impact of individual systematic uncertainties on the overall uncertainty  $\sigma_{total}$  of  $\mu_{EW}$  is the *grouped impact* technique, which is implemented in the **TRexFitter** software. To employ this approach, the uncertainties are initially grouped into categories, such as experimental systematics. For each group, the corresponding nuisance parameters (NPs) are set to their best-fit values, and a new fit is performed to determine the partial uncertainty  $\sigma_{partial}$ . The impact of this specific group of uncertainties is then estimated using the formula  $\sigma_{group} = \sqrt{\sigma_{total}^2 - \sigma_{partial}^2}$ . Table 12.4 presents the grouped impact of the systematic uncertainties on  $\mu_{EW}$ . Furthermore, it presents the estimation of the statistical uncertainty in the data, which is obtained by performing the fit while disregarding all other sources of uncertainty in the process. It is evident from the results that the total uncertainty is predominantly influenced by data statistics. And as expected from previous findings, the major contribution to the systematic uncertainty arises from the uncertainties related to EW theory.

Uncertainty	Value
Monte Carlo Statistics	$\pm 1\%$
Background ( $t\bar{t}\gamma$ , $WZjj$ , $Z$ +jets) Systematics	$\pm 1\%$
Experimental Systematics	$\pm 4\%$
EW- $Z\gamma jj$ Theory Systematics	$+8/-6\%$
QCD- $Z\gamma jj$ Theory Systematics	$\pm 2\%$
Data Statistics	$\pm 9\%$
Total	$+13\%/-12\%$

**Table 12.4.:** The contributions of systematic uncertainties, grouped into categories in the inclusive EW- $Z\gamma jj$  fit. The statistical and total uncertainties are also shown.

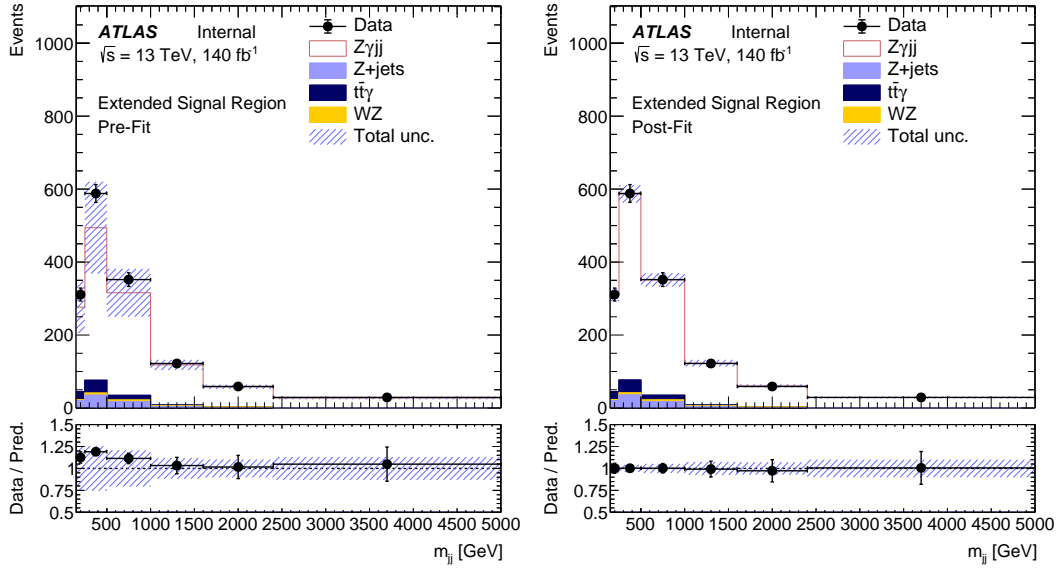


**Figure 12.9.:** Pre-fit (left) and post-fit (right) distributions of  $m_{jj}$  in Extended SR for the inclusive  $Z\gamma jj$  fit. Electron and muon channels are combined. The total uncertainty is shown. The last bin contains overflow events.

The predicted fiducial cross section, determined from simulation in the phase space defined in Section 12.3, is

$$\sigma_{\text{fid, predicted}}^{\text{EW}-Z\gamma jj} = 3.5 \pm 0.2 \text{ fb.} \quad (12.7)$$

where the uncertainty includes the statistics and theory systematics only. The measured signal strength  $\mu_{EW}$  corresponds to  $1.02^{+0.13}_{-0.12}$ . As a result, applying equation 12.6 yields the measured fiducial cross section as

$$\sigma_{\text{fid, measured}}^{\text{EW}-Z\gamma jj} = 3.6 \pm 0.5 \text{ fb.} \quad (12.8)$$

where the uncertainty includes all listed in Table 12.4.

In summary, the measured fiducial cross-section is in agreement with the Standard Model prediction, given by the nominal MADGRAPH5\_aMC@NLO 2.6.5 simulation.

#### 12.4.2. $Z\gamma jj$

Figure 12.9 displays the pre-fit and post-fit distributions of the fit to data, and the corresponding event yields are provided in Tables 12.5 and 12.6. Again, the post-fit distribution shows improved agreement with data, and total uncertainty substantially reduced due to constraints and correlations of NPs from the fit.

	Extended Signal Region		
$Z\gamma jj$	1122.70	$\pm$	163.32
$Z+\text{jets}$	77.00	$\pm$	30.22
$t\bar{t}\gamma$	73.34	$\pm$	11.22
$WZjj$	17.16	$\pm$	3.45
Total	1290.21	$\pm$	166.59
Data	1461		

**Table 12.5.:** Pre-fit yields of the inclusive  $Z\gamma jj$  fit

	Extended Signal Region		
$Z\gamma jj$	1292.15	$\pm$	50.25
$Z+\text{jets}$	77.99	$\pm$	30.50
$t\bar{t}\gamma$	73.54	$\pm$	11.04
$WZjj$	17.15	$\pm$	3.44
Total	1460.83	$\pm$	38.26
Data	1461		

**Table 12.6.:** Post-fit yields of the inclusive  $Z\gamma jj$  fit

The best-fit value of signal strength parameter  $\mu_{Z\gamma jj}$  obtained from the fit is  $1.07 \pm 0.12$ . The results of the fit are displayed in Figures 12.10-12.12, each plot serving a specific purpose:

- Figure 12.10: The correlation matrix of the fit parameters is presented in this plot. Notable (anti-)correlations are evident between the **SCALE\_QCD** NPs and the signal strength parameter  $\mu_{Z\gamma jj}$  (denoted as  $\mu(\text{EWQCD})$  in the plot). This is because the normalisation of the **SCALE\_QCD** NPs, which are uncorrelated into bins and not subtracted before fitting as explained in Section 12.2, is also captured in  $\mu_{Z\gamma jj}$ . Some (anti-)correlations between  $\mu_{Z\gamma jj}$  and EW theory NPs exist, but they are relatively minor.
- Figure 12.11: This plot depicts the pulls of the NPs  $\vec{\theta}$ . A few pulls for the **SCALE\_QCD** and **SCALE\_EW** NPs are visible, but they fall within  $\pm 1\sigma$ . In fact, the decorrelation of **SCALE\_QCD** into bins was performed to address these pulls and constraints.
- Figure 12.12 illustrates the pre-fit and post-fit impacts on the best-fit value of the POI  $\mu_{Z\gamma jj}$ . The ranking plot confirms that the most significant contributors to the uncertainty are primarily associated with QCD and EW theory uncertainties, consistent with the correlation plot.

Finally, Table 12.7 illustrates the grouped impact of the systematic uncertainties on  $\mu_{Z\gamma jj}$ . Additionally, it includes the estimation of the statistical uncertainty in the data, obtained by conducting the fit while excluding all other sources of uncertainty. As anticipated from previous observations, the major contribution to the systematic uncertainty stems from uncertainties associated with theory.

**ATLAS** Internal

zjets_stat	100.0	-0.3	0.2	0.8	0.0	0.3	2.7	-9.1	-8.6	-5.1	0.5	0.4	-10.4
CKKW	-0.3	100.0	0.9	0.2	0.0	1.5	0.3	-21.5	-13.2	3.8	3.4	0.4	9.2
Int	0.2	0.9	100.0	0.0	0.0	-1.3	0.6	15.0	10.7	-1.3	-3.5	-0.2	-22.2
PDF_EW	0.8	0.2	0.0	100.0	-0.0	0.1	-6.1	13.7	13.9	8.5	1.0	-0.8	-11.4
PRW_DATASF	0.0	0.0	0.0	-0.0	100.0	-0.0	-0.0	-0.0	-0.0	-0.0	0.0	0.0	14.6
PS	0.3	1.5	-1.3	0.1	-0.0	100.0	1.1	23.0	18.6	1.9	-6.4	-0.3	-30.3
SCALE_EW	2.7	0.3	0.6	-6.1	-0.0	1.1	100.0	38.9	44.7	39.0	5.2	-2.7	-38.7
SCALE_QCD_Bin1	-9.1	-21.5	15.0	13.7	-0.0	23.0	38.9	100.0	74.1	62.4	35.8	10.5	-74.3
SCALE_QCD_Bin2	-8.6	-13.2	10.7	13.9	-0.0	18.6	44.7	74.1	100.0	70.6	41.3	10.1	-82.0
SCALE_QCD_Bin3	-5.1	3.8	-1.3	8.5	-0.0	1.9	39.0	62.4	70.6	100.0	45.9	3.5	-71.1
SCALE_QCD_high	0.5	3.4	-3.5	1.0	0.0	-6.4	5.2	35.8	41.3	45.9	100.0	-0.4	-43.6
UE	0.4	0.4	-0.2	-0.8	0.0	-0.3	-2.7	10.5	10.1	3.5	-0.4	100.0	-14.7
$\mu(\text{EWQCD})$	-10.4	9.2	-22.2	-11.4	14.6	-30.3	-38.7	-74.3	-82.0	-71.1	-43.6	-14.7	100.0
	zjets_stat	CKKW	Int	PDF_EW	PRW_DATASF	PS	SCALE_EW	SCALE_QCD_Bin1	SCALE_QCD_Bin2	SCALE_QCD_Bin3	SCALE_QCD_high	UE	$\mu(\text{EWQCD})$

**Figure 12.10.:** Correlation coefficients of the parameters in the inclusive  $Z\gamma jj$  fit. All values are given in percentage. Only nuisance parameters with at least one correlation coefficient above 10% are shown.

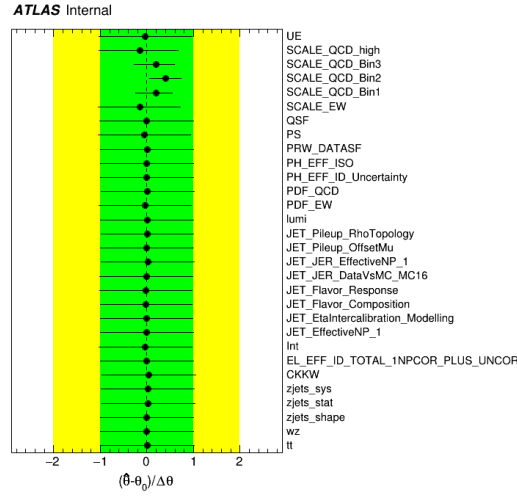


**Figure 12.11.:** Pulls and constraints of all nuisance parameters  $\vec{\theta}$  in the inclusive  $Z\gamma jj$  fit. The green (yellow) area represents the  $\pm 1(2)\sigma$  band on the pre-fit systematic uncertainty. The black dots represent the post-fit values of the NPs, the black lines their post-fit uncertainties.

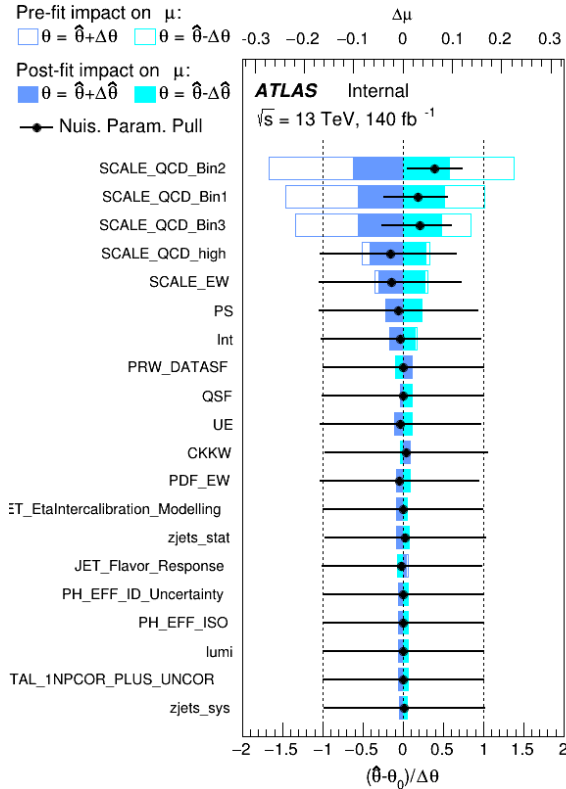


**Figure 12.12.:** Ranking plot showing the impact of each NP on  $\mu_{Z\gamma jj}$  in the inclusive  $Z\gamma jj$  fit. The empty/full boxes show the pre-/post-fit impacts. Only the 20 NPs with the highest post-fit impacts are displayed. The black dots/lines represent the post-fit values/uncertainties of all NPs.

Uncertainty	Value
Monte Carlo Statistics	$\pm 1\%$
Background ( $t\bar{t}\gamma$ , $WZjj$ , $Z$ +jets) Systematics	$\pm 2\%$
Experimental Systematics	$+4/-3\%$
EW- $Z\gamma jj$ Theory Systematics	$+7/-6\%$
QCD- $Z\gamma jj$ Theory Systematics	$+11\%/-10\%$
Data Statistics	$\pm 3\%$
Total	$+12\%/-11\%$

**Table 12.7.:** The contributions of systematic uncertainties, grouped into categories, in the inclusive  $Z\gamma jj$  fit. The statistical and total uncertainties are also shown.

The predicted fiducial cross-section, determined from simulations within the phase space defined in Section 12.3, is

$$\sigma_{\text{fid, predicted}}^{Z\gamma jj} = 15.7^{+5.0}_{-2.6} \text{ fb.} \quad (12.9)$$

where the uncertainty encompasses statistics and theory systematics only. The measured signal strength  $\mu_{Z\gamma jj}$  is found to be  $1.07 \pm 0.12$ . Consequently, the measured fiducial cross-section is

$$\sigma_{\text{fid, measured}}^{Z\gamma jj} = 16.8^{+2.0}_{-1.8} \text{ fb,} \quad (12.10)$$

where the uncertainty includes all listed in Table 12.7.

In conclusion, the measured fiducial cross-section agrees with the Standard Model prediction.

## Chapter 13.

# Differential Measurements

The differential cross section of a measured variable  $X$ , denoted as  $d\sigma/dX$ , is given by:

$$\frac{d\sigma_i}{dX} = \frac{N_i^{signal}}{L \times \Delta X_i} \quad (13.1)$$

where  $i$  represents a particular bin,  $N_i^{signal}$  is the number of signal events in that bin and  $\Delta X_i$  is the bin width. This equation provides the measurement of the differential cross section at the detector level. However, as discussed earlier, the preferred approach is to obtain a measurement in the fiducial phase space for direct comparisons with theoretical predictions. To achieve this, similar to inclusive measurements, corrections for detector acceptance and efficiency must be applied to the detector-level differential cross section. Moreover, since the cross-section is measured in different bins, additional corrections are necessary to address detector resolution-induced event migration between adjacent bins. This entire process of correcting the data for background and detector effects to obtain the underlying distribution at the particle level is known as *unfolding*.

This thesis focuses on the measurement of the first differential cross sections of the EW- $Z\gamma jj$  process, utilising data from the ATLAS detector. In Section 13.1, the unfolding procedure is explained, while Section 13.2 covers the variables studied for unfolding. Detailed information about the setup relevant to this analysis is provided in Section 13.3. The presentation of the data results is found in Section 13.4, and it is worth noting that all the results were accomplished during my PhD. Additionally, for completeness, the thesis includes the differential cross section results of the  $Z\gamma jj$  process- this task was conducted by my collaborators within the analysis team.

### 13.1. Unfolding

As previously mentioned, the measured signal distribution is often subject to distortion due to the limitations of the detector, as depicted schematically in Figure 13.1. Mathematically, for binned distributions, this relation is given by,

$$\nu_i = \sum_j R_{ij} \mu_j$$

where  $\nu_i$  is the  $i$ -th bin at the detector level,  $\mu_j$  is the  $j$ -th bin at the particle level, and  $R_{ij}$  is the  $(i, j)$ -th element of the *response matrix* that describes the probability of finding an event produced in bin  $j$  to be measured in bin  $i$ . When considering background events, the equation

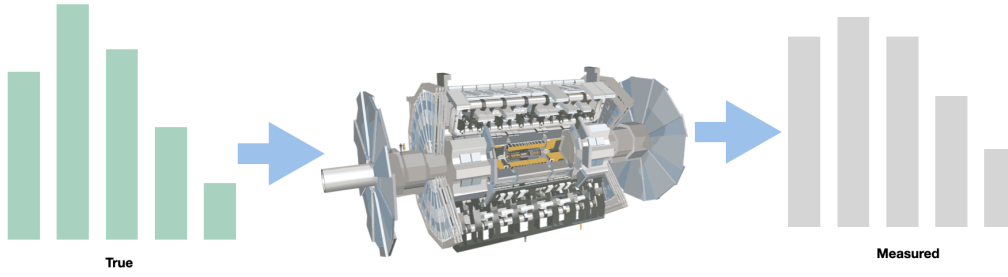


**Figure 13.1.:** Schematic overview showing that the measured distribution is distorted due to the detector effects.

becomes

$$\nu_i = \sum_j R_{ij} \mu_j + \beta_i$$

where  $\beta_i$  represents the background in the  $i$ -th bin at the detector level. Written in matrix form, it translates to

$$\vec{\nu} = R \cdot \vec{\mu} + \vec{\beta}$$

Therefore, unfolding [104] aims to obtain the true distribution  $\vec{\mu}$  as follows

$$\vec{\mu} \equiv R^{-1} \cdot (\vec{\nu} - \vec{\beta}) \quad (13.2)$$

However, this class of *inverse problems* poses well-known statistical challenges. As a result, various unfolding algorithms have been developed to address these challenges. This analysis uses the profile likelihood method, as described later.

### 13.1.1. Unfolding Inputs

As described in Equation 13.2, the essential inputs required for unfolding a measured distribution  $\vec{\nu}$  are:

- i) Background  $\vec{\beta}$ : This accounts for the contribution from background events in the measured distribution. It is estimated using either simulation or data-driven methods.
- ii) Response matrix  $R$ : This matrix describes the relationship between events at the particle and detector levels, specifically, the fiducial and event selection phase spaces. However, it is important to note that while the fiducial criteria are designed to closely match the detector-level event selection criteria, in practice, they are not perfectly aligned, as illustrated in Figure 13.2. To address this misalignment, the response matrix is constructed entirely from simulation and is defined as [106]:

$$R = \frac{1}{\vec{\alpha}} \cdot M \cdot \vec{\epsilon} \quad (13.3)$$

where:

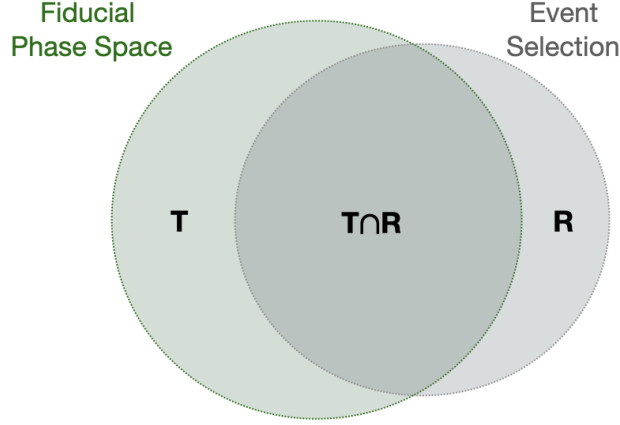


**Figure 13.2.:** A schematic representation of simulated events in the analysis:  $R$  (ellipse to the right) refers to reconstructed events passing the event selection at the detector level, while  $T$  (ellipse to the left) represents truth events in the fiducial phase space at the particle level. Events that satisfy both selection criteria lie in the joint phase space, denoted as  $R \cap T$ .

- Efficiency correction  $\bar{\epsilon}$  accounts for the limited efficiency of the detector, correcting for events that are not reconstructed. It is defined as  $R \cap T / T$ , where  $R$  represents *reconstructed events* that pass the event selection criteria, and  $T$  denotes *truth events* in the fiducial volume.
- Acceptance correction  $\bar{\alpha}$  account for fake events, i.e events that are outside the fiducial region but still selected as part of the detector-level events. The acceptance correction is defined as  $R \cap T / R$ .
- Migration matrix  $M$  is a two-dimensional matrix that accounts for the probability of bin migration, meaning an event generated in bin  $i$  within the fiducial volume gets detected in bin  $j$  at the detector level. The migration matrix is constructed using events that pass both fiducial and detector-level event selections ( $T \cap R$ ). The diagonal components of the migration matrix are related to the *purity*, which corresponds to the fraction of detector-level events that originate from the same bin at the fiducial level.

### 13.1.2. Profile Likelihood Unfolding

The unfolding process in this analysis was carried out using the profile likelihood unfolding (PLU) method implemented with **TRExFitter** [106]. To ensure the reliability and accuracy of this approach, the results were cross-validated against other unfolding algorithms and methods using Asimov data, as outlined in Appendix B.

The PLU procedure simplifies the unfolding problem by transforming it into a more familiar task of fitting the normalisation of distributions. It accomplishes this by applying normalisation factors to each truth level bin of the measured observable.

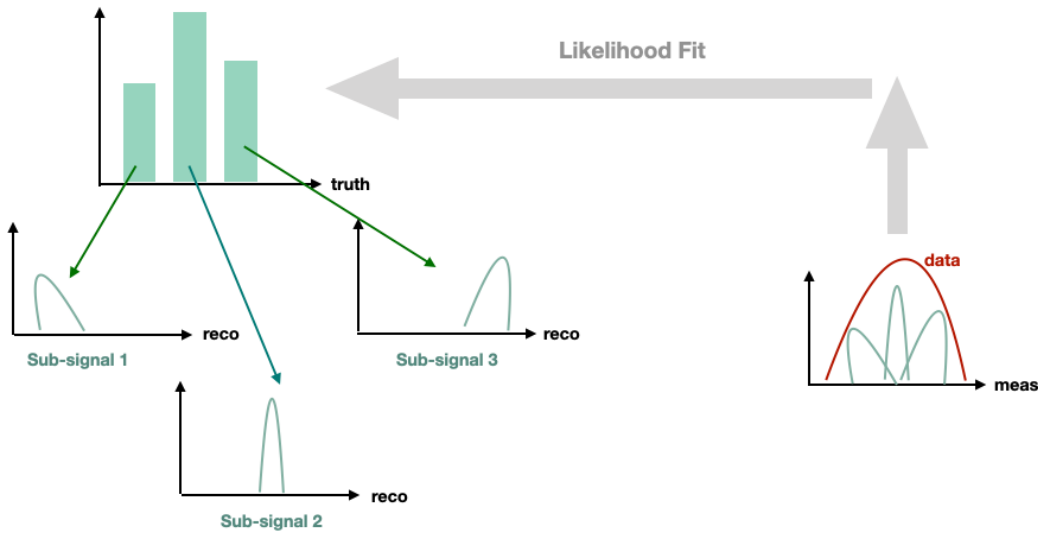


**Figure 13.3.:** Schematic overview showing the profile likelihood unfolding method

To begin, each bin of the truth distribution with  $N_{bins}$  bins is folded to the detector level by multiplying it with the response matrix. This operation yields a set of  $N_{bins}$  detector-level sub-sample templates. The crucial insight to achieve unfolding is recognising that the signal strengths of these folded distributions on the detector level are equivalent to the normalisation factors of the truth distribution. As a result, by performing a standard fit and measuring the normalisation of each folded distribution on the detector level with data, we directly obtain the normalisation factors of the truth level distribution, which is the primary goal of the unfolding process. This procedure is schematically depicted in 13.3.

The primary advantages of using PLU with **TRExFitter** are as follows:

- It allows for straightforward combination of multiple analysis regions. Additionally, systematic uncertainties are naturally incorporated into the measurement as nuisance parameters within the likelihood function and can be constrained by fitting them to the data.
- As depicted in Equation 13.2, traditional unfolding algorithms involve the subtraction of background before initiating the unfolding process. However, PLU takes a different approach by directly fitting background processes to the measured data. Moreover, it provides the advantage of employing bin-by-bin unconstrained normalisation factors (**ShapeFactor** in **TRExFitter**) for background processes during the unfolding procedure.
- The implementation of PLU within the **TRExFitter** framework ensures a cohesive analysis strategy for measuring both inclusive and differential cross-sections, streamlining the overall analysis process.

## 13.2. Variables and Binning

In this analysis, differential cross section measurements have been performed for various variables with different physics motivations, as follows:

- The rapidity difference between two tagging jets  $|\Delta y|$  and the mass of two tagging jets  $m_{jj}$ . These variables are particularly sensitive to the kinematic differences between the EW- $Z\gamma jj$  and QCD- $Z\gamma jj$  processes, making them essential for VBS studies.
- The transverse momentum of the  $Z\gamma$  system  $p_T^{Z\gamma}$ , the transverse energy of the photon  $E_T^\gamma$ , and the difference in azimuthal angle between  $Z\gamma$  and tagging jets  $|\Delta\phi(Z\gamma, jj)|$ . These variables are of interest due to their sensitivity to new physics effects. Notably, the variables  $p_T^{Z\gamma}$  and  $|\Delta\phi(Z\gamma, jj)|$  have been measured differentially for the first time at the LHC.
- Additionally, the transverse momentum of the leading lepton  $p_T^l$  and the leading jet  $p_T^j$  have also been studied as they offer valuable modelling information for both the low and high  $p_T$  regimes.

As is customary, before performing the unfolding with actual data, it was crucial to configure the analysis using Asimov data. To achieve a precision of approximately better than 25% per bin on the unfolded data, the following binning criteria was established:

- Data statistical uncertainty should be less than 10% per bin.
- Purity should be greater than 90% per bin.
- The signal-to-background ratio should exceed 20% per bin.
- Each bin should contain at least roughly 10 events.
- It should be possible to extrapolate QCD- $Z\gamma jj$  MC from CR to SR i.e. the difference between two different QCD MC should not depend on centrality cuts. This evaluation involved examining the ratio between the alternative QCD- $Z\gamma jj$  MC sample (**MADGRAPH**) and the nominal QCD- $Z\gamma jj$  MC sample (**SHERPA 2.2.11**) at the detector-level, as depicted in Figure 13.4.

The optimisation process involved dividing the detector-level simulation into bins with a fine bin width. Then, the bins were merged from left to right until all the specified criteria were satisfied.

### 13.3. Unfolding Procedure

The EW- $Z\gamma jj$  differential cross-section is measured within the SR of the fiducial phase space, as specified in Tables 11.5 and 12.1. The POI is  $\mu_{EW}$  per particle-level bin. Simultaneously, the dominant QCD- $Z\gamma jj$  background is constrained using the **ShapeFactor** setting. Specifically, an unconstrained  $\gamma$  NP<sup>1</sup> is included in the likelihood function for each bin of the QCD- $Z\gamma jj$  template. This nuisance parameter is correlated among regions, meaning that the SR and CR templates need to have the same number of bins. The  $Z$ +jets,  $t\bar{t}\gamma$ , and  $WZjj$  backgrounds are also fit in both regions. Additionally, the small number of EW- $Z\gamma jj$  events in the CR are treated as background and fit to the data as well.

The approach for handling systematic uncertainties in the EW- $Z\gamma jj$  inclusive fit, as described in Section 12.2.1, is also applied in this analysis. However, a minor adjustment is made by

<sup>1</sup> As a reminder, Each  $\gamma$  NP is associated with a specific bin and scales the total MC prediction. Its nominal value is set to 1

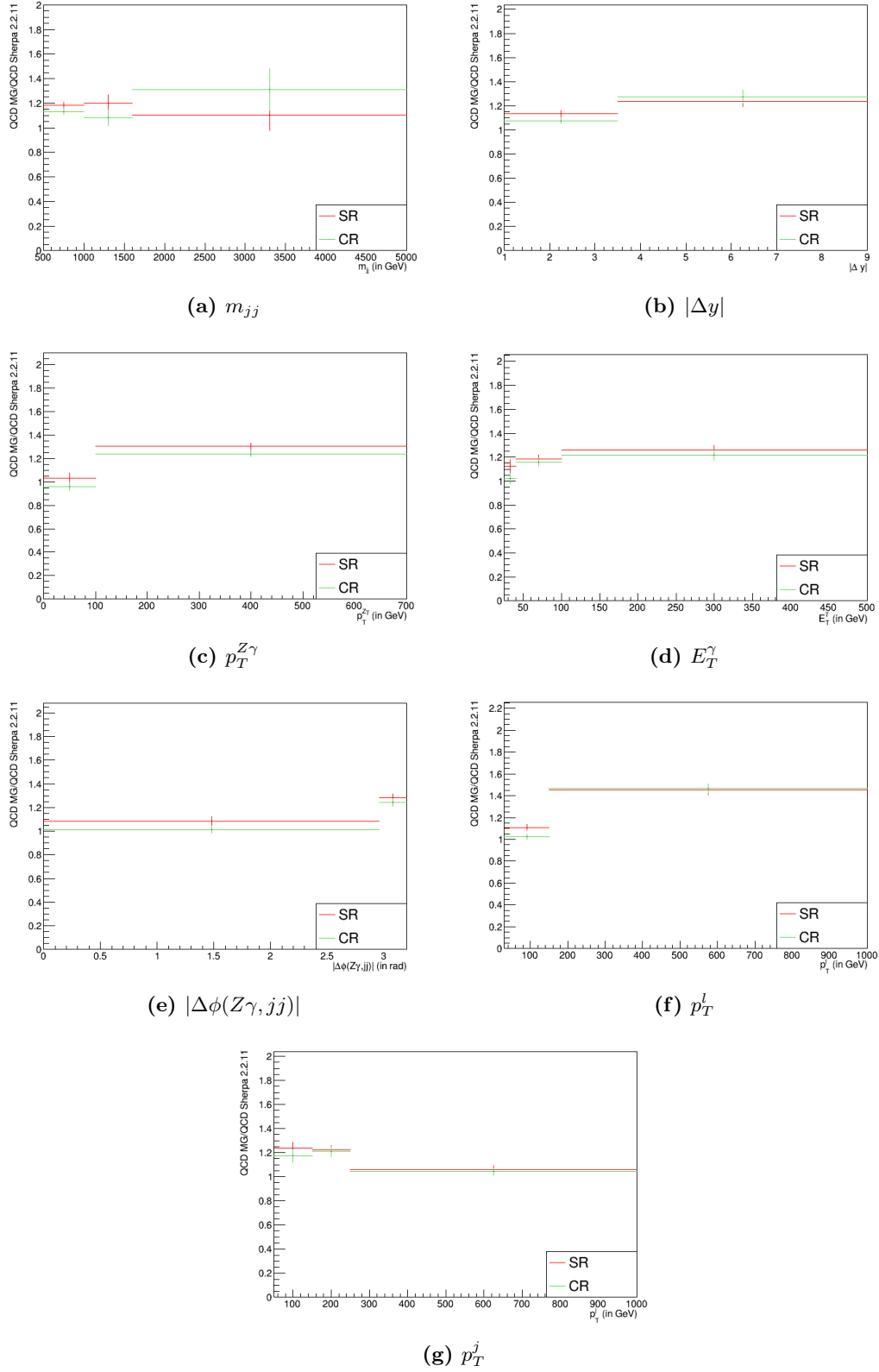


**Figure 13.4.:** Ratio of QCD- $Z\gamma jj$  MADGRAPH to SHERPA 2.2.11 MC samples in SR and CR. All overflow events are in the last bin. The uncertainties are from MC statistics.

setting the pruning threshold to 1% for both shape and normalisation components. This strategy was determined based on the results obtained from unfolding with Asimov data, although these results are not presented in this thesis<sup>2</sup>. No additional uncertainty is attributed to the unfolding procedure, as tests indicate it to be negligible.

Figures 13.5-13.7 show the migration matrix, efficiency correction, and acceptance correction for each studied variable. On average, the acceptance corrections are around 90%, while the efficiency corrections are approximately 45%<sup>3</sup>. Most variables exhibit high purity in the migration matrices, around 90%, except for  $|\Delta\phi(Z\gamma, jj)|$ , which shows a purity of around 80%.

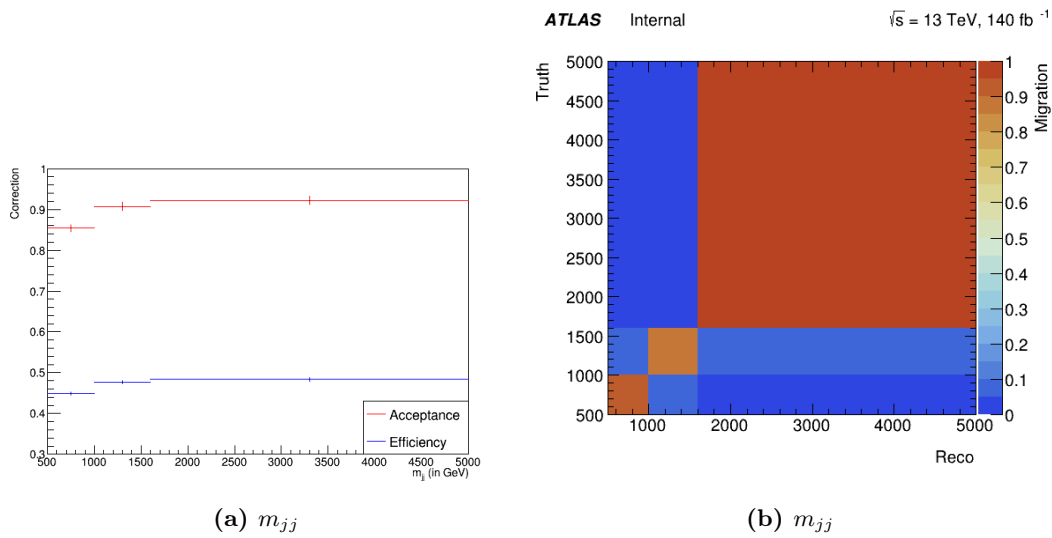


**Figure 13.5.:** Left: acceptance and efficiency corrections, Right: migration matrix with truth events on the  $y$ -axis and reconstructed events on the  $x$ -axis

<sup>2</sup> Although the author of the thesis conducted Asimov studies, they are intentionally omitted to ensure that the main results of the analysis remain the central focus of the thesis.

<sup>3</sup> This drop in efficiency mainly arises from jet cuts

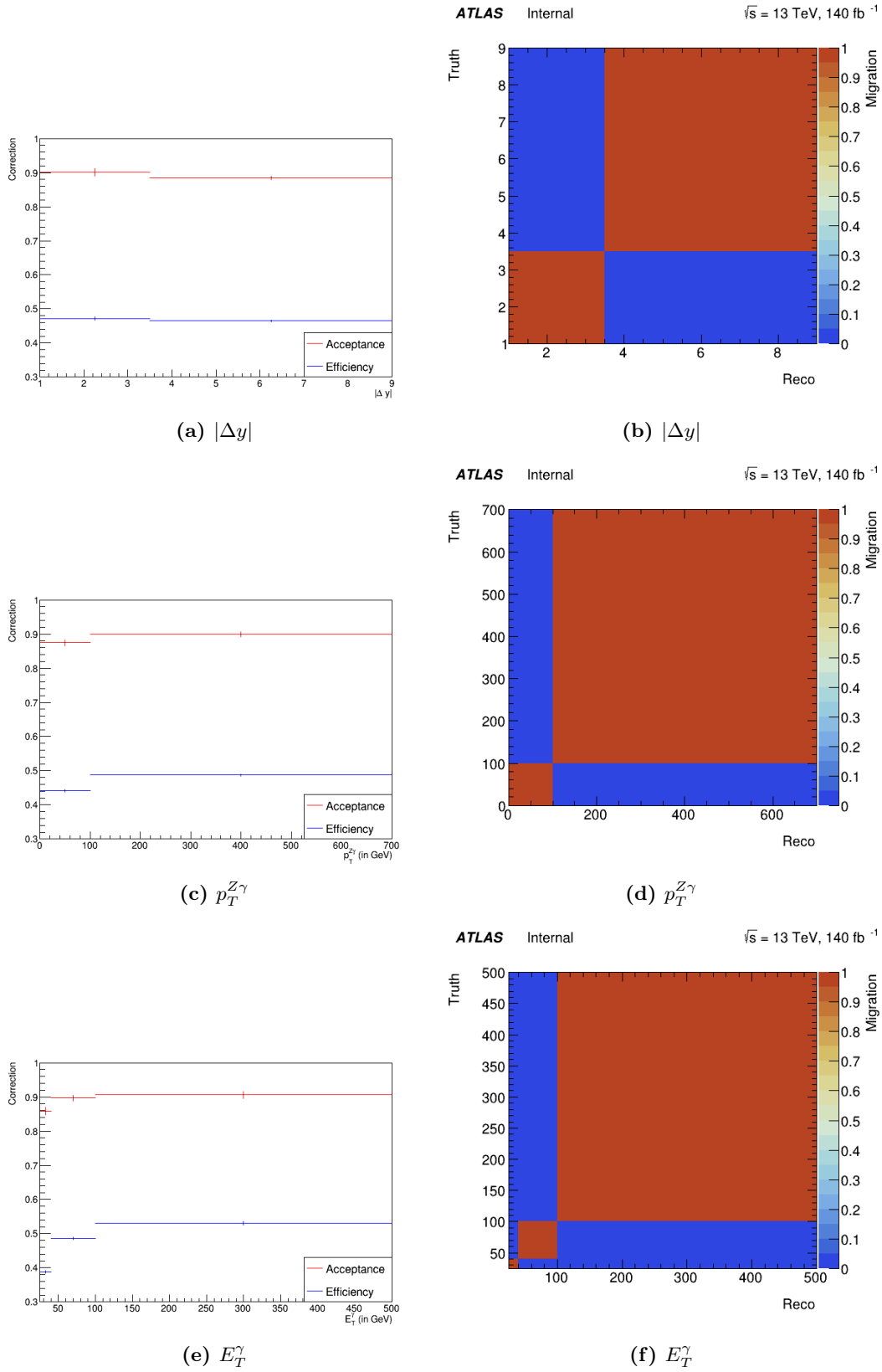


**Figure 13.6.:** Left: acceptance and efficiency corrections, Right: migration matrix with truth events on the  $y$ -axis and reconstructed events on the  $x$ -axis

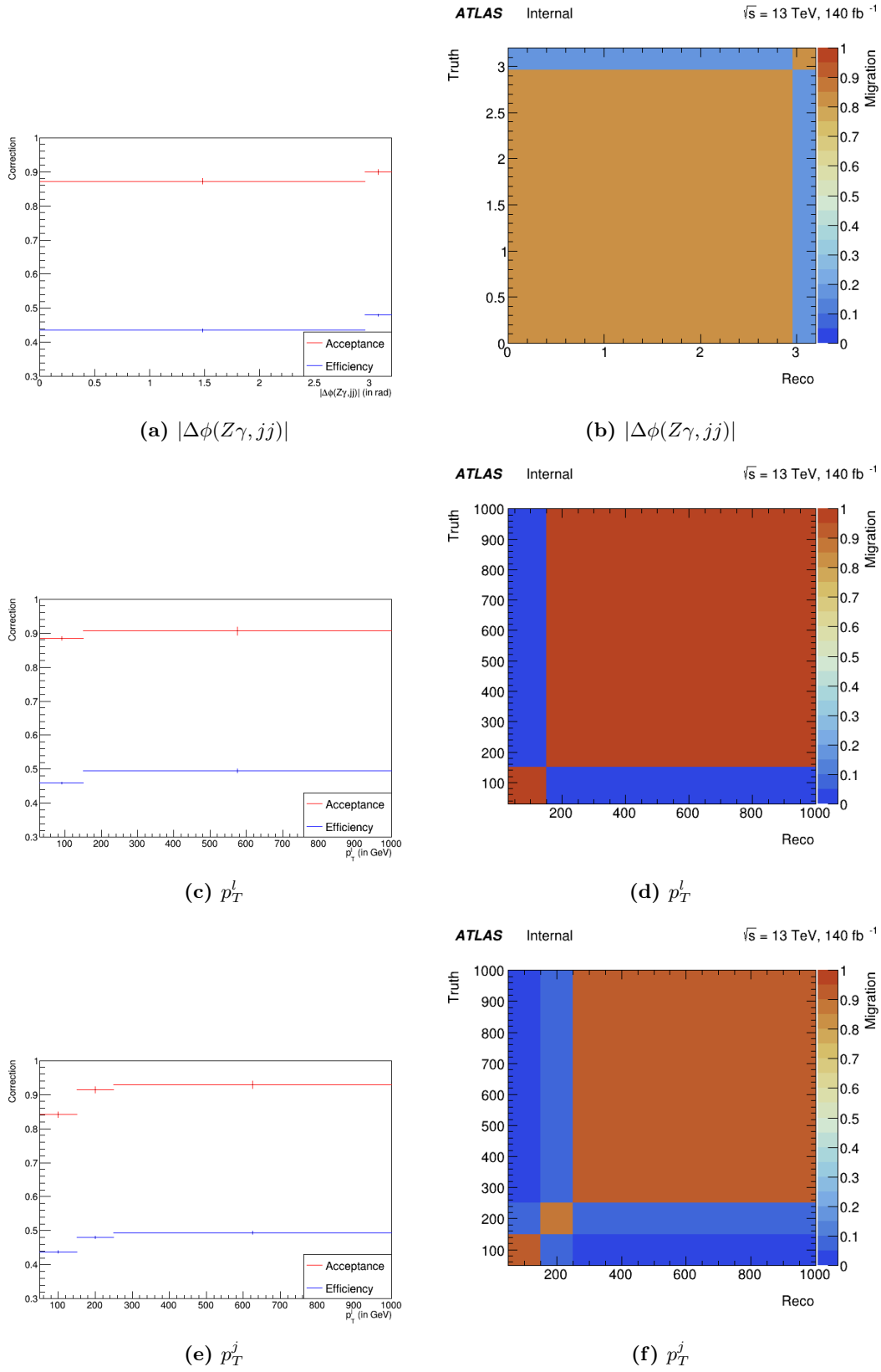


**Figure 13.7.:** Left: acceptance and efficiency corrections, Right: migration matrix with truth events on the  $y$ -axis and reconstructed events on the  $x$ -axis

## 13.4. Results

### 13.4.1. EW- $Z\gamma jj$

The differential cross-section results are displayed in Figures 13.8 and 13.9. The nominal EW- $Z\gamma jj$  MADGRAPH predictions consistently match the data well within uncertainties, except for  $|\Delta\phi(Z\gamma, jj)|$ , where a discrepancy of approximately two standard deviations is observed in the lowest bin.

Regarding the systematic uncertainties, no unexpected correlations, pulls, or constraints were observed during the analysis. In each bin, the dominant impact arises from the  $\gamma_{QCD}$  NP. Figure 13.10 illustrates the grouped impact of systematic uncertainties on  $\mu_{EW}$  per bin. The uncertainties are measured to be approximately 25% of the total uncertainty in each bin. It is evident that data statistics primarily dominate the uncertainties.

Additionally, Table 13.1 provides the differential cross-section values measured in each bin for the variables studied, along with the total cross-section for each variable. Notably, the total cross-section sum aligns consistently with the measured inclusive cross-section value of  $3.6 \pm 0.5$  fb.

The noted disparity in outcomes between summing bins from differential measurements and conducting an inclusive measurement can be ascribed to the nuanced methodologies employed in each case. In the inclusive measurement, the analysis employs a singular global scaling factor. In contrast, in the differential measurement, the analysis incorporates multiple scaling factors corresponding to EW and QCD processes for each bin. Additionally, the systematic increase in the total cross-section from the differential analysis compared to the cross-section from the inclusive measurement signifies the existence of a discernible shape trend (difference between data and Monte Carlo simulations). This trend is appropriately taken into account in the differential analysis.

	Bin 1 (fb)	Bin 2 (fb)	Bin 3 (fb)	Sum (fb)
$m_{jj}$	1.56	1.21	1.02	3.79
$E_T^\gamma$	1.34	1.52	0.96	3.82
$p_T^j$	1.75	1.23	0.79	3.77
$p_T^l$	3.31	0.5	-	3.81
$p_T^{Z\gamma}$	1.92	1.88	-	3.8
$ \Delta y $	0.93	2.87	-	3.8
$ \Delta\phi(Z\gamma, jj) $	1.84	2.01	-	3.85

**Table 13.1.:** Cross-section per bin for each variable in the EW- $Z\gamma jj$  differential study, along with their sum.

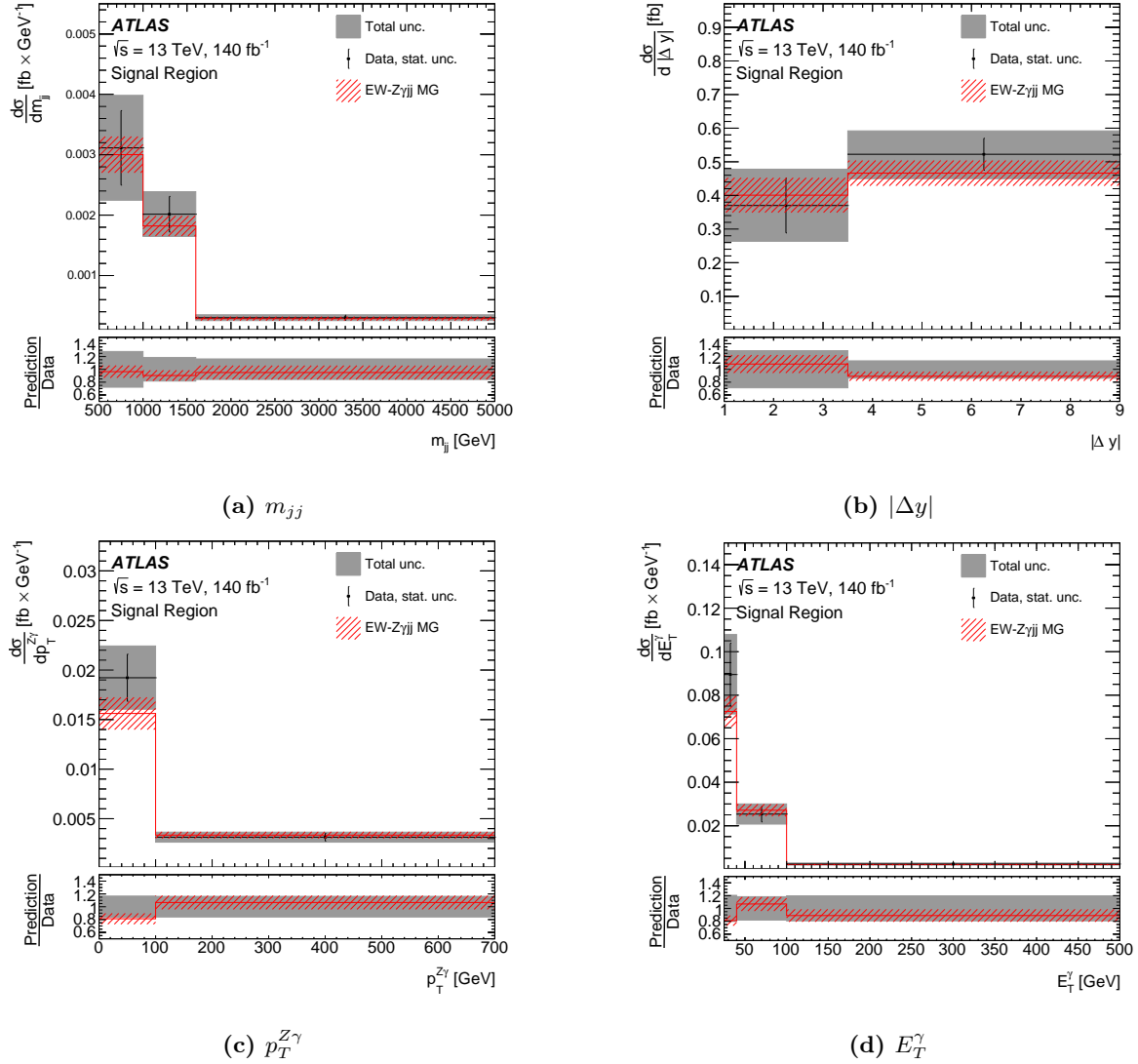


**Figure 13.8.:** The EW- $Z\gamma jj$  differential cross-section in the fiducial region. The lower panels show the ratios of the MC predictions to the data. The band around the unfolded data represents the total uncertainty. The hatched area represents the uncertainty in the prediction. All overflow events are included in the last bin.

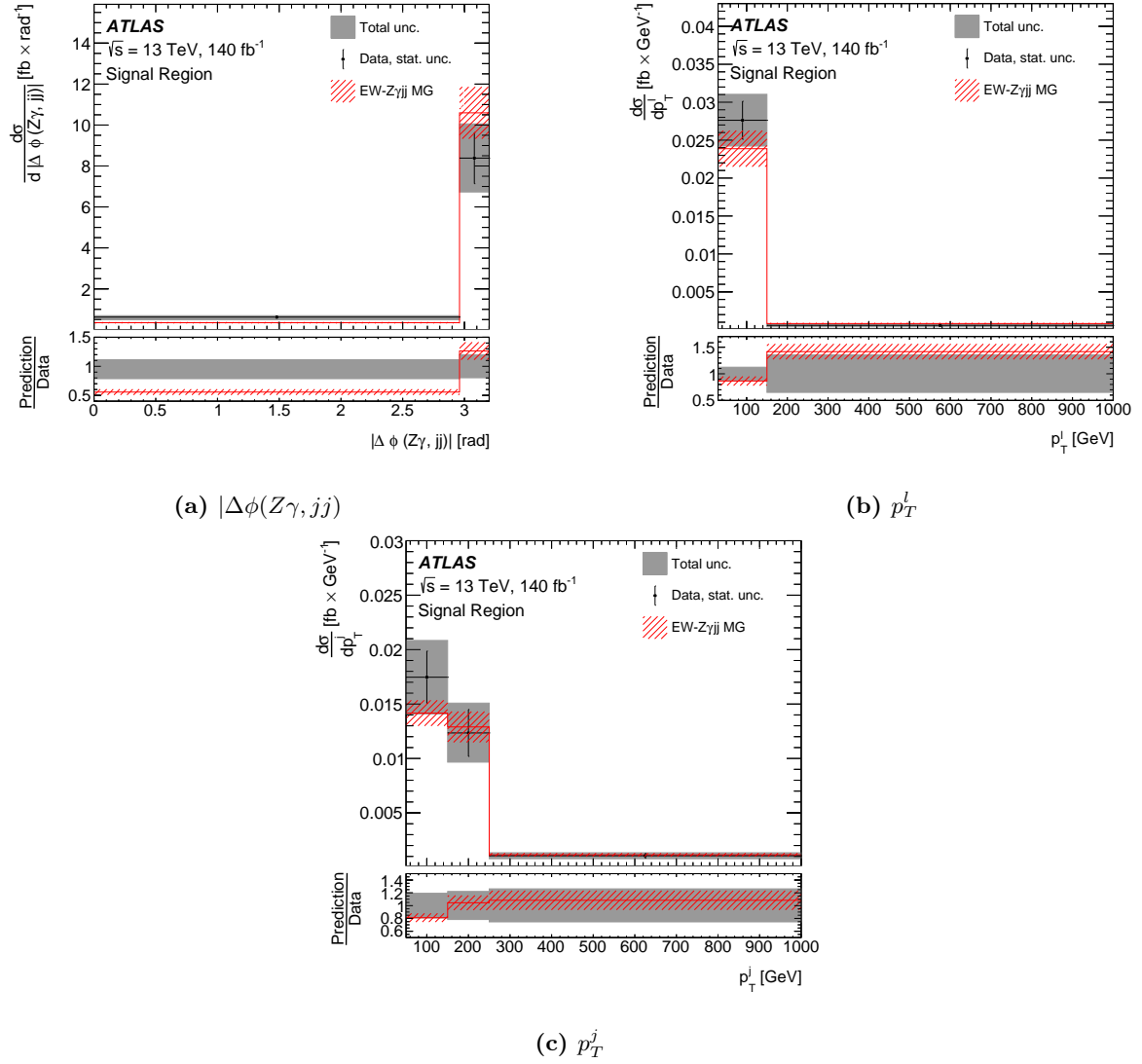


**Figure 13.9.:** The EW- $Z\gamma jj$  differential cross-section in the fiducial region. The lower panels show the ratios of the MC predictions to the data. The band around the unfolded data represents the total uncertainty. The hatched area represents the uncertainty in the prediction. All overflow events are included in the last bin.

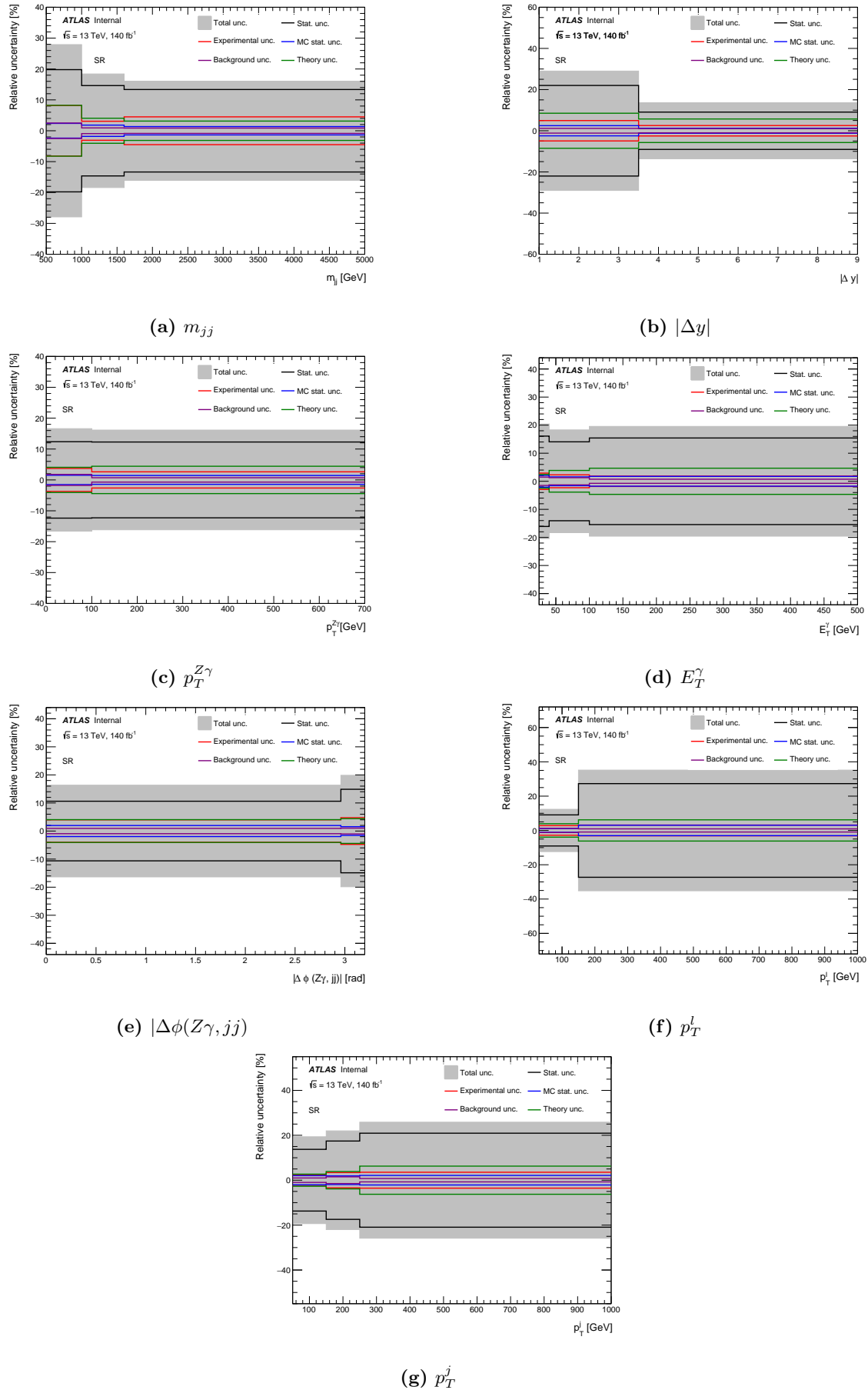


**Figure 13.10.:** The contributions of systematic uncertainties, grouped into categories in the EW- $Z\gamma jj$  differential fit. The statistical and total uncertainties are also shown.

### 13.4.2. $Z\gamma jj$

The  $Z\gamma jj$  differential cross sections have been determined in the extended fiducial region. Figures 13.11 and 13.12 present the differential cross-section results obtained for the same variables as the EW- $Z\gamma jj$  process. However, the binning for these measurements has been optimized specifically for the  $Z\gamma jj$  analysis. Additionally, two novel variables,  $p_T^Z$  and  $\zeta(Z\gamma)$ , have been measured for the very first time at the LHC. These measurements were demonstrate a precision of approximately 10% on average. In conclusion, the predictions for each variable consistently exhibit good alignment with the observed data, taking into account the associated uncertainties.

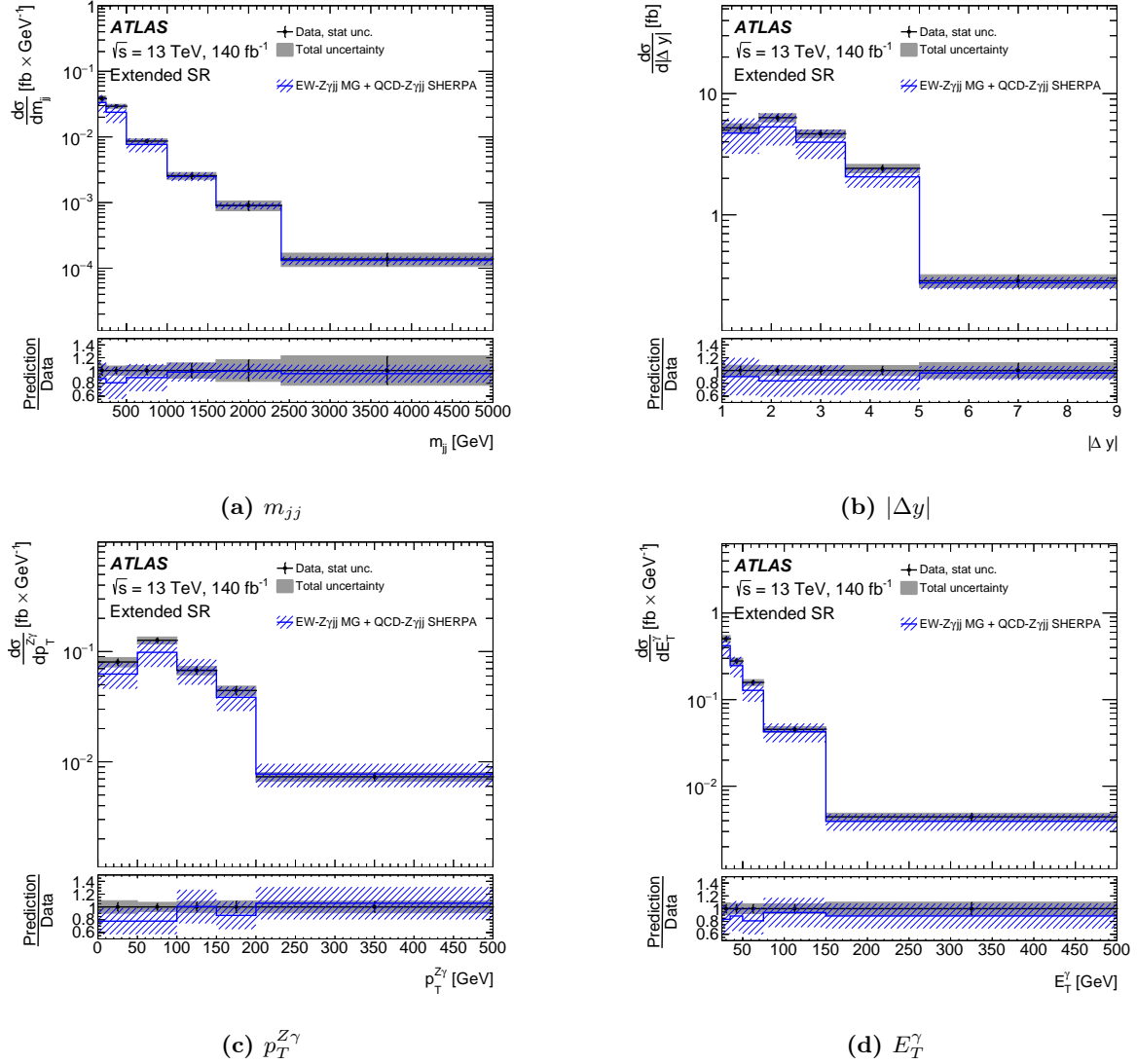


**Figure 13.11.:** The  $Z\gamma jj$  differential cross-section in the extended fiducial region. The lower panels show the ratios of the MC predictions to the data. The band around the unfolded data represents the total uncertainty. The hatched area represents the uncertainty in the prediction. All overflow events are included in the last bin.

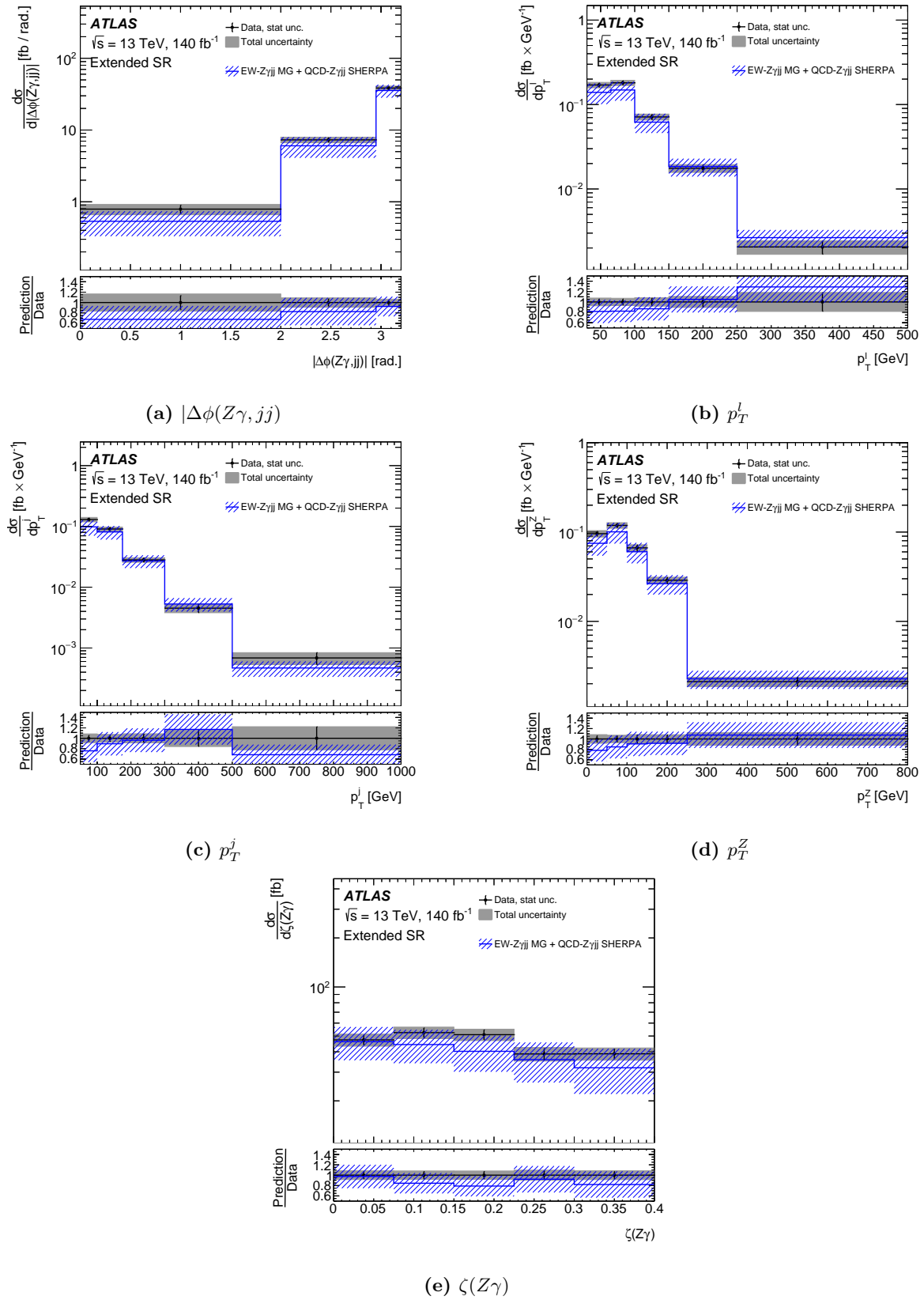


**Figure 13.12.:** The  $Z\gamma jj$  differential cross-section in the extended fiducial region. The lower panels show the ratios of the MC predictions to the data. The band around the unfolded data represents the total uncertainty. The hatched area represents the uncertainty in the prediction. All overflow events are included in the last bin.

# Chapter 14.

## Conclusion

This thesis explores the electroweak production of a  $Z\gamma$  pair associated with two jets, where the  $Z$  boson decays into electrons and muons. The analysis utilises  $140 \text{ fb}^{-1}$  of proton–proton collision data recorded at  $\sqrt{s} = 13 \text{ TeV}$  by the ATLAS detector in LHC Run-2.

The primary outcome is the observation of the EW- $Z\gamma jj$  process with the ATLAS detector, resulting in a measured cross-section of  $\sigma_{\text{fid, measured}}^{\text{EW-}Z\gamma jj} = 3.6 \pm 0.5 \text{ fb}$ . This result is consistent with the SM prediction from MADGRAPH5\_aMC@NLO 2.6.5. The primary source of uncertainty is the theoretical modelling of the EW- $Z\gamma jj$  process. The CMS collaboration has also observed this process in a similar phase space, with results consistent with SM predictions and a precision of approximately 14% too.

The thesis also presents the production cross-section measurement of the  $Z\gamma jj$  process,  $\sigma_{\text{fid, measured}}^{Z\gamma jj} = 16.8^{+2.0}_{-1.8} \text{ fb}$ . Predicted cross-sections from MADGRAPH5\_aMC@NLO 2.6.5 and SHERPA 2.2.11 align with the measured values, demonstrating consistency with SM predictions. The main uncertainty in this measurement arises from the theoretical modelling of the QCD- $Z\gamma jj$  process. The CMS collaboration has achieved comparable results, showing consistency with SM predictions and a precision of around 11% as well.

Moreover, the thesis presents the first set of differential cross-section measurements for the EW- $Z\gamma jj$  process using the ATLAS detector. Examined distributions include the mass of the two tagging jets, the rapidity difference between them, the transverse energy of the photon, the difference in azimuthal angle between the  $Z\gamma$  system and the two jets, as well as the transverse momentum of the leading lepton, the leading jet, and the  $Z\gamma$  system. Notably, the measurements of  $p_T^{Z\gamma}$  and  $\Delta\phi(Z\gamma, jj)$  were performed differentially for the first time at the LHC. All findings are consistent with SM expectations, with data statistics being the primary source of uncertainty. It should be noted that the analysis was designed to uphold a precision of 30% for each bin. Consequently, certain distributions could not be explored beyond two bins.

CMS has also conducted differential cross-section measurements for the same process, utilising single-variable bins for the transverse momentum of the leading photon, leading lepton, and leading jet. Additionally, two-variable bins were employed for the mass and rapidity difference of the two tagging jets. Once again, all results align with SM predictions. However, in their analysis, the precision of some bins extends to around 50% due to a greater number of bins.

Furthermore, the thesis includes differential measurements for the  $Z\gamma jj$  process involving the variables described earlier, along with the transverse momentum of the  $Z$  boson and the centrality of the  $Z\gamma$  system. These latter two variables were measured for the first time at the LHC.

All these ATLAS results have culminated in a publication, marking the first ATLAS publication to include differential measurements of an EW- $VVjj$  process. These outcomes will significantly contribute to future studies, especially in the exploration of aQGCs and in assisting MC modelling studies.

Currently, employing the complete Run-2 dataset, the statistical uncertainty associated with the EW- $Z\gamma jj$  process is 9%. In the upcoming Run-3 of the LHC, with an estimated  $300 \text{ fb}^{-1}$  of data, this uncertainty is expected to decrease to around 6%. Additionally, the Run-3 analysis would benefit from an improved quark-gluon jet tagger adept at differentiating between quark and gluon jets. This development would be particularly significant as VBS processes always include final state quark jets.

The thesis also addresses the forthcoming HL-LHC upgrade that aims to accumulate an extensive dataset of  $3000 \text{ fb}^{-1}$ . This upgrade will introduce a challenging environment marked by a significant increase in pileup. Consequently, the ATLAS detector is slated for substantial enhancements, including the integration of a highly precise Inner Tracker (ITk) capable of extending pseudorapidity up to  $|\eta| = 4.0$ , and the introduction of a High Granularity Timing Detector (HGTD) expected to enhance the reconstruction of jets and leptons in the forward region. These modifications are strategically aligned with the unique topology of a VBS process, featuring central bosons and two highly energetic forward jets. Thus, this upgrade is set to bring substantial benefits to the EW- $Z\gamma jj$  analysis.

It should be noted that in the current Run-2 analysis, the primary systematic uncertainty arises from theory modelling. Consequently, EW NLO corrections will play a pivotal role in the upcoming LHC runs. Additionally, the EW-QCD  $Z\gamma jj$  interference has been treated as a systematic uncertainty since its magnitude is comparable to the current Run-2 statistical uncertainty. However, in the upcoming HL-LHC era with expected statistical precision of about 2%, the interference cannot be handled in the same manner. One possible approach for the HL-LHC analysis would be to include the interference in the cross-section fit, akin to current practices in the  $WZjj$  or  $W^\pm W^\pm jj$  analyses conducted with the ATLAS detector.

Finally, the thesis presents tests on the ATLAS liquid argon calibration boards for the HL-LHC upgrade. Its main specifications involve withstanding the high radiation levels expected at the HL-LHC and maintaining high uniformity among the calibration channels. In this regard, extensive radiation studies were executed using a calibration chip prototype, and comprehensive uniformity tests were devised and conducted with the first prototype of the HL-LHC calibration board. None of the tested prototypes met these requirements; however, the insights gained from this study will help design the final calibration board.

## Appendix A.

### Comparison of Tools: HistFactory and TRexFitter

In 2021, the ATLAS collaboration published the fiducial cross-section measurement of the  $EW\text{-}Z\gamma jj$  process using the full LHC Run2 dataset [92]. The results were obtained using the HistFactory [107] fitting tool. To ensure the reliability of the TRexFitter [106] tool for the analysis presented in this thesis, the same analysis was replicated using TRexFitter.

The main distinctions between the analysis presented in this thesis and the one in [92] are as follows:

- In the previous analysis, the nominal QCD- $Z\gamma jj$  sample used was MADGRAPH, whereas in the current analysis, it has been replaced with the SHERPA 2.2.11 sample.
- The starting point of the measurement region was previously  $m_{jj} = 150$  GeV, but in the current analysis, it has been shifted to 500 GeV.
- The luminosity uncertainty propagated across all samples and regions was  $\pm 1.7\%$  in the previous analysis, following the standard ATLAS recommendation at that time. However, in the current analysis, the recommendation is  $\pm 0.83\%$ .
- In the previous analysis,  $\mu_{QCD}$  was fit separately in the Signal Region (SR) and Control Region (CR). In contrast, the current analysis fits  $\mu_{QCD}$  simultaneously in SR and CR.
- In the previous analysis,  $\mu_{EW}$  was measured simultaneously in SR and CR. However, in the current analysis,  $\mu_{EW}$  is measured solely in SR.
- In the previous analysis, the normalisation components of SCALE\_EW and SCALE\_QCD were separated from the shape components, but they were kept in the fit. In the current analysis, the normalisation components are removed before fitting.

Therefore, for the repeat analysis with TRexFitter, all the mentioned changes were incorporated, except for the last one. An Asimov fit was performed to make the comparison between the two tools.

Table A.1 presents the fit results for the POI  $\mu_{EW}$  and the QCD- $Z\gamma jj$  normalisation factors obtained using both the HistFactory and TRexFitter tools. As expected, the mean value of all parameters consistently remains at 1 since Asimov data is used. Importantly, the obtained  $\mu_{EW}$  is identical in both cases. However, there are some differences in the uncertainties associated with the  $\mu_{QCD}$  parameters, attributed to the distinct treatment of the SCALE\_QCD uncertainty.

Parameter	HistFactory	TRexFitter
$\mu_{EW}$	$1 \pm 0.12$	$1 \pm 0.12$
$\mu_{QCD}^{SR}$	$1^{+0.16}_{-0.15}$	$1 \pm 0.10$
$\mu_{QCD}^{CR}$	$1^{+0.17}_{-0.16}$	$1 \pm 0.07$

**Table A.1.:** Best-fit values of POI and QCD- $Z\gamma jj$  normalisation factors along with their  $\pm 1\sigma$  uncertainties using two different tools

Parameter	HistFactory	TRexFitter
Experimental Systematics	$\pm 5\%$	$\pm 5\%$
EW Theory Systematics	$+5/-4\%$	$+5/-4\%$
QCD Theory Systematics	$+5/-4\%$	$\pm 3\%$
Background ( $t\bar{t}\gamma$ , $WZjj$ , $Z + \text{jets}$ ) Systematics	$\pm 1\%$	$\pm 1\%$
MC Statistics	$\pm 1\%$	$\pm 1\%$

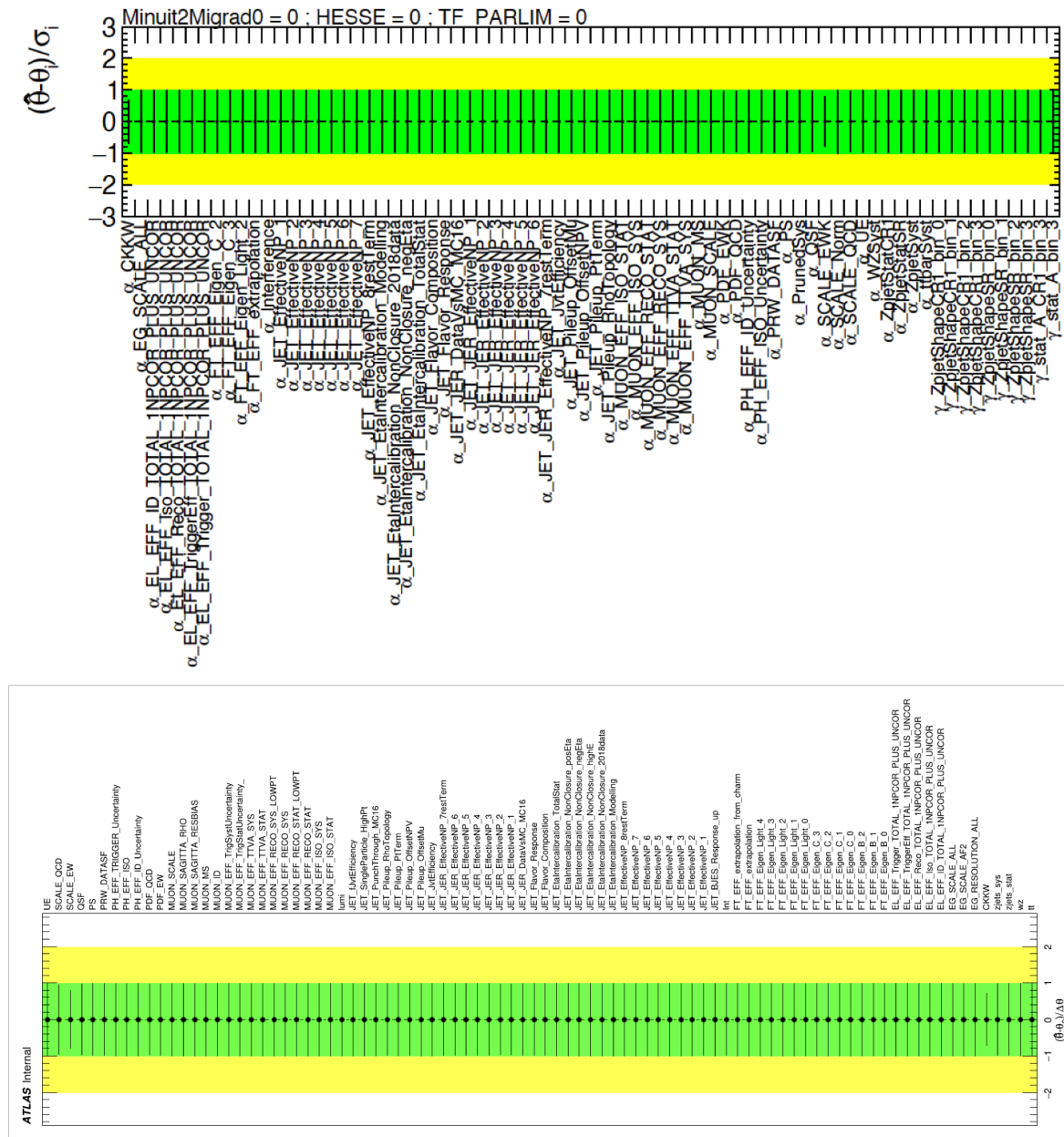
**Table A.2.:** The contributions of systematic uncertainties, grouped into categories, for the two tools.

Figure A.1 illustrates the pulls of the NPs using both tools. As expected, no significant pulls are observed in the NPs since the results are based on Asimov data. Notably, both plots demonstrate constraints in the **SCALE\_EW** and **CKKW** NPs, indicating that the fitting tools exhibit consistent behavior.

Figure A.2 presents the impact of the uncertainties on  $\mu_{EW}$  using both tools. In both cases, the uncertainties with substantial impact are associated with parton shower, pileup-reweighting, CKKW scale, and PDF scale of the EW- $Z\gamma jj$  process. However, the slight variations in the rankings can be attributed to the different handling of the **SCALE\_QCD** and **SCALE\_EW** uncertainties.

Finally, Table A.2 illustrates the grouped impact of the systematic uncertainties on  $\mu_{EW}$  using both tools. In all groups, both tools yield consistent results, except for QCD Theory where some discrepancy is observed, again due to the different treatment of the **QCD\_SCALE** uncertainty.

In conclusion, despite some minor discrepancies in the treatment of systematics, the two tools provided comparable results, thereby validating the use of **TRexFitter** in this analysis.



**Figure A.1.:** Pulls and constraints of all NPs using HistFactory (top) and TRexFitter (below). The green (yellow) area represents the  $\pm 1(2)\sigma$  band on the pre-fit systematic uncertainty. The black dots represent the post-fit values of the NPs, the black lines their post-fit uncertainties.

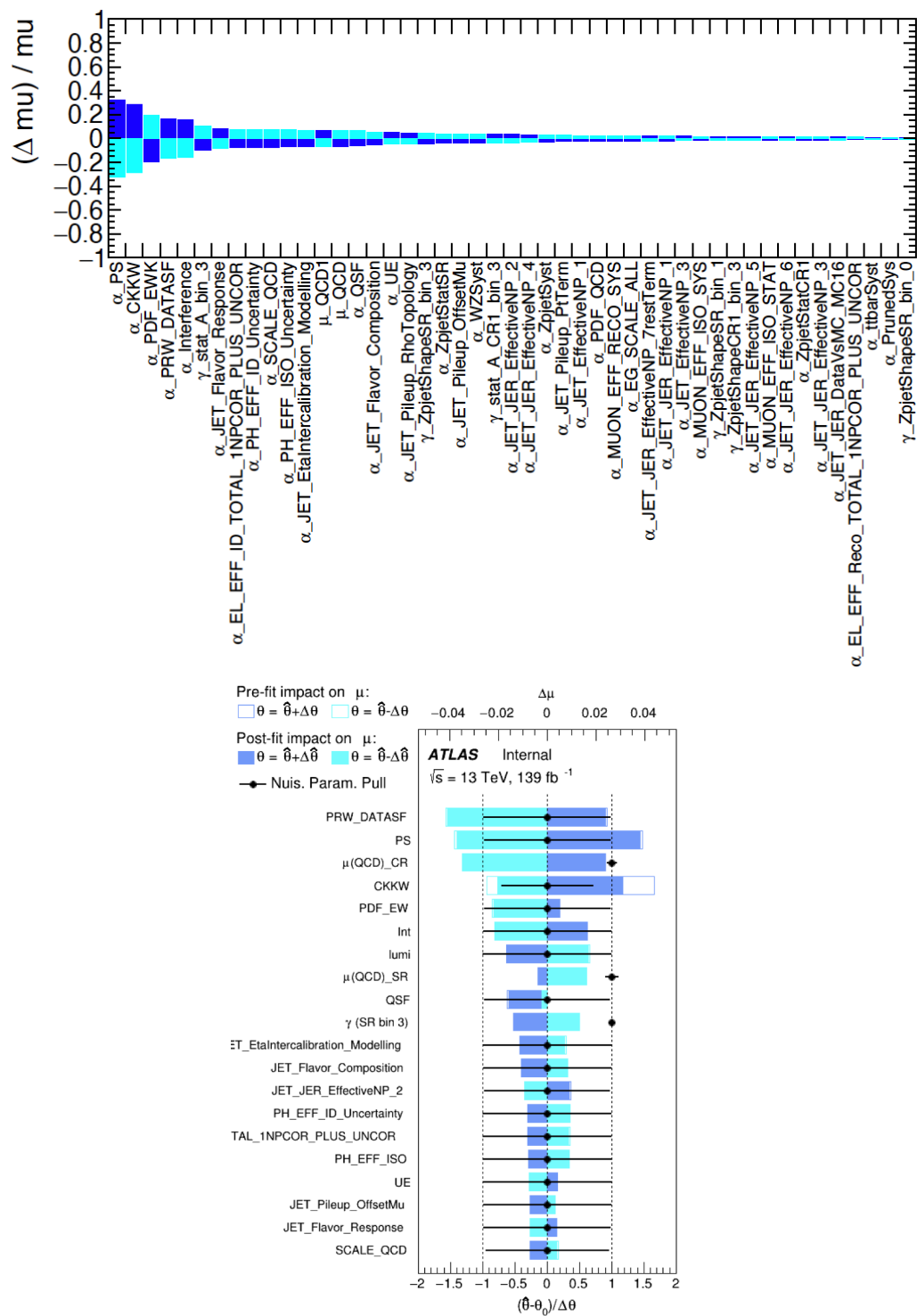


**Figure A.2.:** Ranking plot showing the impact of each NP on  $\mu_{EW}$  using `HistFactory` (top) and `TRExFitter` (below). The empty/full boxes show the pre-/post-fit impacts. Only the NPs with the highest post-fit impacts are displayed. The black dots/lines represent the post-fit values/uncertainties of all NPs.

## Appendix B.

# Comparison of Unfolding Algorithms and Tools

To ensure result consistency among different algorithms and tools, the  $Z\gamma jj$  Asimov data was subject to unfolding using a variety of techniques:

- Matrix Inversion Algorithm[109] using VIPUnfolding Tool:

In this method, the unfolding process involves inverting the response matrix to background subtracted data, as indicated by Equation 13.2. It is important to highlight that for this algorithm to work, the number of bins at the truth and detector levels must be the same, enabling the existence of the inverse of the response matrix. Furthermore, to ensure the uniqueness of the inverse response matrix, it must exhibit strict diagonal dominance, with elements along the main diagonal exceeding 50%. Lastly, it is worth mentioning that the matrix inversion estimate can also be interpreted as a solution derived from the principle of maximum likelihood.

- Iterative Bayesian Algorithm[110] using VIPUnfolding Tool

The iterative Bayesian algorithm, developed by D’Agostini and based on Bayes’ theorem, estimates the number of unfolded events for each truth bin, denoted as  $n(t_i)$ , by multiplying the conditional probability  $P(t_i|r_j)$  with the number of events in the corresponding reconstructed bin,  $n(r_j)$ :

$$n(t_i) = \sum_{j=1}^{n_r} P(t_i|r_j) \cdot n(r_j) \quad (\text{B.1})$$

Here,  $n_r$  represents the number of reconstructed bins. The conditional probability  $P(t_i|r_j)$  is calculated using Bayes’ theorem:

$$P(t_i|r_j) = \frac{P(r_j|t_i) \cdot P(t_i)}{\sum_{l=1}^{n_t} P(r_j|t_l) \cdot P(t_l)} \quad (\text{B.2})$$

where  $n_t$  is the number of truth bins, and  $P(r_j|t_i)$  is obtained from the response matrix. Since the probability of the truth,  $P(t_i)$ , is not known beforehand, an assumption is required, often based on the Monte Carlo (MC) truth distribution. To mitigate the impact of this assumption, the method is applied iteratively. In summary, in this algorithm, the input distribution to be unfolded in an iteration is the unfolded output of the previous one.

- Profile Likelihood Algorithm using TRExFitter Tool

In this approach, the unfolding is performed by conducting a simultaneous maximum likelihood fit of several detector-level signal sub-samples with data, as described in Section [13.2](#).

## B.1. Regularisation

The matrix inversion algorithm assumes that fluctuations in background subtracted data arise from real detector effects rather than statistical variations. Consequently, it incorporates these fluctuations into the unfolded result, leading to significant bin-to-bin variations.<sup>1</sup> Such "oscillation patterns" are frequently observed in inverse problems.

To achieve a more desirable solution, *regularisation* techniques [\[109\]](#) can be applied to smoothen these oscillation patterns. However, it is crucial to be aware that regularisation might introduce bias into the unfolded result. Therefore, in this thesis, the unregularised matrix inversion algorithm was utilised to ensure an unbiased unfolded outcome, adhering to ATLAS recommendations that advocate publishing unregularised results.

Similarly, the profile likelihood algorithm offers the option to include additional constraints in the likelihood term for regularisation purposes. However, in this study, the unregularised profile likelihood was employed.

Furthermore, the number of iterations in the iterative Bayesian algorithm serves as a form of regularisation. Striking a balance between reducing uncertainties and avoiding bias is vital to achieve a reliable unfolding outcome. Thus, the number of iterations was varied in this study to assess its impact on the results.

## B.2. Unfolding Setup

In this study, the unfolding of the  $Z\gamma jj$   $m_{jj}$  Asimov data was performed in the extended SR. The following uncertainties were taken into account during the unfolding process:

- Data statistical uncertainty
- Systematic uncertainties related to background processes ( $t\bar{t}\gamma$ ,  $WZjj$ ,  $Z$ +jets)
- Noteworthy experimental systematic uncertainties, which are detailed in Table [B.1](#)

However, no theory systematic uncertainty or unfolding uncertainty was considered and propagated in this particular study.

---

<sup>1</sup> It is important to emphasise that when the unfolded result obtained through matrix inversion is folded back using the response matrix, it precisely matches the data. Therefore, the result is not incorrect. However, it is considered undesirable because it lacks resemblance to the original distribution and exhibits notable correlations between bins.

---

PRW_DATASF
PH_EFF_ID_Uncertainty
JET_EffectiveNP_1
JET_JER_EffectiveNP_2
JET_JER_EffectiveNP_3
JET_JER_EffectiveNP_6
JET_JER_EffectiveNP_7restTerm
JET_Flavor_Composition
JET_Flavor_Response
JET_Pileup_RhoTopology

---

**Table B.1.:** Significant experimental systematic uncertainties

### B.3. Unfolding Results

As anticipated, the unfolded result from the Asimov data test perfectly aligns with the truth distribution. Figure B.1 illustrates the uncertainty per group. Notably, all algorithms yield comparable outcomes for both background and experimental systematics.

When focusing on data statistics, the iterative Bayesian algorithm with 2 iterations yields the lowest uncertainty, whereas 10 iterations lead to the highest uncertainty. This observation aligns with expectations, as a smaller number of iterations corresponds to a highly regularised outcome, thereby reducing uncertainty. Conversely, with an increased number of iterations, the statistical uncertainty grows. In the case of infinite iterations, the uncertainty converges towards the maximum likelihood solution.

The profile likelihood and matrix inversion methods exhibit the largest uncertainties due to the absence of any regularisation. Furthermore, both methods yield similar results as they are algorithmically similar and provide maximum likelihood estimates. Consequently, it can be inferred that the `VIPUnfolding` and `TRExFitter` tools demonstrate consistent and reliable performance. In conclusion, this study validates the use of the unregularised profile likelihood method with `TRExFitter` for the analysis.

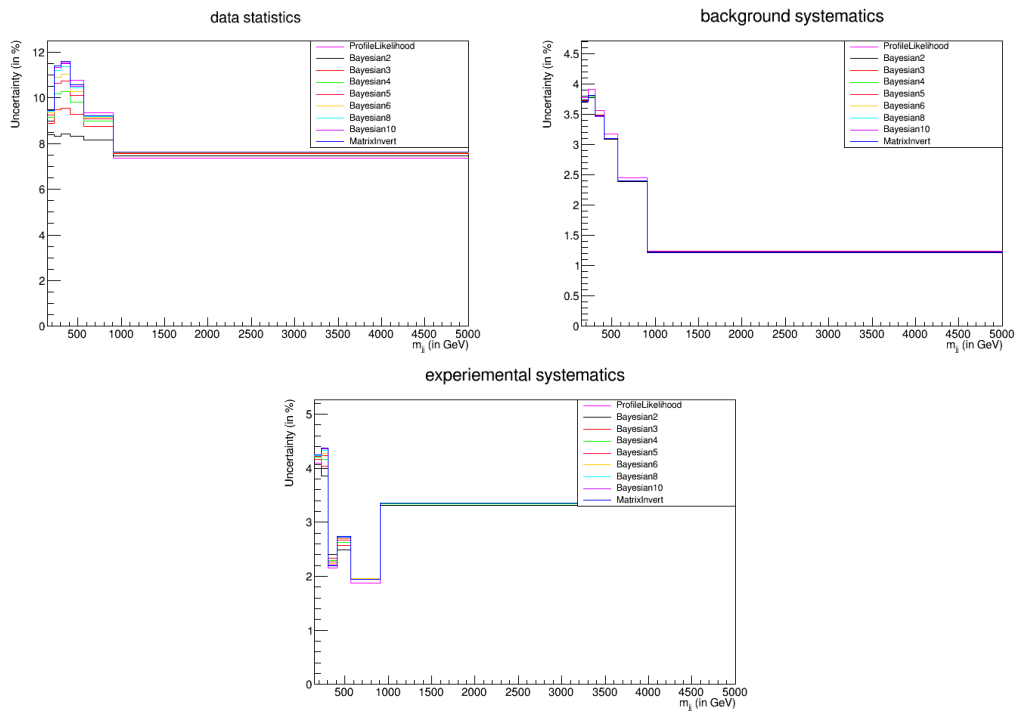


**Figure B.1.:** Uncertainty breakdown for the various algorithms under study. The number after "Bayesian" in the legend refers to the number of iterations.

# Bibliography

- [1] Mark Thomson. *Modern Particle Physics*. Cambridge University Press, 2013. ISBN 978-1107034266.
- [2] Michael E. Peskin and Daniel V. Schroeder. *An Introduction to Quantum Field Theory*. Westview Press, 1995. ISBN 978-0201503975.
- [3] Wolfgang Pauli. Über den zusammenhang des abschlusses der elektronengruppen im atom mit der komplexstruktur der spektren. *Zeitschrift für Physik*, 31:765, 1925.
- [4] Peter W. Higgs. Broken symmetries and the masses of gauge bosons. *Physical Review Letters*, 13:508, 1964.
- [5] C. D. Anderson. Positive electron. *Physical Review*, 43:491, 1933.
- [6] Samoil M. Bilenky and J. Hosek. Glashow-weinberg-salam theory of electroweak interactions and the neutral currents. *Physics Reports*, 90:73–157, 1982.
- [7] The UA1 Collaboration. Experimental observation of isolated large transverse energy electrons with associated missing energy at  $\sqrt{s} = 540$  gev. *Physics Letters B*, 122:103–116, 1983. URL <https://cds.cern.ch/record/142059/files/CM-P00059982.pdf>.
- [8] The UA2 Collaboration. Observation of single isolated electrons of high transverse momentum in events with missing transverse energy at the cern  $p\bar{p}$  collider. *Physics Letters B*, 122:476–485, 1983. URL <https://cds.cern.ch/record/142759/files/198303169.pdf>.
- [9] Emmy Noether. Invariant variation problems. *Gött. Nachr.*, 1918:235–257, 1918.
- [10] Tadao Nakano and Kazuhiko Nishijima. Charge independence for v-particles. *Progress of Theoretical Physics*, 10(5):581–582, 1953.
- [11] The UA1 Collaboration. Experimental observation of lepton pairs of invariant mass around 95 gev/ $c^2$  at the cern sps collider. *Physics Letters B*, 126:398–410, 1983. URL <https://cds.cern.ch/record/163857/files/198306331.pdf>.
- [12] The UA2 Collaboration. Evidence for  $z^0 \rightarrow e^+e^-$  at the cern  $p\bar{p}$  collider. *Physics Letters B*, 129:130–140, 1983. URL <https://cds.cern.ch/record/146503/files/198308375.pdf>.
- [13] François Englert and Robert Brout. Broken symmetry and the mass of gauge vector mesons. *Physical Review Letters*, 13:321–323, 1964.
- [14] A. Denner and T. Hahn. Radiative corrections to  $w^+w^- \rightarrow w^+w^-$  in the electroweak standard model. *Nuclear Physics B*, 525(1-2):27–50, 1998. URL <https://arxiv.org/pdf/hep-ph/9711302.pdf>.

- [15] The ATLAS Collaboration. Observation of a new particle in the search for the standard model higgs boson with the atlas detector at the lhc. *Physics Letters B*, 716:1–29, 2012. URL <https://cds.cern.ch/record/1471031/files/plb-716-1.pdf>.
- [16] The CMS Collaboration. Observation of a new boson at a mass of 125 gev with the cms experiment at the lhc. *Physics Letters B*, 716:30–61, 2012. URL <https://cds.cern.ch/record/1471016/files/plb.716.30.pdf>.
- [17] CERN. Lhc design report vol.1: The lhc main ring. June 2004. doi: 10.5170/CERN-2004-003-V-1.
- [18] The ATLAS Collaboration. The atlas experiment at the cern large hadron collider. *Journal of Instrumentation (JINST)*, 3, 2008. URL [https://cds.cern.ch/record/1129811/files/jinst8\\_08\\_s08003.pdf](https://cds.cern.ch/record/1129811/files/jinst8_08_s08003.pdf).
- [19] The CMS Collaboration. The cms experiment at the cern lhc. *Journal of Instrumentation (JINST)*, 3, 2008. URL [https://cds.cern.ch/record/1129810/files/jinst8\\_08\\_s08004.pdf](https://cds.cern.ch/record/1129810/files/jinst8_08_s08004.pdf).
- [20] Fabienne Marcastel. Cern’s accelerator complex. la chaîne des accélérateurs du cern. 2013. URL <https://cds.cern.ch/record/1621583>. General Photo.
- [21] The ALICE Collaboration. The alice experiment at the cern lhc. *Journal of Instrumentation (JINST)*, 3, 2008. URL [https://cds.cern.ch/record/1129812/files/jinst8\\_08\\_s08002.pdf](https://cds.cern.ch/record/1129812/files/jinst8_08_s08002.pdf).
- [22] Valerie Gibson. The LHCb Experiment. 2007. URL <https://cds.cern.ch/record/1425475>.
- [23] Stefaan Tavernier. *Experimental Techniques in Nuclear and Particle Physics*. Springer Berlin, Heidelberg, 2010. URL <https://doi.org/10.1007/978-3-642-00829-0>.
- [24] Apollinari. High-Luminosity Large Hadron Collider (HL-LHC) : Preliminary Design Report. 2015. URL <https://cds.cern.ch/record/2116337/files/CERN-2015-005.pdf>.
- [25] The ATLAS Collaboration. ATLAS Liquid Argon Calorimeter Phase-II Upgrade: Technical Design Report. 2017. URL <https://cds.cern.ch/record/2285582>.
- [26] Joao Pequenaio. Computer generated image of the whole ATLAS detector. 2008. URL <https://cds.cern.ch/record/1095924>.
- [27] Joao Pequenaio. Computer generated image of the ATLAS inner detector. 2008. URL <https://cds.cern.ch/record/1095926>.
- [28] J. Colas et al. Electronics calibration board for the ATLAS liquid argon calorimeters. *Nucl. Instrum. Meth. A*, 593:269–291, 2008.
- [29] The ATLAS Collaboration. Technical Design Report for the Phase-II Upgrade of the ATLAS Tile Calorimeter. 2017. URL <https://cds.cern.ch/record/2285583>.
- [30] Joao Pequenaio. Computer Generated image of the ATLAS calorimeter. 2008. URL <https://cds.cern.ch/record/1095927>.

- [31] Ilektra A. Christidi. The offline data quality monitoring system of the atlas muon spectrometer. *Journal of Physics: Conference Series*, 219, 2010. URL <https://iopscience.iop.org/article/10.1088/1742-6596/219/4/042035/pdf>.
- [32] The ATLAS Collaboration. Technical Design Report for the Phase-II Upgrade of the ATLAS Muon Spectrometer. . URL <https://cds.cern.ch/record/2285580>.
- [33] M. Aharrouche et al. Response uniformity of the atlas liquid argon electromagnetic calorimeter. *Nuclear Instruments and Methods in Physics Research Section A: Accelerators, Spectrometers, Detectors and Associated Equipment*, 2007. URL <https://arxiv.org/pdf/0709.1094.pdf>.
- [34] N. Massol et al. Atlas/lar calibration system. pages 302–306, 2004.
- [35] Zhaoxia Meng. Performance of the ATLAS liquid argon calorimeter. 2010. URL <http://www-library.desy.de/preparch/desy/proc/proc10-01/meng.pdf>.
- [36] M. Dentan et al. Dmill, a mixed analog-digital radiation-hard bicmos technology for high energy physics electronics. *IEEE Transactions on Nuclear Science*, 43:1763–1767, 1996. URL <https://hal.in2p3.fr/in2p3-00148999>.
- [37] N. Guettouche et al. The lpgbt production testing system. *Journal of Instrumentation*, 17, 2022. URL <https://dx.doi.org/10.1088/1748-0221/17/03/C03040>.
- [38] M. Delmastro et al. Liquid Argon Calibration Pulser ASIC (CLAROC) for HL-LHC: Specifications Document. Technical report, CERN, 2019. URL <https://cds.cern.ch/record/2681333>.
- [39] S. Blin et al. Measurements and results on the second Liquid Argon calibration ASIC prototype (CLAROCv2). Technical report, CERN, Geneva, 2021. URL <https://cds.cern.ch/record/2770628>.
- [40] H Abreu et al. Performance of the Electronic Readout of the ATLAS Liquid Argon Calorimeters. *JINST*, 5, 2010. URL <https://cds.cern.ch/record/1303004>.
- [41] M. Delmastro et al. Liquid argon calorimeter calibration board for Phase-II LHC upgrade: irradiation and test-bench measurements of the CLAROC preliminary 2018 switch ASIC. Technical report, CERN, Geneva, 2019. URL <https://cds.cern.ch/record/2693835>.
- [42] X-fab silicon foundries. URL <https://www.xfab.com>.
- [43] Taiwan Semiconductor Manufacturing Company Limited. URL <https://www.tsmc.com/english>.
- [44] Narei Lorenzo Martinez et al. Liquid Argon Calibration Board: Specifications Document for HL-LHC. Technical report, CERN, Geneva, 2022. URL <https://cds.cern.ch/record/2806656>.
- [45] J. Troska et al. The vtrx+, an optical link module for data transmission at hl-lhc. 2018. URL [https://cds.cern.ch/record/2312396/files/PoS\(TWEPP-17\)048.pdf](https://cds.cern.ch/record/2312396/files/PoS(TWEPP-17)048.pdf).
- [46] VishayDale. ISC1210ER120J. URL <https://www.vishay.com/docs/34060/isc1210.pdf>.

- [47] Mouser. S1812R-123G. URL <https://eu.mouser.com/datasheet/2/28/S1812-23080.pdf>.
- [48] F. Faccio et al. The bpol12v dc/dc converter for hl-lhc trackers: towards production readiness. 2020. URL [https://cds.cern.ch/record/2725200/files/PoS\(TWEPP2019\)070.pdf](https://cds.cern.ch/record/2725200/files/PoS(TWEPP2019)070.pdf).
- [49] LinearTechnology. LTM4619. URL <https://www.analog.com/media/en/technical-documentation/data-sheets/4619fc.pdf>.
- [50] National Instruments. Labview. URL <https://www.ni.com/en/shop/labview.html>.
- [51] The ATLAS Collaboration. Standard Model Summary Plots February 2022. Technical report, Geneva, 2022. URL <https://cds.cern.ch/record/2804061>.
- [52] Buarque Franzosi et al. Vector boson scattering processes: Status and prospects. *Reviews in Physics*, 2022. URL <http://dx.doi.org/10.1016/j.revip.2022.100071>.
- [53] The ATLAS Collaboration. Measurement of the cross-sections of the electroweak and total production of a  $Z\gamma$  pair in association with two jets in  $pp$  collisions at  $\sqrt{s} = 13$  TeV with the ATLAS detector. *Phys. Lett. B*, 846:138222, 2023. URL <https://inspirehep.net/literature/2663725>.
- [54] The ATLAS Collaboration. Studies of  $Z\gamma$  production in association with a high-mass dijet system in  $pp$  collisions at  $\sqrt{s} = 8$  TeV with the ATLAS detector. *JHEP*, 07:107, 2017. URL <https://inspirehep.net/literature/1598259>.
- [55] The CMS Collaboration. Measurement of the cross section for electroweak production of  $Z\gamma$  in association with two jets and constraints on anomalous quartic gauge couplings in proton-proton collisions at  $\sqrt{s} = 8$  TeV. *Phys. Lett. B*, 770:380–402, 2017. URL <https://inspirehep.net/literature/1512924>.
- [56] The ATLAS Collaboration. Evidence for electroweak production of two jets in association with a  $Z\gamma$  pair in  $pp$  collisions at  $\sqrt{s} = 13$  TeV with the ATLAS detector. *Phys. Lett. B*, 803:135341, 2020. URL <https://inspirehep.net/literature/1759885>.
- [57] The CMS Collaboration. Measurement of the cross section for electroweak production of a Z boson, a photon and two jets in proton-proton collisions at  $\sqrt{s} = 13$  TeV and constraints on anomalous quartic couplings. *JHEP*, 06:076, 2020. URL <https://inspirehep.net/literature/1781935>.
- [58] The CMS Collaboration. Measurement of the electroweak production of  $Z\gamma$  and two jets in proton-proton collisions at  $\sqrt{s} = 13$  TeV and constraints on anomalous quartic gauge couplings. *Phys. Rev. D*, 104:072001, 2021. URL <https://inspirehep.net/literature/1869513>.
- [59] The ATLAS Collaboration. Measurements of  $Z\gamma$ +jets differential cross sections in  $pp$  collisions at  $\sqrt{s} = 13$  TeV with the ATLAS detector. *JHEP*, 07:072, 2023. URL <https://inspirehep.net/literature/2614196>.
- [60] Schaelicke. Event generator for particle production in high-energy collisions. *Progress in Particle and Nuclear Physics*, 53:329–338, 2003. URL <https://arxiv.org/abs/hep-ph/0311270>.

- [61] Frank Siegert. Monte-Carlo event generation for the LHC, 2010. URL <http://etheses.dur.ac.uk/484/>.
- [62] Michael H. Seymour. Monte carlo for the lhc. 2010. URL <https://arxiv.org/abs/1008.2927>.
- [63] J. Alwall et al. The automated computation of tree-level and next-to-leading order differential cross sections, and their matching to parton shower simulations. *Journal of High Energy Physics*, 2014, 2014. URL [http://dx.doi.org/10.1007/JHEP07\(2014\)079](http://dx.doi.org/10.1007/JHEP07(2014)079).
- [64] Richard D. Ball et al. Parton distributions for the lhc run ii. *Journal of High Energy Physics*, 2015(4), 2015. URL [http://dx.doi.org/10.1007/JHEP04\(2015\)040](http://dx.doi.org/10.1007/JHEP04(2015)040).
- [65] Torbjörn Sjöstrand et al. An introduction to pythia 8.2. *Computer Physics Communications*, page 159–177, 2015. URL <http://dx.doi.org/10.1016/j.cpc.2015.01.024>.
- [66] ATLAS Pythia 8 tunes to 7 TeV data. Technical report, CERN, Geneva, 2014. URL <https://cds.cern.ch/record/1966419>.
- [67] Sherpa manual version 2.2.11. URL <https://sherpa.hepforge.org/doc/SHERPA-MC-2.2.11.html>.
- [68] Enrico Bothmann et al. Event generation with sherpa 2.2. *SciPost Physics*, 7, 2019. URL <http://dx.doi.org/10.21468/SciPostPhys.7.3.034>.
- [69] Stefan Höche et al. Qcd matrix elements + parton showers. the nlo case. *Journal of High Energy Physics*, (4), 2013. URL [http://dx.doi.org/10.1007/JHEP04\(2013\)027](http://dx.doi.org/10.1007/JHEP04(2013)027).
- [70] Stefano Catani et al. Qcd matrix elements + parton showers. *Journal of High Energy Physics*, (11):063–063, 2001. URL <http://dx.doi.org/10.1088/1126-6708/2001/11/063>.
- [71] Paolo Nason. A new method for combining nlo qcd with shower monte carlo algorithms. *Journal of High Energy Physics*, (11):040–040, 2004. URL <http://dx.doi.org/10.1088/1126-6708/2004/11/040>.
- [72] Stefano Frixione et al. Matching nlo qcd computations with parton shower simulations: the powheg method. *Journal of High Energy Physics*, (11):070–070, 2007. URL <http://dx.doi.org/10.1088/1126-6708/2007/11/070>.
- [73] Simone Alioli et al. A general framework for implementing nlo calculations in shower monte carlo programs: the powheg box. *Journal of High Energy Physics*, (6), 2010. URL [http://dx.doi.org/10.1007/JHEP06\(2010\)043](http://dx.doi.org/10.1007/JHEP06(2010)043).
- [74] Marco Guzzi et al. Ct10 parton distributions and other developments in the global qcd analysis. 2011. URL <https://arxiv.org/abs/1101.0561>.
- [75] Richard D. Ball et al. Parton distributions with lhc data. *Nuclear Physics B*, (2): 244–289, 2013. URL <http://dx.doi.org/10.1016/j.nuclphysb.2012.10.003>.
- [76] Joao Pequeno. How ATLAS detects particles: diagram of particle paths in the detector. 2013. URL <https://cds.cern.ch/record/1505342>.

- [77] Performance of the ATLAS Inner Detector Track and Vertex Reconstruction in the High Pile-Up LHC Environment. Technical report, CERN, Geneva, 2012. URL <https://cds.cern.ch/record/1435196>.
- [78] The ATLAS Collaboration. Topological cell clustering in the ATLAS calorimeters and its performance in LHC run 1. *The European Physical Journal C*, 77, 2017. URL <https://doi.org/10.1140/2Fepjc%2Fs10052-017-5004-5>.
- [79] The ATLAS Collaboration. Jet reconstruction and performance using particle flow with the ATLAS detector. *The European Physical Journal C*, 77, 2017. URL <https://doi.org/10.1140/2Fepjc%2Fs10052-017-5031-2>.
- [80] The ATLAS Collaboration. Electron and photon reconstruction and performance in ATLAS using a dynamical, topological cell clustering-based approach. Technical report, CERN, Geneva, 2017. URL <https://cds.cern.ch/record/2298955>.
- [81] The ATLAS Collaboration. Electron and photon performance measurements with the ATLAS detector using the 2015–2017 LHC proton-proton collision data. *Journal of Instrumentation*, 14:P12006–P12006, 2019. URL <https://doi.org/10.1088/2F1748-0221/2F14/2F12/2Fp12006>.
- [82] The ATLAS Collaboration. Muon reconstruction and identification efficiency in ATLAS using the full Run 2  $pp$  collision data set at  $\sqrt{s} = 13$  TeV. *Eur. Phys. J., C*, 81:578, 2021. URL <https://cds.cern.ch/record/2746302>.
- [83] The ATLAS Collaboration. Studies of the muon momentum calibration and performance of the atlas detector with  $pp$  collisions at  $\sqrt{s}=13$  tev, 2022. URL <https://arxiv.org/abs/2212.07338>.
- [84] Matteo Cacciari et al. The anti-ktjet clustering algorithm. *Journal of High Energy Physics*, 2008(04), 2008. URL <http://dx.doi.org/10.1088/1126-6708/2008/04/063>.
- [85] Matteo Cacciari et al. Fastjet user manual: (for version 3.0.2). *The European Physical Journal C*, 72(3), 2012. URL <http://dx.doi.org/10.1140/epjc/s10052-012-1896-2>.
- [86] The ATLAS Collaboration. Jet energy scale and resolution measured in proton–proton collisions at  $\sqrt{s} = 13$  TeV with the ATLAS detector. *Eur. Phys. J. C*, 81:689, 2021. URL <https://cds.cern.ch/record/2722869>.
- [87] The ATLAS Collaboration. Selection of jets produced in 13TeV proton-proton collisions with the ATLAS detector. Technical report, CERN, Geneva, 2015. URL <https://cds.cern.ch/record/2037702>.
- [88] The ATLAS Collaboration. Tagging and suppression of pileup jets with the ATLAS detector. Technical report, CERN, Geneva, 2014. URL <https://cds.cern.ch/record/1700870>.
- [89] The ATLAS Collaboration. Forward jet vertex tagging using the particle flow algorithm. Technical report, CERN, Geneva, 2019. URL <https://cds.cern.ch/record/2683100>.
- [90] The ATLAS Collaboration. ATLAS  $b$ -jet identification performance and efficiency measurement with  $t\bar{t}$  events in  $pp$  collisions at  $\sqrt{s} = 13$  TeV. *Eur. Phys. J. C*, 79(11): 970, 2019. URL <https://cds.cern.ch/record/2682119>.

- [91] Angela Maria Burger. Efficiency calibrations for ATLAS  $b$ -jet identification algorithms. Efficiency calibration for ATLAS  $b$ -jet identification algorithms. Technical report, CERN, Geneva, 2021. URL <https://cds.cern.ch/record/2743909>.
- [92] The ATLAS Collaboration. Measurement of the cross-section of the electroweak production of a  $Z\gamma$  pair in association with two jets in  $pp$  collisions at  $\sqrt{s} = 13$  TeV with the ATLAS detector. Technical report, CERN, Geneva, 2021. URL <https://cds.cern.ch/record/2779171>.
- [93] The ATLAS Collaboration. Performance of pile-up mitigation techniques for jets in  $pp$  collisions at  $\sqrt{s} = 8$  tev using the atlas detector. *The European Physical Journal C*, 76(11), . ISSN 1434-6052. URL <http://dx.doi.org/10.1140/epjc/s10052-016-4395-z>.
- [94] The ATLAS Collaboration. Luminosity determination in  $pp$  collisions at  $\sqrt{s}=13$  tev using the atlas detector at the lh. *The European Physical Journal C*, 14:P12006–P12006, 2022. URL <https://arxiv.org/abs/2212.09379>.
- [95] William Buttinger. Using Event Weights to account for differences in Instantaneous Luminosity and Trigger Prescale in Monte Carlo and Data. Technical report, CERN, Geneva, 2015. URL <https://cds.cern.ch/record/2014726>.
- [96] Jon Butterworth et al. PDF4LHC recommendations for LHC Run II. *J. Phys. G*, 43, 2016. URL <https://cds.cern.ch/record/2059563>.
- [97] Herwig++ physics and manual. *The European Physical Journal C*, 58(4):639–707, 2008. URL <http://dx.doi.org/10.1140/epjc/s10052-008-0798-9>.
- [98] J. Bellm et al. Herwig++ 2.7 release note, 2013. URL <https://arxiv.org/abs/1310.6877>.
- [99] Olympia Dartsis. Search for the electroweak production of  $Z\gamma$  pairs and measurement of the differential cross section of the  $Z\gamma$  production in association with two jets with the ATLAS experiment at LHC.. Recherche de la production électrofaible de paires  $Z\gamma$  et mesure de la section efficace différentielle de production de  $Z\gamma$  en association avec deux jets dans l’ATLAS expérience du LHC., 2019. URL <https://cds.cern.ch/record/2703156>.
- [100] The ATLAS Collaboration. Performance of electron and photon triggers in atlas during lh. run 2. *The European Physical Journal C*, 80(1), . URL <http://dx.doi.org/10.1140/epjc/s10052-019-7500-2>.
- [101] The ATLAS Collaboration. Performance of the atlas muon triggers in run 2. *Journal of Instrumentation*, 15(09), . URL <http://dx.doi.org/10.1088/1748-0221/15/09/p09015>.
- [102] D. Rainwater et al. Probing color-singlet exchange in  $z+2$ jet events at the cern lh. *Physical Review D*, 54(11):6680–6689, 1996. URL <https://doi.org/10.1103/2Fphysrevd.54.6680>.
- [103] The ATLAS Collaboration. Measurements of inclusive and differential fiducial cross-sections of  $t\bar{t}\gamma$  production in leptonic final states at  $\sqrt{s}=13$  tev in atlas. *The European Physical Journal C*, 79(5), 2019. URL <https://doi.org/10.1140/2Fepjc/2Fs10052-019-6849-6>.

- [104] Glen Cowan. *Statistical Data Analysis*. Clarendon Press, Oxford, 1998.
- [105] Kyle Cranmer. Practical statistics for the lhc, 2015. URL <https://arxiv.org/abs/1503.07622>.
- [106] Trexfitter. URL <https://trexfitter-docs.web.cern.ch/trexfitter-docs/>.
- [107] K. Cranmer et al. HistFactory: A tool for creating statistical models for use with RooFit and RooStats. Technical report, New York U., New York, 2012. URL <https://cds.cern.ch/record/1456844>.
- [108] *Proceedings of the 1974 CERN School of Computing: Godøysund, Norway 11 - 24 Aug 1974. 3rd CERN School of Computing*, Geneva, 1974. CERN. URL <https://cds.cern.ch/record/186223>.
- [109] A Armbruster et al. Practical considerations for unfolding. Technical report, CERN, Geneva, 2014. URL <https://cds.cern.ch/record/1694351>.
- [110] Giulio D’Agostini. A multidimensional unfolding method based on Bayes’ Theorem. Technical report, DESY, Hamburg, 1994. URL <https://cds.cern.ch/record/265717>.